AN OPTICAL INVESTIGATION OF DISI ENGINE COMBUSTION, FUEL SPRAY AND EMISSIONS AT COLD-START TEMPERATURES

By

Petros Efthymiou

MEng (Hons) DIS

A Doctoral Thesis submitted in partial fulfilment of the
requirements for the award of
Doctor of Philosophy of Loughborough University

2015

ABSTRACT

Particulate number (PN) standards in current and future emissions legislation pose a challenge for designers and calibrators during the warm-up phases of cold direct injection spark ignition (DISI) engines. To achieve catalyst light-off conditions in the shortest time, engine strategies are often employed that inherently use more fuel to attain higher exhaust temperatures. These can lead to the generation of locally fuel-rich regions within the combustion chamber and hence the formation and emission of particulates.

To meet these emissions requirements, further understanding of the DISI in-cylinder processes during cold-start are required. This thesis investigates the effect of cooling an optical research engine to temperatures as low as -7°C, one of the legislative test conditions. A high-speed 9 kHz optical investigation of the in-cylinder combustion and fuel spray along with in-cylinder pressure measurements was completed with the engine motored and fired at 1500 rpm during combustion conditions that were essentially homogeneous and stoichiometric.

Results showed significant differences between the flame growth structures at various operating temperature conditions with the notable presence of fuel-rich regions, which are understood to be prominent areas of particulate formation. Measured engine performance parameters such as indicated mean effective pressure (IMEP) and mass fraction burned (MFB) times correlated with the observed differences in combustion characteristics and flame growth speed. It was shown that flash boiling of the fuel spray was present in the fully heated engine case and significantly reduced the penetration of the spray plume and the likelihood of piston crown and cylinder liner impingement.

The flow and combustion processes of a transient production cold start-up strategy were analysed using high-speed particle image velocimetry (HSPIV). Results highlighted a broad range of flame structures and contrasting flame stoichiometry occurring at different times in the start-up process. Turbulent flow structures were identified that have an effect on the fuel spray development and combustion process as well as providing a path for cold-start emissions reduction.

PN and transient hydrocarbon (HC) emissions were measured at cold conditions to further elucidate the effect of operating temperature and correlate emissions data with in-cylinder measurements. A clear link between the quantity and size range of particulate and HC emissions and operating temperature was shown and the precise in-cylinder location of HC emissions, caused by fuel impingement, was inferred from the HC emissions data.

ACKNOWLEDGEMENTS

"Success is a journey, not a destination. The doing is often more important than the outcome"
Arthur R. Ashe

CONTENTS

NOMENCLATURE

Abbreviations

AFR   Air Fuel Ratio

AIT   After Ignition Timing

ASOI   After Start of Injection

ATDC   After Top Dead Centre

BDC   Bottom Dead Centre

BSFC   Brake Specific Fuel Consumption

BTDC   Before Top Dead Centre

CA   Crank Angle

CAE   Computer Aided Engineering

CCD   Charge-Coupled Device

CFD   Computational Fluid Dynamics

CI   Compression Ignition

CO_2 Carbon dioxide

COV   Coefficient of Variation

Da   Damköhlor number

DAQ   Data Acquisition

DI   Direct Injection

DISI   Direct Injection Spark Ignition

DPIV   Digital Particle Image Velocimetry

EGR   Exhaust Gas Recirculation

EIVC   Early Intake Valve Closing

EIVO   Early Intake Valve Opening

EU   European Union

FFT   Fast Fourier Transform

FID   Flame Ionisation Detector

HC   Hydrocarbon

HCCI   Homogeneous Charge Compression Ignition

HSPIV   High-Speed Particle Image Velocimetry

HWA   Hot Wire Anemometry

IC   Internal Combustion

IMEP   Indicated Mean Effective Pressure

IVC	Inlet Valve Closing
IVO	Inlet Valve Opening
LDA	Laser Doppler Anemometry
LDV	Laser Doppler Velocimetry
LES	Large Eddy Simulation
LEVC	Late Exhaust Valve Closing
LIF	Laser Induced Fluorescence
LII	Laser Induced Incandescence
LIVC	Late Intake Valve Closing
LIVO	Late Intake Valve Opening
LMV	Local Mean Velocity Decomposition
MFB	Mass Fraction Burned
NA	Naturally Aspirated
NEDC	New European Drive Cycle
NO_x	Nitrogen Oxides
NVH	Noise, Vibration and Harshness
PDA	Phase Doppler Anemometry
PFI	Port Fuel Injection
PIV	Particle Image Velocimetry
PLIF	Planar Laser Induced Fluorescence
PM	Particulate Matter
PN	Particulate Number
PPM	Parts Per Million
PV	Pressure-Volume
QPLIF	Quantitative Planar Laser Induced Fluorescence
RMS	Root Mean Square
RPM	Revolutions per minute
BSFC	Brake Specific Fuel Consumption
SCR	Selective Catalyst Reduction
SI	Spark Ignition
SMD	Sauter Mean Diameter
SR	Swirl Ratio
TDC	Top Dead Centre
TWC	Three-Way Catalyst
TR	Tumble Ratio

UHC	Unburned Hyrdocarbon	
VVA	Variable Valve Actuation	

Symbols

a	Crank Radius	[m]
a_p	Radius of Required Seeding Particle	[m]
A_c	Camera Chip Size	[m^2]
A_f	Flame Area	[m^2]
A_i	Imaged Area Size	[m^2]
B	Engine Bore	[m]
d_{diff}	Diffraction Limited Spot Size	[m]
d_p	Diameter of Seeding Particle	[m]
$f^{\#}$	F-Number of Camera Lens	-
f_{max}	Maximum Frequency of Flow Oscillations	[Hz]
f_u	Maximum Frequency Particles Can Follow	[Hz]
l	Connecting Rod Length	[m]
I	Number of Images	-
L	Engine Stroke	[m]
L	Size of Largest Eddies	[m]
M	Magnification Factor	-
n	Polytropic Index	-
P	Cylinder Pressure	[bar]
P_f	Flame Perimeter	[m]
P_{Max}	Maximum In-Cylinder Pressure	[bar]
P_n	Known Pressure	[bar]
P_{n+1}	Cylinder Pressure in Next Time Step	[bar]
Re	Reynolds Number	-
s	Distance between Crank Axis and Piston Pin Axis	[m]
S_f	Flame Growth Speed	[m·s^{-1}]
u	Mean Piston Speed	[m·s^{-1}]
$u'(\theta)$	RMS Velocity Fluctuation	[m·s^{-1}]
$\overline{U}_{(\theta,x,y)}$	Ensemble Average Velocity	[m·s^{-1}]
$U_{(\theta,i,x,y)}$	Instantaneous Velocity of Cycle	[m·s^{-1}]
υ	Kinematic Viscosity	[m^2·s^{-1}]
V	Cylinder Volume	[m^3]

V_C	Clearance Volume	[m^3]
V_{n+1}	Cylinder Volume in Next Time Step	[m^3]
V_S	Swept Volume	[m^3]
$\bar{x}$	Mean Across All Images	-
x_i	Pixel Intensity of Image I	-
ΔP	Change in Pressure	[bar]
ΔP_C^*	Normalised Change in Pressure due to Combustion	[bar]
η_k	Kolmogorov Scale	-
θ	Crank Angle	[°CA]
θ_{PMax}	Crank Angle Location of Maximum In-Cylinder Pressure	[°CA]
λ	Wavelength	[m]
μ_{fluid}	Viscosity of Fluid	[m·s^{-1}]
σ	Standard Deviation	-
ρ_p	Density of Seeding Particles	[kg·m^{-3}]

CHAPTER 1

INTRODUCTION

1.1   BACKGROUND AND LEGISLATION

There is an ever increasing need in the automotive industry to reduce vehicle carbon dioxide (CO_2) emissions by developing new and innovative engine technologies. Increasingly stringent European legislation has driven the average CO_2 emissions of passenger cars down from above 150 g $CO_2 \cdot km^{-1}$ in the year 2000 and targets average CO_2 emissions of 95 g $CO_2 \cdot km^{-1}$ by the year 2020 for petrol, diesel and alternative fuel vehicles (AFV) (Figure 1.1.1). The financial penalties for non-compliance of these emissions targets, along with industry competitiveness that strives for more fuel-efficient technologies, have forced manufacturers to devise novel methods to improve engine emissions.
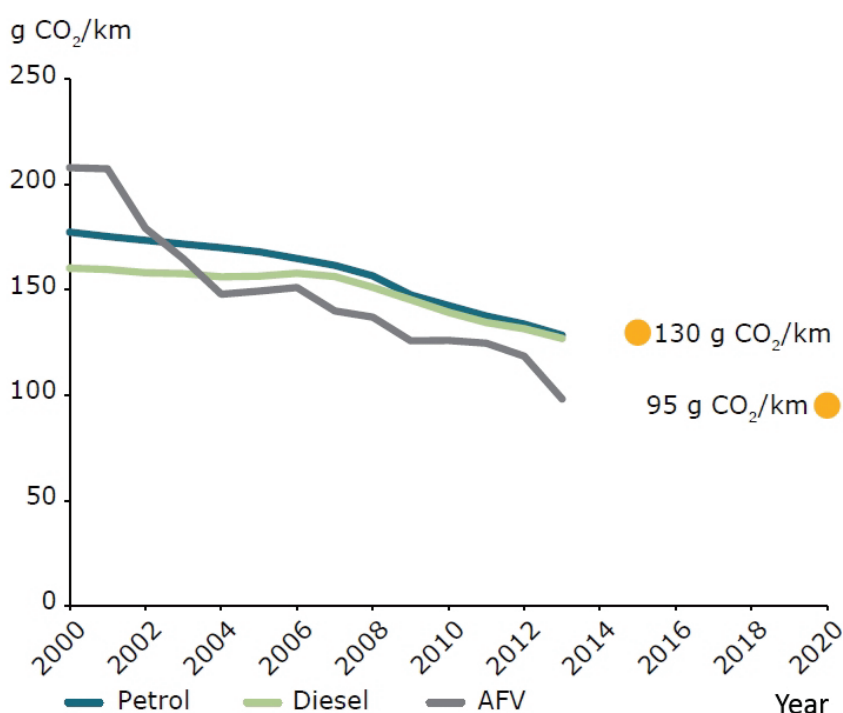
Figure 1.1.1: Average CO_2 emissions of new passenger cars by fuel type and EU targets by 2020 (adapted from European Environment Agency (EEA) (2014))

Direct injection spark ignition (DISI) engines meet many of the needs of these new emissions targets and hold the benefit of utilising existing internal combustion (IC) engine technologies. Alternative technologies such as hybrid engines, electric vehicles and fuel cells are undergoing a recent surge in popularity due to emissions legislation and changing consumer trends. Due to the extensive level of IC engine development, with their inherent low cost, high performance and high reliability, in addition to the continued prevalence of fossil fuels, it is likely that IC engine technology will remain on the forefront of engine development to allow manufacturers to meet legislative and consumer demands.

DISI engine technology holds a number of benefits over other engine technologies such as port fuel injected (PFI) engines, including improved fuel consumption and lower carbon dioxide emissions. These inherent advantages have been discussed in considerable detail in *Chapter 2*. More recently, DISI engine technology has been focussed on improving fuel consumption to bridge the gap to diesel engine technology through downsizing and downspeeding. In order to maintain powertrain performance, turbocharging is being widely introduced for gasoline engines, which, with DISI engine technology, facilitates higher compression ratios when compared to PFI engines (Berndorfer *et al.* 2013). A critical drawback, however, is that they emit higher quantities of combustion derived nanoparticulates (Zhao *et al.* 2002, Zhan *et al.* 2010, Piock *et al.* 2011, Berndorfer *et al.* 2013).

DISI engines operating under stoichiometric conditions have been able to fulfil all current global exhaust emissions requirements due to exhaust after-treatment systems based on the three-way catalyst (TWC) (Piock *et al.* 2011, Berndorfer *et al.* 2013). The Euro Stage 5a emissions standards released in September 2009 restricted particulate matter (PM) emissions (on a mass basis) on DISI engines for the first time (Table 1.1.1). Furthermore, recent Euro Stage 6 standards have introduced a particulate number (PN) count restriction on DISI engine technology, which will increase by an order of magnitude by 2017.

		Euro 4	Euro 5a	Euro 5b	Euro 6
	Units	Jan. 2005	Sept. 2009	Sept 2011	Sept 2014
CO	mg.km^{-1}	1000	1000	1000	1000
THC	mg.km^{-1}	100	100	100	100
NMHC	mg.km^{-1}	-	68	68	68
NO$_x$	mg.km^{-1}	80	60	60	60
CO	mg.km^{-1}	1000	1000	1000	1000
PM	mg.km^{-1}	-	5	4.5	4.5
PN	#.km^{-1}	-	-	-	***6 x 10^{11}**
*6 x 10^{12} within first three years from Euro 6 effective dates					

Table 1.1.1: EU emissions standards for passenger cars (EU regulation 715/2007). Data from DieselNet (2015)

Benchmarking activities by Berndorfer *et al.* (2013) have shown that current DISI engine technology does not meet the needs of Euro Stage 6 PN legislation, to be released in 2017, highlighting the significant development challenges of DISI engine technology.
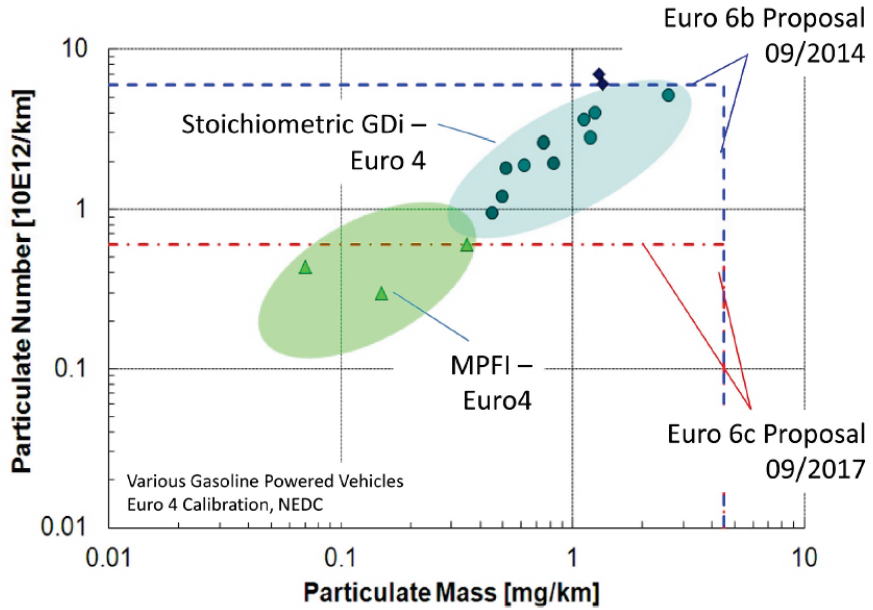
Figure 1.1.2: Particulate matter (PM) number and mass emissions legislation compared to current DISI engine system benchmarking results (Berndorfer *et al.* 2013)

It is well understood that the highest concentration of PN emissions in DISI engines occurs within the first 100 seconds of the Euro Stage 5 New European Drive Cycle (NEDC) (Piock *et al.* 2011, Whitaker *et al.* 2011, Berndorfer *et al.* 2013) whilst the engine is still at a cool operating temperature and during the first transient events as shown in Figure 1.1.3. This is further compounded by the fact that the TWC system has not yet achieved light-off temperatures, requiring combustion strategies that inherently need to generate high exhaust temperatures, but also generate high levels of PM.
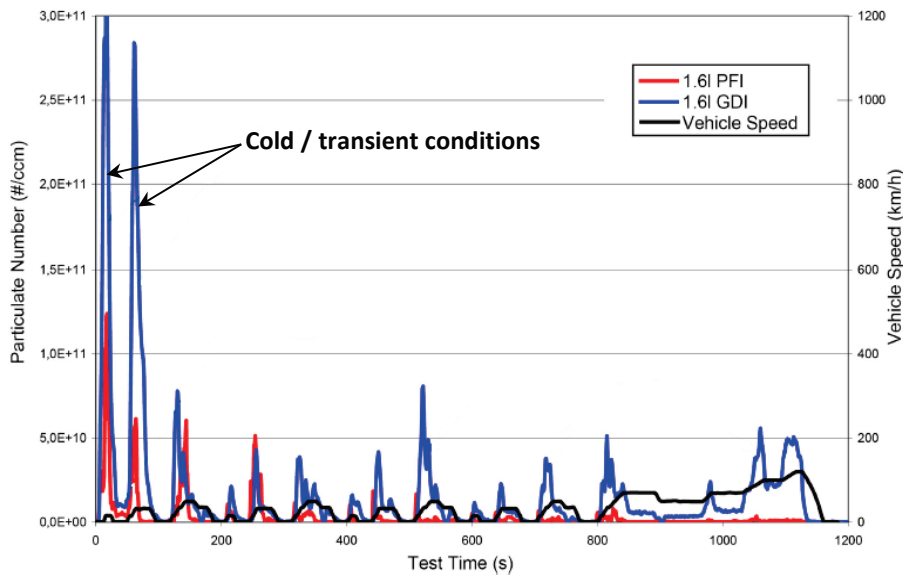
Figure 1.1.3: PN emissions plot during the Euro 5 NEDC comparing a DISI engine and PFI engine (adapted from Whitaker *et al.* (2011))

TWCs effectively reduce emissions of CO, HC and NO$_x$ by above 95% (Shelef and McCabe 2000, Gandhi *et al.* 2003) when they reach a typical light-off temperature of approximately 300°C (Shelef and McCabe 2000), but are markedly less effective below this temperature, so it essential that this operating condition is reached as soon as possible. It has also been shown that a TWC can reduce the total particle number density of volatile particles by up to 65% during a cold-start test (Whelan *et al.* 2013).

The importance of PM emissions from DISI engines and the current lack in meeting future emissions targets is widely acknowledged. There has been little optical research that analyses the in-cylinder physical processes within an optical engine during cold-start temperatures as low as -7°C. The modes of PM generation within DISI engines are generally understood, but little data exists precisely linking the complex interaction of the in-cylinder engine flow, fuel spray and combustion to particulate generation within the cylinder.

1.2   THESIS OVERVIEW

__Chapter 1__ of this thesis has identified DISI engine technology as an area of future development to meet the needs of reducing CO$_2$ emissions and other harmful greenhouse gases. The requirement of reducing PM emissions in DISI engine technology has been discussed and highlighted the prevalence of PM emissions during the cold-start and transient phases of a legislative drive cycle. Understanding the nature of PM generation within the cylinder will help engine designers and calibrators meet the challenges of stringent future emissions legislation.

__Chapter 2__ reviews the current literature surrounding DISI engine technology and research. Control methods that are used to regulate engine emissions are analysed to better understand the interaction between flow, fuel injection and combustion processes. Focus has been placed on experimental investigations but a concise review of numerical studies has been made. The subject of cold-start performance and the limitations of optical research in this area have been identified.

__Chapter 3__ describes the single cylinder optical research engine used to investigate the flow, injection, combustion and emissions processes. The optical diagnostics techniques used to analyse these areas are discussed, along with the imaging and illumination methods that facilitated them. An overview of the ancillary systems used to achieve the desired range of engine operating conditions is made. The experimental instrumentation of the emissions measurement equipment is also presented.

Chapter 4 investigates the effect of engine operating temperature on the in-cylinder combustion process within a DISI engine. High-speed flame imaging data observed through the optical piston crown is presented and processed into quantitative data. In-cylinder pressure measurements and engine performance data is discussed and correlated to the optical results.

Chapter 5 analyses the fuel injection process using laser illumination and high-speed imaging through the optical cylinder liner. Statistical processing of repeated fuel spray injection events are used to further understand the effect of engine operating temperature on the fuel spray structure, atomisation, vaporisation and surface impingement. These results are used to further interpret the combustion imaging data and engine performance data presented in *Chapter 4.*

Chapter 6 discusses the effect of in-cylinder flow structures during the intake and compression strokes of the DISI engine during a production cold start-up strategy. The subsequent combustion process is also analysed using colour optical imaging though the piston crown and in-cylinder pressure measurements. The complex stoichiometry of the flame is commented on and a number of particulate generation regions are identified throughout the cold-start process.

Chapter 7 presents PM and HC exhaust measurements over a range of engine operating temperatures to correlate previous results that indicated the presence of fuel-rich regions where PM generation was anticipated. Fast FID transient HC measurements allow the precise in-cylinder location of HCs to be recorded during individual exhaust strokes, allowing the effect of fuel impingement that was imaged in *Chapter 5* to be commented on.

Chapter 8 summarises the main conclusions from this research and discusses potential areas of further work in the field of DISI engine emissions during cold-start.

1.3   CONTRIBUTION TO KNOWLEDGE

The work presented in this thesis using the single cylinder DISI optical engine has contributed significantly to the understanding of DISI cold-start flow processes, fuel spray, combustion and emissions. These contributions include:

1. *High-speed combustion flame imaging and fuel spray visualisation within an optical DISI engine at cold-start temperatures as low as -7°C whilst simultaneously measuring in-cylinder pressure data.* This experimental investigation has highlighted the striking effect that cold-start engine operating temperatures have on the combustion process, fuel injection process and engine performance of a DISI engine. Results highlighted striking differences between the flame growth structures and fuel spray structures at different operating temperatures and the presence of fuel-rich regions in both the flame and fuel spray data. Engine performance was significantly affected by operating temperature and correlated with the optical measurements.

2. *The application of high-speed particle image velocimetry (HSPIV) and colour high-speed combustion imaging to a production NEDC engine cold start-up process whilst simultaneously measuring in-cylinder pressure data at cold-start temperatures.* This revealed a wealth understanding of the in-cylinder physical processes that occur during engine cold start-up. The complex and dynamic stoichiometry of the flame were highlighted and linked to in-cylinder pressure and engine performance data. The in-cylinder flow field measurements facilitated an improved understanding of their important contributory effect to fuel injection, transportation and mixing, as well as the subsequent combustion process during cold-start.

3. *The particulate matter (PM) emissions from a DISI engine operating at a range of cold-start temperatures as low as -7°C have been quantified in the particle size range of 5 nm – 1 µm alongside cycle-resolved HC emissions data.* The evolution of particle size and number concentration across an engine warm-up period has been described to give further insight into the origin of PM emissions. Detailed HC emissions data has allowed the precise in-cylinder location of HCs to be commented on and linked to the observed fuel spray impingement analysed in *Chapter 5.*

1.4   PUBLICATIONS ARISING FROM THIS WORK

EFTHYMIOU, P., DAVY, M., GARNER, C., HARGRAVE, G., RIMMER, J. E. T. & RICHARDSON, D. (2013) Insights into Cold-Start DISI Combustion in an Optical Engine Operating at −7°C. SAE. Int. J. Engines, Vol 6(2), pp. 1059-1074.

- Presented at the SAE World Congress in Detroit, Michigan, USA in April 16th - 18th 2013 and later published in the SAE International Journal of Engines in June 2013.
- Received the SAE Myers Award for Outstanding Student Paper in 2014.

EFTHYMIOU, P., DAVY, M. H., GARNER, C. P., HARGRAVE, G. K. & RIMMER, J. E. T. (2013) An optical investigation of a cold-start DISI engine startup strategy. IMechE: Fuel Systems for IC Engines, Vol 2013, pp. 33-52.

- Presented at the IMechE Internal Combustion Engines: Performance, Fuel Economy and Emissions Conference in London, UK in Novmeber 27th - 28th 2013.

EFTHYMIOU, P., GARNER, C. P., HARGRAVE, G. K. & RICHARDSON, D. (2015) An Optical Analysis of a DISI Engine Cold Start-Up Strategy. JSAE 2015 Powertrains, Fuels & Lubricants International Meeting, SAE Paper 2015-01-1877.

- Presented at the JSAE Powertrains, Fuels and Lubricants International Meeting in Kyoto, Japan in September 1st - 4th 2015.

1.5   CHAPTER 1 REFERENCES

BERNDORFER, A., BREUER, S., PIOCK, W. & BACHO, P. V. (2013) Diffusion Combustion Phenomena in GDi Engines caused by Injection Process, SAE Paper 2013-01-0261.

EUROPEAN ENVIRONMENT AGENCY (EEA) (2014) Monitoring CO_2 emissions from passenger cars and vans in 2013. *EEA Technical Report,* Vol 19(2014), pp. 14 - 30.

GANDHI, H. S., GRAHAM, G. W. & MCCABE, R. W. (2003) Automotive exhaust catalysis. *Journal of Catalysis,* Vol 216(2003), pp. 433-442.

PIOCK, W., HOFFMANN, G., BERNDORFER, A., SALEMI, P. & FUSSHOELLER, B. (2011) Strategies Towards Meeting Future Particulate Matter Emission Requirements in Homogeneous Gasoline Direct Injection Engines, SAE Paper 2011-01-1212.

SHELEF, M. & MCCABE, R. W. (2000) Twenty-five years after introduction of automotive catalysts: what next? *Catalysts Today,* Vol 62(2000), pp. 35-50.

WHELAN, I., TIMONEY, D., SMITH, W. & SAMUEL, S. (2013) The Effect of a Three-Way Catalytic Converter on Particulate Matter from a Gasoline Direct-Injection Engine During Cold-Start. *SAE Int. J. Engines,* Vol 6(2).

WHITAKER, P., KAPUS, P., OGRIS, M. & HOLLERER, P. (2011) Measures to Reduce Particulate Emissions from Gasoline DI engines, SAE Paper 2011-01-1219.

ZHAN, R., EAKLE, S. T. & WEBER, P. (2010) Simultaneous Reduction of PM, HC, CO and NOx Emissions from a GDI Engine, SAE Paper 2010-01-0365.

ZHAO, F., HARRINGTON, D. L. & LAI, M. C. (2002) *Automotive Gasoline Direct-Injection Engines*, SAE International, pp. 1-50, 166-188, 223-260.

CHAPTER 2

LITERATURE REVIEW

2.1   INTRODUCTION

This chapter discusses DISI engine operation in more detail and examines the complex combustion processes involved as well as their control techniques. Fundamental flow and combustion processes are described as well as the experimental techniques that are used to measure them. The control methods that are used to regulate engine emissions have been analysed in order to attain a better understanding of the complex in-cylinder flow, injection and combustion processes involved. New and novel approaches taken by other research groups have also been discussed. The aim of this chapter is to identify research areas that require further understanding and have the need for experimental investigation. By identifying these gaps in knowledge, research can be conducted to provide new information and useful findings for supporting other research groups and engine developers.

2.2   DISI ENGINE METHODOLOGY

Over the past 30 years, a major research goal in the automotive sector has been to develop internal combustion engines that combine the specific power of gasoline engines with the higher efficiency of diesel engines at part load, enabling brake specific fuel consumption (BSFC) approaching that of the diesel engine (Zhao *et al.* 2002). Significant contributions to this area of research have realised the best approach taken is using a four-stroke DISI engine with the potential to not throttle the intake mixture to control the load as in port fuel-injected (PFI) engines. At present, most major automobile manufacturers including BMW, General Motors, Ford, Jaguar, Volkswagen, Audi, Mazda and Porsche utilise DISI engine technology in their fleets.

In their methodology of operation, DISI gasoline engines have fundamental differences to PFI engines in the way the charge mixture is prepared and delivered into the cylinder. DISI engines inject fuel directly in the cylinder either during intake (e.g., homogeneous charge systems) or near TDC_{comp} (e.g., stratified charge systems), these modes are discussed in detail later in the literature review. PFI engines spray fuel into the inlet manifold upstream of the intake valves and use the intake flow to initiate the charge delivery to the cylinder. This has the potential to lead to significant wall wetting and in extreme cases such as cranking and cold-start, PFI engines can develop fuel films near the intake valves. In worst case scenarios, PFI engines operate on fuel metered from a pool rather than fuel delivered by the injector (Zhao and Lai 1995). Figure 2.2.1 illustrates the results of a study by Stanglmaier *et al.* (1999) observing the effect of hydrocarbon (HC) emissions when specific wall wetting locations are identified. It can be seen that certain locations such as the piston crown and exhaust side of the cylinder exhibit

higher HC emissions than others, which highlights the sensitivity of wall wetting on HC emissions and the importance of their control. Wall wetting can occur in the intake manifold and in-cylinder and is difficult to eliminate completely, especially during cold-start. This emphasises the importance of reducing wall wetting and highlights a potential operational advantage of DISI engines at this condition when compared to PFI engines.
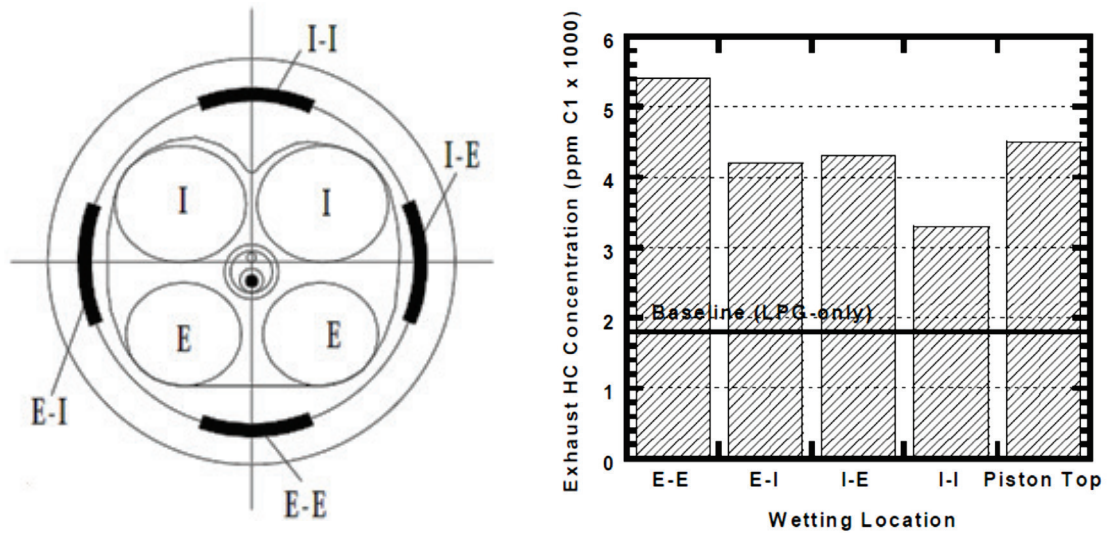
Figure 2.2.1: Effects of wall wetting location on HC emissions (Injection Timing = 160 °CA ATDC, 90°C coolant temperature) (adapted from Stanglmaier *et al.* (1999))

DISI engines hold a number of benefits over PFI engines that can lead to improvements in break specific fuel consumption (BSFC) as well as contributing towards improving exhaust emissions. A significant contributor is the reduction of pumping losses when stratified combustion is used during low-load requirements. In these stratified lean mixture systems, the charge is not throttled to control the load of the engine so the mechanical efficiency loss associated with throttle pumping work is eliminated. Fuel is injected directly into the cylinder, which produces a charge cooling effect and allows a higher knock-limited compression ratio to be used, resulting in a higher thermal efficiency. Direct injection also allows more precise fuel control that helps maintain a more consistent air-fuel ratio (AFR) and potentially reduces the chance of forming a rich charge mixture that can lead to significant CO and unburned HC emissions. Similarly, an accurately maintained stoichiometric mixture can ensure efficient and stable combustion that is especially important during initial cranking and transient loads. By having a precise and rapid response of the delivery of fuel into the cylinders, less acceleration enrichment is required due to the absence of a manifold fuel-film and improved load control enables more aggressive fuel cut-off during deceleration that in turn benefits BSFC (Zhao *et al.* 1999). These transient operation modes are of particular importance during the new European drive cycle (NEDC) legislative test, since, for example, it is well understood that a large

proportion of HC and particulate number (PN) emissions occur during the first few seconds when the engine is at a cold operating temperature and during the first transient events (Whitaker *et al.* 2011).

In order to promote charge mixing in the reduced mixture preparation time before combustion, DISI engine injection systems operate at high pressures (e.g., 150-200 bar) (Sanford *et al.* 2009, Spegar 2011). This has the benefit of improved fuel atomisation and vaporisation compared to PFI engines, producing average Sauter mean diameter (SMD) fuel droplet sizes of 16 μm compared to 120 μm (Zhao *et al.* 2002).

The factors discussed outlining the BSFC benefits of DISI engines when compared to PFI engines have been summarised in Table 2.2.1 listing identified improvements obtained by different research groups attributed to different factors. This shows that the advantages of DISI engine technology have the potential to be significant, with benefits in BSFC of up to 31% being reported.

Source	Cause	Kume *et al.* (1996)	Alkidas and Tahry (2003)
Reduced Pumping Losses	Less throttling	15%	10%
Improved Charge Mixing	Lean combustion	7%	7.5%
Higher Compression Ratio	Charge air cooling	4%	3%
Reduced Heat Losses	Lower temperature combustion	5%	2%
Fuel Delivery Response	Better transient operation	-	3.5%
Total		31%	26%

Table 2.2.1: Summary of DISI contributions to BSFC improvement when compared to PFI engines (Kume *et al.* 1996, Alkidas and Tahry 2003)

Despite increased legislative pressures, there is a continuing industry competitive requirement to improve vehicle performance, fuel economy and enhance existing products, particularly in the premium vehicle market. A study by Jaguar Cars Ltd outlined a market demand in 2010 for a 35% increase in engine performance compared to previous generation V8 engines in the 4.2 to 4.5 litre range (Sanford *et al.* 2009). This highlights the on-going future demand for DISI engine technology and inevitable industry investment in DISI engine architecture, including fuel injection systems, calibration and emissions control.

A number of drawbacks also exist in DISI engine technology. Whilst operating in a stratified combustion mode, despite having a globally decreased peak thermodynamic temperature, a higher NO_x formation rate is present due to the high temperatures within the rich core of the burning charge (Zhao *et al.* 2002). Potential methods of reducing NO_x in a DISI engine include exhaust gas recirculation (EGR) and lean NO_x aftertreatment technologies such as three-way catalyst (TWC) and urea-based selective catalyst reduction (SCR) systems. These ancillaries, however, will inevitably increase the complexity and cost of combustion and aftertreatment systems.

A critical drawback of DISI engines and an area of considerable research within the context of this literature review, are particulate number (PN) emissions. Compared to diesel engines and PFI engines, DISI engines emit a higher number of smaller sized particulates (generally < 100 nm) that consist not just of carbon, but high and low volatile compounds that depend highly on engine operating conditions (Price *et al.* 2007, Schreiber *et al.* 2007). As highlighted by Table 1.1.1 in *Chapter 1*, these PN emissions need to be addressed for current and future DISI engine technology, due to increasingly stringent legislation. Particulate filtering is an option but the inevitable requirements of nanoparticulate filters (such as regeneration) would introduce an increased complexity and cost to the after-treatment system. Also, a resultant higher exhaust gas flow back pressure would adversely affect engine performance. It is therefore the task of engine designers and researchers to combat these drawbacks using appropriate combustion systems and robust engine calibration, alongside new and novel techniques. It has been suggested that future targets can be met without the use of a particulate filter (Piock *et al.* 2011, Whitaker *et al.* 2011, Berndorfer *et al.* 2013).

The rest of this literature review analyses the research into engine flow and combustion, parameter control and engine measurement to identify critical areas of research that require further knowledge and understanding.

2.3   DISI ENGINE FLOW AND FUEL INJECTION

In order to optimise SI engines so that emissions targets can be met and performance demands can be maintained, a number of key shortcomings need to be overcome. For example, variability in intake flow structures, injection and combustion are major factors that limit engine optimisation. Reducing cycle-to-cycle variability is a key area of engine development and can facilitate the reduction of incomplete burning and emissions, as well as addressing knock and the resultant limitations on compression ratio. Figure 2.3.1 shows an in-cylinder pressure trace taken from the DISI optical research engine utilised in the investigation contained within this thesis and illustrates this cycle-to-cycle variability by highlighting a 5 bar difference in peak cylinder pressure over 100 engine cycles. This section analyses the distinctive flow, injection and combustion characteristics of DISI engines alongside the methods that have been employed in their control, in order to prepare an ideal in-cylinder charge for successful turbulent combustion.
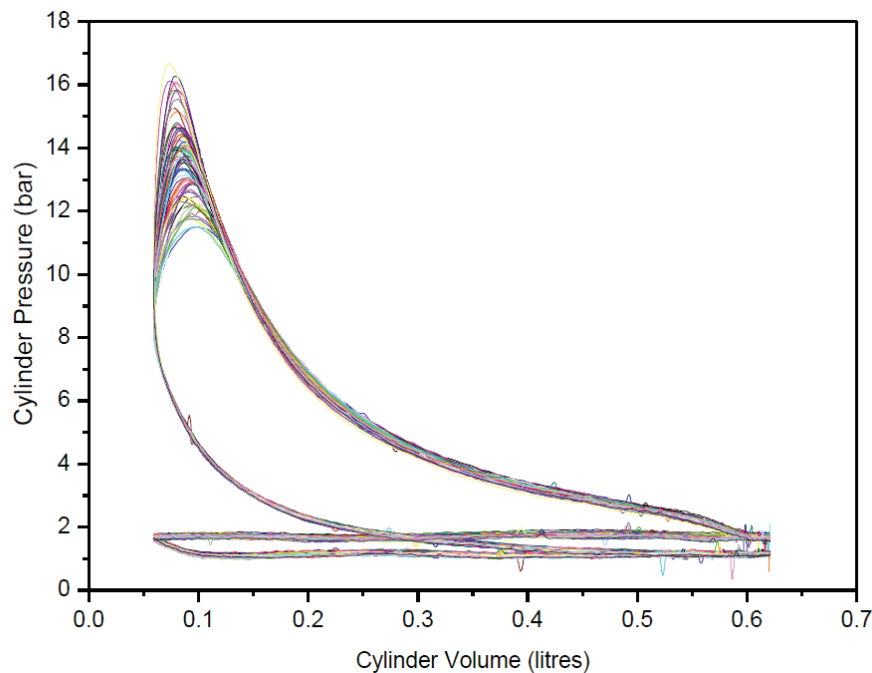
Figure 2.3.1: Pressure vs. volume graph from a DISI optical research engine highlighting variability in peak cylinder pressure

2.3.1   Intake Flow

The dominant in-cylinder flow structures that are present during intake and combustion are critical to the successful operation of a DISI engine. These structures control important parameters such as air-fuel mixing, fuel vaporisation and turbulence generation that are of paramount importance for rapid flame propagation in SI engines to deliver maximum work output (Heywood 1988, Rimmer *et al.* 2009).

Most IC engines utilise spring-loaded poppet valves controlled by the engine camshaft. These are of relatively low cost and have good sealing characteristics. The maximum distance the valve opens (valve lift) is typically 5 to 10 mm for automobile engines (Pulkrabek 2004). Annand and Roe (1974) outline the flow through a valve and its geometric parameters in Figure 2.3.2. At low valve lifts, the conical jet flow is attached to the valve head and seat and its direction is influenced strongly by the seat width and angle. The flow in this case has a high discharge coefficient, C_D, which is defined as

$$C_D = \frac{A_e}{A_c}$$

<div align="right">Eqn. (2.3.1)</div>

where A_e is the effective flow area, defined by the separated flow and A_c is the curtain area, defined by the physical geometry of the orifice area.

The small effective flow area relative to the port and the large pressure difference during this early phase of induction create high velocities that are approximately 10 times the mean piston speed (Heywood 1988). The high velocity in-cylinder flow and shear that is produced forms the basis of bulk flow vortex structures such as tumble and swirl, these are described in more detail in later sections of this literature review.

At intermediate valve lifts, the flow separates from the surface of the valve head at its corners and the actual flow area is less than the available geometric area giving the flow a lower discharge coefficient (Figure 2.3.2). At high valve lifts the flow is influenced less by the valve geometry until a free jet is formed, the properties of which are influenced predominantly by the intake port and upstream manifold geometry. The understanding of detailed intake flow around the valves is of importance to researchers and engine designers. Computational fluid dynamics (CFD) turbulence models use the accurate prediction of the discharge coefficient to accurately predict the main flow characteristics and as such, place emphasis on correctly predicting the discharge coefficient as shown by Bianchi *et al.* (2002).

Intake valve flow experiments have been predominantly carried out on steady flow rigs with upstream diffusers and settling chambers to reduce the effect of turbulence. The transition points between attached, separated and free flow have been studied in detail by Annand and Roe (1974) who concluded that a 30° seat angle with a minimum width seat with a 10° angle at the upstream surface gives the best results. Figure 2.3.2 shows these transition points and how the discharge coefficient varies with valve lift. The effective flow area is shown to reach a maximum when the non-dimensional valve lift is approximately 0.23 (Annand and Roe 1974).
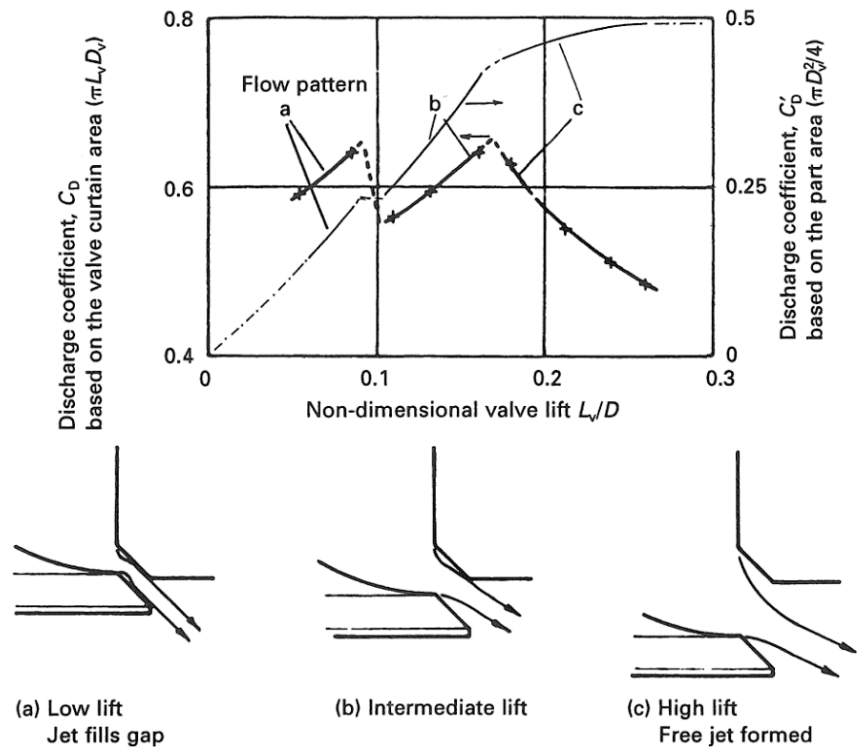
Figure 2.3.2: Flow characteristics of outlining discharge coefficient, CD, against valve lift and schematic of air flow through an intake valves with different lifts (Annand and Roe 1974))

As mentioned previously, the in-cylinder velocity field around the intake ports is known to have an important effect on fuel mixing and turbulence, as well as contributing to cycle-to-cycle variation. A particle image velocimetry (PIV) study was conducted in this area by Lee and Farrell (1993) for four different valve lift positions at 150 rpm and 300 rpm. Thin intake jets were observed from the valve edge that expanded as they travelled further into the cylinder volume. Several vortices were observed at the edge of these jets, which entrained the ambient air into the main jet stream. These were caused by the high levels of shear from the interaction between the high velocity jet flow and stationary ambient air. Yasar *et al.* (2006) conducted more detailed experimentation at higher engine speeds up to 2500 rpm and showed similar flow structure results as outlined in Figure 2.3.3. These illustrations show the rotation of two main counter-rotating vortices created from each side of the valve emphasising the significant effect of the shear layer caused by the jets. These form the basis of bulk in-cylinder tumble motion and were confirmed by (Stansfield *et al.* 2007b). Cycle-to-cycle variations in the flow were consistently observed throughout these studies in regions such as the jet boundary, but flow with a higher velocity, such as near the valve jets, were consistently shown to behave more repeatably.

These studies have shown the fundamental effect that the conical valve jets have on the formation of bulk in-cylinder flow structures that affect the subsequent injection and combustion events in an engine. However, it is the subsequent dissipation of these bulk in-cylinder structures into small scale turbulence structures that has a dominant effect on engine performance as shown by Rimmer *et al.* (2009). It was discovered that it is the small scale structures with frequency fluctuations above 600 Hz that predominantly influence indicated mean effective pressure (IMEP) and burn rate.

Instantaneous **Time-averaged**
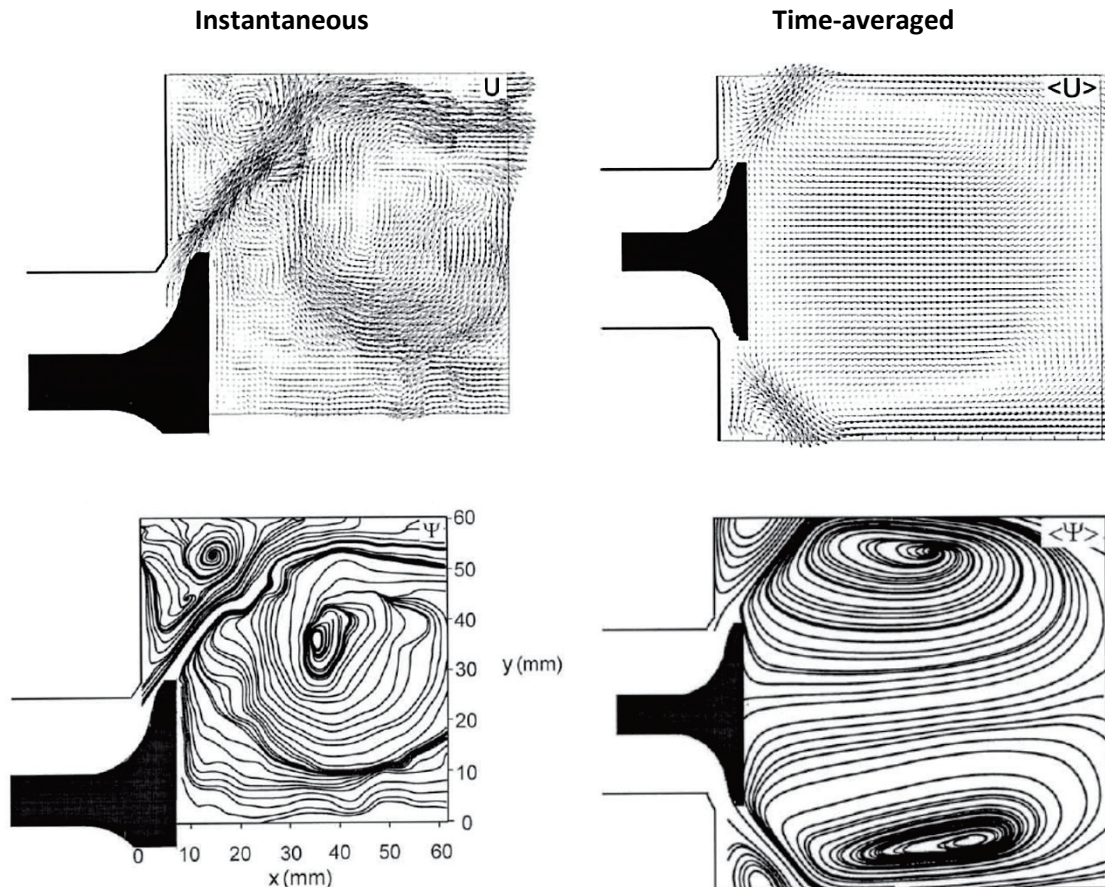
Figure 2.3.3: Instantaneous and time-average PIV velocity vectors and streamline topology for a 7 mm valve lift (L/D = 0.12) (adapted from Yasar *et al.* (2006))

The flow upstream of the valves has also been shown to have an effect on the subsequent in-cylinder flow field. Justham *et al.* (2006a, 2006b) investigated this intake region using PIV at engine speeds of 1500 rpm in a single cylinder optical research engine. Relationships were highlighted between cycle-to-cycle variations in the intake manifold and in-cylinder flows, whereby variation in the intake manifold later affected the in-cylinder bulk flow structures, albeit not as predominantly as the valve itself. Further work from Justham (2010) used high-speed PIV (HSPIV) at 5 kHz to observe the temporal flow field development in the intake manifold. Turbulence oscillations in the intake manifold flow were observed along with the

presence of backflow that contributed to variations in the intake bulk flow. Despite these variations not having a dominant influence on the intake flow, their presence contributes to the global cycle-to-cycle variability in an engine's in-cylinder flow field.

Developments in experimental PIV equipment and the use of HSPIV have allowed the decomposition of time-resolved flow fields and an improved understanding of the turbulent behaviour around the intake valves. Kapitza *et al.* (2010) studied the transient flow behaviour and flow fluctuations in the intake port of a 1.6 litre 4-cylinder production cylinder head using 10 kHz stereoscopic HSPIV. Fast Fourier transform (FFT) frequency analysis was used to identify the origins of the main flow fluctuations. It was shown that the transient flow behaviour was predominantly caused by the interaction between vortices (varying in magnitude and position) and the wavelike fluctuations of valve jet flow near the walls. The levels of fluctuation in these transient flows were shown to be caused by increasing mass flow and decreasing valve lift. This type of analysis allows a progression in the understanding of transient intake flow that can be utilised to achieve better influence transient flow behaviour.

2.3.2 Variable Valve Actuation and Lift

Valve timing events, particularly in SI engines, influence engine performance, efficiency and emissions due to the effect of pumping losses from partially open valves and throttling. Like compression ignition Diesel engines, DISI engines have the potential to operate without throttling, in stratified operation. The development of variable valve actuation (VVA) systems presents the potential for these engines to operate without a throttle. The following section discusses the four main valve opening and closing strategies and their effect on an engine.

Early intake valve closing (EIVC) reduces the mass of charge in the cylinder by closing the valve early in the intake stroke. This results in reduced pumping losses due to reduced charge induction and the negative area represented in the corresponding PV diagram (Figure 2.3.4) is reduced. A 40% reduction in pumping losses compared to a conventional engine with a throttle has been achieved that can lead to a 7% reduction in brake specific fuel consumption (BSFC) and a 24% reduction in NO_x at part load (Tuttle 1982). This strategy also holds potential for generating ideal sprays, particularly in high-pressure DISI injection systems. EIVC can lower the in-cylinder pressure to below the saturation pressure of the fuel and induce flash boiling during injection. Xu *et al.* (2013) demonstrated this technique can be used to reduce fuel spray droplet size, shorten penetration and increase fuel spray dispersion in a DISI engine. These effects are of particular significance during cold-start, when fuel rail pressure is not fully

developed and fuel spray penetration needs to be minimised to reduce cold-surface impingement.

Late intake valve closing (LIVC) delays the closure of the intake valves until a point within the compression stroke, which expels some of the charge back into the intake manifold. The charge expelled back into intake manifold is at a slightly higher pressure than atmospheric, due to compression and the subsequent stroke will induct a charge with higher pressure, reducing pumping losses. At higher engine speeds, LIVC offers the benefit of improved volumetric efficiency as the higher intake air momentum continues to charge the cylinder during compression (Asmus 1982). As with EIVC, a 40% reduction in pumping losses has been reported at part load conditions using this strategy as well as a reduction in NO_x emissions (Tuttle 1982).
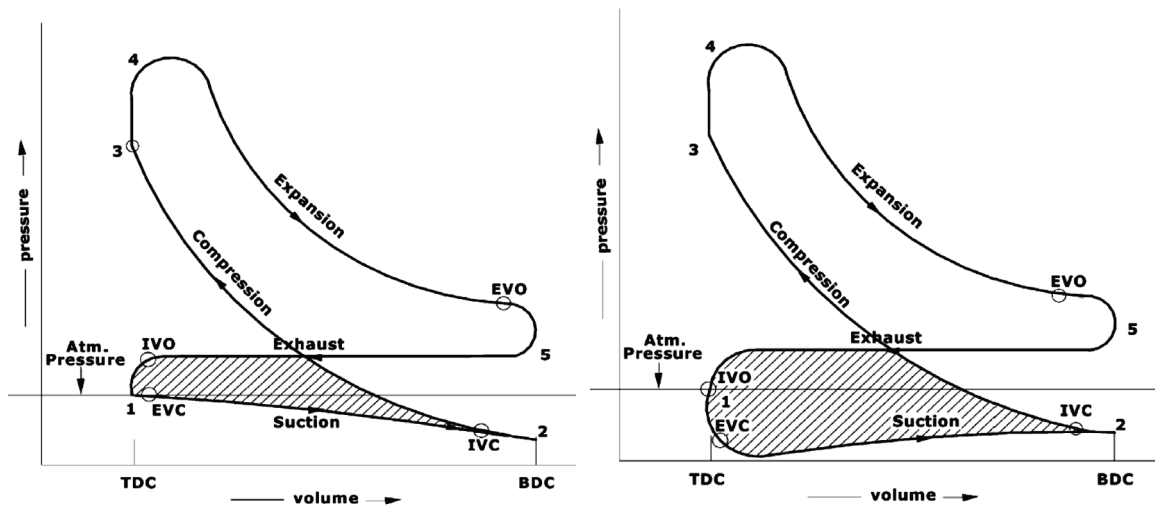
Figure 2.3.4: PV diagrams for early intake valve closure (EIVC) and late intake valve opening (LIVO) (adapted from Hong *et al.* (2004))

Late intake valve opening (LIVO) delays the induction of air into the cylinder and increases the pressure difference between the cylinder and the intake manifold. Pumping losses will actually be increased as illustrated in Figure 2.3.4 with the larger negative work loop area. Volumetric efficiency will not be affected, however, as the complete mass of the charge will eventually be drawn into the cylinder at a higher velocity. As a result, benefits can be seen in the creation of turbulence in the charge mixture, which assists fast and efficient combustion (Stone *et al.* 1993, Reeves *et al.* 1999, Rimmer *et al.* 2009) and is considered an effective technique to reduce unburned hydrocarbon (UHC) emissions (Hong *et al.* 2004, Morita *et al.* 2005). The creation of turbulence in the intake stroke is essential in enhancing the air-fuel mixing process and improving the evaporation of fuel (Rimmer *et al.* 2012), creating a more homogeneous charge mixture. Furthermore, the dissipation of bulk air flow into high-frequency turbulence

during compression increases the interaction between the flame and unburned charge promoting rapid flame propagation in SI engines (Heywood 1988).

LIVO has the added benefit of being able to induce flash boiling of fuel by injecting into cylinder pressures lower than that of the fuel's saturation pressure. Xu *et al.* (2013) showed that flash boiled sprays had smaller droplet sizes, shorter penetration and quicker evaporation rates without the need for higher pressure injection systems. The present author (Efthymiou *et al.* 2013) confirmed the benefits of flash boiling sprays during cold-start conditions of -7°C. Lower penetration, due to less fuel spray momentum and improved atomisation resulted in a reduction in cold-surface impingement and contributed to a more homogeneous charge and flame structure and improved engine performance. Flash boiling strategies offer an alternative approach to higher injection pressures and negate the added complexity and higher costs associated with them.

Early intake valve opening (EIVO) increases the amount of exhaust residuals in the intake and the level of internal EGR that has the potential to reduce NO_x due to a reduction of peak flame temperatures in subsequent combustion events. Late exhaust valve closing (LEVC) produces similar effects to EIVO. Morita *et al.* (2005) utilised a variable valve timing (VVT) system along with a spark retardation strategy to reduce HC emissions by a total of 3 g.kWh^{-1}, this strategy is discussed in more detail later in this literature review.

As well as valve scheduling, other valve control strategies have been utilised to influence the flow and subsequent combustion in SI engines. Wilson *et al.* (2005) investigated the effect of short duration negative valve overlap using PIV in a homogeneous charge compression ignition (HCCI) research engine. Peak flow velocities were shown to be up to three times higher and flow fluctuations increased by 50% during the compressions stroke (when compared to typical valve overlapping strategies in SI engines). These increased flow fluctuations highlight the potential benefits to a DISI engine operating in a homogeneous mode, as increased turbulence offers improved mixture preparation and homogeneity in the charge. Low lift and the complete deactivation of a single valve can also have potential benefits, as later investigated by Patel *et al.* (2008). A low lift valve strategy was shown to exhibit faster burn speeds and reduced HC, NO_x, CO emissions by approximately 25% whilst a single valve strategy improved fuel consumption and reduced PM emissions substantially. These benefits were seen to be amplified at low load cases highlighting the benefit of these strategies during cold engine start-up.

Future legislative emissions levels have been mentioned as one of the critical challenges facing engine designers and the discussed strategies have shown potential for their improvement. The majority of system design and engine operating variables, however, are interdependent, thus a proposed alteration of a component or strategy must be examined to evaluate the very important compromise between performance, fuel economy and emissions (Zhao *et al.* 2002).

2.3.3   Fuel Injection

The control and optimisation of fuel injection durations and timing parameters facilitates the good transient response that is inherent in DISI engines. A number of manufacturers and researchers have implemented injection strategies such as multiple injection, which during cold-start has been shown to improve combustion stability and reduce emissions.

Three main atomisation concepts for DISI injectors are currently available, swirl, outward opening and multi-hole. While the swirl-type injector has been widespread for first generation DISI engines it is now increasingly being replaced by multi-hole fuel injectors for homogeneous combustion systems (Stach *et al.* 2007).

Swirl injectors can induce the presence of a transient phase pre-spray that is created at the beginning of an injection event due to fuel trapped in tangential slots from the previous injection event that consequently lack high swirl (Chryssakis *et al.* 2003). This solid cone pre-spray structure can generate large fuel droplets, resulting in high HC emissions. A laser induced fluorescence (LIF) study by Ahmed *et al.* (2010) confirmed the presence of liquid fuel droplets and also showed that the spray plume was more affected by changes in cylinder pressure. Moreover, the dynamic variations of fuel spray structure, such as spray collapse, when engine operating conditions change, have the potential to cause engine misfire (Ahmed *et al.* 2010). A comparison between injector types and their parameters has been made by Stach *et al.* (2007) and is shown in Figure 2.3.5. While similarities are present in spray quality, in terms of fuel atomisation, multi-hole injectors were shown to have advantages in terms of spray flexibility, backpressure influence and cost. These findings, however, will be highly dependent on spray pattern, which is of fundamental importance to multi-hole injectors. The combustion mode also affects the performance of injectors, for example, an injector's resistance to backpressure is not so relevant to early fuel injection in homogeneous DISI combustion systems.

The spray from early multi-hole injectors was shown by Tomoda *et al.* (1997) to be more stable and repeatable, but have a wider range of droplet size distribution when compared to swirl injectors. More recently, with the development of multi-hole injection systems from

companies such as Bosch, it has become possible to increase injection pressure up to 200 bar (Lee *et al.* 2013) and stabilise the Sauter mean diameter (SMD) of fuel droplets to 14-19 μm and eliminate large droplets such as those found within the pre-spray of swirl injectors (Ahmed *et al.* 2010).

	Swirl	Outward Opening	Multi-Hole
Spray Stability / Tolerance	+	++	+
Flexibility of Spray Pattern	+	O	++
Multi-Injection capability	O	+	O
Costs	O	-	+
Robustness against plugging	+	+	+

Figure 2.3.5: Atomisation techniques for DISI fuel injectors (adapted from (Stach *et al.* 2007))

In its fundamental form, fuel injection control in homogeneous charge DISI engines involves controlling the quantity and pressure of fuel delivered to achieve the required combustion conditions, controlling the trajectory of the spray and controlling the timing of the spray to optimise the balance between mixture preparation time and combustion chamber surface impingement. Figure 2.3.6 illustrates the effect of injector timing in a spray-guided DISI engine with a centrally mounted fuel injector and homogeneous combustion mode. The requirements of the fuel spray in homogeneous combustion systems are as early injection as possible to increase vaporisation and mixture preparation time, along with a well atomised and dispersed spray to increase mixing, decrease penetration and avoid piston impingement (Kume *et al.* 1996, Zhao *et al.* 2002, Xu *et al.* 2013). Kume *et al.* (1996) suggested such a timing strategy whereby the spray 'chases' the piston to avoid surface impingement. A range of fuel droplet sizes are also preferable to ensure an adequate range of penetration into the cylinder to facilitate good charge mixing.
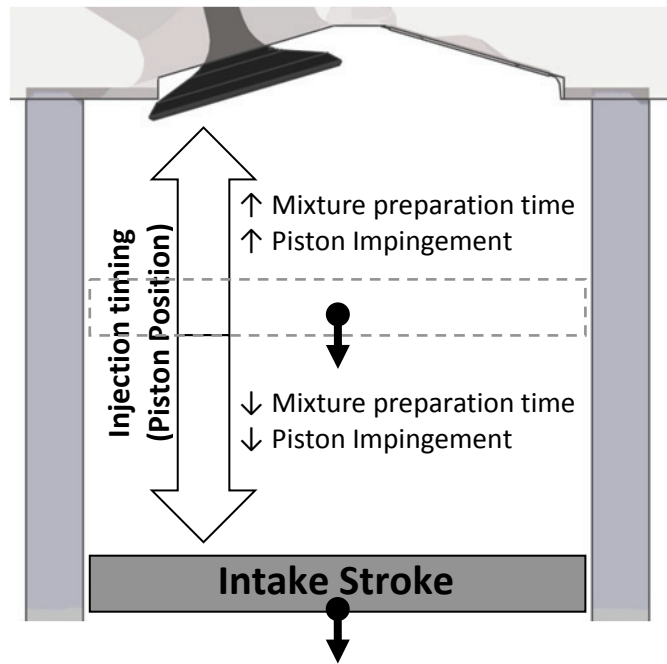
Figure 2.3.6: Injection timing schematic highlighting mixture preparation and piston impingement during induction stroke

Figure 2.3.7 highlights the importance of fuel injection pressure with images from an AVL optical engine at cold-start. The improvements in atomisation are clearly illustrated with an increasing fuel injection pressure up to 15 MPa (150 bar) showing a significant improvement of atomisation and reduced presence of liquid fuel. Whilst increasing pressure improves atomisation and evaporation, which can decrease PM generation due to improved mixture quality, the penetration depth increases, which can increase the likelihood of piston impingement (Whitaker *et al.* 2011). Penetration depth, however, is limited and highly dependent on fuel particle size and breakup. A number of researchers have extensively analysed and predicted sprays in diesel engines, indicating that spray penetration is approximately proportional to the square root of time after injection (Schweitzer 1938, Xu *et al.* 1992). The effect of better atomisation due to higher injection pressure will also determine penetration, since smaller fuel spray droplets will have less momentum due to their reduced mass and hence penetration.
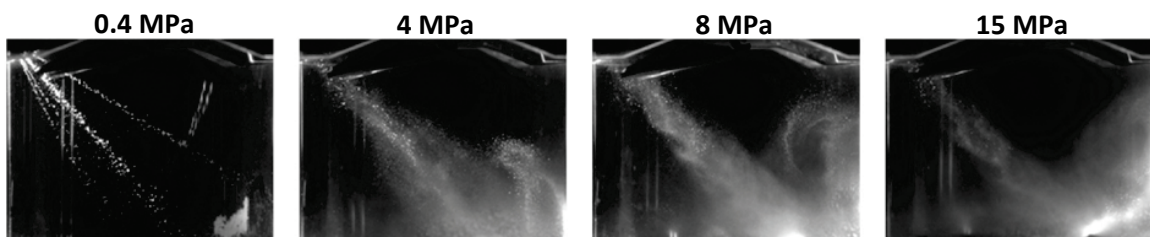
Figure 2.3.7: Laser Induced Fluorescence (LIF) images of fuel spray using an AVL optical engine at increasing fuel pressures at 250 rpm, multi-hole injector, first injection for cold-start particulate optimisation (Whitaker *et al.* 2011)

2.3.4 Fuel Spray and Air Flow Interaction

The interaction of the fuel spray with the broad range and scales of air flow structure and turbulence are fundamental for adequate charge mixing and vaporisation. The limited time available in DISI engines (when compared to PFI) exemplifies the importance of charge preparation in providing successful combustion and minimising exhaust emissions.

The interaction of the fuel spray with the in-cylinder flow at a range of injection timings was investigated by Davy et $al.$ (1998) who showed that early injections (up to 60 °CA ATDC$_{Intake)}$) were unaffected by intake flow structures. This was hypothesised to be due to the relatively low flow momentum at this time during the intake stroke, despite the flow structures during early intake having a considerably high velocity magnitude due to the small effective flow area and large pressure difference across the intake valves (Reeves et $al.$ 1999, Jarvis et $al.$ 2006). It is likely that the high velocity of the fuel spray and short time for flow to take effect are dominant factors as to why earlier injections are less affected.

With injection timings nearer that of modern homogeneous charge combustion systems (90 to 120 °CA ATDC$_{Intake}$), Davy et $al.$ (1998) demonstrated that injected sprays were deflected away from the intake side of the cylinder due to the more developed bulk flow vortex structures and higher intake momentum. Stansfield et $al.$ (2007b) confirmed these bulk flow structures using PIV, which showed the effect of the conical vortex jets forming two distinct vortices (Figure 2.3.8). Path 1 forms the inherent tumble flow in pent-roof combustion systems (this is discussed in more detail in Section 2.7 of this literature review). Spray structures during 150 – 210 °CA ATDC$_{Intake}$ injection were shown to be influenced considerably more by developed bulk flow structures, which can be attributed to tumble flow, whilst injections during the compression stroke were shown to be influenced far less, due to the decay of bulk flow structures around this time (Rimmer et $al.$ 2009). Steady-state flow experimentation has been used to attain a more fundamental understanding of fuel spray interaction with engine flow. Choi et $al.$ (2000) used 17 m·s^{-1} cross flow velocities inside a cylinder to simulate the in-cylinder mean velocity during injection. As cross flow velocity was increased, the intensity of the Mie scattered images of the spray decreased and it was concluded that the rate of vaporisation had increased. The spray width and main spray penetration was shown to be unaffected but the spray drift at the tip of the plume was measured to be approximately 2 m·s^{-1}.
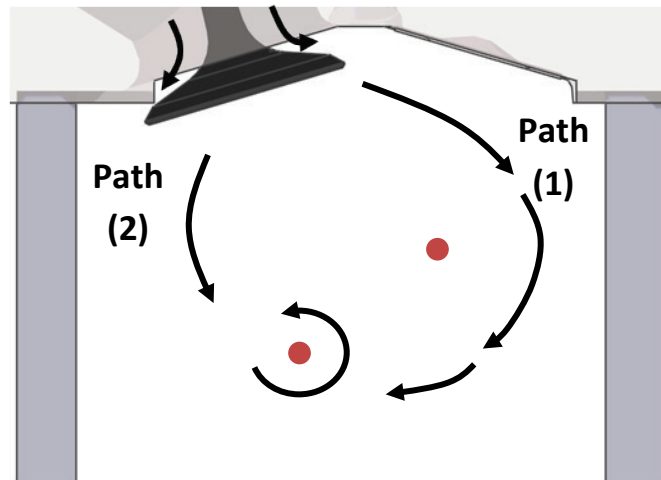
Figure 2.3.8: Schematic of valve jet path flows and formation of bulk flow structures during intake

Similar findings have been observed by Efthymiou *et al.* (2013), Rimmer *et al.* (2012) and Serras-Pereira *et al.* (2007a) who showed that the fuel spray was influenced by bulk in-cylinder structures only after adequate penetration and dispersion into the cylinder. Numerical studies (Han *et al.* 1997a, Han *et al.* 1997b) have predicted that this is due to the increased momentum of intake flow structures that are formed in the centre of the cylinder due to the interaction between the intake valve jets. The fuel spray has also been shown to have a suppression effect on the dominant tumble flow with early injection, which is observed as a more uniform velocity field (Han *et al.* 1997b, Rimmer 2010). This can likely be attributed to the momentum transfer involved with the transportation of the fuel spray. Conversely, later injections toward BDC intake were actually shown to enhance the tumble motion, which can have the benefit of increased turbulence around the time of spark ignition. Figure 2.3.9 illustrates the effect that these bulk flow structures can have on a fully heated DISI engine fuel spray that is highly atomised. The effect of the main clockwise vortex can be seen to influence the right spray plume of the highly atomised spray once it has started to disperse and transport the plume away from the wall towards the intake side of the cylinder.

| 10 °CA ASOI | 11 °CA ASOI | 17 °CA ASOI | 20 °CA ASOI |
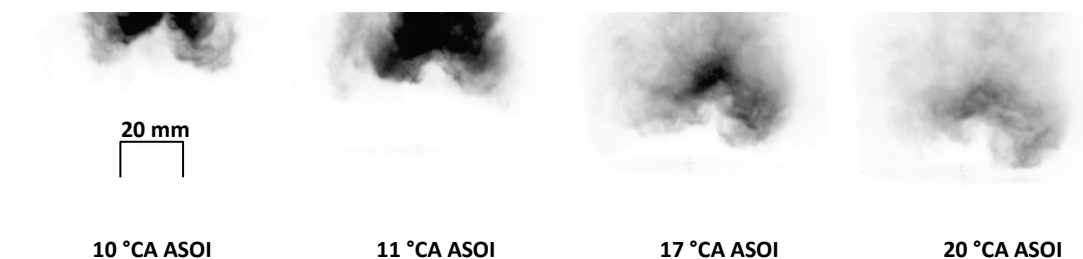
Figure 2.3.9: The effect of in-cylinder bulk flow structures on a DISI engine fuel plume in fully heated DISI optical engine (intake valves on LHS, ASOI – after start of injection) (Efthymiou *et al.* 2013)

The described intake bulk flow structures have also been shown to be beneficial for the evaporation and transportation of fuel that is consistently seen to have impinged onto in-cylinder engine surfaces (Stanglmaier *et al.* 1999, Serras-Pereira *et al.* 2007b). Rimmer *et al.* (2012) showed evidence of the flow sweeping the spray across the top of the piston away from the liner wall. These flow processes are beneficial to the transportation of fuel deposits away from impingement locations, especially in scenarios where impingement is difficult to avoid, such as cold-start.

As discussed previously, utilisation of intake valve timing can have a profound effect on the operation of a DISI engine and specifically, the ability to control the interaction between the air flow and fuel spray. Deactivation of a single intake valve is a technique that increases intake flow velocity due to the smaller effective flow area available and induces some degree of swirl flow due to the non-symmetrical intake of air into the cylinder. Stansfield *et al.* (2007a) observed the spray plume being convected away from the single open valve whilst maintaining its spray pattern, along with strong swirl structures present in the cylinder. The increased swirl will have an effect on charge mixing and may also aid the vaporisation of fuel films on the cylinder wall surfaces. A more in-depth study by Patel *et al.* (2008) confirmed the disruption of the fuel spray plume with single valve operation and a reduction in piston impingement was also observed during early injection cases. The luminosity of the Mie scattered spray also appeared lower, which indicates a higher rate of vaporisation may have taken place. As expected from the favourable air-fuel mixing conditions, subsequent combustion analysis revealed an improvement in heat release rate, which is likely due to the improved air-fuel mixing, as well as a fuel consumption improvement of 5% at low engine loads. Deactivation of one of the intake valves is a strategy that holds a number of benefits to charge mixing and engine performance but parameters such as fuel injector location will have a profound influence on its effectiveness. Investigations into the effect on bulk flow structures such as tumble should also be considered, as these are of paramount importance to the generation of high-frequency turbulence structures around the time of combustion.

In the discussed studies, a number of optical diagnostics techniques have been used to analyse fuel spray parameters such as droplet size, atomisation and vaporisation rate. It is important to interpret the data from these techniques in the correct manner in order to avoid false conclusions. Vaporisation of the fuel, for example, has two modes and when using typical Mie scattering techniques. The initial vaporisation of particles of a certain size is detectable whilst the subsequent vaporisation of particles below a certain size, is not. Multiple complementary diagnostics techniques such as laser Doppler anemometry (LDA), phase Doppler anemometry

(PDA) and Mie imaging analysis helps to facilitate the interpretation of a complex spray flow field (Wigley *et al.* 2004). Wigley *et al.* (1998) stated that a single technique alone could lead to false conclusions about the atomisation of fuel.

2.4   DISI ENGINE COMBUSTION

This section analyses the subsequent spark ignited turbulent combustion in a DISI engine and the parameters and techniques used in its analysis. Two modes of combustion have been focussed on: homogeneous stoichiometric combustion that involves early fuel injection during the intake stroke, and stratified combustion whereby fuel is injected much later during the compression stroke and the mixture, by definition, is not homogeneous.

2.4.1   Homogeneous Combustion

The stages of fuel injection and turbulent flame combustion that specifically apply to homogeneous charge DISI engines are outlined in Figure 2.4.1. The process of combustion initiation involves an electrical discharge across the spark plug gap of which 95% of the energy is transferred to a plasma (Maly and Vogel 1978). During the subsequent phases, 90% of the energy is transferred to the spark and the efficiency of energy transfer to the charge mixture can be up to 60% under typical in-cylinder conditions that initiates the development of a flame kernel (Kalghatgi 1987). If the early flame kernel survives without being extinguished, the flame becomes fully established and the turbulent flow structures present at the time of ignition allow the interaction of the flame with the unburned charge in the form of flame wrinkling, which helps to establish an effective burning velocity by increasing the surface area of the flame (Williams 1985). Flame kernel location during ignition is an important factor in engine performance, stability and variability (Rimmer *et al.* 2009, Twiney *et al.* 2010a). The turbulent flow structures present around the time of spark ignition affect the rate at which the kernel develops into a flame.

The surface area of the flame increases approximately in proportion to the root mean square (RMS) turbulent velocity (or turbulence intensity), *u'* (Bradley *et al.* 2000), which is expanded upon later in this survey. This increases the burning rate as well as the rate of entrainment of cold reactants into the leading cold front (Bradley *et al.* 2000). The remainder of the charge combusts during the early stages of the expansion stroke until it is extinguished at the walls and crevices.
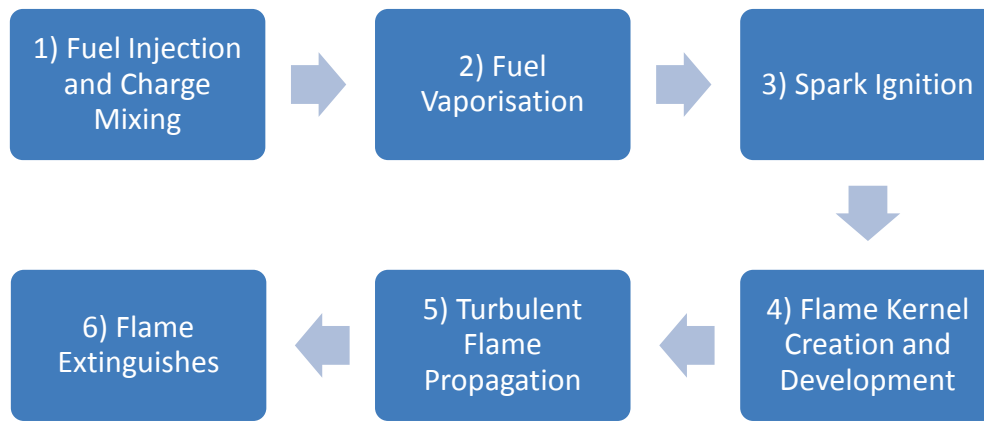
Figure 2.4.1: Stages of injection and turbulent flame combustion

A number of studies regarding the sensitivity of spark plug parameters and the effect of spark characteristics on the flame kernel have been undertaken. Spark ignition and flame kernel creation and development are considered to be important in terms of cycle-to-cycle variation (Bradley *et al.* 2000, Pajot and Mounaïm-Rousselle 2000, Chen *et al.* 2009, Rimmer *et al.* 2009, Twiney *et al.* 2010a, Twiney *et al.* 2010b). Misfire has been shown to occur with an excessively high air flow across the spark plug, which stretches the arc, as well as when liquid fuel is present in the spark plug gap (Twiney *et al.* 2010a). Pischinger and Heywood (1990) previously investigated the effect of velocity flow in the spark plug gap on early flame kernel development and identified an optimum flow velocity of 3 m·s^{-1} to 5 m·s^{-1}.

There are a number of parameters that are used to characterise turbulent premixed flames. The Damköhler number (*Da)*, is the ratio of the characteristic eddy turnover time (τ_T), to the laminar burning time (τ_T), given by the equation (Heywood 1988)

$$Da = \frac{\tau_T}{\tau_L} = \left(\frac{l_I}{\delta_L}\right)\left(\frac{S_L}{u'}\right)$$

Eqn. (2.4.1)

where l_I is the integral length scale, δ_L is the laminar burning velocity, S_L is the laminar flame thickness and u' is the turbulence intensity.

The turbulent Reynolds number Re_T

$$Re_T = \frac{u'l_I}{v}$$

Eqn. (2.4.2)

is used to define flame turbulence. It relates the inertia of the turbulence defined as a product of the turbulence intensity (u') and integral length scale (l_I)*,* to the dissipative effect of the fluid kinematic viscosity (v).

By comparing the Damköhler number, Da to the turbulent Reynolds number, Re_T (Figure 2.4.2), Heywood (1988) identified a number of different turbulent flame regimes. In SI engine combustion, typical Da and Re_T numbers lie predominantly in the reaction sheet flame region as shaded in Figure 2.4.2. The structure of a developed flame in this case is therefore expected to have a thin reaction sheet wrinkled and convoluted by the turbulent flow (Heywood 1988).

The creation and successful development of the flame kernel is known to be an important parameter in the subsequent propagation of the flame through the remaining unburned charge. Flow structures around the spark plug region directly affect early flame displacement and influence the remainder of the flame's propagation. Pajot and Mounaïm-Rousselle (2000) used PIV and chemiluminescent flame imaging to show that the flame is displaced in the predominant direction of the in-cylinder bulk flow. In-depth PIV analysis of the spark plug region (Rimmer *et al.* 2009) confirmed these findings and also discovered that the early bulk flow structures around the time of spark ignition affected the global convection of the flame in the cylinder.
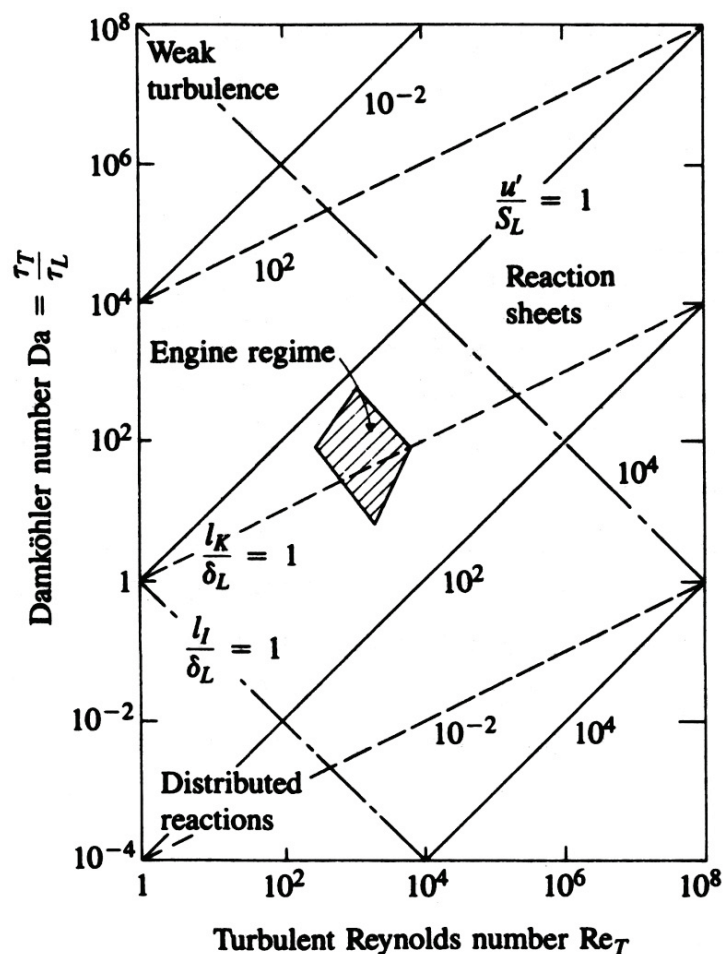
Figure 2.4.2: Different turbulent flame regimes shown on plot of Damköhler number vs. turbulent Reynolds number (Heywood 1988)

Fundamental research into the interaction of a flame front with flow structures can be used to better understand flame propagation in a DISI engine. Long (2010) used in-depth combustion bomb analysis to reveal that the charge motion does not only influence the propagation of the flame, but the reaction itself influences the charge motion, culminating in a symbiotic relationship. Toroidal flow structures were also shown to have an effect on flame propagation. It was observed that when a flame front encounters a vortex structure, its burning velocity is increased where the flame directly interacts with the rotation, particularly with smaller vortices, which were shown to have a profound effect on the local and global burning velocity. This knowledge agrees with the fact that small-scale turbulence structures help wrinkle the flame front (Figure 2.4.3), and high-frequency turbulence increases flame propagation rate and engine performance (Jarvis *et al.* 2006, Rimmer *et al.* 2009).

| 27 °CA AIT | 33 °CA AIT | 39 °CA AIT |
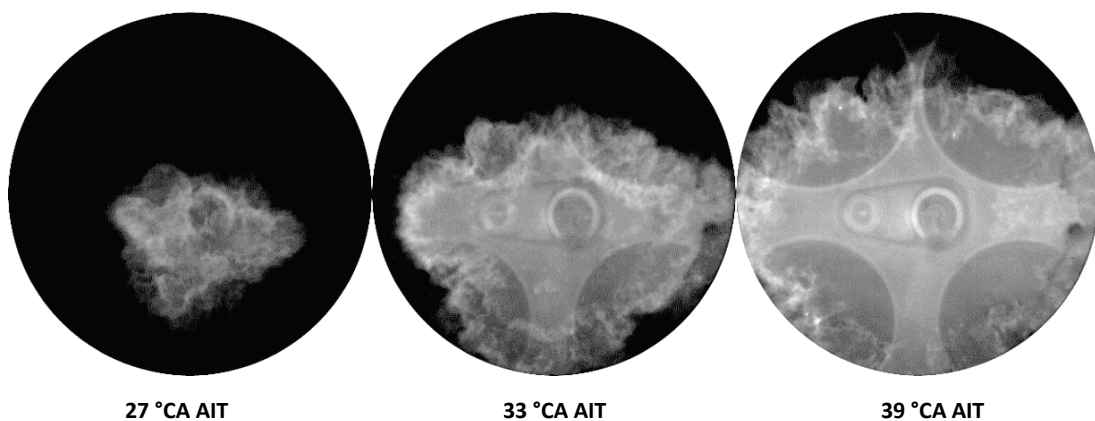
Figure 2.4.3: Flame front wrinkling in a DISI engine operating at 80°C (AIT – after ignition timing) (Efthymiou *et al.* 2013)

2.4.2   Stratified Combustion

Stratified combustion in DISI engines typically involves the injection of fuel late during the compression stroke to create an overall-lean stratified charge with an air-fuel ratio (AFR) around the spark plug to allow successful ignition and flame propagation.

For idle-load to medium-load applications in DISI engines, stratified charge operation along with throttle-less operation is generally used to achieve maximum fuel economy. This is due to a significant reduction in pumping losses associated with throttling the intake air. Other benefits arise from reduced heat loss, reduced dissociation from lower cycle temperatures and an increased specific heat ratio, which improves thermal efficiency (Queiroz and Tomanik 1997, Zhao *et al.* 2002).

Zhao *et al.* (2002) presented a detailed comparison between stratified and homogeneous charge combustion. A successful stratified charge typically contains a slightly rich mixture

around the spark plug gap at the time of ignition. When this is achieved, the reaction rate will be high enough to sustain efficient and stable combustion. The initial flame kernel during stratified combustion develops more rapidly in the spark plug region but the rate of flame propagation is reduced in the lean outer region of the charge (Figure 2.4.4). This significantly reduces the combustion rate near the end of the combustion process. The extent of this early flame propagation speed is highlighted with a 2% mass fraction burned (MFB) time of 7.5 °CA for a stratified charge, compared to 13.3 °CA with homogeneous charge. From the pressure-volume (PV) diagram presented in Figure 2.4.4, it is evident that stratified combustion releases heat more rapidly, culminating in a steeper pressure rise that peaks at a larger magnitude.
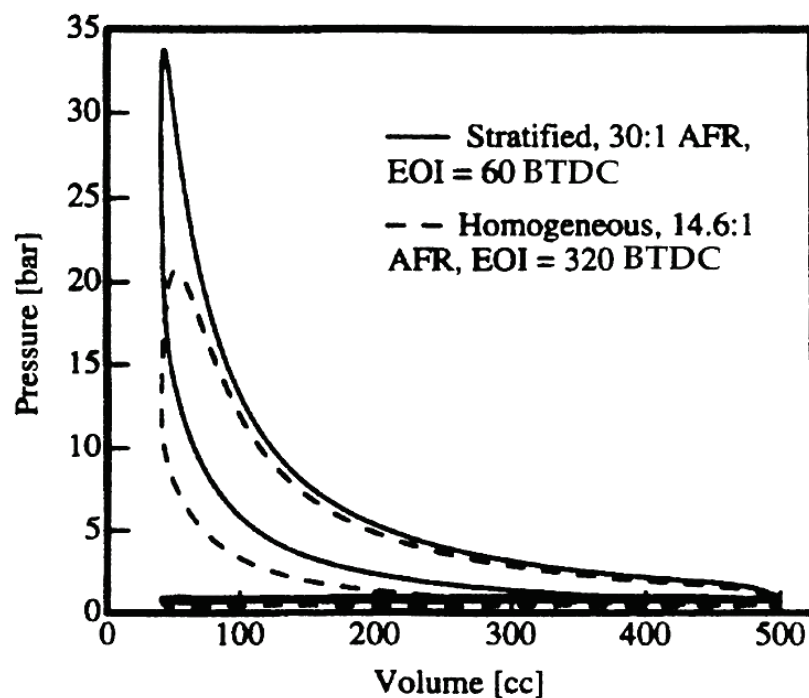
Figure 2.4.4: Pressure-volume diagram for homogeneous and stratified operation at 1500 rpm (Zhao *et al.* 2002)

With direct injection, particularly when injection occurs late, such as in stratified combustion, incomplete vaporisation may lead to the presence of liquid fuel droplets in the flame (Bradley *et al.* 2000). Increased mixture heterogeneity is a known source of hydrocarbon emissions and particulates, Bradley *et al.* (2000) analysed this type of combustion in terms of gas phase equivalence ratio in the spray (φ_g) and showed that as φ_g decreases and the droplet size increases, the burning velocity of the aerosol increased above that of a corresponding completely gaseous mixture. Schlieren photography was used to observe the flames and it was concluded that the burning velocity enhancement is due to the greater propensity of aerosol flames to become unstable and develop a cellular structure.

Greenberg *et al.* (1999) previously confirmed this effect and further concluded that even when a non-aerosol flame is cellular, the equivalent aerosol flame will have a finer cellular structure. The primary effect of the spray on the stability of these flames was observed to be due to heat loss from the absorption of heat by the droplets due to vaporisation. This heat loss mechanism was theorised as a plausible reason for the velocity enhancement induced by the use of spray fuel droplets (Greenberg *et al.* 1999). This phenomenon will not be relevant for a broad range of DISI operating conditions but may be applicable in the area of cold-start (discussed later in this literature review) where cold conditions increase the propensity of poor fuel atomisation and vaporisation, and catalyst heating strategies utilise stratified combustion.

2.5 THE EFFECT OF MULTIPLE INJECTION ON FLAME PROPAGATION AND EMISSIONS

Research has shown that performance advantages and reductions in emissions can be achieved using more than one injection per engine cycle. The flexibility of electronic common-rail systems implemented into DISI engines readily permits the use of multiple injection strategies (Zhao *et al.* 2002, Schmidt *et al.* 2011). The characteristics of the fuel injector itself are fundamental in defining the injection strategy, since the number of injections is restricted by the minimum injector pulse width and injector separation time. These parameters need to be met to achieve successful atomisation and stable spray geometry. Cycle-to-cycle variation may also be induced with a poorly designed strategy that further contributes to global cyclic variability in the engine. For these reasons, multiple injection strategies are typically limited to two or three injections per cycle due to the limitations of an injector's response time (such as needle lift) and the time available during an engine cycle. Schmidt *et al.* (2011), however, demonstrated the potential of five injections with independent injection quantities and timing.

Figure 2.5.1 illustrates the potential benefit of using multiple injections of shorter durations, especially during cold-start, which allows this strategy to be more readily implemented at lower engine speeds. The triple injection strategy shown highlights the reduction in fuel spray impingement with the piston compared to single injection case, which can be seen to deflect off the piston crown and will result in significant wetting of other engine surfaces. Reducing the amount of liquid fuel impingement, particularly on cold surfaces, is essential for cold-start and the reduction of PM emissions.
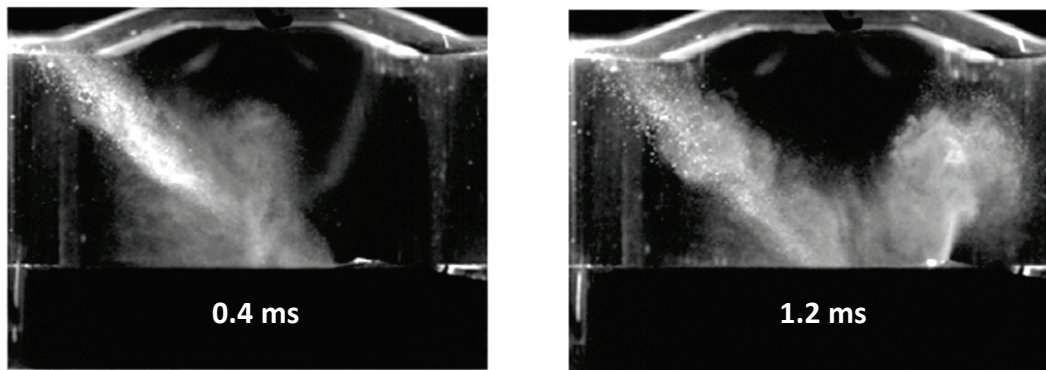
Figure 2.5.1: Comparison of single and triple injection strategies with different injection durations, highlighting on piston impingement during cold-start (Whitaker *et al.* 2011)

Serras-Pereira *et al.* (2007b) used multiple injection strategies in an optical research engine to observe liquid impingement as well as mixture preparation and combustion. A multi-hole injector was used in a homogeneous combustion setup and high-speed imaging was used to capture injection and combustion events for a triple injection strategy. As expected, it was shown that the use of a multiple injection strategy can reduce the amount of direct liquid fuel impingement during intake and shorter split injections can promote more rapid evaporation and mixing than a single injection. Combustion, however, was observed to be slower using a triple-injection strategy and the flame growth was observed to be more spherical and deviated less from the central cylinder position of the injector. It was hypothesised that a number of mechanisms such as AFR concentrations around the spark plug and increased heat transfer could have caused this effect. These results still highlighted a potential reduction of soot formation with a substantial reduction in high luminosity regions that illustrate fuel-rich areas and the potential for PM formation, as confirmed by Block *et al.* (2000), Gupta *et al.* (2000) and Rimmer (2010). Block *et al.* (2000) utilised Laser-induced incandescence (LII) to detect the broadband light emission of soot particles in fuel rich regions of the flame. Interestingly, it has been noted that lower luminosity flames with spherical growth are typical of PFI combustion systems and high levels of charge mixing and homogeneity (Aleiferis *et al.* 2000a, Aleiferis *et al.* 2000b).

Serras-Pereira *et al.* (2007b) also observed a more stable flame centroid for a triple-injection strategy when compared to a single injection. This was concluded to be due to possible flame independence to the convecting currents during flame growth. This stability in flame position indicates a potential improvement in combustion variability that contributes to global cyclic variability.

Multiple injections have the potential to increase the fuel spray interaction with the in-cylinder flow field. Rimmer *et al.* (2009) used high-speed particle image velocimetry (HSPIV) to investigate the effect of multiple-injection strategies during homogeneous combustion on turbulence during the compression stroke and around the time of ignition. It was shown that turbulence increased during double and triple injection but 10% and 90% mass fraction burned (MFB) times were detrimentally effected. These results correspond to the reduction in flame growth speed observed by (Serras-Pereira *et al.* 2007b) in a similar engine configuration.

In order to further understand the potential causes of the engine performance decrease, Rimmer *et al.* (2009) conducted high-frequency turbulence filtering and found a decrease in turbulence near TDC prior to the point of ignition. These high-frequency turbulence structures are known to correlate with engine performance parameters such as IMEP and MFB, which explains the observed performance drop. As turbulence is generated by the squish of large-scale structures such as tumble (Zhao *et al.* 1999), the previously discussed flow suppression from the fuel spray (Han *et al.* 1997b, Rimmer 2010) could be a potential cause for the diminished turbulence. Furthermore, with a higher number of fuel-spray events and therefore flow disruption, the effect of multiple injections may be greater on the flow field.

The extra-urban NEDC comprises long acceleration phases from cold-start and high vehicle speeds once the engine is fully warmed. In these combustion modes, fuel impingement is a potential issue due to the increased fuelling requirements and therefore penetration, which can lead to an increase in PM emissions. To simulate these conditions, Whitaker *et al.* (2011) tested a DISI triple-injection strategy during transient engine operation with a variety of engine loads and speeds. A single injection strategy at low speed was shown to produce high smoke levels that were stated to be the result of ineffective air motion to deflect the fuel spray and reduce impingement. At high speed, the increased bulk flow tumble was said to be sufficient enough to reduce impingement and improve mixture preparation, which resulted in a smoke reduction. The triple injection strategy resulted in a smoke reduction across all engine speeds. This also corresponded to a significant reduction in measured PN emissions when simulating the NEDC. A numerical study on the effect of multiple injection on soot emissions by Bonandrini *et al.* (2012) agreed with these findings. Wall impingement was also shown to be reduced and mixture homogeneity was improved due to the influential effect of fuel injection scheduling at low engine speeds, corresponding with previous experimental findings by Rimmer *et al.* (2009).

HSPIV has been used to analyse the effect of multiple injection in a DISI engine operating in a stratified mode. As bulk flow structures are less dominant, due to the absence of intake valve jet flow, the effect of the fuel spray will be more influential on the in-cylinder flow field. Disch *et al.* (2013) conducted an experimental study using HSPIV and cinematographic particle tracking to investigate the effect of a second fuel spray injection near TDC. Figure 2.5.2 illustrates the in-cylinder flow field immediately after each injection event and it was shown that the turbulent kinetic energy of the larger vortex (labelled with a red 'X') was temporarily higher. These results show the potential of using multiple injections to influence the flow field near TDC and subsequently the combustion performance of an engine operating in a stratified mode.
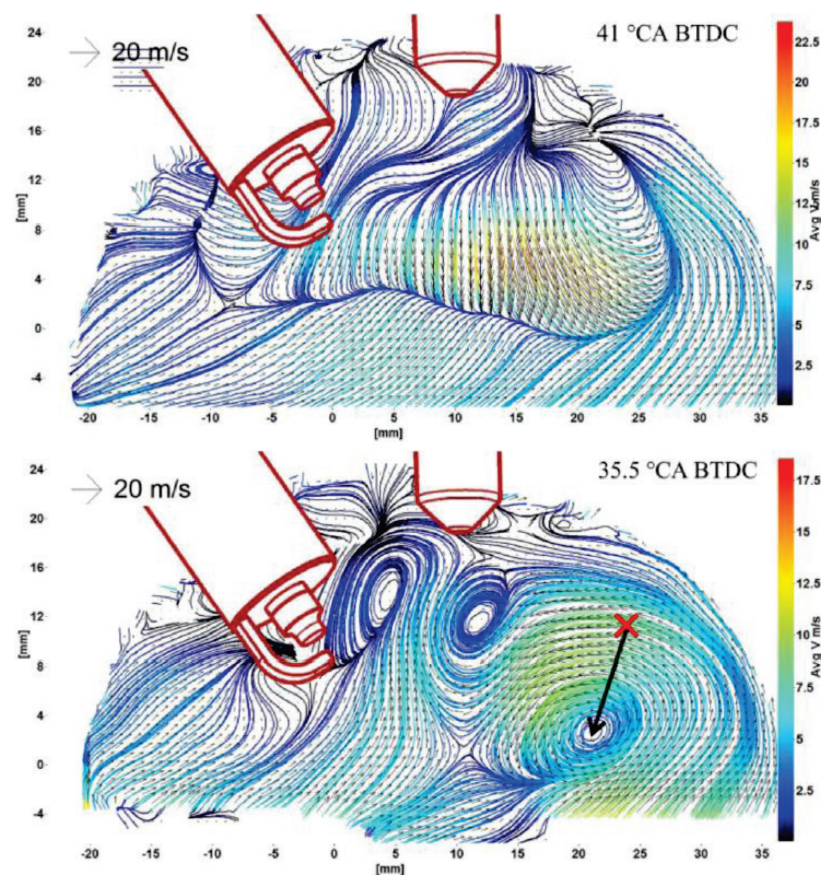
Figure 2.5.2: HSPIV data showing spray break-up and vortices formation immediately after each injection event during stratified combustion (Disch *et al.* 2013)

The introduction of multiple injection scheduling within cold-start strategies by some manufacturers, utilises some of the beneficial effects observed within the presented research, as engine designers and researchers follow a particular trend to improve the quality of combustion to meet emissions legislation. These cold-start strategies are discussed in more detail in the next section of this literature review.

2.6   COLD-START CONTROL STRATEGIES

As discussed in *Chapter 1*, DISI cold-start engine performance is critical with the recently released Euro Stage 6 legislation, which also includes an operating temperature of -7°C in the NEDC. Two main factors are important with regards to cold-start in DISI engines: catalyst light-off and PM generation. DISI engines hold a benefit over PFI engines because strategies such as late injection can be implemented. These strategies generate higher exhaust temperatures and therefore reduce the time to reach catalyst light-off. Up to this light-off point, however, the quantity of PM emissions is at its highest, as illustrated by Whitaker *et al.* (2011) in Figure 2.6.1. Two distinct peaks in particulate number (PN) count are shown to occur during the first two transient stages of the NEDC, which then decrease by an order of magnitude. These significant PN reductions after an initial cold-start have been supported by (Price *et al.* 2007).

In the catalyst heating operation, the first injection occurs during induction (as in homogeneous charge combustion) and the second occurs close to the point of ignition. The ignition is retarded past the point of TDC to increase the exhaust temperature, which leads to a rise in catalyst temperature (Hattori *et al.* 1995, Ando 1997, Kuwahara *et al.* 1998, Lee *et al.* 2002, Eng 2005, Morita *et al.* 2005). This is due to the reduced expansion work delivered from combustion and the consequently higher in-cylinder temperature at the end of combustion. A twin injection strategy of this nature has also been shown to improve combustion stability when compared to single injection (Morita *et al.* 2005, Chen *et al.* 2009). This has been theorised due to the fuel rich mixture around the spark plug from the second injection and the turbulence created by this late injection.
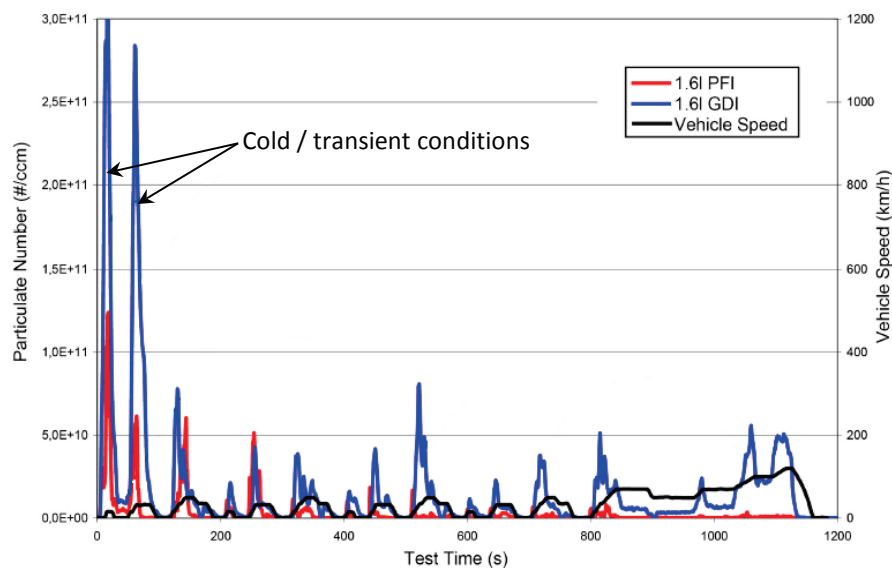
Figure 2.6.1: PN emissions plots during the Euro 5 NEDC comparing a DISI engine and PFI engine (adapted from Whitaker *et al.* (2011)) (also Figure 1.1.3)

A number of research studies have utilised different methods to raise the exhaust temperature and achieve a quicker catalyst light-off. Choi *et al.* (2000) retarded the spark timing up to 8 °CA ATDC on a cold-start PFI engine operating at 25° C. This reduced the catalyst light-off time by 16 seconds, which lowered HC emissions by 39%, whilst maintaining the level of IMEP variability. When combined with a double-injection strategy in a DISI, it has been shown that the spark can be retarded further to 20 °CA ATDC (Morita *et al.* 2005). MFB times using this strategy were also shortened by 36% when compared to a standard homogeneous strategy.

Morita *et al.* (2005) also carried out a computational fluid dynamics (CFD) study that showed that the second injection generated a strong turbulent flow that promoted fuel-air mixing, as discussed in the previous section by Disch *et al.* (2013). This was confirmed by laser induced florescence (LIF) experimentation that showed the AFR heterogeneity around the spark plug area was improved and the standard deviation of AFR fell by 7% when compared to a 50% injection strategy.

Engine misfire is of particular importance during cold-start due to its increase propensity and importance on engine stability and emissions. Chen *et al.* (2009) investigated the effect of spark timing and spark plug orientation on engine misfire tolerance in a DISI engine during cold-start. The results showed that an optimal misfire-free window was present when changing spark plug protrusion, spark plug orientation and injector orientation, highlighting the sensitivity of combustion initialisation with a catalyst heating strategy. It was hypothesised that misfire mechanisms during this operation could include a lack of fuel vapour around the spark plug, the presence of liquid fuel near the spark plug electrodes and high velocity bulk flow created by the second spray. However, CFD results from Piock *et al.* (2011) and experimental data from Rimmer *et al.* (2009) have since shown that the second injection does not have a dominant impact on the overall turbulent energy level around the spark plug region. It was concluded by Piock *et al.* (2011) and Berndorfer *et al.* (2013) that the primary stabilisation effect of combustion by the late injection is due to the creation of a locally rich mixture.

Spark plug misfire was investigated in more detail by Twiney *et al.* (2010b, 2010a) during a catalyst heating operating mode and in a similar configuration engine to Chen *et al.* (2009). An injection and ignition timing sweep, alongside a twin spark strategy, showed misfire tendency increased as injection was retarded (with up to 40% cycles misfiring). Interestingly, certain spark plug orientations had a significant effect on misfire with up to 75% of cycles and a double spark strategy not improving this rate. This study highlights the number of factors that

contribute to the sensitivity of successful combustion during a catalyst heating operation that are sensitive to engineering tolerances in production.

Further investigations from Twiney *et al.* (2010b, 2010a) using high-speed photography revealed the fuel jet impacting on the spark plug electrode in certain orientations and fuel remaining in the spark plug gap. This helps supports the theory by Chen *et al.* (2009) that liquid fuel can extinguish the early flame kernel leading to misfire. Other mechanisms for misfire can also be suggested that included an excessively rich AFR in the spark plug gap and an overly stretched spark across the spark plug electrode.

The ever-increasing stringency of emissions legislation against PN count in DISI engines requires the implementation of reduction strategies across the entire NEDC in order to meet these targets. Whitaker *et al.* (2011) carried out an in-depth experimental study across the NEDC and showed that PN reduction could be achieved in the follow areas: cold-start (10%), catalyst heating (10%), transients during cold engine operation (60%) and transients during hot engine operation (20%). It was stated that the very first injection needed to be of the highest atomisation quality for lowest PM generation during cold-start by raising the fuel pressure as high as possible. This was shown to reduce the PN count and mass of PM emission from start-up by a factor of 4-5 when the engine was started from 22°C, which is approximately the typical NEDC cold-start test condition when measuring particulates.

During cold-start, the low rotational velocity of the engine allows multiple injection strategies to be fully utilised and as previously discussed, up to five injections can be made per cycle (Schmidt *et al.* 2011). Whitaker *et al.* (2011) tested up to 4 injections from a 22° C cold-start and showed a reduction in peak PN generation by a factor of over 6.

Transients during a cold-start NEDC are major contributors to total PN emissions (Piock *et al.* 2011, Berndorfer *et al.* 2013) with up to 60% of the total number being emitted during the first three hills of the NEDC shown in Figure 2.6.1 (Whitaker *et al.* 2011), which were shown to reduce significantly after the engine had heated up. The combination of the techniques discussed and tested by Whitaker *et al.* (2011) were shown to reduce the PN emissions from a baseline of 2.0×10^{12} #.km^{-1} by an order of magnitude to 4.5×10^{11} #.km^{-1}, which falls below the EU Stage 6 levels of 6.0×10^{11} #.km^{-1} (European Parliament 2007, DieselNet 2015) without the use of any particulate treatment systems. This proposed potential in DISI engines for achieving reduced emissions has was also confirmed by Piock *et al.* (2011) who reduced the PN emissions of a baseline engine to 4.4×10^{11} #.km^{-1} using a number of similar control strategies.

The focus in strategies used by manufacturers and research groups in cold-start conditions have been summarised in Table 2.6.1. Catalyst heating and spark timing are widely used to increase combustion temperatures and reduce TWC light-off time. A trend towards increasing fuel injection pressures to improve atomisation can also be seen, along with increasing use of multiple injection strategies. Further research would be valuable in the areas of VVT and the use of flow structures to influence PM generation as is highlighted by the reduced application of these factors.

Research Group	Stratified Catalyst Heating	Spark Scheduling	Multiple Injection	Increased Fuel Pressure	VVA	Utilisation of Flow Structures
Berndorfer *et al.* (2013) Delphi	▓	▓	▓	▓		
Whitaker *et al.* (2011) AVL	▓	▓	▓	▓		
Piock *et al.* (2011) Delphi	▓	▓	▓	▓	▓	
Chen *et al.* (2009) Jaguar Land Rover	▓	▓	▓			
Morita *et al.* (2005) Toyota	▓	▓				▓
Choi *et al.* (2000) Hyundai		▓		▓		▓

Table 2.6.1: Summary of cold-start strategies utilised by various research groups

The subject of cold-start performance in DISI engines has become an increasing focus in experimental research due to the known shortfall of current DISI engines when evaluated against future legislation. This highlights the needs of engine manufacturers and researchers alike to attain an improved understanding of this area and meet future legislation requirements with intelligently designed combustion systems in order to avoid the use of costly ancillary systems such as nanoparticulate filters. The presented research highlights focus on engine calibration for reducing PM emissions at the exhaust. Less information is available regarding the formation of PM at the initial transient stages of an IC engine cold-start cycle as well as the fuel spray structures and flame characteristics at these very low initial engine speeds, which are responsible for a significant proportion of PM emissions. There is also a significant lack of optical research data available relating to DISI engine operation at low

temperatures, such as the EU Stage 6 NEDC cold-start condition of -7°C (DieselNet 2015). This condition is of particular importance as it poses a significant challenge for DISI engines in meeting proposed PN count legislation.

The next section discusses the influential flow structures that are predominantly present in DISI engine systems or can be created using available engine architecture. The successful measurement and understanding of these structures is of paramount importance in controlling exhaust emissions.

2.7 THE EFFECT OF TUMBLE ON FLAME PROPAGATION AND EMISSIONS

A number of bulk flow structures are present during an engine cycle. These are formed due to the complex flow interaction across the intake valves and the later interaction with the combustion chamber, cylinder walls and piston crown. Tumble motion is used to describe the presence of large scale rotating vortices that are generated during intake relative to engine crankshaft rotation.

Figure 2.3.8, presented previously, illustrates the typical bulk flow structures formed during the intake of a single cylinder four-valve pent roof DISI engine viewed from the tumble plane, with the intake valves on the left hand side. Two dominant structures are highlighted, the majority of the intake flow (Path 1) travels over the top of the intake valves and across the pent roof combustion chamber before making contact with the exhaust side of the cylinder wall and being inducted downwards towards the piston crown to form a clockwise recirculation region. This flow feature is commonly referred to as 'tumble' and is typically present during the entire intake stroke as well as most of the compression stroke until it is dissipated into small-scale turbulence towards TDC. Flow that travels over the bottom of the intake valves (Path 2) during the early stage of intake contacts the intake side of the cylinder to form a higher velocity counter-clockwise vortex on the surface of the piston that follows its motion before dissipating during the latter part of the intake stroke as the more dominant tumble flow vortex is established. This type of recirculating flow has been observed by a number of authors (Fischer *et al.* 2002, Jarvis *et al.* 2006, Justham *et al.* 2006a) with Stansfield *et al.* (2007b) demonstrating its presence in an optical research engine for engine speeds up to 3500 rpm.

Various methods exist for describing bulk flow tumble from the velocity vector fields measured using particle image velocimetry (PIV) (Lumley 1999, Stansfield *et al.* 2007b). A commonly used

dimensionless parameter is tumble ratio (TR), which relates the cross product of the magnitude and distance of individual velocity vector fields from the vortex centre, to the engine speed and dot product of the distance of the individual velocity vector fields from the vortex centre, as shown below (Pitcher and Wigley 2001, Li *et al.* 2004):

$$TR = \frac{\sum_{i=1}^{N} r_{(x,y,i)} \times u_{(x,y,i)}}{\omega_c \sum_{i=1}^{N} r_{(x,y,i)} \cdot r_{(x,y,i)}}$$

Eqn. (2.7.1)

where:

N	Number of vectors
ω	Engine speed (Rad s^{-1})
ω_c	Engine crankshaft angular speed (m·s^{-1})
$r_{(x,y,i)}$	Distance of the cell position of the ith velocity vector to the vortex centre.

The location of the vortex centre of the bulk tumble flow is required for the calculation of the tumble ratio. Stansfield *et al.* (2007b) describes a mathematical algorithm (Eqn. (2.7.2)) that takes into account every vector from a mean velocity flow field. The algorithm calculates the sine of the angle between the position vector and flow vector for the surrounding eight vectors of every individual vector in the flow field. The average of the eight surrounding angle sines is plotted to produce a scalar field that will approach unity at the point of the vortex centre. A Gaussian peak fit is then applied to the field to locate the position of the vortex centre.

$$R(n) = \frac{1}{N} \sum_s \frac{(\underline{M} \times \underline{U}) . \hat{\underline{Z}}}{\|M\| \|U\|} = \frac{1}{N} \sum_s \sin(\theta)$$

Eqn. (2.7.2)

where:

R	Vortex identifier (dimensionless scalar)
N	Position
S	2D area surrounding n
N	Number of points inside s
M	Radius
$\underline{M}$	Radius vector
U	Velocity
$\underline{U}$	Velocity vector
$\underline{Z}$	Unit vector normal to the measurement plane
θ	Angle between U and M.

Tumble flow and its effect on combustion has been studied and utilised for over 20 years. Four-valve engines employing high-tumble induction systems have been noted to result in lower combustion times in addition to reductions in harmful exhaust emissions (Mahmood *et al.* 1996). It has been discussed that to enhance the tumble ratio of an engine, it is essential to increase the air flow to the upper valve area to allow for increased air flow across the combustion chamber towards the exhaust valve side of the cylinder (Omori *et al.* 1991).

de Boer *et al.* (1990) assessed the combustion of three different four-valve engines that were fitted with low to high tumble cylinder heads. It was shown that tumble was able to reduce the ignition delay, burn duration (for 10% to 90% MFB) and lower the levels of cycle-to-cycle variation. Exhaust gas recirculation (EGR) tolerance was shown to be higher in a high-tumble system resulting in pumping loss reductions that benefitted fuel economy by 3-6%. Hydrocarbon emissions were also reduced by 18% and CO emissions were reduced by 25%. However, it was observed that excessively high levels of tumble led to an increase in unburned hydrocarbon (HC) emissions and an increase in BSFC. A potential reason for this is an excessive flow velocity around the spark plug area, which could adversely affect the spark discharge and flame kernel, leading to a poor flame establishment.

This was also suggested by Reeves *et al.* (1999) who used PIV to measure the in-cylinder flow field with a high and low tumble ratio of 1.2 and 1.8 respectively (originally referred to as 'barrel swirl' and defined by Chapman *et al.* (1991)). The flow over the top of the intakes valves was shown to create a rotating vortex at 45 °CA ATDC accompanied by a counter rotating vortex of similar size beneath the intake valves. The high tumble case was observed to produce a more centrally distributed vortex during intake that remained through to compression, where it was observed rotating at a greater angular velocity in the clearance volume of the engine (at 260 °CA ATDC). It is the conservation of angular momentum as the field is forced into a smaller volume that causes of the increased velocity, along with the increased shear forces, which alter the structure of the vortex. Reeves *et al.* (1999) suggested if peak velocities at TDC were scaled up linearly with engine speed, it would likely cause excess flow velocity around the spark plug. Therefore, a fine balance needs to be made when inducing in-cylinder tumble motion, as this dissipation of rotational energy into turbulence is an important parameter in flame growth speed and engine performance, which has been detailed in a number of studies (Jarvis *et al.* 2006, Rimmer *et al.* 2009).

Inducing tumble has also been shown to have benefits on the cycle-to-cycle variation of the in-cylinder flow field. By generating a dominant flow that is more repeatable, greater consistency

can be achieved by the time the bulk flow structures dissipate into performance-critical small-scale turbulence at TDC. Li *et al.* (2003) modified a three-valve SI engine to increase the level of tumble and analysed the effects using PIV. It was observed that an ensemble-averaged tumble ratio of 1.5 reduced the cycle-to-cycle variation of the main tumble vortex, with 95% of individual cycles displaying a strong and consistent tumble motion with a clear tumble centre. Fluctuating kinetic energy, a measure of turbulence, reached 15 m^2s^{-2} during the compression stroke that was three times that of the unmodified engine. Li *et al.* (2003) believed that the distortion and breakup of the tumbling vortex into velocity fluctuation (turbulence) would accelerate the formation of the flame kernel and aid flame propagation. This suggestion was confirmed by Rimmer *et al.* (2009) who correlated the high frequency turbulence structures at ignition with engine performance.

Lee *et al.* (2007) analysed flame propagation in an optical research engine with modified intake ports along using laser Doppler velocimetry (LDV) analysis of the flow field. A tumble ratio of 2.0 achieved the fastest flame propagation and heat release analysis showed improved MFB time improvements of up to 5%. These findings agree with much of the presented research indicating that certain levels of tumble motion in DISI engines (1.5 - 2.0 tumble ratio) can enhance flame propagation and reduce exhaust emissions. The requirement to further understand the specific effects of tumble flow on PM emissions has been highlighted, as well as the lack of experimental investigation on the interaction of tumble with fuel spray atomisation, vaporisation and impingement.

2.8 THE EFFECT OF SWIRL ON FLAME PROPAGATION AND EMISSIONS

Swirl is created from an imbalance in velocity between the two intake ports creating a bulk toroidal flow structure that rotates around the cylinder axis as outlined in Figure 2.8.1. As with tumble, swirl has been utilised and researched in spark ignition engines to produce combustion systems that have higher burning velocities. Axial swirl is predominantly utilised and associated with diesel engines, but it is also effective in spark ignition engines (Collins and Stokes 1983). In the studies presented here, tumble is normally present as well as swirl due to the intake manifold geometry, pent roof combustion chamber and the complex swirl-flow cylinder interaction.
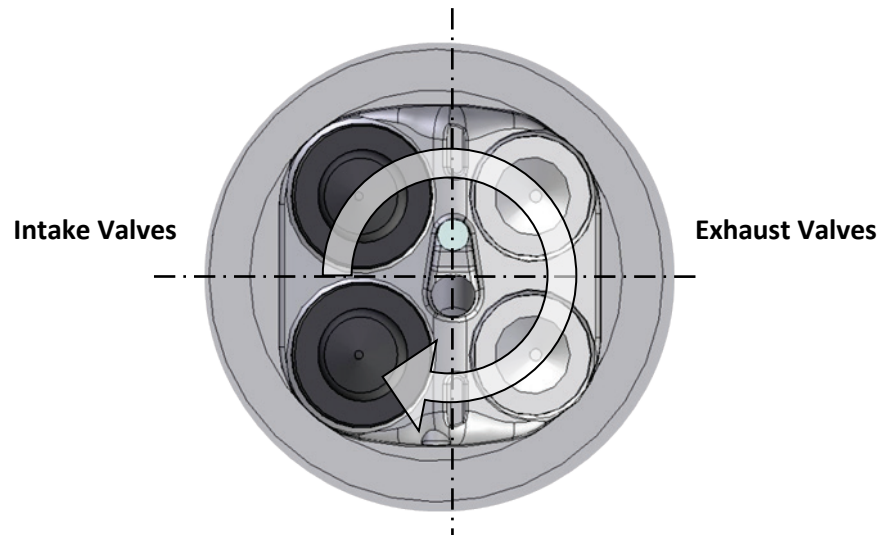
Figure 2.8.1: Schematic of in-cylinder swirl flow when viewed across intake and exhaust valves

Swirl ratio (SR) is a common method used to characterise in-cylinder swirl and is typically measured on a steady flow rig consisting of either an impulse or vane swirl meter. The dimensionless Ricardo swirl ratio (S_R), is defined below (Stone *et al.* 1993):

$$S_R = \frac{BS}{nD^2} \frac{\int_{\alpha_o}^{\alpha_c} C_F(\alpha) N_R(\alpha)\, d\alpha}{\left\{ \int_{\alpha_o}^{\alpha_c} C_F(\alpha)\, d\alpha \right\}^2}$$

Eqn. (2.8.1)

$$N_R = \frac{8T}{\dot{m} B v_0}$$

Eqn. (2.8.2)

where:

B	Bore
S	Stroke
n	Number of intake valves
D	Inner valve seat diameter
$C_F(\alpha)$	C_F (flow coefficient) at the valve lift corresponding to a particular crank angle
α_o, α_c	Crank angle for intake valve opening and closing
$N_R(\alpha)$	N_R (Ricardo swirl ratio) at the valve life corresponding to a particular crank angle
T	Moment of momentum flux (measured by a swirl torque meter)
$\dot{m}$	Air mass flowrate
v_0	Velocity for frictionless flow with the applied pressure difference across intake port.

The most commonly utilised method of inducing swirl in a four-valve engine without swirl-creating intake geometry is valve deactivation. Stone *et al.* (1993) disabled one of the intake valves in a four-valve pent roof arrangement engine in order to generate axial swirl and observe combustion performance at speeds of 1500 rpm to 2400 rpm. The speed of combustion was seen to increase with 10% and 90% MFB times that were 23% shorter. Peak

pressure increases were also seen that correlated with the faster observed combustion and the peak pressures that were closer to TDC.

Stone *et al.* (1993) also showed considerable benefits to cyclic variability using swirl, with coefficients of variation (COV) of IMEP decreasing by 3%. This improvement can be attributed to the decreased 10% MFB times, which reduced the time for random displacements of the flame kernel and the swirling bulk flow structures and led to a dominant mean flow. Reuss (2000) later showed similar findings in the flow field using PIV. It was shown inducing a swirl ratio (SR) of 5 reduced the standard deviation of the in-cylinder flow to a point where individual cycle flow fields accurately followed the trends of their ensemble mean flow fields. Further analysis of the flow showed that turbulence fluctuation was strongest in the central 50 mm diameter region of the cylinder.

Due to the nature of DISI in-cylinder fuel spray, swirl flow has a direct impact on fuel spray distribution and impingement. Alger *et al.* (2000) used Mie scattering techniques to visualise the fuel spray whilst measuring the equivalence ratio in an optical research engine with a SR of 2. At 750 rpm the fuel was shown to concentrate in the centre of the cylinder. This is because swirl inherently decreases turbulent radial diffusion and creates a radial pressure gradient that results in a low pressure in the centre of the cylinder and higher pressure near the walls (Lumley 1999, Alger *et al.* 2000). This effect was previously outlined by Moriyoshi *et al.* (1997). Alger *et al.* (2000) also observed the swirling bulk flow remain throughout the compression stroke. When a higher speed of 1500 rpm was tested, it was found that the swirl effect on the fuel jet was more pronounced and distorted the spray. At both engine speeds, the quantity of residual liquid fuel and amount of surface impingement (particularly on the piston crown) increased. Piston wetting is a well-known contributor to PM generation (Gupta *et al.* 2000, Rimmer *et al.* 2012).

Emissions analysis from Stone *et al.* (1993) when inducing swirl from valve deactivation showed reductions in NO_x as well as a reduction of 5.6% in fuel consumption. These findings were consistent with those seen by Fraidl *et al.* (1990) who conducted tests at 2000 rpm with intake valve deactivation and Lee *et al.* (2007) as discussed previously, who utilised a combination of swirl and tumble. Moriyoshi *et al.* (1997) also showed this effect and was able to achieve a maximum IMEP using a combination of swirl and injection scheduling at 90 °CA ATDC that was shown to reduce NO_x and CO emissions.

It has been shown that a combination of both tumble and swirl further enhances turbulence structures near TDC (Lee and Lee 2003, Lee *et al.* 2007). This is more significant during lean

combustion, which has shown a considerable increase in flame propagation and agrees with findings from Lee *et al.* (2007), Rimmer (2010) and suggestions by Reeves *et al.* (1999), who discussed the importance of turbulence on flame growth speed and engine performance.

2.9   MEASUREMENT TECHNIQUES

In order gain an in-depth understanding of the mechanisms of in-cylinder flow processes and combustion, detailed measurements of in-cylinder fluid flow are required. A number of authors have successfully studied the complex flow field structures, fuel injection and flame propagation inside IC engines (Reeves *et al.* 1999, Reuss 2000, Li *et al.* 2002, Jarvis *et al.* 2006, Justham *et al.* 2006a, Serras-Pereira *et al.* 2007b, Stansfield *et al.* 2007b, Rimmer *et al.* 2009, Xu *et al.* 2013). A number of optical measurement techniques discussed here require the introduction of small tracing particles that follow the motion of the flow and can be recorded, known as seeding. The operational parameters required when seeding for accurate flow field analysis are described within the particle image velocimetry experimental setup subsections in *Chapter 3* and *Chapter 6*. This section analyses a number of invasive and non-invasive diagnostic techniques that can be applied to the measurement of IC engine flow, species composition and emissions. These are:

1. Hot Wire Anemometry (HWA)
2. Mie Scattering
3. Laser Doppler Velocimetry (LDV)
4. Particle Image Velocimetry (PIV)
5. Laser Induced Fluorescence (LIF)
6. Laser Induced Incandescence (LII).

2.9.1   Hot Wire Anemometry (HWA)

Hot wire anemometry (HWA) is a commonly used technique utilised in the vast majority of production IC engines to measure the mass flow rate of intake air into the engine. It operates on the principle of heat loss from a thin hot wire as gas flows past it. The change in electrical response of the wire can be measured and this is related to the velocity of the gas. As a non-linear relationship exists between the electrical response and the magnitude of gas velocity, extensive calibration is required to maintain accuracy. Two methods of measuring the electrical response of the wire exist, maintaining the temperature of the wire by varying the electrical current (constant temperature method), or maintaining the electrical current and measuring the reduction in resistance due to the temperature drop (constant current method).

HWA provides a good frequency response and it can be used without optical access but its point measurement nature only provides a limited spatial velocity measurement of the flow field and flow direction cannot be deduced. The physical use of a probe also disturbs the flow and affects the accuracy of the velocity measurement. Despite these limiting factors, Erdil and Kodal (2007) successfully used HWA method to measure in-cylinder engine flows around the piston bowl at engine speed up to 2000 rpm and at flow frequencies up to 75 Hz.

2.9.2 Mie Scattering

A qualitative understanding of the physics of a particle can be readily acquired when an incident electromagnetic wave is applied to it. If a single particle is considered as a number of conceptually subdivided regions, when a wave is applied, a dipole moment is induced in each region. These dipoles oscillate at the frequency of the applied field and therefore scatter secondary radiation, which can be detected (Bohren and Huffman 1998).
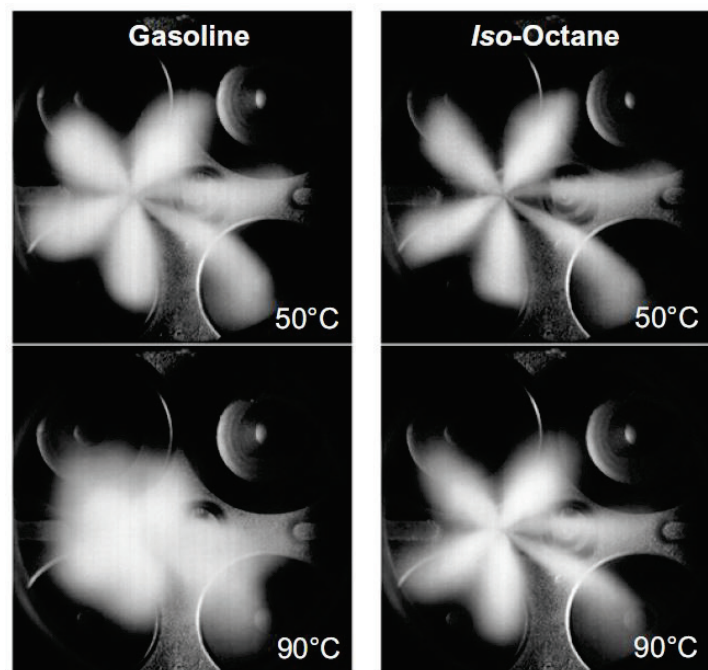
Figure 2.9.1: Mean fuel-spray images scattered from an Nd:YLF laser at 527 nm comparing temperature and fuel effects on spray formation (Serras-Pereira *et al.* 2007b)

Mie scattering is a valuable tool in two-dimensional (2D) fuel spray measurement and has been utilised by a number of research groups to provide a qualitative understanding of in-cylinder fuel spray location and distribution (Hargrave *et al.* 2000, Serras-Pereira *et al.* 2007a, Rimmer 2010, Efthymiou *et al.* 2013, Xu *et al.* 2013). The fuel droplets themselves scatter the incident light so there is no need to add a dopant to the fuel. Figure 2.9.1 illustrates Mie scattering of a fuel spray in a DISI engine using different fuel types and operating temperatures. The illumination of all spray plumes over a number of engine cycles allowed the

quantitative processing of important spray parameters such as RMS of spray location to be calculated. Care must be taken, however, when commenting on the results from Mie scattered particles as not all particles may be perfectly spherical (such as those formed from fuel spray particle clusters). It has been shown that non-spherical particles scatter light similarly to area-equivalent spherical particles (Bohren and Huffman 1998).

2.9.3   Laser Doppler Velocimetry (LDV)

Laser Doppler velocimetry (LDV) provides a time-resolved point measurement of the fluid velocity within a velocity flow field. In a single-component dual-beam system, two coherent laser beams intersect in the measurement region and create dark and light interference fringes in an ellipsoidal volume as illustrated in the lower left region of Figure 2.9.2. When a seeding particle passes through this volume, its scattered light fluctuates as it crosses the fringe pattern. The scattered light is detected by a photomultiplier tube and converts the light into a fluctuating voltage signal that represents the velocity component perpendicular to the light fringes. The velocity is deduced using the knowledge that the frequency of this fluctuation is equivalent to the Doppler shift between the incident and the scattered light and therefore relates to the velocity of the particle in the ellipsoidal volume.

LDV provides a non-intrusive method of measuring velocity at a high temporal resolution up to sub crank angle resolution with an experimental setup that is more simplified when compared to other optical techniques such as PIV. The technique is limited however, by its point measurement nature that does not provide any measurement for larger spatial flow structures unless the measuring volume is traversed across the required measurement region. This process can be time-consuming reduces the accuracy of velocity data as it is not spatially or temporally resolved and requires cyclic averaging. Considering the typical measurement region area and the nature of complex flow structures that exist in an IC engine, LDV is not ideally suited for measuring IC engine fluid flow over a large region.
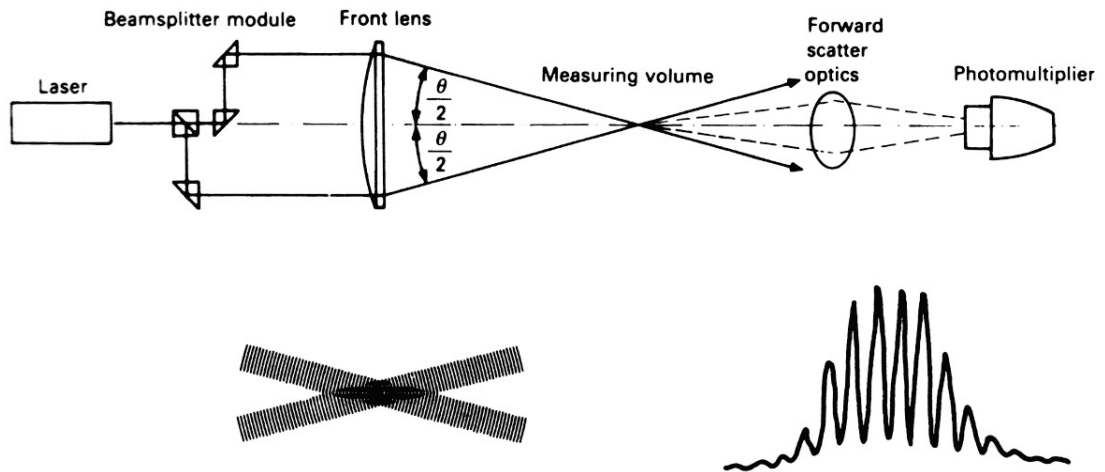
Figure 2.9.2: Optical arrangement schematic for a Laser Doppler Velocimetry (LDV) system showing the interference fringe pattern and lights scattered by particles (Stone 1999)

2.9.4 Particle Image Velocimetry (PIV)

Particle image velocimetry (PIV) is an optical measurement technique that has the capability of mapping 2D velocity fields with a high temporal and spatial resolution and as such is a commonly used method of analysing the flow field of an IC engine.

Figure 2.9.3 illustrates the schematic of a typical PIV setup that consist of focussing a thin sheet of high energy density laser light in the required velocity measurement region and seeding the flow with small tracer particles. These particles need to follow the bulk flow as well as the highest frequency structures as accurately as possible in order to maximise the resolution and spatial accuracy of the measured velocity flow field as well as maximising turbulence characterisation. Typical seeding materials used in IC engine measurement are olive oil and silicone oil that can be seeded into 1-2 µm diameter particles, with silicone oil being capable of better withstanding vaporisation from high in-cylinder compression pressures and temperatures. When these particles pass through the laser sheet, their scattered light can be detected as Gaussian peaks on the image plane of the recording camera that is situated perpendicular to the laser sheet. Typical single-shot PIV systems capture image pairs at up to 15 Hz, allowing every engine cycle to be captured up to 1800 rpm. A known time separation between pairs allows a velocity vector field to be formulated by dividing the flow field into small interrogation regions and correlating the displacement of several particles into a single vector for each region. Interframing times of less than 1 µs are possible (Raffel *et al.* 2007) allowing the capture of high-speed flows typical of engine flow.
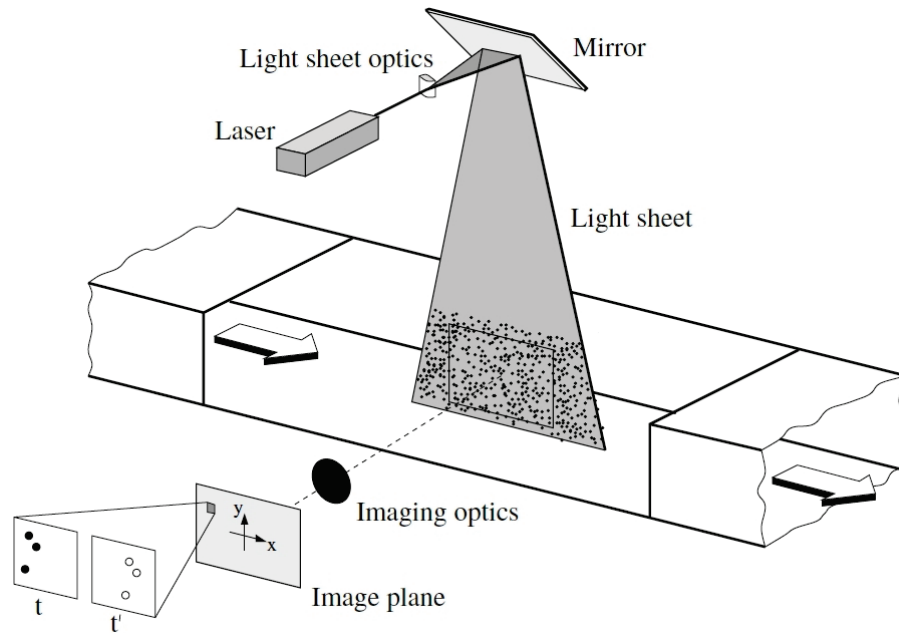
Figure 2.9.3: Experimental arrangement for a PIV system (adapted from Raffel *et al.* (2007))

High-speed digital PIV (HSPIV) systems using high-repetition lasers and high-speed cameras to allow velocity vector fields to be captured at rates of 10 KHz (Kapitza *et al.* 2010). Vector fields with high temporal resolutions can be quantified using these systems, allowing the development of complex flow structures to be observed at high engine speeds. PIV systems rely on individual aspects of the experimental setup to be precisely calibrated to achieve results that accurately represent the measured flow field. Parameters such as seeding density, diffraction limited particle image size, particle displacement and velocity gradient, are amongst a number of important factors that need consideration to achieve high-quality accurate PIV results.

2.9.4.1   *Application of HSPIV to Engine Flow*

Previous PIV experimentation in IC engines has been restricted to single-shot PIV, whereby one laser pulse and one image capture event occurred per engine cycle (Reuss 2000, Li *et al.* 2002, Justham *et al.* 2006a). More recent advances in camera technology and laser systems have demonstrated the use of HSPIV to quantify the in-cylinder flow to both a high temporal and spatial resolutions in a number of studies (Reeves *et al.* 2000, Ghandhi *et al.* 2005, Jarvis *et al.* 2006, Rimmer *et al.* 2009, Kapitza *et al.* 2010).

Early use of HSPIV, however, was somewhat restricted by camera and laser technology as highlighted by Reeves *et al.* (2000) and Towers and Towers (2004) who recorded engine flows at temporal resolutions of 9 kHz and 13.5 kHz respectively but were restricted to low image sizes between 128 x 128 pixels to 256 x 256 pixels at realistic engine speeds, which resulted in

low spatial resolutions of approximately 5 mm and limited the smallest measureable eddy diameter to 2.9 mm. The use of frame-straddling CMOS cameras and dual-head Nd:YLF lasers improved the spatial resolution of recorded IC engine flow. Ghandhi *et al.* (2005) demonstrated the increase of turbulent kinetic energy when increasing the cut-off length and decreasing the cut-off frequencies for high-pass filtering of flow measured within an engine operating at 1200 rpm with a temporal resolution of 1 kHz and an image resolution of 1024 x 1024 pixels.

Jarvis *et al.* (2006) and Rimmer *et al.* (2009) extended the application of HSPIV systems to engine flow at 1500 rpm, with a high temporal resolution of 5 kHz and image resolution of 512 x 512 pixels, which enabled the time between images to be as low as 1.8 crank angle degrees. The spatial resolution of 0.56 mm was high enough in these experiments to detect the cyclic variability in both the in-cylinder large scale bulk motions and small scale high-frequency components, which were shown to be linked to various engine parameters. Jarvis *et al.* (2006) used a fast Fourier transform (FFT) low-frequency filter to link large variations in the in-cylinder flow field to the recorded variations in the intake valve jets and location of tumble centres. Rimmer *et al.* (2009) measured the turbulent flow field around the spark plug area at the time of ignition and demonstrated that turbulent fluctuations greater than 600 Hz influence the IMEP and burn rate, which confirmed previous work by Gillespie *et al.* (2000) and Bradley *et al.* (2003) carried out in a combustion bomb.

More recent studies by Muller *et al.* (2010) and Kapitza *et al.* (2010) have utilised HSPIV rates of 6 kHz and 10 kHz respectively, at images sizes of at least 512 x 512 pixels. These high temporal and spatial resolution studies have enabled the temporal evolution of turbulent flow structures to be quantified at realistic engine speeds. These studies highlight HSPIV as a vital tool in further elucidating the link between turbulence flow structures, fuel spray structure and impingement, combustion and emissions processes.

2.9.5   Stereoscopic PIV

The flow field measurement capability of 2D PIV is greatly restricted when the flow is of a three-dimensional (3D) complex nature, as is seen within IC engines. The third out-of-plane velocity component is not captured with 2D PIV systems so a full understanding of the 3D field is not achieved. Stereoscopic PIV is an approach that involves using a second camera with both cameras at an angle of 45° from the axis normal to the laser sheet focussed onto the same flow imaging region. The velocity components from each camera exert a slight difference that is due to the third velocity component parallax error. To quantify the third velocity

component, camera calibration is required using physical the parameters of the imaging system such as the viewing angle and magnification factor, along with the use of precision manufactured planar calibration targets, which are placed coincident with the light sheet plane.

Less research literature is available for stereoscopic PIV analysis of in-cylinder fluid flow, particularly in DISI engines, highlighting the requirement for continued investigation into this area. Calendini and Durveger (2000) used stereo-PIV on a single cylinder DISI engine to better visualise the bulk flow tumble motions in the centre of the cylinder during intake and compression. In-cylinder flow structures were measured that showed flow motions of a highly complex and 3D nature with no clear and discernible tumble motion when compared to 2D measurements. Due to the measurement of the third component of flow, cycle-to-cycle variability, especially within large eddies, was described to be higher when compared to 2D PIV measurements. High-swirl intake flow, typically found in compression ignition (CI) engines, can benefit significantly from stereo-PIV measurements due to the increased prevalence of out-of-plane motion when measuring in the tumble plane. Singh *et al.* (2015) measured the in-cylinder flow field near the intake valves of a CI engine operating at 1200 rpm and 2100 rpm using stereo-PIV. The flow during the compression stroke was shown to be more turbulent at higher engine speeds due to the increased level of flow rotation and vorticity measured in the third component plane. This flow behaviour is vital for CI engine performance as it promotes better fuel-air mixing and affects engine performance and emissions characteristics (Singh *et al.* 2015).

Due to the nature of engine flow, along with the added complexity of tumble and swirl flow structure present in DISI engines, this type of analysis would be invaluable in better understanding and quantifying the in-cylinder three-dimensional flow. Further understanding of in-cylinder turbulence and the mechanisms that lead to turbulent flame propagation as well as their correlation with engine performance would contribute greatly to the existing research that links turbulence to engine performance parameters.

As highlighted, a significant benefit of all PIV measurement techniques, is the ability to simultaneously capture high resolution spatial and temporal velocity flow fields. Capturing data over a planar region enables flow field derivatives such as strain and shear rates to be quantified, which are not readily available through single point measurement techniques such as LDV. It is understood that these gradient-based quantities are involved in energy

production, dissipation and in the mechanisms responsible for the energy transfer down to the smallest scales in the energy cascade (Rimmer 2010).

2.9.6 Laser Induced Fluorescence (LIF)

Laser induced fluorescence (LIF) is a technique used for the detection of species within a flow or flame. It is widely used for the investigation of fuel spray atomisation, vaporisation and charge mixing whereby it can measure the AFR distribution of the charge (Stevens *et al.* 2006, Kirchweger *et al.* 2007, Williams *et al.* 2008).

A pulsed laser forms a light sheet into the required flow region with a frequency that is tuned to cause a specific species or tracer to excite electrons and subsequently light. Various intensities of the emitted fluorescence allow a species concentration to be detected by a camera that is perpendicular to the laser sheet. Quantitative planar laser induced fluorescence (QPLIF) was successfully implemented by Williams *et al.* (2008) in a DISI engine and by Mederer *et al.* (2012) in a hydrogen engine to quantitatively determine the homogeneity of the fuel mixture and the cyclic-to-cycle variations present in the fuelling. An extensive amount of experimental setup and calibration, however, was required with the selection of a suitable fuel tracer, in order to attain accurate quantitative data. Non-quantitative LIF does have the advantage, however, of being able to capture useful spatial and temporal species data qualitatively with reduced experimental calibration.

A number of LIF studies have investigated important physical processes that contribute to emissions in DISI engines. Fuel spray breakup, distribution and evaporation of gasoline-based and ethanol-base fuel sprays in a DISI engine were measured using a combination of LIF and Mie scattering by Andersson *et al.* (2011). It was shown that at air temperatures of 363 K, the light components of gasoline fuel evaporated much faster than the medium to heavy components. The ethanol-base fuel spray, however, was measured to evaporate much slower and required an air temperature of 473 K to produce similar evaporation rates to gasoline. Fuel spray impingement is also a known cause of PM and HC emissions and was fundamentally investigated using LIF by Uchida *et al.* (2015), who utilised a doped fuel spray and it was found that the impingement behaviour on a cylinder liner oil film can be linked to the Weber number of the impinging fuel droplet.

2.9.7   Laser Induced Incandescence (LII)

With the increasing requirement to monitor and reduce PM emissions in DISI engines, laser induced incandescence (LII) is a measurement technique that offers useful measurement of soot volume fraction as low as nanoparticle sizes. LII is one of the most commonly used techniques to study soot formation processes in an engine because it can prove in-situ quantitative measurements of soot volume fraction (Zhao and Ladommatos 1998). The principle of the technique is straightforward in that a laser pulse heats the soot particles up to their vaporisation temperature of approximately 4500 K that emits near-ultraviolet light more intense than that emitted at a flame temperature of approximately 2200 K. This enables the light emitted by combustion-heated particles to be removed from the LII images using an appropriate filter (Francqueville *et al.* 2010). Using collection optics and photo detectors, the incandescence of the soot particles is measured. The decay rate of the short LII signal is then monitored and related to the soot size of the particle with a larger particle exerting a longer decay period. The dominant cooling mechanisms for the soot particles are conduction to the surrounding gas, sublimation and radiative emissions (Francqueville *et al.* 2010). To convert the LII signal to an absolute volume fraction and primary soot particle size, calibration with a known source is required (Rimmer 2010).

2.10   FLOW FIELD ANALYSIS TECHNIQUES

The analysis of instantaneous velocity vector fields attained through PIV measurement gives an indication of the nature of the flow velocity and turbulence but does not attain an adequate in-depth understanding of the complex flow typically observed in IC engines. The development of high-speed systems that spatially and temporally resolve flow field data allow a number of techniques to extract further information on the nature of the flow so a better understanding can be derived.

2.10.1 Reynolds Decomposition

Instantaneous velocity fields can be broken down in an ensemble mean and fluctuating component using Reynolds decomposition as illustrated in Figure 2.10.1. This method is very common in describing turbulent velocity fields over a number of cycles. The amount that the instantaneous component differs from the ensemble mean depends on how large the cycle-to-cycle fluctuations are.
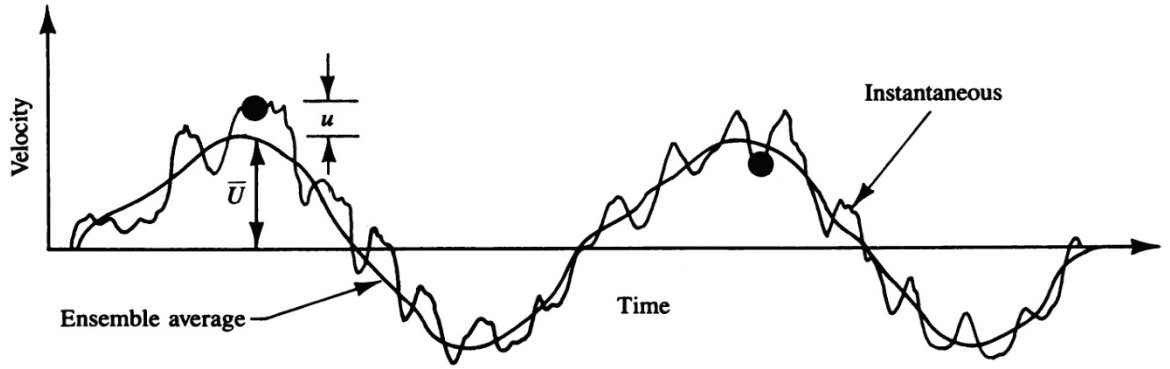
Figure 2.10.1: Schematic of velocity variation with crank angle showing high and low frequency components (adapted from Heywood (1988)

The Reynolds decomposition is formulated below and links the instantaneous velocity, $U_{(\vartheta,i,x,y)}$, ensemble average, $\bar{U}_{(\vartheta,x,y)}$ and turbulence fluctuation , $u_{(\vartheta,i,x,y)}$ as shown below. Reynolds decomposition can be space-averaged, which averages the vectors in a single spatial field and compares it to each individual velocity vector or time-averaged, which averages the vectors in a certain position over a time.

$$U_{(\theta,i,x,y)} = \bar{U}_{(\theta,x,y)} + u_{(\theta,i,x,y)}$$

Eqn. (2.10.1)

and

$$\bar{U}_{(\theta,x,y)} = \frac{1}{n}\sum_{i=1}^{n} U_{(\theta,i,x,y)}$$

Eqn. (2.10.2)

where:

$\bar{U}_{(\vartheta, x, y)}$ = Ensemble average velocity at crank angle θ, position x, y

$\bar{U}_{(\vartheta, i, x, y)}$ = Instantaneous velocity of cycle i, for n cycles.

The ensemble average velocity is a useful parameter in quantifying the flow field development through an engine cycle when used with time-resolved HSPIV data. The development of bulk flow structures can be observed through a cycle as well as the comparisons between instantaneous vector fields. To maintain an accurate ensemble average of a spatial or temporal velocity field, the number of average cycles must be adequate. Reuss (2000) highlighted that a small cycle sample size can result in an extreme statistical bias in the ensemble mean when an unsteady parameter is analysed.

The turbulence fluctuation velocity u, is defined as the difference between the instantaneous and the mean velocities. The turbulence intensity (or RMS velocity fluctuation) u', can be deduced thus

$$u'(\theta) = \sqrt{\overline{(U - \bar{U})^2}}$$

Eqn. (2.10.3)

$$u'(\theta) = \sqrt{\frac{1}{N} \sum_{i=1}^{N} (U_{(\theta,i,x,y)} - \bar{U}_{(\theta,x,y)})^2}$$

Eqn. (2.10.4)

Local mean velocity (LMV) decomposition is a technique that calculates the ensemble average over small regions compared to the entire field. The fluctuation component *u*, is compared to this LMV that reveals eddies in one area of the vector field where the fluid flows at exactly the chosen mean velocity, while remaining hidden in all other regions where the fluid is moving faster or slower (Rimmer 2010).

2.10.2 Large Eddy Simulation (LES)

Large eddy simulation (LES) involves decomposition of velocity flow fields into small scale, high frequency and large scale, low frequency components. To achieve this, the *x* and *y* velocity vector components are transposed into the spatial frequency domain using a fast Fourier transform (FFT). A low pass filter is then applied to filter out the high frequency components using a cut-off frequency and the velocity signal is reconstructed into the time domain to obtain the low frequency velocity components (Rimmer *et al.* 2009). The low frequency and high frequency velocity components can then be deduced the instantaneous velocity such that

$$U_{(\theta,i,x,y)} = U_{LF(\theta,i,x,y)} + U_{HF(\theta,i,x,y)}$$

where:

U	Instantaneous velocity vector of cycle i, at crank angle θ, and location x, y
U_{LF}	Low frequency velocity vector component
U_{HF}	High frequency velocity vector component.

The selection of the cut-off frequency for the low-pass filter has been discussed by a number of authors (Reuss 2000, Jarvis *et al.* 2006, Rimmer *et al.* 2009) with typical frequencies between 200 Hz and 600 Hz. The cut-off frequency, however, is dependent on the analysed flow field and is usually an arbitrary approach. Rimmer (2010) discussed an alternative approach for the correct selection of cut-off frequency. The RMS turbulence is first calculated using Reynolds decomposition along with a range of cut-off frequencies. The calculated high-frequency RMS turbulence is then compared to the engine parameter IMEP, calculated for each engine cycle. A correlation coefficient between these two parameters is then determined, which quantifies the relationship between turbulent flow structures and engine

performance. A suitable cut-off frequency can then be selected depending on where the highest correlation coefficient is observed. This method has been successfully implemented experimentally and in CFD modelling (Rimmer *et al.* 2009, Laget *et al.* 2010).

2.11   CONCLUDING REMARKS

This literature review has discussed DISI engine methodology and the processes involved with in-cylinder flow and combustion. The review of control strategies available to DISI engine designers with particular focus on meeting future emissions legislation has highlighted an array of techniques that can be utilised to affect combustion parameters. Increasingly investigated cold-start strategies has highlighted the ever increasing focus in this field as well as the requirement to better understand the complex in-cylinder processes taking place. It was also noted that further experimental research into initial transient engine start-up is needed to better understand the mechanisms that generate PM in this critical phase. Considerable research has been presented highlighting the use of tumble and swirl to influence turbulent flow structures and the effect these have on combustion and emissions. The importance of attaining a good understanding of these complex flow structures and the way they interact with the fuel spray is vital in understanding fuel spray impingement and fuel mixture homogeneity. A number of in-cylinder velocity measurement techniques and methods of analysing their results have been studied. The need for third-component fluid flow analysis in an IC engine and the potential benefits in understanding in this field of research are very apparent. A number of velocity vector analysis techniques exist that successfully decompose the data into useful information. There is, however, no standardised methodology for selecting the cut-off frequency in the analysis of turbulent flow field data in engine studies, highlighting the necessity of developing improved analysis techniques.

The next chapter discusses the experimental setup and configuration of the optical engine facility and details the setup of the experimental equipment that has been used to investigate the research areas identified in this literature review.

2.12   CHAPTER 2 REFERENCES

AHMED, F., KAWAHARA, N., TOMITA, E. & MAMORU, S. (2010) Characterization of the Spray of the DISI Multi-hole Injector by Means of Phase Doppler Anemometer. *Journal of Thermal Science and Technology,* Vol 5(1), pp. 36-47.

ALEIFERIS, P. G., TAYLOR, A. M. K. P., ISHII, J. & URATA, Y. (2000a) The Relative Effects of Fuel Concentration, Residual Gas Fraction, Gas Motion, Spark Energy and Heat Losses to the Electrodes in a Lean-Burn Spark-Ignition Engine. *Journal of Automobile Engineering (Proceedings of IMechE, Part D),* Vol 218, pp. 411-425.

ALEIFERIS, P. G., TAYLOR, A. M. K. P. & WHITELAW, J. H. (2000b) Cyclic Variations of Initial Flame Kernel Growth in a Honda VTEC-E Lean-Burn Spark-Ignition Engine, SAE Paper 2000-01-1207.

ALGER, T., HALL, M. & MATTHEWS, R. D. (2000) Effects of Swirl and Tumble on In-Cylinder Fuel Distribution in a Central Injected DISI Engine, SAE Paper 2000-01-0533.

ALKIDAS, A. C. & TAHRY, S. H. (2003) Contributors to the Fuel Economy Advantage of DISI Engines Over PFI Engines, SAE Paper 2003-01-3101.

ANDERSSON, M., WÄRNBERG, J., HEMDAL, S., DAHLANDER, P. & DENBRATT, I. (2011) Evaporation of Gasoline-Like and Ethanol-Based Fuels in Hollow-Cone Sprays Investigated by Planar Laser-Induced Fluorescence and Mie Scattering SAE Paper 2011-01-1889.

ANDO, H. (1997) Mitsubishi GDI engine strategies to meet the European requirement. *Proceedings of AVL Conference on Engine and Environment,* Vol 2, pp. 55-77.

ANNAND, W. J. D. & ROE, G. E. (1974) Gas Flow in the Internal Combustion Engine. *Yeovil Annual Book of ASTM Standards - Test Methods for Rating Motor, Diesel and Aviation Fuels,* Vol 05(04).

ASMUS, T. W. (1982) Valve Events and Engine Operation, SAE Paper 820749.

BERNDORFER, A., BREUER, S., PIOCK, W. & BACHO, P. V. (2013) Diffusion Combustion Phenomena in GDi Engines caused by Injection Process, SAE Paper 2013-01-0261.

BIANCHI, G. M., CANTORE, G. & FONTANESI, S. (2002) Turbulence Modelling in CFD Simulation of ICE Intake Flows: The Discharge Coefficient Prediction, SAE Paper 2002-01-1118.

BLOCK, B., OPPERMANN, W. & BUDACK, R. (2000) Luminosity and Laser-Induced Incandescence Investigations on a DI Gasoline Engine, SAE Paper 2000-01-2903.

BOHREN, C. F. & HUFFMAN, D. R. (1998) *Absorption and Scattering of Light by Small Particles*, Wiley-Interscience, Vol. 2.

BONANDRINI, G., GIOIA, R. D., PAPALEO, D. & VENTUROLI, L. (2012) Numerical Study on Multiple Injection Strategies in DISI Engines for Particulate Emission Control, SAE Paper 2012-01-0400.

BRADLEY, D., HAQ, M. Z., HICKS, R. A., KITAGAWA, T., LAWES, M., SHEPPARD, C. G. W. & WOOLLEY, R. (2003) Turbulent burning velocity, burned gas distribution, and associated flame surface definition. *Combustion and Flame 133,* Vol 133(2003).

BRADLEY, D., LAWES, M. & SHEPPARD, C. G. W. (2000) Combustion and the thermodynamic performance of spark ignition engines. *Proc Instn Mech Engrs,* Vol 214(C), pp. 257-268.

CALENDINI, P. O. & DURVEGER, T. (2000) In-Cylinder Velocity Measurements with Stereoscopic Particle Image Velocimetry in a SI Engine, SAE Paper 2000-01-1798.

CHAPMAN, J., GARRETT, M. W. & WARBURTON, A. (1991) A new standard for barrel swirl movement. *IMechE Birmingham, 12-15 November 1991,* Vol C427/18/156, pp. 157.

CHEN, X., FU, H., SMITH, S. & SANDFORD, M. (2009) Investigation of Combustion Robustness in Catalyst Heating Operation on a Spray Guided DISI Engine, SAE Paper 2009-01-1489.

CHOI, J., LEE, S., SHIN, H. & BAE, C. (2000) Fuel-Spray Characteristics of High Pressure Gasoline Injection in Flowing Fields. *JSME Int J Fluids Thermal Eng B* Vol 43, pp. 576-581.

CHRYSSAKIS, C. A., ASSANIS, D. N., LEE, J. K. & NISHIDA, K. (2003) Fuel Spray Simulation of High-Pressure Swirl-Injector for DISI Engines and Comparison with Laser Diagnostic Measurements, SAE Paper 2003-01-0007.

COLLINS, D. & STOKES, J. (1983) Gasoline combustion chambers - compact or open?, SAE Paper 830866.

DAVY, M. H., WILLIAMS, P. A. & ANDERSON, R. W. (1998) Effects of Injection Timing on Liquid-Phase Fuel Distributions in a Centrally-Injected Four-Valve Direct-Injection Spark-Ignition Engine, SAE Paper 982699.

DE BOER, C. D., JOHNS, R. J. R., GRIGG, D. W., TRAIN, B. M., DENBRATT, I. & LINNA, J. R. (1990) Refinement with performance and economy for four-valve automotive engines. *Proc. I.Mech.E. Conf. on Automotive Power Systems,* Vol Paper C394(53), pp. 147-155.

DIESELNET (2015) European Union Emission Standards for Cars and Light Trucks, Available from: http://www.dieselnet.com/standards/eu/ld.php, [Accessed 01/06/2015].

DISCH, C., KUBACK, H., SPICHER, U., PFEIL, J., ALTENSCHMIDT, F. & SCHAUPP, U. (2013) Investigations of Spray-Induced Vortex Structures during Multiple Injections of a DISI Engine in Stratified Operation Using High-Speed-PIV, SAE Paper 2013-01-0563.

EFTHYMIOU, P., DAVY, M., GARNER, C., HARGRAVE, G., RIMMER, J. E. T. & RICHARDSON, D. (2013) Insights into Cold-Start DISI Combustion in an Optical Engine Operating at −7°C. *SAE. Int. J. Engines,* Vol 6(2), pp. 1059-1074.

ENG, J. A. (2005) The Effect of Spark Retard on Engine-out Hydrocarbon Emissions, SAE Paper 2005-01-3867.

ERDIL, A. & KODAL, A. (2007) A comparative study of turbulent velocity fields in an internal combustion engine with shrouded valve and flat/bowl piston configurations. *Proc. IMechE Part C: J. Mechanical Engineering Science,* Vol 221, pp. 1597-1607.

EUROPEAN PARLIAMENT, COUNCIL (2007) REGULATION (EC) No 715/2007 OF THE EUROPEAN PARLIAMENT AND OF THE COUNCIL of 20 June 2007 on type approval of motor vehicles with respect to emissions from light passenger and commercial vehicles (Euro 5 and Euro 6) and on access to vehicle repair and maintenance information. *Official Journal of the European Union,* Vol COD 2005/0282.

FISCHER, J., KETTNER, M., NAUWERCK, A., PFEIL, J. & SPICHER, U. (2002) Influence of an Adjustable Tumble-System on In-Cylinder Air Motion and Stratification in a Gasoline Direct Injection Engine, SAE Paper 2002-01-1645.

FRAIDL, G. K., MIKULIC, L. A. & QUISSSEK, F. (1990) Development strategies for low emission high performance four-valve engines. *Proc. Instn Mech. Engrs, Part D,* Vol 204(D1), pp. 59-65.

FRANCQUEVILLE, L. D., BRUNEAUX, G. & THIROUARD, B. (2010) Soot Volume Fraction Measurements in a Gasoline Direct Injection Engine by Combined Laser Induced Incandescence and Laser Extinction Method, SAE Paper 2010-01-0346.

GHANDHI, J. B., HEROLD, R. E., SHAKAI, J. S. & STRAND, T. E. (2005) Time-resolved particle image velocimetry measurements in an internal combustion engine, SAE Paper 2005-01-3868.

GILLESPIE, L., LAWES, M., SHEPPARD, C. G. W. & WOOLLEY, R. (2000) Aspects of Laminar and Turbulent Burning Velocity Relevant to SI Engines, SAE Paper 2000-01-0192.

GREENBERG, J. B., MCINTOSH, A. C. & BRINDLEY, J. (1999) Instability of a flame front propagating through a fuel-rich droplet–vapour–air cloud. *Combust. Theory Modelling,* Vol 3(1999), pp. 567-584.

GUPTA, S., POOLA, R., O.L., K. & SEKAR, R. (2000) Particulate Emissions Characteristics of Port-Fuel Injected SI Engine. *US Dept. of Energy*.

HAN, Z., FAN, L. & REITZ, R. D. (1997a) Multidimensional Modelling of Spray Atomization and Air-Fuel Mixing in a Direct-Injection Spark-Ignition Engine, SAE Paper 970884.

HAN, Z., REITZ, R. D., YANG, J. & ANDERSON, R. W. (1997b) Effects of Injection Timing on Air-Fuel Mixing in a Direct-Injection Spark-Ignition Engine, SAE Paper 970625.

HARGRAVE, G. K., WIGLEY, G., ALLEN, J. & BACON, A. (2000) Optical Diagnostics and Direct Injection of Liquid Fuel Sprays. *Journal of Visualization,* Vol 2(3/4 2000), pp. 293-300.

HATTORI, H., OTA, M., SATO, E. & KADOTA, T. (1995) Fundamental study on DISC engine with two-stage fuel injection. *JSME Int J 1995,* Vol B38(1), pp. 129-35.

HEYWOOD, J. B. (1988) *Internal Combustion Engine Fundamentals,* 1st Ed., McGraw-Hill, pp. 42-61, 205-278, 400-450, 797-819.

HONG, H., PARVATE-PATIL, G. B. & GORDON, B. (2004) Review and analysis of variable valve timing strategies - eight ways to approach. *Proc. Instn Mech. Engrs, Part D: J. Automobile Engineering,* Vol 218, pp. 1179-1200.

JARVIS, S., JUSTHAM, T., CLARKE, A., GARNER, C. P. & HARGRAVE, G. K. (2006) Motored SI IC Engine In-Cylinder Flow Field Measurement Using Time Resolved Digital PIV For Characterisation of Cyclic Variation, SAE Paper 2006-01-1044.

JUSTHAM, T. (2010) Cyclic Variation in the Flow Field Behaviour within a Direct Injection Spark Ignition Engine: A High Speed Digital Particle Image Velocimetry Study, Loughborough, PhD Thesis, Loughborough University.

JUSTHAM, T., JARVIS, S., CLARKE, A., GARNER, C. P., HARGRAVE, G. K. & HALLIWELL, N. A. (2006a) Simultaneous Study of Intake and In-Cylinder IC Engine Flow Fields to Provide

an Insight into Intake Induced Cyclic Variations. *Journal of Physics: Conference Series,* Vol 45, pp. 146-153.

JUSTHAM, T., JARVIS, S., GARNER, C. P., HARGRAVE, G. K. & CLARKE, A. (2006b) Single Cylinder Motored SI IC Engine Intake Runner Flow Measurement Using Time Resolved Digital Particle Image, SAE Paper 2006-01-1043.

KALGHATGI, G. T. (1987) Spark Ignition, Early Flame Development and Cyclic Variation in IC Engines, SAE Paper 870163.

KAPITZA, L., IMBERDIS, O., BENSLER, H. P., WILLAND, J. & THÉVENIN, D. (2010) An experimental analysis of the turbulent structures generated by the intake port of a DISI-engine. *Exp Fluids (2010),* Vol 48, pp. 265-280.

KIRCHWEGER, W., HASLACHER, R., HALLMANNSEGGER, M. & GERKE, U. (2007) Applications of the LIF method for the diagnostics of the combustion process of gas-IC-engines. *Exp. Fluids,* Vol 43, pp. 329-340.

KUME, T., IWAMOTO, Y., LIDA, K., MURAKAMI, M., AKISHINO, K. & ANDO, H. (1996) Combustion Control Technologies for Direct Injection SI Engine, SAE Paper 960600.

KUWAHARA, K., YAMAMOTO, S., IWACHIDOU, K. & ANDO, H. (1998) Two-Stage Combustion for Quick Catalyst Warm-up in Gasoline Direct Injection. *The Fourth International Symposium COMODIA 98*, pp. 293-298.

LAGET, O., ZACCARDI, J. M., GAUTROT, X., MANSION, T. & COTTE, E. (2010) Establishing New Correlations Between In-Cylinder Charge Motion and Combustion Process in Gasoline Engines Through a Numerical DOE. *SAE Int. J. Engines, SAE Paper 2010-01-0349,* Vol 3(1).

LEE, J. & FARRELL, P. V. (1993) Intake Valve Flow Measurements of an IC Engine Using Particle Image Velocimetry, SAE Paper 930480.

LEE, K., BAE, C. & KANG, K. (2007) The effects of tumble and swirl flows on flame propagation in a four-valve S.I. engine. *Elsevier, Applied Thermal Engineering,* Vol 27, pp. 2122-2130.

LEE, K. & LEE, C. S. (2003) Effects of tumble and swirl flows on turbulence scale near top dead centre in a four-valve spark ignition engine. *Proc. Instn Mech. Engrs, Part D: J Automobile Engineering,* Vol 217, pp. 607-615.

LEE, S., BAE, C., LEE, Y. & TAESIK, H. (2002) Engine, Effects of Engine Operating Conditions on Catalytic Converter Temperature in an SI, SAE Paper 2002-01-1677.

LEE, S., OH, Y. & PARK, S. (2013) Characterization of the spray atomization process of a multi-hole gasoline direct injector based on measurements using a phase Doppler particle analyser. *Proc IMechE Part D: J Automobile Engineering,* Vol 227(7), pp. 951-965.

LI, Y., LEACH, B., MA, T. & LADOMMATOS, N. (2004) Characterization of an in-cylinder flow structure in a high-tumble spark ignition engine. *Int. J. Engine Res.,* Vol 5(5), pp. 375-400.

LI, Y., ZHAO, H. & LADOMMATOS, N. (2002) Analysis of large-scale flow characteristics in a four-valve spark ignition engine. *Proc Instn Mech Engrs,* Vol 216 Part C: J Mechanical Engineering Science, pp. 923-928.

LI, Y., ZHAO, H., LEACH, B., MA, T. & LADOMMATOS, N. (2003) Optimisation of In-Cylinder Flow for Fuel Stratification in a Three-Valve Twin-Spark-Plug SI Engine, SAE Paper 2003-01-0635.

LONG, E. J. (2010) The Influence of Reactant Flow Structure on Flame Front Propagation, Loughborough, PhD Thesis, Loughborough University.

LUMLEY, J. L. (1999) *Engines: An Introduction*, Cambridge University Press.

MAHMOOD, Z., CHEN, A. & YIANNESKIS, M. (1996) On the structure of steady flow through dual-intake engine ports. *International Journal for Numerical Methods in Fluids,* Vol 23, pp. 1085-1109.

MALY, R. & VOGEL, M. (1978) Initiation and Propagation of Flame Fronts in Lean CH_4-Air Mixtures by the Three Modes of Ignition Spark. *17th Symposium (International) on Combustion,* Vol 821-831.

MEDERER, T., WENSING, M. & LEIPERTZ, A. (2012) Laser-Induced Fluorescence to Visualize Gas Mixture Formation in an Optically Accessible Hydrogen Engine. *COMODIA.* Fukuoka, Japan.

MORITA, K., SONODA, Y., KAWASE, T. & SUZUKI, H. (2005) Emission Reduction of a Stoichiometric Gasoline Direct Injection Engine, SAE Paper 2005-01-3687.

MORIYOSHI, Y., NOMURA, H. & SAISYU (1997) Evaluation of a Concept for DI Gasoline Combustion Using Enhanced Gas Motion, SAE Paper 980152.

MULLER, S. H. R., BOHM, B., GLEISNER, M., GRZESZIK, R., ARNDT, S. & DREIZLER, A. (2010) Flow field measurements in an optically accessible, direct injection spray guided internal combustion engine using high-speed PIV. *Exp. Fluids,* Vol 48, pp. 281-290.

OMORI, S., IWACHIDO, K., MOTOMOCHI, M. & HIRAKO, O. (1991) Effect of Intake Port Flow Pattern on the In-Cylinder Tumbling Air Flow in Multi-Valve SI Engine, SAE Paper 910477.

PAJOT, O. & MOUNAÏM-ROUSSELLE, M. (2000) Instantaneous Flow Field Effects on the Flame Instantaneous Flow Field Effects on the Flame Optical Diagnostics, SAE Paper 2000-01-1796.

PATEL, R., LADOMMATOS, N., STANSFIELD, P., WIGLEY, G., GARNER, C. P., PITCHER, G., TURNER, J. W. G. & NUGLISCH, H. (2008) Comparison between Unthrottled, Single and Two-valve Induction Strategies Utilising Direct Gasoline Injection: Emissions, Heat-release and Fuel Consumption Analysis, SAE Paper 2008-01-1626.

PIOCK, W., HOFFMANN, G., BERNDORFER, A., SALEMI, P. & FUSSHOELLER, B. (2011) Strategies Towards Meeting Future Particulate Matter Emission Requirements in Homogeneous Gasoline Direct Injection Engines, SAE Paper 2011-01-1212.

PISCHINGER, S. & HEYWOOD, J. B. (1990) How heat losses to the spark plug electrodes affect flame kernel development in an SI Engine, SAE Paper 900021.

PITCHER, G. & WIGLEY, G. (2001) LDA Analysis of the Tumble Flow Generated in a Motored 4 Valve Engine. *9th Internal Conference, Laser Anemometry Advances and Applications.* Limerick.

PRICE, P., STONE, R., OUDENIJEWEME, D. & CHEN, X. (2007) Cold Start Particulate Emissions From a Second-Generation DI Gasoline Engine, SAE Paper 2007-01-1931.

PULKRABEK, W. W. (2004) *Engineering Fundamentals of the Internal Combustion Engine*, Pearson Prentice-Hall, Vol. 2, pp. 198-230.

QUEIROZ, C. & TOMANIK, E. (1997) Gasoline Direct Injection Engines - A Bibliographical Review, SAE Paper 973113.

RAFFEL, M., WILLERT, C. E., WERELEY, S. T. & KOMPENHANS, J. (2007) *Particle Image Velocimetry: A Practical Guide,* 2nd Ed., Springer-Verlag.

REEVES, M., HASTE, M., GARNER, C. P. & HALLIWELL, N. A. (1999) Barrel swirl breakdown in spark-ignition engines: insights from particle image velocimetry measurements. *Proc Instn Mech Engrs,* Vol 213(Part D), pp. 595-609.

REEVES, M., TOWERS, D. P., TAVENDER, B. & BUCKBERRY, C. H. (2000) A technique for routine, cycle-resolved 2-D flow measurements and visualisation within SI engine cylinders in an engine development environment. *Proceedings of the 10th International Symposium on Applications of Laser Techniques to Fluid Mechanics.* Lisbon, Portugal.

REUSS, D. L. (2000) Cyclic Variability of Large-Scale Turbulent Structures in Directed and Undirected IC Engine Flows, SAE Paper 2000-01-0246.

RIMMER, J. E. T. (2010) An Optical Investigation into the Effect of Fuel Spray, Turbulent Flow and Flame Propagation on DISI Engine Performance, Loughborough, PhD Thesis, Loughborough University.

RIMMER, J. E. T., DAVY, M. H., GARNER, C. P., HARGRAVE, G. K. & RICHARDSON, D. (2012) Fuel spray structure, flame propagation and charge motion at fuel impingement locations within a DISI engine. *IMechE: Fuel Systems for IC Engines,* Vol 2012, pp. 199-214.

RIMMER, J. E. T., LONG, E. J., GARNER, C. P., HARGRAVE, G. K., RICHARDSON, D. & WALLACE, S. (2009) The Influence of Single and Multiple Injection Strategies on In-Cylinder Flow and Combustion within a DISI Engine, SAE Paper 2009-01-0660.

SANFORD, M., PAGE, G. & CRAWFORD, P. (2009) The All New AJV8, SAE Paper 2009-01-1060.

SCHMIDT, L., SEABROOK, J., STOKES, J., FAIZAN, M., ZUHDI, A., BEGG, S., HEIKAL, M. & KING, J. (2011) Multiple Injection Strategies for Improved Combustion Stability under Stratified Part Load Conditions in a Spray Guided Gasoline Direct Injection (SGDI) Engine, SAE Paper 2011-01-1228.

SCHREIBER, D., FORSS, A. M., MOHR, M. & DIMOPOULOS, P. (2007) Particle Characterization of Modern CNG, Gasoline and Diesel Passenger Cars, SAE Paper 2007-24-0123.

SCHWEITZER, P. H. (1938) Penetration of Oil Sprays. *J. Appl. Phys.,* Vol 9(735), pp. 735-741.

SERRAS-PEREIRA, J., ALEIFERIS, P., RICHARDSON, D. & WALLACE, S. (2007a) Spray Development in a Direct-Injection Spark-Ignition Engine, SAE Paper 2007-07-2712.

SERRAS-PEREIRA, J., ALEIFERIS, P. G., RICHARDSON, D. & WALLACE, S. (2007b) Mixture Preparation and Combustion Variability in a Spray-Guided DISI Engine, SAE Paper 2007-01-4033.

SINGH, A. P., GUPTA, A. & AGARWAL, K. (2015) Tomographic Particle Image Velocimetry for Flow Analysis in a Single Cylinder Optical Engine. *SAE Int. J. Mater. Manf.,* Vol 8(2).

SPEGAR, T. D. (2011) Minimizing Gasoline Direct Injection (GDi) Fuel System Pressure Pulsations by Robust Fuel Rail Design, SAE Paper 2011-01-1225.

STACH, T., SCHLERFER, J. & VORBACK, M. (2007) New Generation Multi-hole Fuel Injector for Direct-Injection SI Engines - Optimization of Spray Characteristics by Means of Adapted Injector Layout and Multiple Injection, SAE Paper 2007-01-1404.

STANGLMAIER, R. H., LI, J. & MATTHEWS, R. D. (1999) The Effect of In-Cylinder Wall Wetting Location on the HC Emissions from SI Engines, SAE Paper 1999-01-0502.

STANSFIELD, P., WIGLEY, G., GARNER, C. P., PATEL, R., LADOMMATOS, N., PITCHER, G., TURNER, J. W. G., NUGLISCH, H. & HELIE, J. (2007a) Unthrottled Engine Operation using Variable Valve Actuation: The Impact on the Flow Field, Mixing and Combustion, SAE Paper 2007-01-1414.

STANSFIELD, P., WIGLEY, G., JUSTHAM, T., CATTO, J. & PITCHER, G. (2007b) PIV analysis of in-cylinder flow structures over a range of realistic engine speeds. *Exp Fluids (2007),* Vol 43, pp. 135-146.

STEVENS, R. E., MA, H., STONE, C. R., WALMSLEY, H. L. & CRACKNELL, R. (2006) On planar laser-induced fluorescence with multi-component fuel and tracer design for quantitative determination of fuel concentration in internal combustion engines. *Proc IMechE Part D,* Vol 221, pp. 713-721.

STONE, C. R., CARDEN, T. R. & PODMORE, I. (1993) Analysis of the effect of inlet valve disablement on swirl, combustion and emissions in a spark ignition engine. *Proc Instn Mech Engrs,* Vol 207, pp. 295-305.

STONE, R. (1999) *Introduction to Internal Combustion Engines,* 3rd Ed., MacMillan Press Ltd., pp. 25-35, 285-293.

TOMODA, T., SASAKI, S., SAWADA, D., SAITO, A. & SAMI, H. (1997) Development of direct injection gasoline engines - study of stratified mixture formation, SAE Paper 970539.

TOWERS, D. P. & TOWERS, C. E. (2004) Cyclic variability measurements of in-cylinder engine flows using high-speed particle image velocimetry. *Meas. Sci. and Technol.,* Vol 15, pp. 1917-1925.

TUTTLE, J. H. (1982) Controlling Engine Load by Means of Early Intake-Valve Closing, SAE Paper 820408.

TWINEY, B., STONE, R., CHEN, X. & EDMUNDS, G. (2010a) Investigation of Combustion Robustness in Catalyst Heating Operation on a Spray Guided DISI Engine, Part 1 - Measurements of Spark Parameters and Combustion, SAE Paper 2010-01-0593.

TWINEY, B., STONE, R., CHEN, X. & EDMUNDS, G. (2010b) Investigation of Combustion Robustness in Catalyst Heating Operation on a Spray Guided DISI Engine, Part II - Measurements of Spray Development, Combustion Imaging and Emissions, SAE Paper 2010-01-0603.

UCHIDA, R., TANAKA, D. & NODA, T. (2015) Impingement Behaviour of Fuel Droplets on Oil Film, SAE Paper 2015-01-0913.

WHITAKER, P., KAPUS, P., OGRIS, M. & HOLLERER, P. (2011) Measures to Reduce Particulate Emissions from Gasoline DI engines, SAE Paper 2011-01-1219.

WIGLEY, G., GOODWIN, M., PITCHER, G. & BLONDEL, D. (2004) Imaging and PDA analysis of a GDI spray in the near-nozzle region. *Experiments in Fluids 36,* Vol 2004, pp. 565-574.

WIGLEY, G., HARGRAVE, G. K. & HEATH, J. (1998) A High Power, High Resolution LDA/PDA System Applied to Dense Gasoline Direct Injection Sprays. *9th International Symposium on Applications of Laser Techniques to Fluid Mechanics, Lisbon, Portugal*, pp. 9.4.1-9.4.8.

WILLIAMS, B., EWART, P., STONE, R., MA, H., WALMSLEY, H., CRACKNELL, R., STEVENS, R., RICHARDSON, D., QIAO, J. & WALLACE, S. (2008) Multi-Component Quantitative PLIF: Robust Engineering Measurements of Cyclic Variation in a Firing Spray-Guided Gasoline Direct Injection Engine, SAE Paper 2008-01-1073.

WILLIAMS, F. A. (1985) *Combustion Theory: The fundamental theory of chemically reacting flow systems*, The Benjamin/Cummings Publishing Company.

WILSON, T., HASTE, M., XU, H., RICHARDSON, S., YAP, D. & MEGARITIS, T. (2005) In-cylinder Flow with Negative Valve Overlapping - Characterised by PIV Measurement, SAE Paper 2005-01-2131.

XU, M., NISHIDA, K. & HIROYASU, H. (1992) A Practical Calculation Method for Injection Pressure and Spray Penetration in Diesel Engines, SAE Paper 920624.

XU, M., ZHANG, Y., ZENG, W., ZHANG, G. & ZHANG, M. (2013) Flash Boiling: Easy and Better Way to Generate Ideal Sprays than the High Injection Pressure. *SAE Int. J. Fuels Lubr.,* Vol 6(1), pp. 137-148.

YASAR, A., SAHIN, B., AKILLI, H. & AYDIN, K. (2006) Effect of inlet port on the flow in the cylinder of an internal combustion engine. *Proc. IMechE Part C: J. Mechanical Engineering Science,* Vol 220, pp. 73-82.

ZHAO, F., HARRINGTON, D. L. & LAI, M. C. (1999) Automotive spark-ignited direct-injection gasoline engines. *Progress in Energy and Combustion Science 25,* Vol 1999, pp. 437-562.

ZHAO, F., HARRINGTON, D. L. & LAI, M. C. (2002) *Automotive Gasoline Direct-Injection Engines*, SAE International, pp. 1-50, 166-188, 223-260.

ZHAO, F. & LADOMMATOS, N. (1998) Optical diagnostics for soot and temperature measurement in diesel engines. *Progress in Energy and Combustion Science,* Vol 24(3), pp. 221-255.

ZHAO, F. & LAI, M. C. (1995) Optical diagnostics for soot and temperature measurement in diesel engines, SAE Paper 950506.

CHAPTER 3

EXPERIMENTAL SETUP AND EQUIPMENT

3.1   INTRODUCTION

The importance of PM generation in DISI engines has been discussed in *Chapters 1 and 2*, highlighting its particular significance during cold-start and transient operating modes. In-cylinder turbulence, and engine calibration and control have the potential to influence injection and combustion processes to improve engine emissions.

The literature review highlighted the lack of knowledge and understanding of in-cylinder processes during the cold-start and transient phases of DISI engine start-up. This chapter describes the experimental setup and implementation of an optical DISI engine for operation and measurement at low temperature. The optical engine facility was originally commissioned for an EPSRC project and has been continually utilised and developed for a number of combustion and in-cylinder flow studies (Jarvis *et al.* 2006, Justham *et al.* 2006a, Justham *et al.* 2006b, Rimmer *et al.* 2009, Rimmer *et al.* 2012, Efthymiou *et al.* 2013).

The engine modifications required to simulate an NEDC -7°C 'cold soak' test have been outlined along with the setup of all ancillary and data acquisition systems. Secondly, a description of the imaging systems used to acquire fuel spray and combustion visualisation data, using the wide array of available optical access, have been presented. Exhaust emissions analysis of both transient hydrocarbon emissions as well as PM emissions were made in order to correlate results with optical data and further the understanding of the complex in-cylinder combustion processes. A description of the HSPIV system that was used to measure the in-cylinder velocity field and its instrumentation on the optical engine, has also been presented.

3.2   OPTICAL ENGINE SPECIFICATION

A single cylinder optical research engine with a combustion system similar to that of the Jaguar AJ133 V8 was used (Sandford *et al.* 2009). This allowed the data obtained from the engine to be used for the design and calibration of production engines. Fundamental components such as the cylinder liner and piston could be interchanged between optical and thermodynamic variants depending on the level of optical access required. Figure 3.2.1 illustrates the engine configured for combustion imaging through the optical piston crown in cold conditions alongside basic engine configuration details. It should be noted that engine timing parameters are relative to after top dead centre (ATDC) of the intake stroke unless stated otherwise.
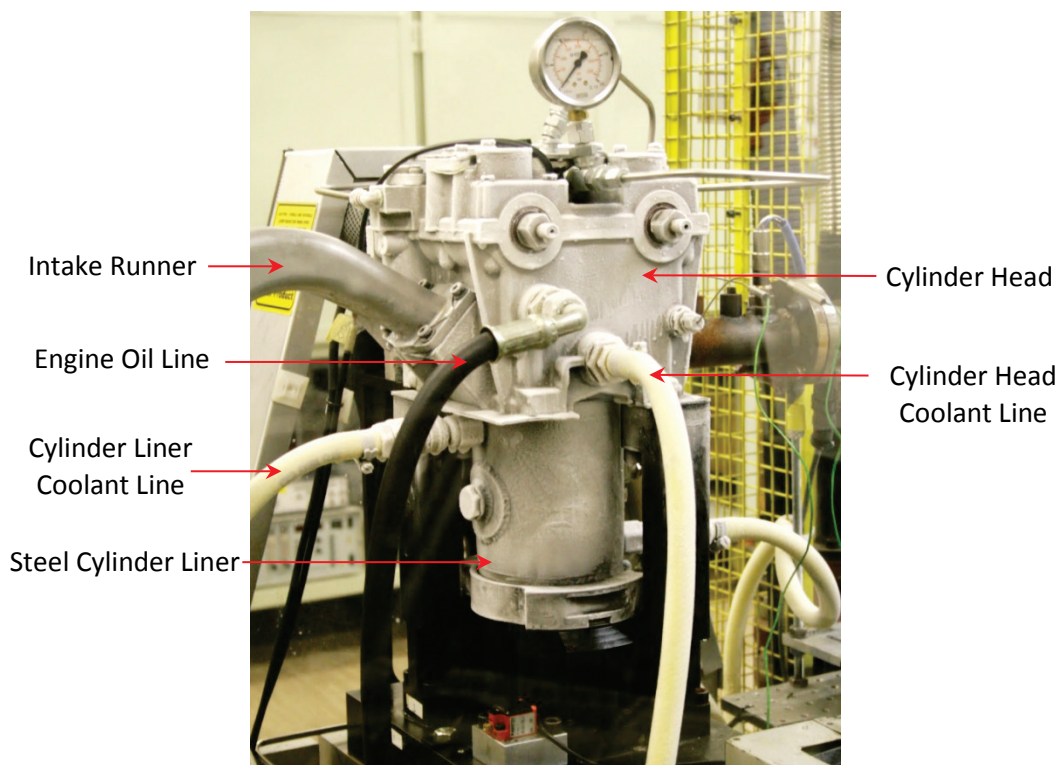
Maximum Engine Speed	2000 rpm
Bore	89.0 mm
Stroke	90.3 mm
Compression Ratio	10.5:1
Number of Valves	2 Intake, 2 Exhaust
Fuel Delivery	6-hole direct injection
Max Fuel Pressure	150 bar
Valve Timings (ATDC)	IVO 24°, IVC 274°
	EVO 475°, EVC 6°
Injection Timing (ATDC)	60°, 0°, 7°
Ignition Timing (ATDC)	335°, 361.5°

Figure 3.2.1: Jaguar optical engine cooled to -7°C and corresponding engine configuration details (Efthymiou *et al.* 2013)

The engine crankcase assembly incorporated primary and secondary balancing to compensate for the forces of inertia caused by a single cylinder piston design. An extended Bowditch piston was attached to the primary piston within the engine crankcase and base block and the cylinder head is attached using three pillar supports. The Bowditch piston allowed the positioning of a 45° mirror beneath it to allow optical access through an optical piston crown into the combustion chamber (Figure 3.4.1). Sealing of the cylinder liner was achieved using a pneumatic ram that was driven from a 6 bar regulated supply of compressed air for motoring and a 20 bar supply of nitrogen for combustion. This equated to optical liner sealing forces of 2.6 kN and 8.9 kN respectively.

3.2.1   Optical Access

The Jaguar optical research engine allows for measurements of in-cylinder processes such as charge motion, fuel spray injection and flame propagation. To accomplish this there are several optical access configurations available:

i) Pent-roof window – for imaging around the spark plug and injector tip region and investigating parameters such as fuel impingement and flame kernel creation.

ii) Piston crown window – allowing optical access from the 45° mirror into the combustion chamber for imaging fuel injection and flame propagation.

iii) Quartz cylinder liner – providing access to the full cylinder bore and stroke during fuel injection, combustion and exhaust.

In addition to these optical components, a liquid-cooled steel version of the cylinder liner was used along with an aluminium pent-roof insert. This facilitated precise temperature control when the engine was cooled and allowed extended fired operation of over three minutes, which is the temperature-dependent time limit of optical components. Extended operation periods of up to ten minutes were required during the investigation of particulate matter (PM) emissions during the warm-up phase after a cold-start. The optical and thermodynamic engine components are shown in Figure 3.2.2.
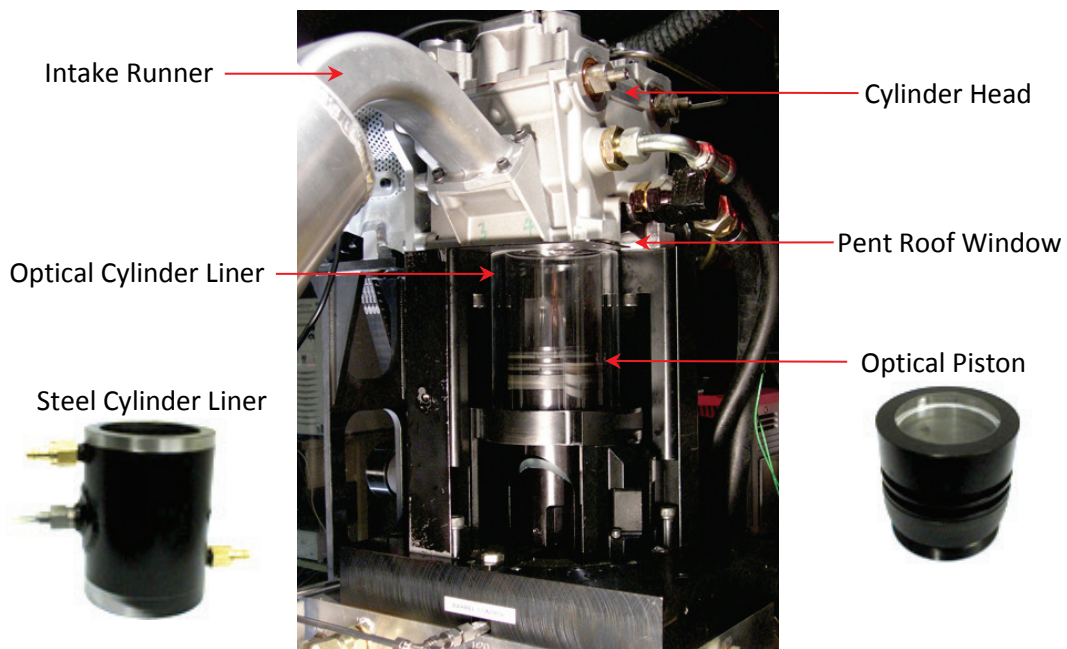
Figure 3.2.2: Interchangeable optical and thermodynamic engine components

3.2.2 Fuel Injection and Ignition

Fuel injection was provided by a 6-hole prototype injector mounted vertically and located centrally within the cylinder head, in close proximity to the spark plug. This configuration allows the engine to operate in homogeneous or stratified charge combustion modes. The injector nozzle consisted of two groups of three nozzle holes, all with a 0.5 mm outlet diameter. The six holes each have a different injection angle, producing the distinctive spray pattern (Figure 3.2.3). The individual injection angles for each fuel plume were designed to achieve maximum spray coverage of the cylinder bore, necessary for mixing with the intake air prior to ignition. Plumes 1 and 6 are orientated such that they passed around the spark plug in-order to minimise wetting of the electrode during fuel injection. The fuel rail was pressurised and regulated using a nitrogen-driven accumulator piston and fuel pressure was fully adjustable up to a maximum pressure of 150 bar. The fuel injector assembly comprised a reservoir of fuel that had a volume large enough to deliver a single engine test run of 100 cycles. This ensured that all of the fuel injected during a test run was of a consistent temperature to the head and liner after hot or cold-soaking.

A coil-on-plug type ignition system was used with a 12 V, 9A supply that delivered ignition energy of 35-40 mJ. The orientation of the spark plug electrode was maintained perpendicular to the pent roof window to avoid disturbance of the initial flame kernel growth if viewing through the pent roof window and to maintain the default orientation used recently in

research on the engine (Rimmer *et al.* 2009, Rimmer *et al.* 2012, Efthymiou *et al.* 2013). Spark plug orientation in a similar DISI engine has also been shown to have a notable effect on spark duration, flame kernel location, cycle-to-cycle variation and misfire (Twiney *et al.* 2010a, Twiney *et al.* 2010b). This is of particular importance in the presented research whereby a range of spark scheduling has been tested during the combustion sensitive mode of cold-start.

Injection and ignition timing was controlled using an AVL engine timing unit synchronised to an engine crankshaft encoder and TDC sensor, which allowed a timing resolution of 0.1 °CA. Air-fuel ratio (AFR) and engine load were controlled manually with the engine timing unit.
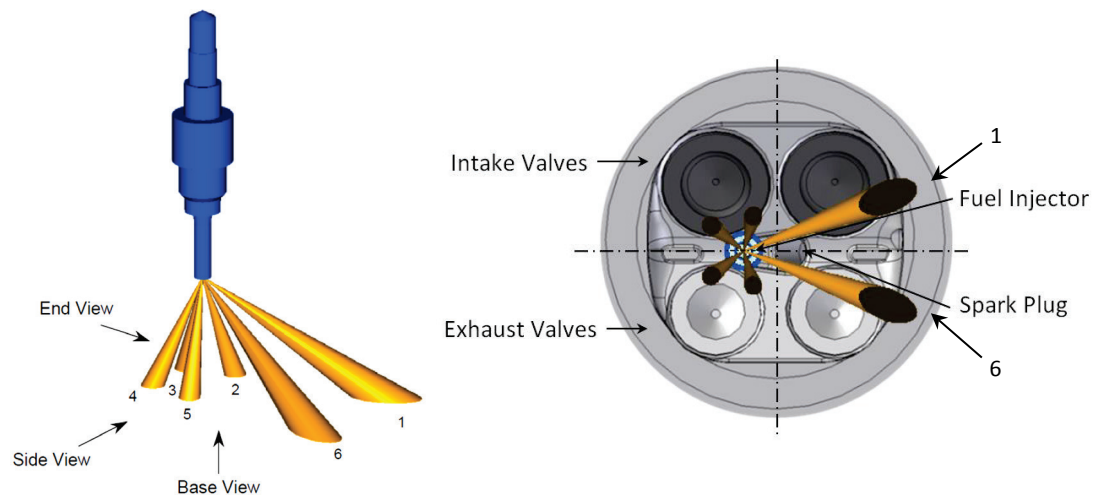
Figure 3.2.3: Schematic of six-hole fuel injector showing orientation of spray plumes relative to the cylinder head (adapted from (Serras-Pereira *et al.* 2007a))

3.2.3   Cylinder Head and Liner Temperature

A 6 kW vapour chiller was required to cool an antifreeze-water (80:20) mixture to -20°C and achieve an operating condition of -7°C. This was connected to the coolant circuit that flowed through the cylinder head and steel liner. When an operating temperature above ambient conditions was required, the coolant circuit was connected to a coolant tank that heated the fluid using a 3 kW thermostat-controlled immersion heater. The operating condition temperature was defined by a thermocouple embedded within the cylinder head on the exhaust-side of the engine away from the coolant circuit, this ensured the recorded temperature was representative of all of the cylinder head components. The thermocouple was coated with a silicone-based thermal compound to achieve good thermal contact with the cylinder head surface. A 'dry' oil sump design was used in the engine so the crankcase was heated separately using a crank-driven pump that also supplied oil to the overhead cams. When the engine was heated, the coolant and engine oil were fully heated prior to engine operation.

3.2.4   Intake Air Temperature

For the first time a vortex tube was used to cool the intake air of the engine in order to simulate a cold-soak at -7°C (Figure 3.2.4). The device was connected to a 6.0 bar compressed air supply that enters the device tangentially to create a rotating high velocity vortex along a heat transfer tube. The outer region of the vortex is restricted through a hot exhaust whilst the lower velocity cold air stream is restricted through a smaller hole which is centrally located with respect to the rotational axis. The fundamental operation of the vortex tube is governed by energy transfer from the inner to the outer vortex region in the form of heat. A precise cold air stream of -7°C was achieved by adjustment of the exhaust valve that controls the flow rate ratio between the two exhaust streams. The cooled air was fed into the intake plenum of the engine, which prevented any induction pressure waves in the vortex tube and allowed stable measurement of the air temperature using a thermocouple located inside the plenum.
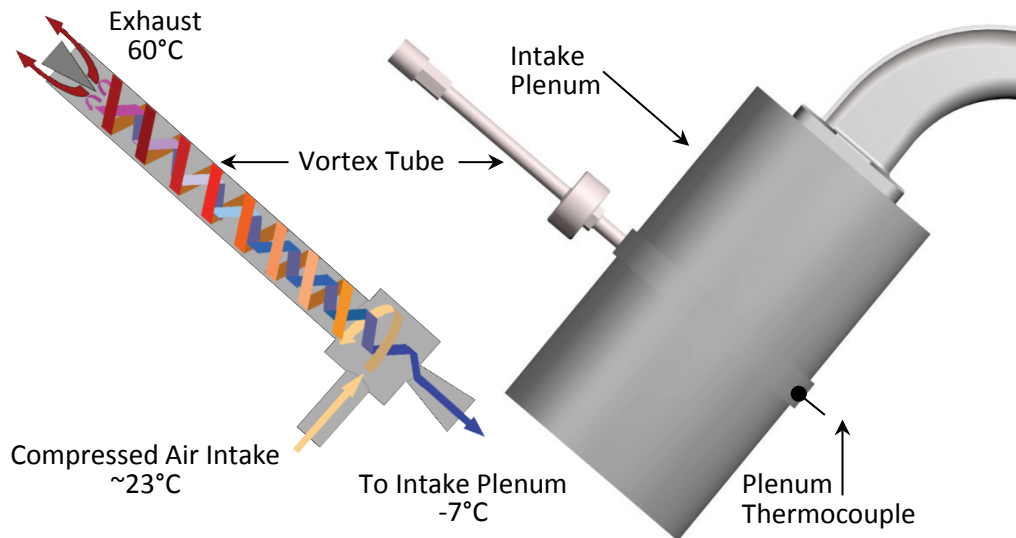
Figure 3.2.4: Arrangement of the vortex tube and plenum thermocouple in the engine intake plenum (Efthymiou *et al.* 2013)

3.2.5   Engine Speed and Load Control

A DC motor with an energy-absorbing drive system was used to crank the engine. When the engine was fired, a resistive load was applied that absorbed the power generated. This allowed the engine speed to be kept within a tightly controlled window of ±2 rpm. Engine load was controlled using a combination of varying the fuel injection duration (as discussed in Section 3.2.2) and throttling the intake air. For coarse pressure adjustments, an industry standard cable-driven throttle was used, whilst a needle valve controlled fine pressure adjustments.

When the engine was operated under cold conditions, a needle valve between the vortex tube and intake plenum was used to throttle the intake air. The pressure within the intake plenum was monitored using a digital display piezo-resistive pressure transducer.

3.2.6 Air-Fuel Ratio (AFR) Measurement

The Air-fuel equivalence ratio (λ) during fired engine operation was manually maintained at a stoichiometric level for the majority of the results presented in this thesis. This was controlled during engine running using a combination of altering the intake plenum pressure and fuel injection duration. An ECM Lambda Pro 1200 sensor supported the measurement of fuels with H:C, O:C and N:C ratios, as well hydrogen, allowing standard hydrocarbon gasoline fuels and ethanol blended fuels to be used if desired. A visual display of λ was used during engine running whilst an analogue output from the sensor was logged by the data acquisition system. The accuracy of the lambda sensor was ±1% at stoichiometry and ±2% otherwise, with a response time of < 150 ms.

3.2.7 Pressure Measurement

In-cylinder pressure was measured with a Kistler 6041A piezo-capacitive pressure transducer mounted from the camshaft side of the engine into the top of the pent-roof combustion chamber. The sensor allowed operation in a wide temperature range with a fast response time of 1.0 µs and a linearity of < 0.5%. A reference pressure was required, however, as the transducer only measured relative pressure change. A Kistler 4045A piezo-resistive pressure transducer was installed into the lower part of the steel cylinder liner and measured absolute pressure at BDC. When the full length optical liner was used, the reference pressure was taken from the intake plenum when the intake valves were open.

3.2.8 Data Acquisition

An AVL engine timing unit and National Instruments data acquisition system with 16 separate data channels were synchronised to the engine crankshaft position so that parameters such as fuel injection and spark timing could be controlled and in-cylinder pressure could be measured. Triggering events for data acquisition were also controlled so that simultaneous measurements, such as pressure and PIV data, could be synchronised. A Leine and Linde crankshaft encoder with 3600 pulses per revolution was used to determine crankshaft position. One channel on the encoder provided a TDC pulse every revolution and the other outputted a signal every 0.1 °CA/revolution.

In order to stop early triggering of data acquisition systems, an individually controllable channel filter was developed and situated between the output channels of the AVL engine timing unit and the data acquisition system. This both allowed certain channels to be blocked until desired engine stability had been achieved and to synchronise multiple data acquisitions systems.

3.3   FUEL-SPRAY IMAGING

The fuel spray was imaged using a Photron FASTCAM APX-RS high-speed camera viewing through the quartz optical cylinder liner with the camera positioned perpendicularly to the cylinder liner. Illumination of the combustion chamber was provided by a Copper Vapour Laser, capable of producing a pulse repetition rate of 50 kHz with a pulse duration of 10-30 ns with wavelengths of 511 nm and 578 nm. The camera and laser were synchronised at 9 kHz to allow for a high temporal resolution of 1 °CA per frame at 1500 rpm engine speed with illumination energy in the order of 2 mJ per pulse. The copper vapour laser used an optical fibre system in order to allow for greater positional flexibility, the beam was reflected on the 45° mirror below the extended Bowditch piston and through the piston crown. By using an illumination source through the piston crown window, reflection was minimised from the optical cylinder liner which reduced the presence of optical artefacts in the recorded images and improved the accuracy of post-processed groups of fuel spray images.

A system using a traversable spherical lens was used to reduce the divergence of the conical beam as it exited the fibre and maximise the energy density of the laser by restricting the beam's diameter to that of the optical piston crown. The flood-fill illumination of the beam allowed all injector plumes to be detected optically and the camera was then focused on the central axis of the cylinder in line with the injector. Figure 3.3.1 outlines the optical arrangement of the illumination system and high-speed camera on the optical engine.

The camera recorded an imaging area of 80 mm by 60 mm at a resolution of 640 by 480 pixels at a rate of 9 kHz producing a spatial resolution of 0.124 mm/pixel. Images were recorded at 9 kHz allowing a high temporal resolution of 1 °CA at a tested engine speed of 1500 rpm. A Nikon lens with a focal length of 28 mm was used with a wide-open aperture setting of f2.8 to maximise the detection of scattered light from the fuel spray without the requirement for any post image enhancement.
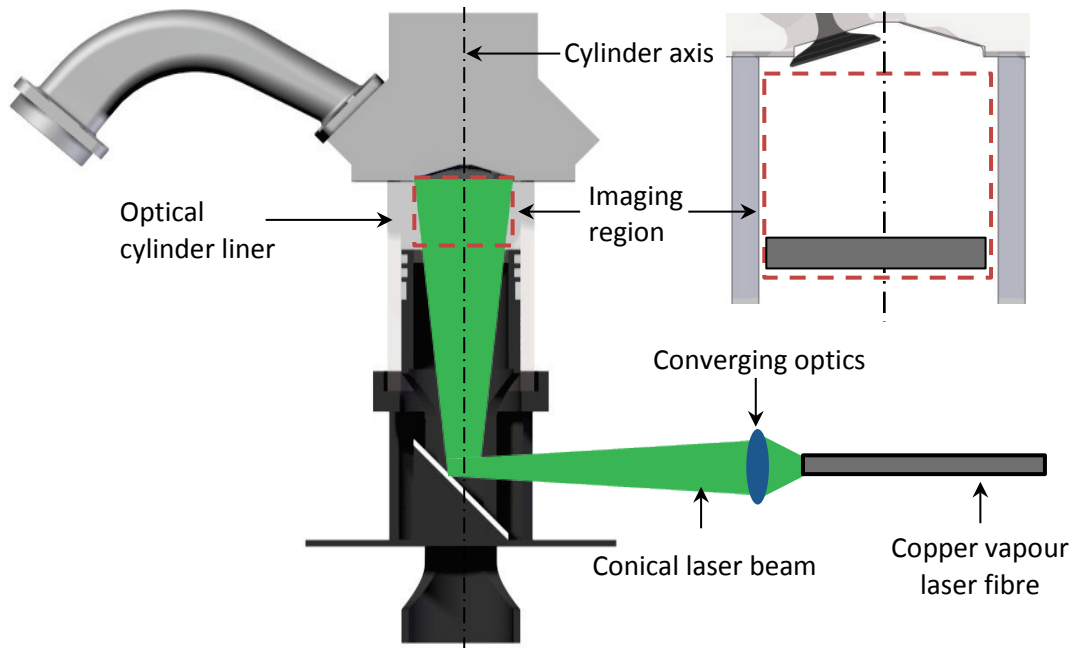
Figure 3.3.1: Experimental setup of fuel-spray visualisation through optical cylinder liner (Efthymiou *et al.* 2013)

The camera memory was partitioned to allow 70 frames per trigger to be captured, with the camera trigger occurring 10 °CA before fuel spray injection (Figure 3.3.2). The increased delay time of the image trigger before the injection event allowed any liquid fuel deposits present in the cylinder from the intake ports to be detected during intake.
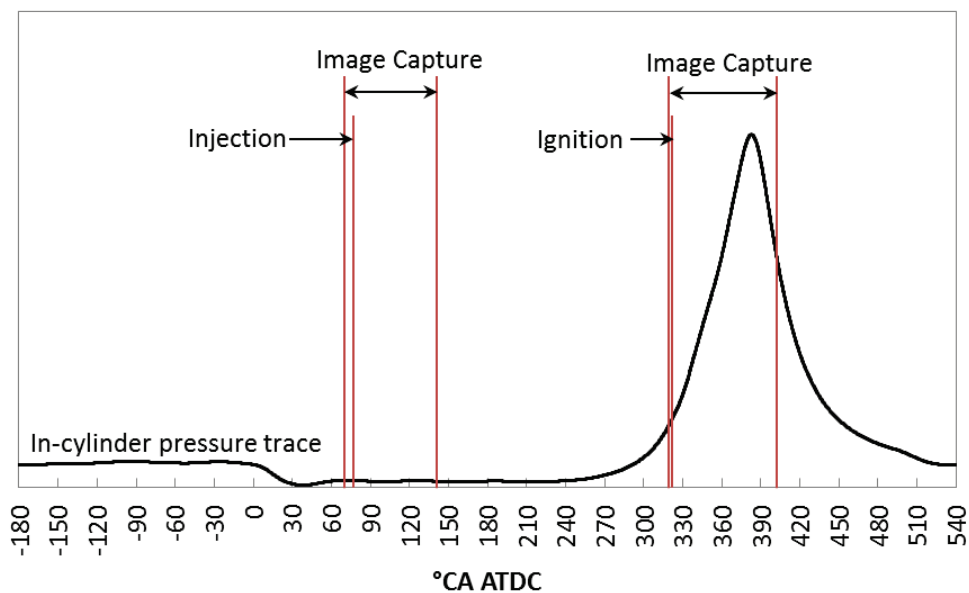
Figure 3.3.2: Timing graph outlining camera trigger events during injection and combustion relative to ATDC$_{Injection}$ (Efthymiou *et al.* 2013)

The engine was motored continuously with fuel injection and without spark ignition. This allowed the conditions over a single test run of 97 cycles to be kept as consistent as possible by avoiding the high temperature build-up from combustion, which would ultimately have an impact on the fuel spray. Compressive heating and friction were still considered, but their effect would be far less than the energy released during combustion and this heating was considered to be offset by the evaporative cooling effect of the evaporating fuel spray.

3.4   COMBUSTION IMAGING

3.4.1   Greyscale High-Speed Imaging

In-cylinder combustion imaging was obtained via the quartz optical piston crown window using a Photron FASTCAM APX-RS high-speed camera viewing across the 45° mirror located inside the extended Bowditch piston (Figure 3.4.1). The camera recorded an imaging area of 640 by 480 pixels at a rate of 9 kHz producing a spatial resolution of 0.142 by 0.142 mm/pixel and a temporal resolution of 1 °CA/frame at the standardised engine speed test point of 1500 rpm.

The camera memory was partitioned to allow 80 frames per trigger to be captured, with the camera trigger occurring 5 °CA before spark ignition. Each test run recorded 85 engine cycle events which was limited by the 2GB on-board memory of the camera, this produced a total of 6800 images through the optical piston crown. Figure 3.3.2 illustrates the location of the camera trigger and image capture time relative to the pressure curve during the engine's cycle ATDC relative to the intake stroke.

3.4.2   Colour High-Speed Imaging

Analysis of a simulated cold-start engine start-up strategy was completed using a Photron FASTCAM SA1.1 high-speed colour 24-bit camera with different specifications. The camera recorded an imaging area of 832 by 800 pixels at a rate of 9 kHz producing a spatial resolution of 0.087 by 0.087 mm/pixel and a temporal resolution range of 0.1 °CA to 1.3 °CA per frame depending on the tested engine speed (150 rpm to 2000 rpm).

The camera memory was partitioned to allow from 80 to 300 frames per trigger to be captured depending on the speed of the piston, combustion process and the presence of any scheduled engine events, such as a second injection or spark. Each test run recorded from 29 to 108 engine cycles that was limited by the 16GB on-board memory of the camera, this produced a total of 8600 24-bit colour images.
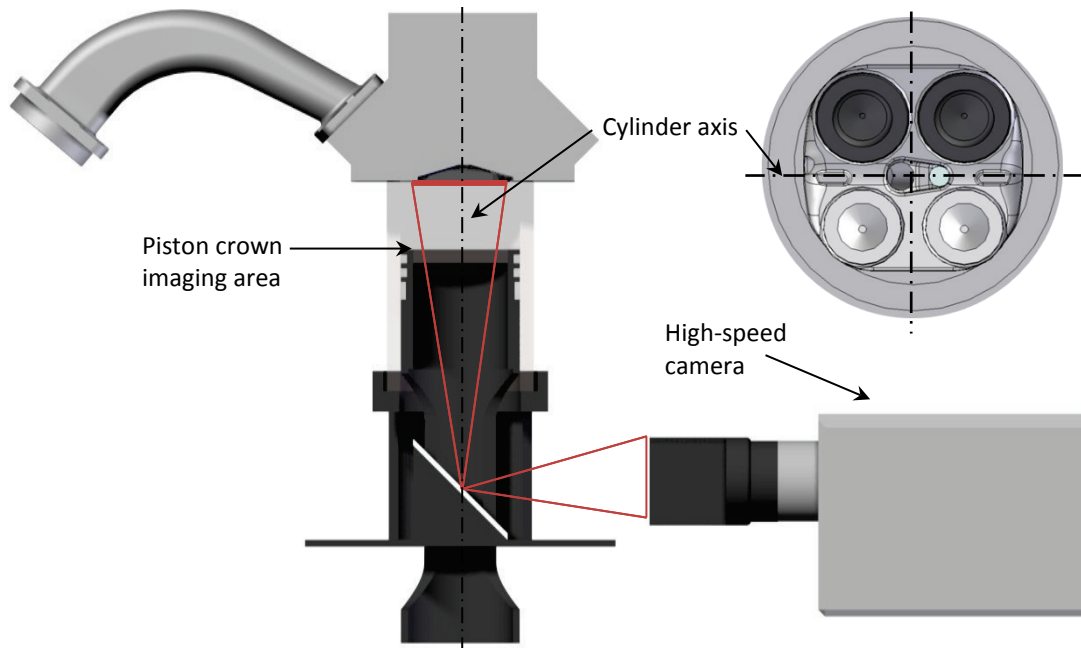
Figure 3.4.1: Schematic of visible imaging region during combustion imaging (Efthymiou *et al.* 2013)

Figure 3.4.2 illustrates the viewing area available through the optical piston crown for all types of combustion imaging along with the orientation of the presented images relative to key engine components such as the intake and exhaust valves. Due to the diameter of the piston crown window (65 mm) compared to the cylinder bore (89 mm), the cylinder bore could be imaged up to a radius of 35 mm from the centre.
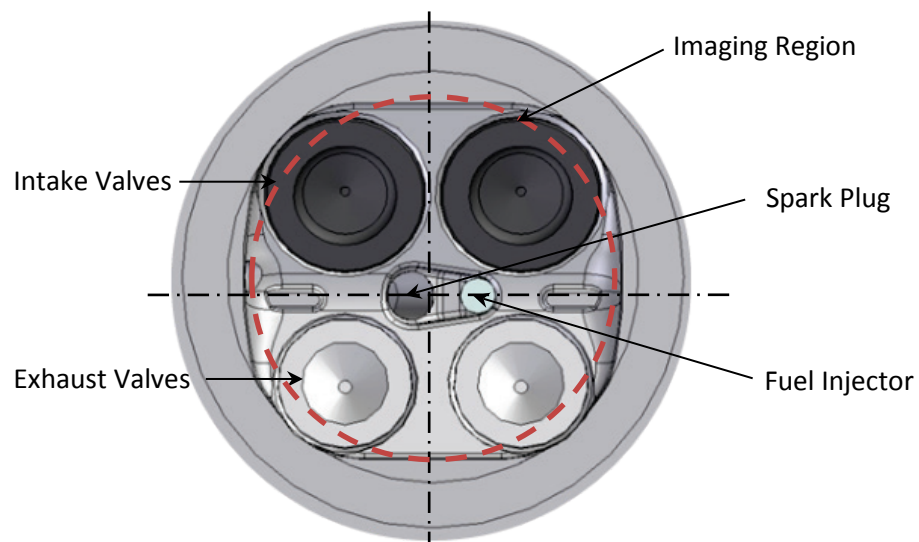
Figure 3.4.2: Schematic of available imaging region relative to cylinder head

3.5   EXHAUST EMISSIONS MEASUREMENTS

To facilitate the interpretation and build upon the knowledge and understanding gained from the optical data, exhaust emissions analysis was carried out on the optical engine. The data acquisition system allowed in-cylinder pressure measurement data and emissions results to be synchronised to better understand the effects of in-cylinder fuel injection and combustion processes on exhaust emissions.

A modified exhaust was manufactured for the engine allowing up to seven sample points, which could be used simultaneously (Figure 3.5.1). Sampling equipment was situated in the exhaust manifold such that any upstream flow effects were minimised and data accuracy was not compromised.

Exhaust Sample Points

Exhaust Temperature 1

AFR Measurement

Exhaust Temperature 2

Horiba Mexa Exhaust Gas Analyser

Exhaust Temperature 3

Exhaust Temperature 4

DMS500 Particulate Analyser

DMS Sample Head and Heated Line
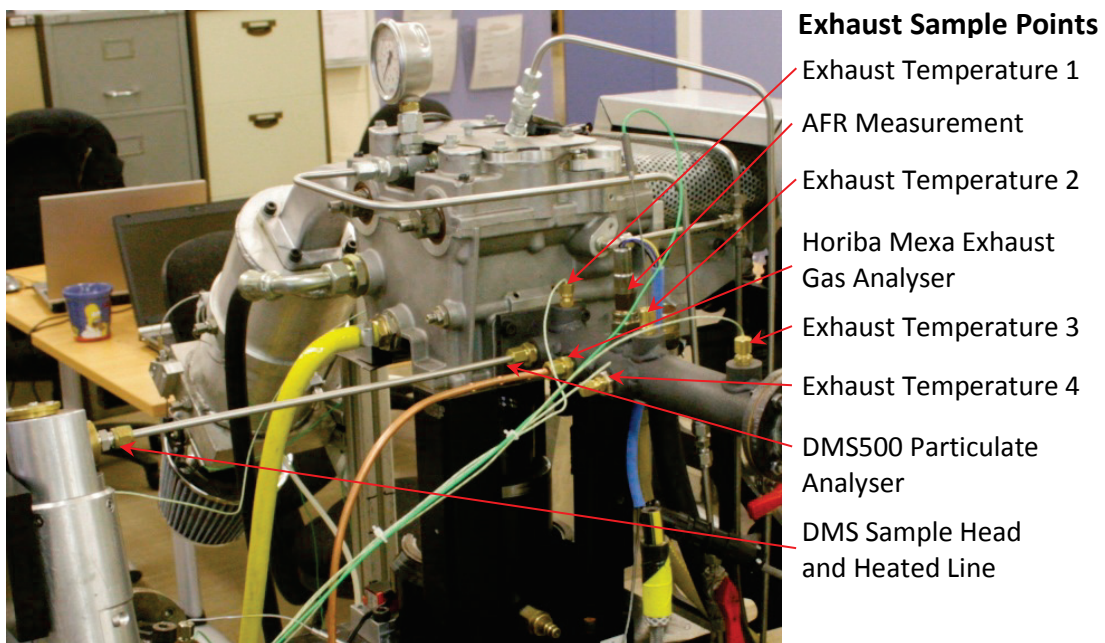
Figure 3.5.1: Modified optical engine exhaust manifold

3.5.1   Particulate Emissions Sampling

A Cambustion DMS500 MkII fast particulate analyser was used to measure particulate number (PN) emissions during extended periods following cold-start and whilst simulating a cold-start engine start-up strategy. The DMS500 was capable of measuring PM number concentration and size distribution with a response time of 200 ms at a sample rate of 10 Hz. The sampled gas first enters a vortex to remove large un-measurable particles and the remaining particles are diffusion charged. The aerosol then passes through a classifier column which is subjected to a strong radial electrical field. Depending on their electrical mobility, which is a function of particle size, particles are deflected and subsequently detected at different positions along the column of electrometer detectors.

Before entering the classifier column, the sampled exhaust gas travelled through a 90°C heated sample line which applied primary dilution using a compressed air source, the heated lined prevents condensates forming between the exhaust and classifier column. Secondary dilution is then applied if required, consisting of a rotating disc dilutor (Figure 3.5.2). The DMS500 facilitated the dynamic alteration of primary and secondary dilution during testing, allowing the dynamic measurement range to be optimized. This was of particular benefit in a single cylinder DISI engine, which has an increased sensitivity to changes when measuring particle concentration. This is due the inherent low size and reduced quantity of particulate emissions that were exhausted compared to, for example, diesel engine.
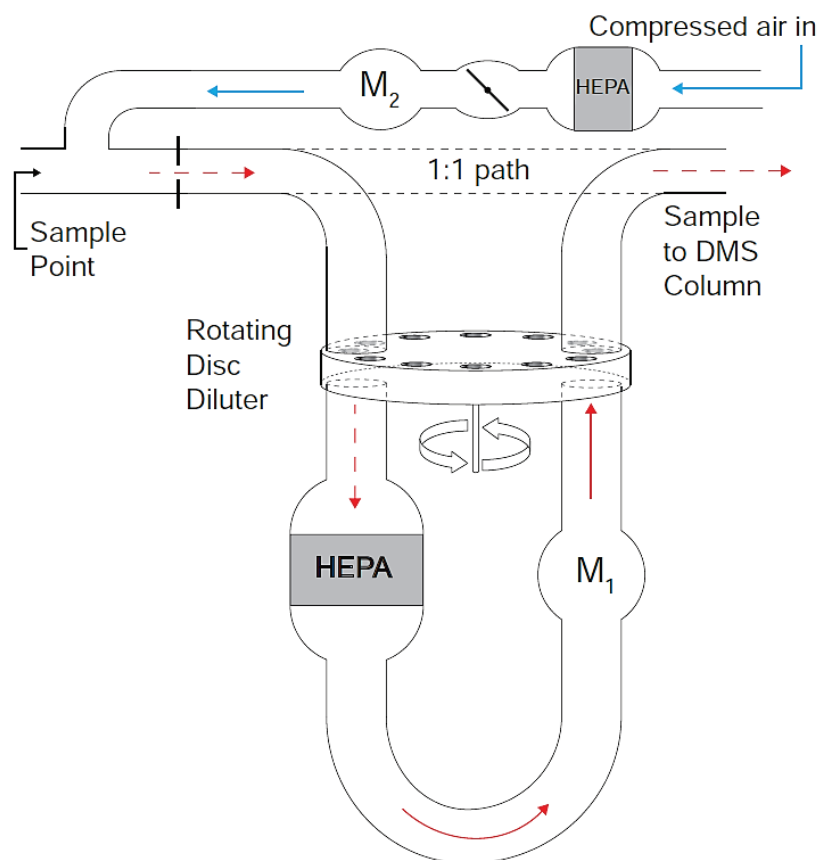
Figure 3.5.2: DMS500 sample and dilution system (Cambustion 2013)

Due to the sensitivity of PN number measurement in low-count applications such as single cylinder SI engines, the sample probe for the DMS500 was located in the centre of the exhaust flow and as close to the exhaust valve as possible (Figure 3.5.1). This prevented flow disturbance from other sampling equipment which could affect the accuracy and sensitivity of the sampled particulates. The 5 mm stainless steel sample pipe was given a smooth 90° bend to facilitate the induction of particulates and prevent any stagnation on the surfaces of the sample pipe (Figure 3.5.3).
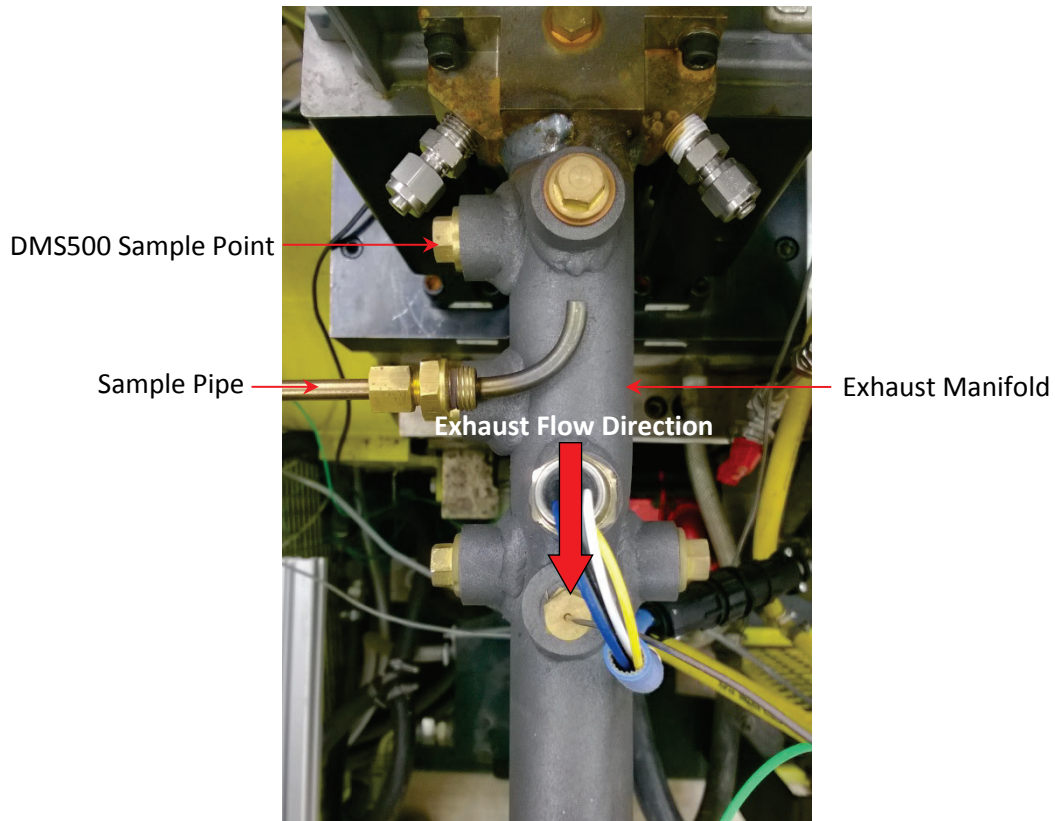
Figure 3.5.3: DMS500 exhaust sample pipe overlaid over exhaust manifold

To maximise the accuracy of the PN measurements, fired engine operation was extended from a 3 minute limit, which was dictated by thermal loading on optical components, to 10 minutes. Longer sample times allowed a larger quantity of particles to be sampled, improving the accuracy of mean-averaged data and improving the understanding of PN emission variability over a longer period of time. The increased time also facilitated the data capture of PN emissions during a complete engine warm-up to full operating temperature, from cold-start conditions. To allow extended fired operation, an aluminium piston crown insert was manufactured and used in combination with the steel cylinder liner. The optical pent roof window remained as it was embedded within the aluminium cylinder head and as a result able to withstand the thermal loading during extended runs.

In all engine tests a gas sample rate of approximately 8 litres/min was taken from the exhaust manifold, which was kept constant by the DMS500. The dilution ratio was manually controlled during engine operation to maintain an appropriate range of sampled particulates, this allowed the DMS500 to account for any dynamic changes in PN during engine combustion.

3.5.2   Unburned Hydrocarbon (HC) Emissions Measurement

Unburned hydrocarbon (HC) emissions are generally caused by poor fuel atomisation and vaporisation, air-fuel mixture heterogeneity and cold-surface impingement prior to combustion. An understanding of the precise in-cylinder location of these emissions can help the development of HC reduction through engine calibration and control strategies.

A Cambustion HFR500 fast flame ionisation detector (FID) was used to measure the exhaust HC emissions during a range of engine operating temperatures as well as whilst simulating a cold-start engine start-up strategy. The fast FID was instrumented into the main data acquisition system and synchronised with the engine crankshaft encoder allowing fully cycle-resolved emissions analysis with a response time as low as 0.7 ms.

To minimise the HC measurement delay time and more accurately synchronise the results to the engine crank angle, the fast FID measurement probe was located close to one of the engine's exhaust valves. An adapter was manufactured to position the probe angularly in the exhaust manifold, allowing location within the exhaust port with the probe tip approximately 5 mm from the valve head (Figure 3.5.4).
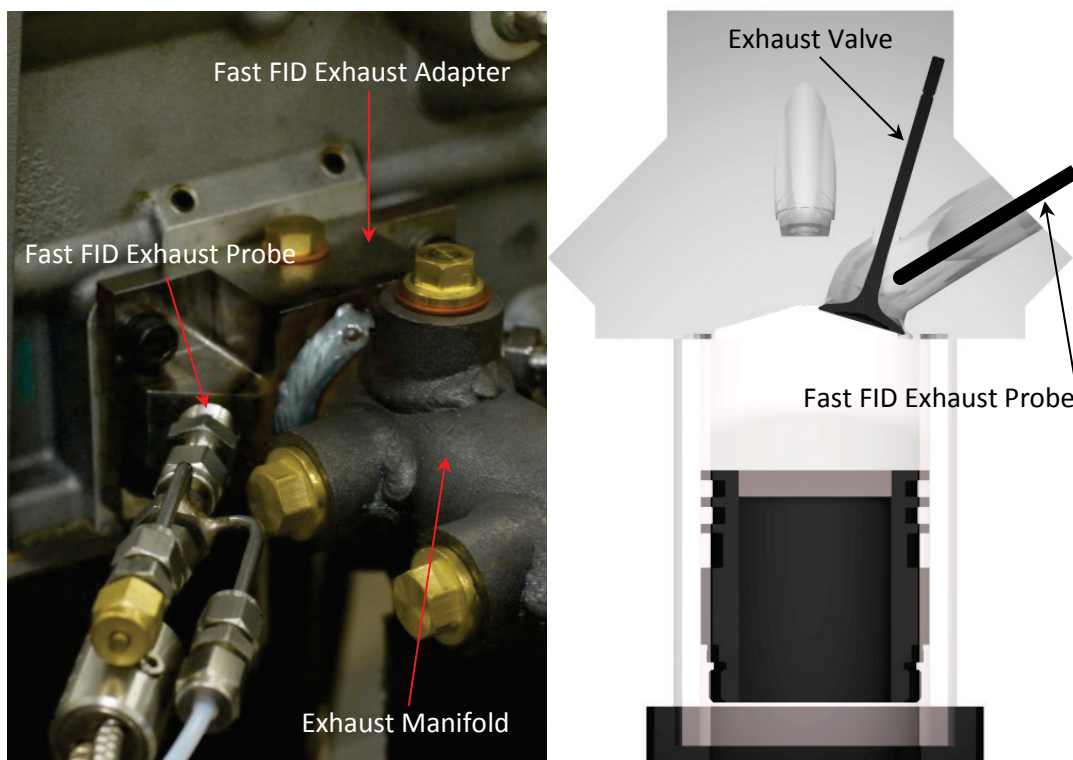
Figure 3.5.4: Fast FID exhaust adapter installed on exhaust manifold and exhaust probe located in exhaust port

To calibrate the Fast FID, a propane span gas with a known HC concentration (ie. propane 2000 ppm C_3H_8) was used along with a pure air source to zero the equipment. The output voltage was adjusted with a potentiometer at these two known calibration points. When testing various engine operating conditions with the HFR500, it was necessary to skip fire the engine to prevent the cumulative accumulation of residual HCs in the cylinder and exhaust manifold, which has been detailed in *Chapter 7*. This also allowed the comparison of HC emissions between individual engine cycles.

3.6 HIGH-SPEED PARTICLE IMAGE VELOCIMETRY (HSPIV) SETUP

The in-cylinder flow field has a dominant influence on the fuel spray penetration, atomisation and vaporisation, as well as the proceeding flame kernel growth and propagation. To develop better knowledge and understanding during cold-start conditions, particle image velocimetry (PIV) was used to measure the in-cylinder flow field during the induction and compression strokes. More recently, advancement in high-speed PIV (HSPIV) systems have enabled high temporal and spatial resolution data to be capture over a large spatial areas within engines (Jarvis *et al.* 2006, Stansfield *et al.* 2007b, Rimmer *et al.* 2009, Rimmer *et al.* 2012, Disch *et al.* 2013). This detailed data can be used to validate computer-aided engineering (CAE) models and further develop the knowledge and understanding of fluid dynamics within engines. The following section details the experimental setup on the optical engine. A fundamental analysis of the PIV technique and sources of error, as well as an in-depth PIV error analysis is detailed later in *Chapter 6*.

3.6.1 Light Source, Beam Delivery and Image Recording

A Litron LDY304 ND:YLF laser with pulse energy of 30 mJ/pulse was projected onto the 45° mirror under the Bowditch piston to produce a laser sheet approximately 1 mm thick through the cylinder, full specifications of the laser are given in Table 3.6.1. The collimated raw beam was passed through a bi-convex spherical lens with a variable focal length and a cylindrical lens in series. This created a laser sheet approximately 100 mm wide with a focussed waist at the area of interest.

The laser sheet was positioned on the central axis of the cylinder in between the both sets of valves in order to capture the flow field structure created by both intake valves (Figure 3.6.1). A LaVision Imager pro HS 4M high-speed camera and synchroniser unit was used to image the seeded flow area of 60 x 90 mm, at a resolution of 1008 x 1512 pixels and a record rate of 3 kHz, producing a PIV rate of 1.5 kHz and a spatial resolution of 0.060 by 0.060 mm/pixel. The

PIV rate was limited by the resolution of the images and subsequently the available processing power of the camera.

Litron Nd:YLF Laser	
Parameter	Specification
Wavelength [nm]	527
Pulse Energy [mJ]	30
Pulse Duration [ns]	150
Peak Power [W]	30
Pulse Frequency [kHz]	3
Beam Diameter [mm]	5

Table 3.6.1: Nd:YLF Laser Specifications
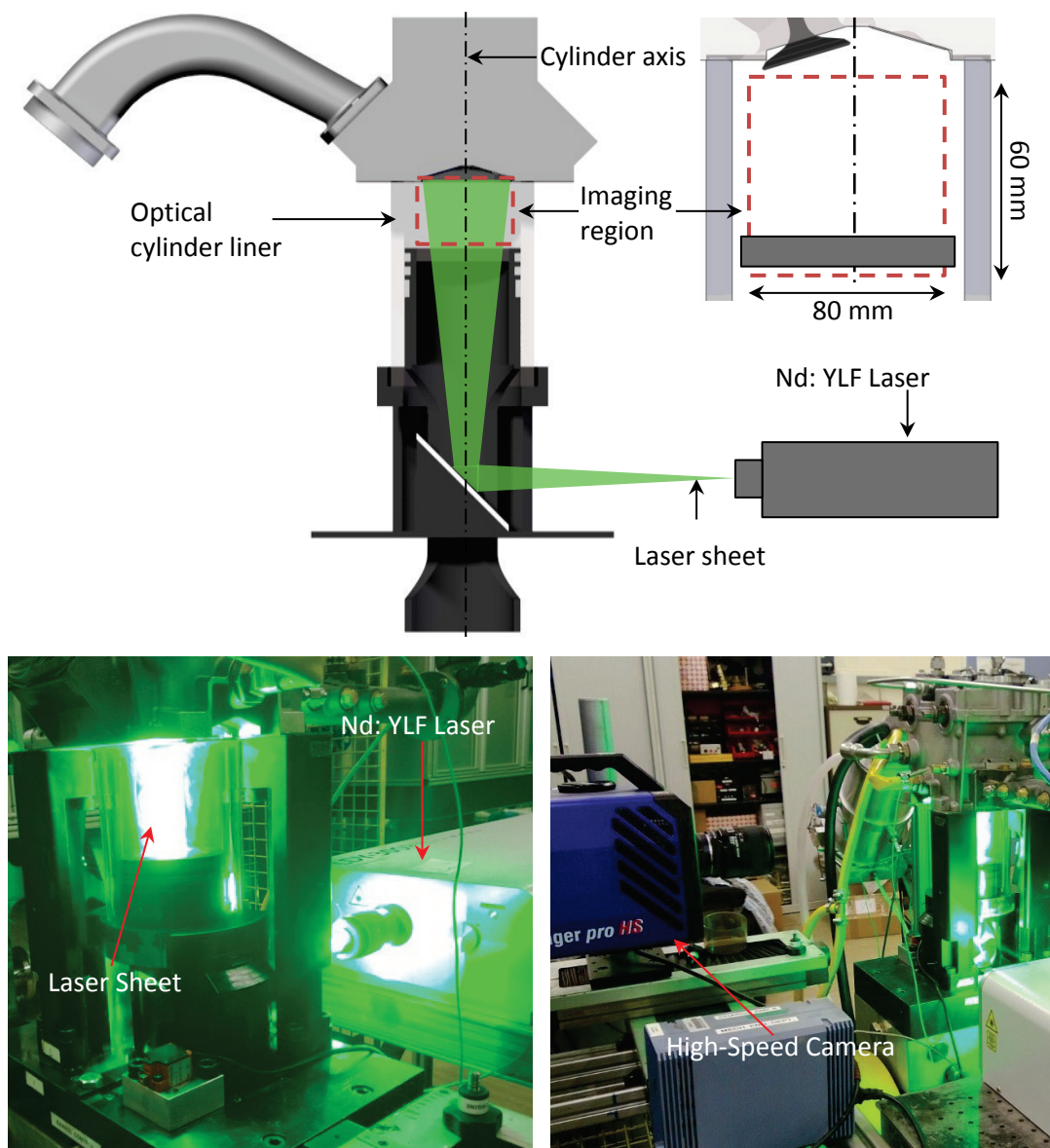
Figure 3.6.1: Experimental setup of PIV system setup with optical cylinder liner and piston crown

The camera's on-board memory of 18 GB allowed 4100 image pairs to be recorded per engine run which equated to approximately 97 engine cycles for the majority of speeds tested during the cold-start cycle.

3.6.2 Flow Seeding

A TSI six jet atomiser was used to generate seeding particles with nominal diameters of 1-2 μm from a source of silicon oil (Dow Corning 200). Dow Corning 200 oil was used due to its non-abrasive, lubricating properties and high vapour pressure, allowing the particles to remain visible during the increased temperatures of the compression stroke.

Fundamentally, seeding particles need to be small enough to accurately follow the complex flow path in an engine, especially the high frequency turbulence structures which are important to SI engine combustion. They also need to be large enough to scatter a sufficient quantity of light, so that there location can be accurately recorded. The ability of the used seeding particles to follow in the in-cylinder engine flow has been assessed in *Chapter 6* using Stokes' drag law.

3.7 CONCLUDING REMARKS

This chapter has described the experimental procedure that was undertaken to setup and modify the single cylinder optical engine to simulate cold-start operational conditions. The methodology to capture high-quality optical imaging and diagnostics data from the engine has been described along with the implementation of exhaust emissions analysis. The simultaneous utilisation of these techniques has enabled the capture of data which develops the understanding of cold engine operation and particulate formation during these conditions. The data collected from this experimental setup is presented and discussed in the following chapters. Chapter 4 investigates the effect of operating temperature on the combustion processes within the engine.

3.8   CHAPTER 3 REFERENCES

CAMBUSTION   (2013)   Cambustion   DMS50   MkII,   Available   from: http://www.cambustion.com/sites/default/files/instruments/DMS500/DMS500aeroso l.pdf, [Accessed 06/11/2013].

DISCH, C., KUBACK, H., SPICHER, U., PFEIL, J., ALTENSCHMIDT, F. & SCHAUPP, U. (2013) Investigations of Spray-Induced Vortex Structures during Multiple Injections of a DISI Engine in Stratified Operation Using High-Speed-PIV, SAE Paper 2013-01-0563.

EFTHYMIOU, P., DAVY, M., GARNER, C., HARGRAVE, G., RIMMER, J. E. T. & RICHARDSON, D. (2013) Insights into Cold-Start DISI Combustion in an Optical Engine Operating at −7°C. *SAE. Int. J. Engines,* Vol 6(2), pp. 1059-1074.

JARVIS, S., JUSTHAM, T., CLARKE, A., GARNER, C. P. & HARGRAVE, G. K. (2006) Motored SI IC Engine In-Cylinder Flow Field Measurement Using Time Resolved Digital PIV For Characterisation of Cyclic Variation, SAE Paper 2006-01-1044.

JUSTHAM, T., JARVIS, S., CLARKE, A., GARNER, C. P., HARGRAVE, G. K. & HALLIWELL, N. A. (2006a) Simultaneous Study of Intake and In-Cylinder IC Engine Flow Fields to Provide an Insight into Intake Induced Cyclic Variations. *Journal of Physics: Conference Series,* Vol 45, pp. 146-153.

JUSTHAM, T., JARVIS, S., GARNER, C. P., HARGRAVE, G. K. & CLARKE, A. (2006b) Single Cylinder Motored SI IC Engine Intake Runner Flow Measurement Using Time Resolved Digital Particle Image, SAE Paper 2006-01-1043.

RIMMER, J. E. T., DAVY, M. H., GARNER, C. P., HARGRAVE, G. K. & RICHARDSON, D. (2012) Fuel spray structure, flame propagation and charge motion at fuel impingement locations within a DISI engine. *IMechE: Fuel Systems for IC Engines,* Vol 2012, pp. 199-214.

RIMMER, J. E. T., LONG, E. J., GARNER, C. P., HARGRAVE, G. K., RICHARDSON, D. & WALLACE, S. (2009) The Influence of Single and Multiple Injection Strategies on In-Cylinder Flow and Combustion within a DISI Engine, SAE Paper 2009-01-0660.

SANDFORD, M., PAGE, G. & CRAWFORD, P. (2009) The All New AJV8, SAE Paper 2009-01-1060.

SERRAS-PEREIRA, J., ALEIFERIS, P., RICHARDSON, D. & WALLACE, S. (2007) Spray Development in a Direct-Injection Spark-Ignition Engine, SAE Paper 2007-07-2712.

STANSFIELD, P., WIGLEY, G., JUSTHAM, T., CATTO, J. & PITCHER, G. (2007) PIV analysis of in-cylinder flow structures over a range of realistic engine speeds. *Exp Fluids (2007),* Vol 43, pp. 135-146.

TWINEY, B., STONE, R., CHEN, X. & EDMUNDS, G. (2010a) Investigation of Combustion Robustness in Catalyst Heating Operation on a Spray Guided DISI Engine, Part 1 - Measurements of Spark Parameters and Combustion, SAE Paper 2010-01-0593.

TWINEY, B., STONE, R., CHEN, X. & EDMUNDS, G. (2010b) Investigation of Combustion Robustness in Catalyst Heating Operation on a Spray Guided DISI Engine, Part II - Measurements of Spray Development, Combustion Imaging and Emissions, SAE Paper 2010-01-0603.

CHAPTER 4

THE EFFECT OF ENGINE OPERATING TEMPERATURE ON DISI ENGINE COMBUSTION

4.1 INTRODUCTION

Chapters 1 and 2 discussed the effects of low operating temperatures on the fuel injection and proceeding combustion processes. Cold-start conditions have been shown to lead to poor fuel spray atomisation and vaporisation, as well as combustion chamber surface impingement (Stanglmaier *et al.* 1999, Whitaker *et al.* 2011, Efthymiou *et al.* 2013). These factors adversely affect AFR distribution during the combustion process and are known to contribute to unburned HC and PM generation.

This chapter presents the results collected from the optical investigation of operating temperature on in-cylinder DISI engine combustion. High-speed optical diagnostics were employed to capture the combustion processes following spark ignition, which include flame kernel growth and development, and lead on to flame propagation, until being extinguished at the cylinder and piston surfaces. Simultaneous in-cylinder pressure data were recorded in order to analyse combustion performance and cycle-to-cycle variability, as well as correlating results and findings with the processed optical data.

The experimental setup of the engine simulated continuous steady-state combustion at engine operating temperatures from 80°C to -7°C. This facilitated analysis of the complete engine temperature range and allowed any intermediate effects between temperatures to be observed. A detailed explanation of the experimental setup of the optical engine and ancillary systems were described in *Chapter 3*. In this chapter, the specific test conditions and optical setup are described.

A range of data processing routines were developed to transpose the in-cylinder pressure data into mass fraction burned (MFB) and indicated mean effective pressure (IMEP) parameters as well as there corresponding COVs. The high-quality qualitative optical combustion data combined with the in-cylinder pressure data provides a novel insight into cold-start DISI combustion in an optical engine. Results show striking differences between the flame growth structures at various operating conditions with the notable presence of significant fuel-rich regions which are understood to be prominent areas of PM formation. A clear link was also shown between operating temperature, engine performance and in-cylinder combustion parameters which contribute to the formation of PM.

4.2   OPTICAL ENGINE EXPERIMENTAL CONFIGURATION

High-speed visualisation of the in-cylinder combustion processes was obtained through the quartz optical piston crown as previously shown in the experimental arrangement in *Chapter 3*. A 105 mm Nikon lens with a wide-open aperture of f2.8 was used to record through the 45° mirror, which allowed as much light as possible from the combustion to be detected without the need for added illumination or image intensification. Figure 4.2.1 outlines the optical engine and its ancillaries when set up for temperature-varied combustion imaging.
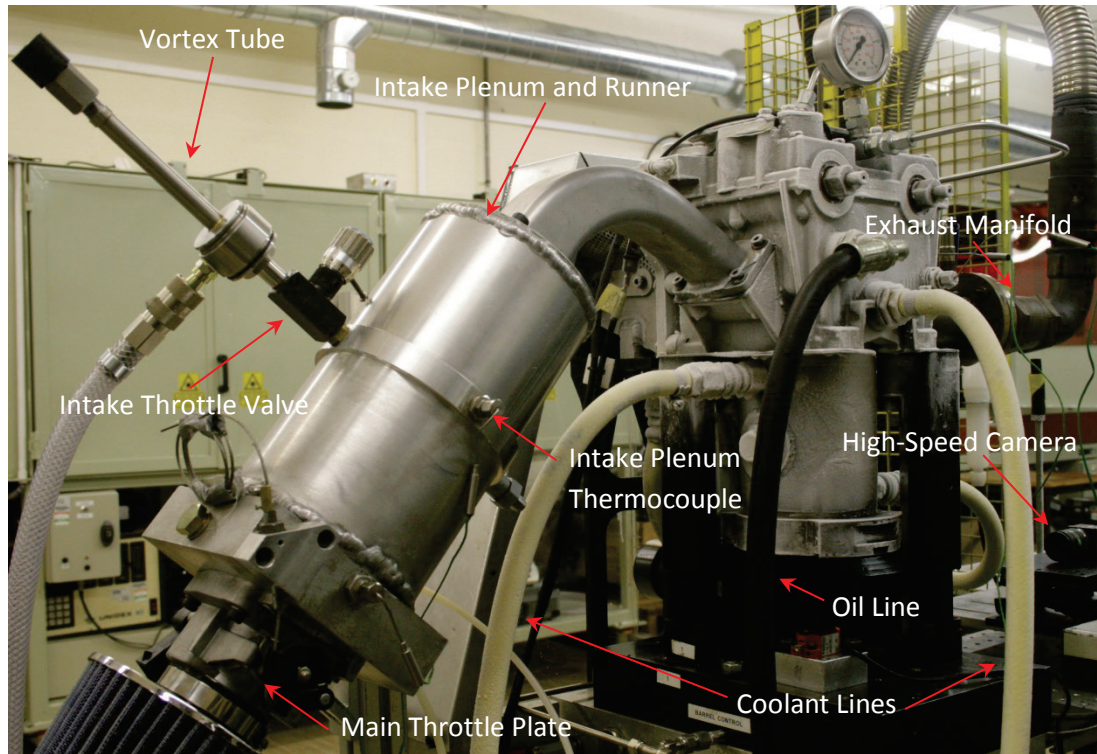
Figure 4.2.1: Experimental setup of optical engine for combustion imaging at various operating temperatures (showing engine cooled to -7°C)

In order to change the operating conditions of the engine, three key aspects of the engine system were modified:

1. Head and liner temperature: These affect in-cylinder surfaces that act as a heat source or heat sink for the air flow, fuel spray and flame kernel. These regions also create impingement zones which can lead to the build-up of liquid fuel, particularly during cold conditions.

2. Fuel injector temperature: This is governed by head and liner temperature, directly influences the fuel in the injector sac and affects fuel atomisation, penetration, breakup and vaporisation. The detrimental effect this has on the fuel spray is compounded by the increased potential for cold-surface impingement.

3. Intake air temperature: This affects the temperature of the charge and acts as a heat transfer medium for the fuel spray and flame kernel.

The temperature of the coolant circulating through the cylinder head and liner was set to achieve engine operating temperatures of 80°C, 23°C, 10°C and -7°C as described in Table 4.2.1. The vapour chiller was used for all temperatures at 23°C and below whilst the immersion heater was used to heat the coolant during the 80°C test condition. Intake temperatures of 23°C and -7°C were used in conjunction with all head and liner test conditions. The main throttle plate was utilised solely to regulate the intake charge during the 23°C intake condition. When -7°C intake air was required, the throttle plate was sealed off and flow was controlled using the intake throttle valve between the vortex tube and plenum (Figure 4.2.1). The intake plenum thermocouple was used to monitor the intake air temperature, which was adjusted by means of altering the hot exhaust valve on the vortex tube.

Cylinder Head and Liner Temperature	Description
80°C	Fully heated engine
23°C	Ambient lab conditions
10°C	Intermediate condition
-7°C	Euro 6 cold-start temperature (DieselNet 2015)

Table 4.2.1: Description of selected engine head and liner temperatures

4.3 PRESSURE DATA AND IMAGE POST-PROCESSING

Analysis of the in-cylinder combustion events was carried out using a number of post-processing routines on the recorded in-cylinder pressure data. The data acquisition system saved a data file of all recorded output channels at the end of each run, which was subsequently transcribed into Matlab for further processing. The parameters that were deduced from the pressure data included:

- Peak pressure and the crank angle (CA) location at which this occurred (P_{Max}, θ_{PMax});
- Gross indicated mean effective pressure (IMEP);
- Mass fraction burned (MFB) times for 10%, 50% and 90% of the total charge.

The in-cylinder pressure was deduced using the absolute pressure from the piezo-resistive pressure transducer located either in the cylinder liner or intake plenum. At bottom dead centre (BDC) of the intake stroke, the absolute pressure from the piezo-resistive sensor was used as a reference pressure for the in-cylinder pressure transducer. Pressures throughout the entire engine cycle were recorded at a temporal resolution of 0.1 °CA.

The data acquisition (DAQ) system was triggered to record after receiving a TDC voltage signal from the crankshaft encoder. For the start of each recorded engine run, it was necessary to determine whether the outputted data file commenced at TDC of the intake stroke or compression stroke. This was completed in the Matlab code by analysing the in-cylinder pressure at TDC to determine whether compression had taken place. If so, the preceding 360 °CA of pressure data was removed to ensure every engine run commenced at TDC of the intake stroke.

The calculation of P_{Max}, θ_{PMax} and $dP/d\theta$ was straightforward from the available pressure data and this could also be referenced to the crank angle from the encoder. The cylinder volume (V) could be calculated from the equation (Heywood 1988)

$$V = V_c + \frac{\pi B^2}{4}(l + a - s) \qquad \text{Eqn. (4.3.1)}$$

where V_c is the clearance volume, B is the engine bore, l is the connecting rod length, a is the crank radius and s is the distance between the crank axis and piston pin axis given by

$$s = a\cos\theta + (l^2 - a^2 sin^2\,\theta)^{1/2} \qquad \text{Eqn. (4.3.2)}$$

where θ is the crank angle (in degrees) from the encoder.

To calculate the mass fraction burned, the well-established technique developed by Rassweiler and Withrow (1938) was utilised. The combustion process was considered using a series of very small crank angle intervals $(\Delta\theta)$, each of which contains a change in pressure (ΔP) that is caused by two processes: the pressure rise due to the motion of the piston (ΔP_V) and the pressure rise due to combustion (ΔP_C). It was assumed the charge was compressed as a polytropic process after which some of the charge was burned and caused a rise in pressure.

Utilising the knowledge of in-cylinder volume at any known crank angle, the change in pressure due to the piston motion over a time step (ΔP_V) can be approximated as a polytropic process at any known point, i, such that

$$\Delta_{P_V} = P_i\left[\left(\frac{V_i}{V_{i+1}}\right)^n - 1\right] \qquad \text{Eqn. (4.3.3)}$$

where P_i is the known pressure, V_{n+1} is the cylinder volume in the next time step and n is the polytropic index.

The pressure change due to combustion was then defined as

$$\Delta_{P_C} = P_{i+1} - P_i \left(\frac{V_i}{V_{i+1}}\right)^n$$

<div align="right">**Eqn. (4.3.4)**</div>

where P_{i+1} is the cylinder pressure in the next time step. Since combustion is not taking place at a constant volume, a known arbitrary reference volume is needed. This was chosen at TDC (the clearance volume of the engine, V_c) so the normalised change in pressure due to combustion $(\Delta P_C{*})$ could be normalised and expressed as

$$\Delta_{P_C}{}^{*} = \Delta P_C \left(\frac{V_i}{V_C}\right)$$

<div align="right">**Eqn. (4.3.5)**</div>

The time taken to reach a specific MFB percentage was then calculated from the time taken to reach a proportion of the total normalised pressure change due to combustion $(\Sigma \Delta P_C{*})$.

The IMEP was calculated from the in-cylinder pressure data. It is defined as the ratio of work on the piston per cycle to the swept volume of the cylinder and is defined as

$$IMEP = \frac{1}{V_S} \int P.\,dV_S$$

<div align="right">**Eqn. (4.3.6)**</div>

where V_S is the swept volume of the cylinder and P is the cylinder pressure (Heywood 1988).

The coefficient of variation (COV) has also been stated for all presented parameters and is defined as the ratio of the standard deviation (σ) to the mean (μ). The COV is a useful indicator of the cycle-to-cycle variability and of an engine's combustion stability.

4.3.1   IMAGE POST-PROCESSING

The combustion images from the camera were stored as an 8-bit uncompressed grey-scale video file (AVI format). Photron PFV software was then used to separate these frames into uncompressed image files (TIF format) for further processing in Matlab. The steps taken in the program are outlined below:

1. Image files are loaded into Matlab and the filename is read to identify the operating conditions and frame number in the cycle;
2. The cylinder walls of the engine run to be processed are edge detected and a geometric mask is applied;

3. The presence of a flame is detected for each image and is the image is binarised. The threshold of the flame detection was predetermined depending on operating condition;

4. The binary flame images are processed to calculate parameters such as flame perimeter, flame area and flame growth speed;

5. The calculated parameters are exported in Excel for data interpretation and presentation.

For the presented image-processed parameters, calculations were made based on a straightforward pixel count of the binarised images (with respect to time when calculating flame growth speeds). In order to convert the units of measurement into SI units, a calibration grid was used to accurately calculate the total number of pixels per mm, which was subsequently integrated into the Matlab code. To identify the flame centroid location a function named 'regionprops' was used on the binarised image, which extracts measurement properties of a supplied image. The threshold level within the Matlab program was iterated for each operating condition until the flame was no longer overestimated or underestimated for the majority of combustion cycles during each engine run. As no image intensification was used, relatively low threshold levels of approximately 8/255 were used so that the early flame kernel growth was captured. Figure 4.3.1 illustrates the results from the flame image processing routine on a single arbitrary engine cycle. Flame growth speed ($S_{f(i)}$) was calculated based on the change in flame area ($A_{f(i+1)}$) across images (i), flame perimeter (P_f) and time between images (dt) such that

$$S_{f(i)} = \frac{A_{f(i+1)} - A_{f(i)}}{P_f dt}$$

<div align="right">**Eqn. (4.3.7)**</div>

where *dt* is the camera frame rate.

The viewable region of the optical piston crown had a diameter of 68.0 mm, which allowed 58% of the 89.0 mm cylinder bore to be viewed during combustion. The processed optical data enabled a significant proportion of the flame kernel growth and expansion to be described and correlated with in-cylinder pressure data, however, the pressure data was required to accurately describe the latter part of the combustion process to the cylinder walls.

Original Image	Binarised Image	Edge-Detected and Flame Centroid Image

14 °AIT

19 °AIT

25 °AIT

31 °AIT

35 °AIT
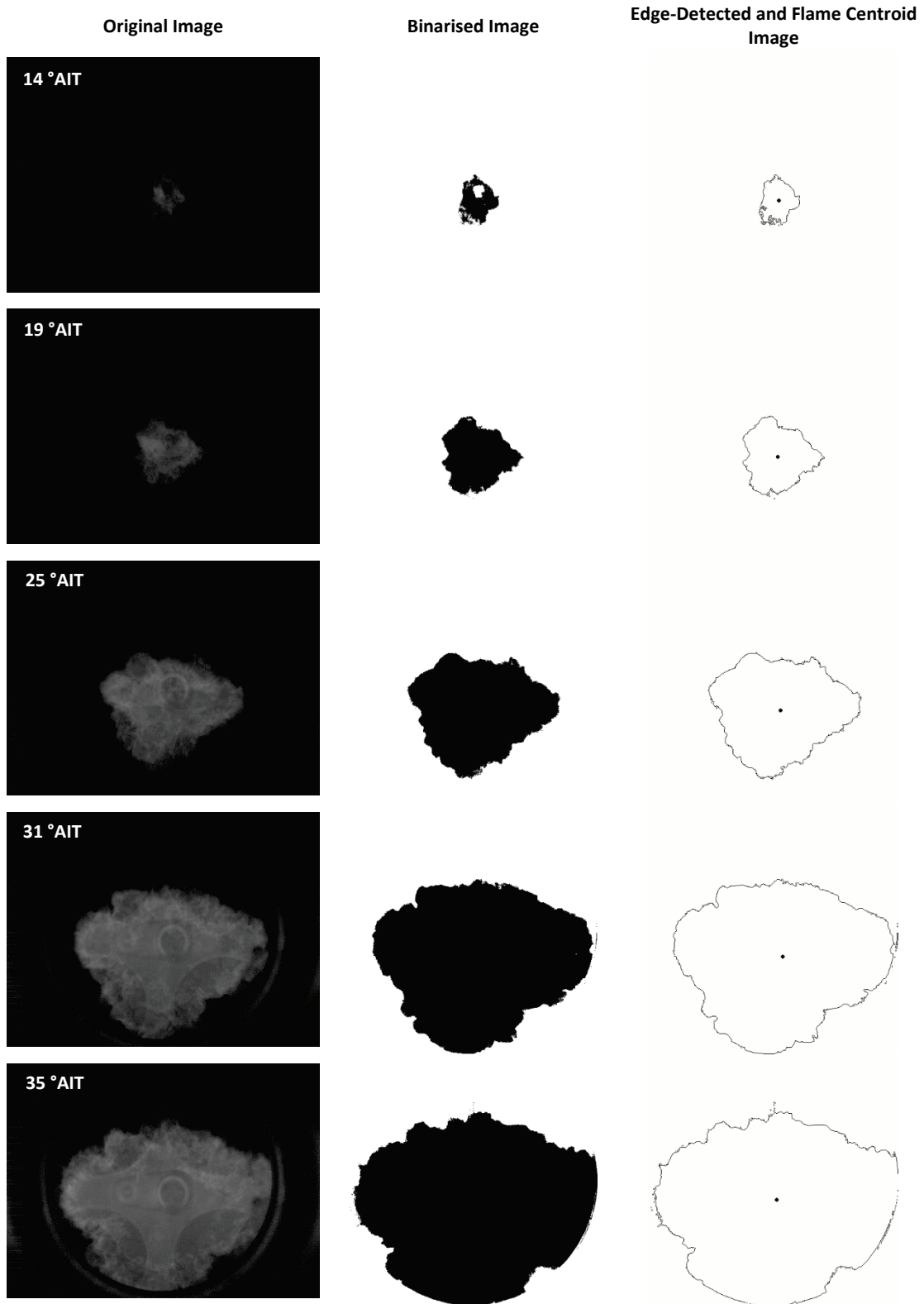
Figure 4.3.1: Results from Matlab flame image processing routine at various points after ignition timing (AIT)

4.4   RESULTS AND DISCUSSION

The data presented in this section aims to develop an understanding of the effect that operating temperature has on in-cylinder combustion and particulate emission generation. The combination of optical and quantitative in-cylinder data has allowed a better understanding of the in-depth physical processes occurring during spark ignition and flame growth, along with the benefit of detecting flame features such as burning fuel droplets.

4.4.1   In-Cylinder Pressure

The graphs in Figure 4.4.1 outline the in-cylinder pressure relative to after top dead centre (ATDC) of the compression stroke as well as the mass fraction burned (MFB) profile for all head and liner temperatures tested with an intake temperature of 23°C. There is clear and strong correlation evident between the engine operating temperature and the peak cylinder pressure achieved, with a range from 13.16 bar at 80°C, to 8.79 bar at -7°C.

The location of the peak pressure in the engine cycle remained relatively consistent at 23 °CA with a maximum deviation of 2 °CA. Notably, the difference in peak pressure increased as operating temperature deviated from 80°C, with a less significant difference in peak pressure evident between the 10°C and -7°C operating conditions.

The MFB profiles presented show the rate at which the charge is consumed from spark ignition to the complete consumption of the unburned charge and is mathematically defined as a fraction between 0 - 1. When observing the initial 30 °CA after ignition, the ignition delay and start of pressure rise was shown to be longer for the colder operating conditions, with the 10°C and -7°C test points showing very similar profiles. The rates at which MFB increased were also lower at colder conditions, indicating longer times for the charge to be burned. These key differences can be used to further explain the contrasting peak pressures that were shown. The increased rate of pressure rise and therefore energy release at warmer temperatures, allowed a greater proportion of the charge to be burned by the time the piston reached TDC. After this point, the remaining charge was burned into an increasing cylinder volume and at a lower flame growth speed during the expansion stroke, resulting in a decrease in peak pressure.

The in-cylinder pressure traces and burn profiles when -7°C intake air was introduced into the engine are also illustrated in Figure 4.4.2. As expected, the correlating trends relating to head and liner temperature were again present, along with the differences in the MFB rates. A consistent rise in peak pressures of approximately 0.5 to 0.6 bar was observed at all cylinder head and liner temperatures, which can be attributed to a denser charge caused by the colder intake air.
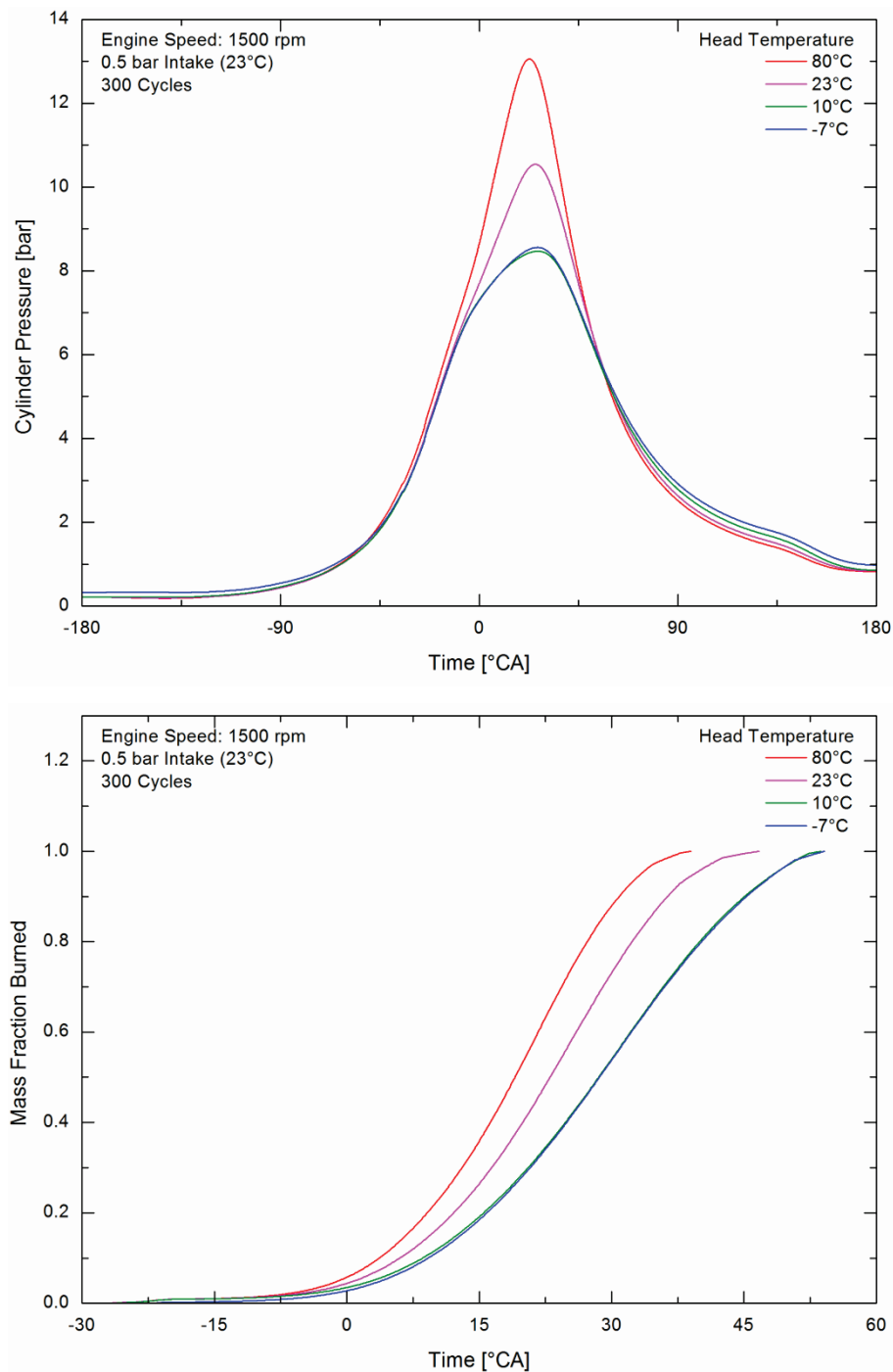
Figure 4.4.1: Mean in-cylinder pressure and mass fraction burned profile for a range of cylinder head and liner temperatures tested at a 23°C intake temperature

These subtle peak pressure differences are highlighted in more detail in Figure 4.4.3 with corresponding coefficients of variation (COV). The COV of IMEP was analysed for a number of properties processed from the pressure data and are defined as the ratio of the standard deviation to the mean. Interestingly, the MFB profile of the 23°C head and liner operating condition was much more similar to the colder cases when a cooled charge was used, this demonstrates the notable effect a cooled charge had on the flame growth speed.
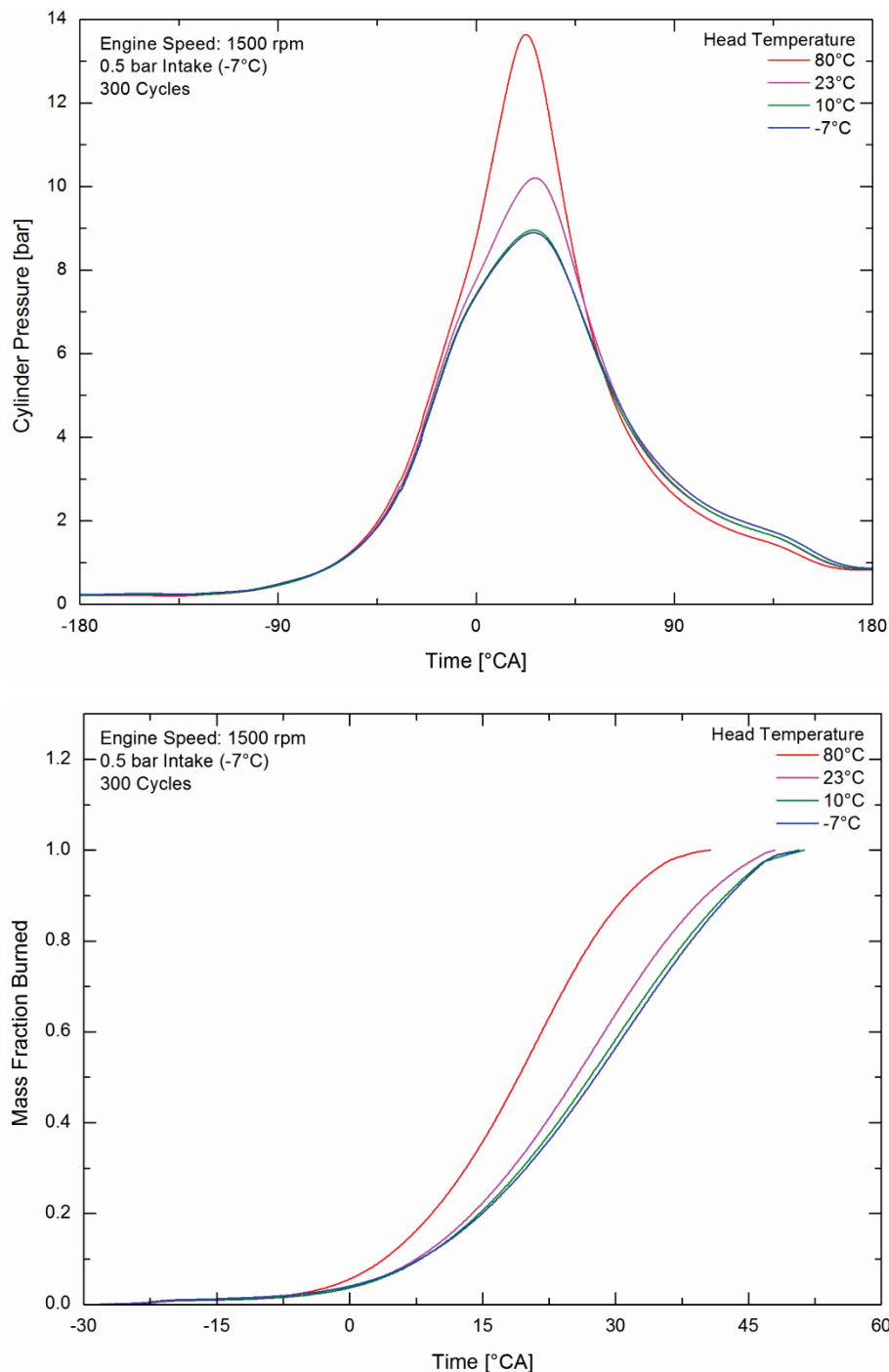
Figure 4.4.2: In-cylinder pressure and mass fraction burned profile for a range of cylinder head and liner temperatures tested at a -7°C intake temperatures

The upper bar graph in Figure 4.4.3 illustrates the peak pressures and their corresponding COVs for all operating points tested. The COV of the peak cylinder pressures can be seen to have risen from 10% to 17% as engine operating temperature was decreased. This rise in variation is further compounded with the colder -7°C intake air condition which increases COV by up to a further 2% in each operating temperature case. The COV parameter is a measure of the cycle-to-cycle variability during an engine run and gives a good indication to combustion stability. As expected, colder operating conditions in terms of head and liner temperature as well as intake air led to increased combustion instability in the engine, this is discussed later in the chapter.
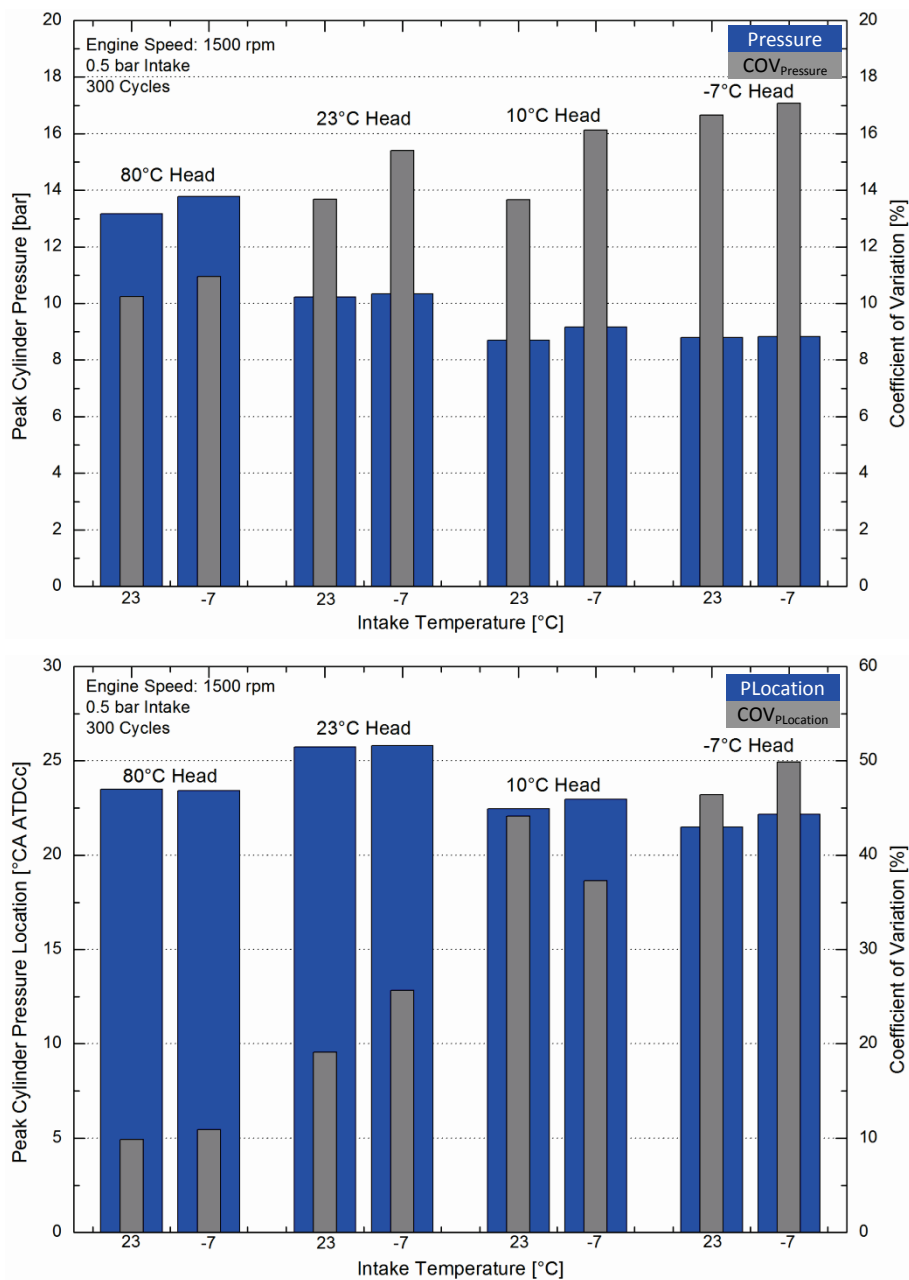
Figure 4.4.3: Mean peak pressures and corresponding COVs for a range of engine operating temperatures and intake temperatures

The location of peak cylinder pressure has been presented in the lower bar graph in Figure 4.4.3 and shows a fairly consistent peak pressure location across the range of operating conditions due to the consistent fuel spray and spark ignition timings. Interestingly, the 23°C condition peaks above the other temperatures with a slightly later peak pressure location, however, the relatively high COV at this condition means that the mean of this data does not give an overall accurate representation of the individual engine cycles in the data. A striking trend is the large increase in the COV of peak pressure location at lower engine temperatures. The COV of the -7°C condition reaches 50% highlighting the instability of the combustion events and wide spread of data.

This variability has been highlighted further in Figure 4.4.4, which illustrates the raw peak pressure locations for the coolest and most unstable condition (-7°C head, liner and intake temperature). The peak pressure locations can be seen to range from 0.4 °CA to 40.5 °CA ATDC and are grouped into two distinct locations at approximately 30 °CA and 5 °CA ATDC. The extremely large spread of peak pressure locations highlights the instability of the engine, which limits the delivery of an efficient power stroke. As the charge had not burned at an optimum crank angle position during the compression and expansion stroke, the flow conditions to deliver a fast flame growth (and therefore efficient burn) are not present. The different colours in the scatter graph plot represent separate engine test runs and highlight the consistency of the collected data.

4.4.2   MFB and IMEP

When the processed MFB times to 10%, 50% and 90% of the charge are considered (Figure 4.4.5), the trend of poorer performance at lower operating temperatures continues. The 90% MFB time varied as much 14.6 °CA AIT from the 80°C to the -7°C operating condition, which supports the hypothesis that the flame growth speed is slower at lower temperatures.

As with the other presented parameters, the COV of MFB time shows a clear correlation with decreasing operating temperature, the effect of which is compounded at higher MFB percentages due to the increased time from spark ignition. Cooling the charge to -7°C (not presented here) had a very small effect on the MFB times and COV which increased by 1 - 2 °CA AIT and 1% respectively.
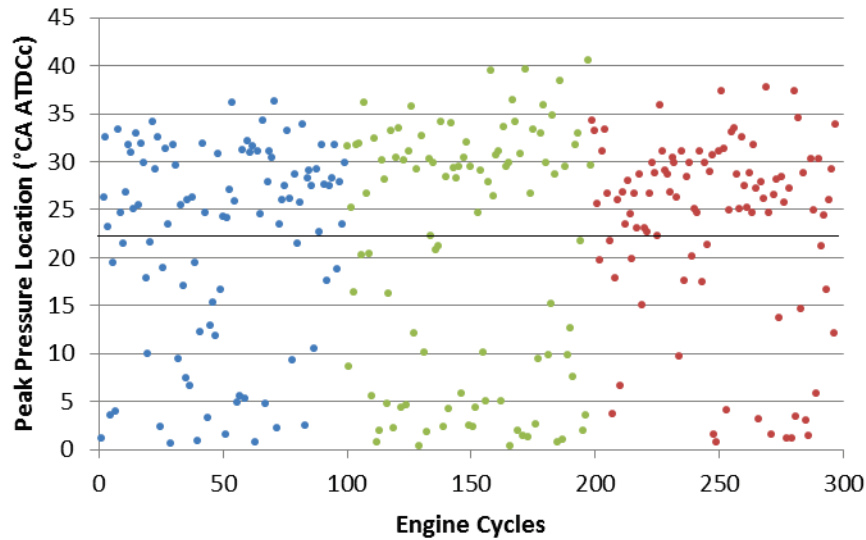
Figure 4.4.4: Peak pressure location of engine cycles at -7°C cylinder head and liner conditions, -7°C intake air temperature (engine speed = 1500 rpm, intake manifold pressure = 0.5 bar, fuel injection = 80 °CA ATDC, ignition timing = 325 °CA ATDC, λ = 1.0)
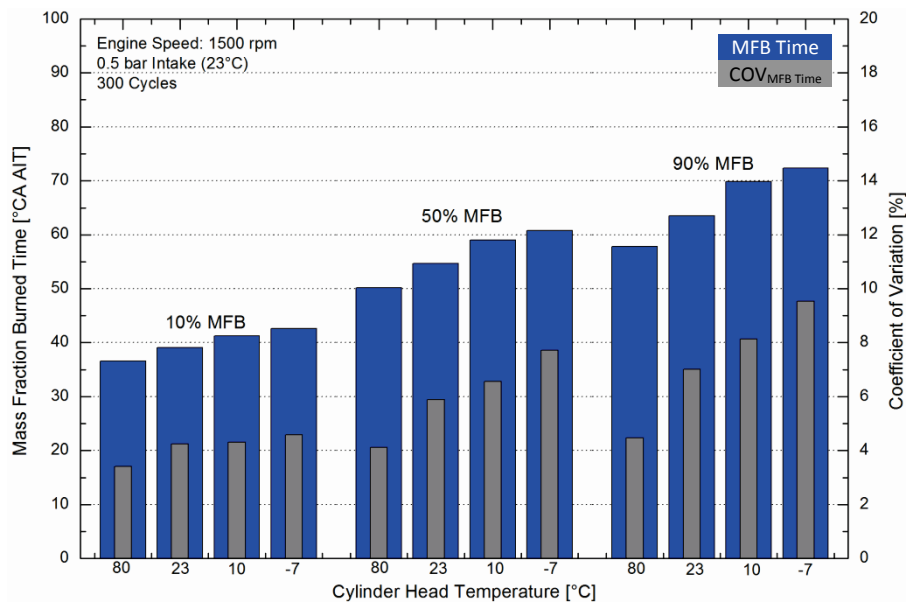
Figure 4.4.5: Mean mass fraction burned to 10%, 50% and 90% times after ignition timing (AIT) and corresponding COVs for a range of cylinder head and liner temperatures tested at 23°C intake temperature

Gross indicated mean effective pressure (IMEP) is a universally recognised parameter when analysing and comparing engine performance and efficiency. In this thesis the values of IMEP are relatively low, which is indicative of the start-up conditions tested. Figure 4.4.6 compares gross IMEP for all engine operating temperatures as well as their COV values. IMEP decreased as the temperature of the engine was reduced, correlating with the observed reduction in peak pressures, rates of MFB and poor in-cylinder combustion performance, which is described later in this chapter. COV increased significantly with falling temperatures, highlighting the effect on engine stability, particularly at the -7°C condition. Higher COVs during cold-start in a DISI engine have also been shown by Bruno *et al.* (2003).

A number of factors that contribute to instability in spark ignition (SI) engines were reviewed by Ozdor *et al.* (1994), such as fluctuations in equivalence ratio and flow field turbulence, as well as random convection of the spark kernel away from the electrodes. Williams *et al.* (2008), when using a similarly configured engine, showed a 10% variation in fuel distribution at the time of ignition using a quantitative planar laser induced fluorescence (QPLIF) technique. At the colder temperatures tested on this engine, with non-ideal mixing conditions, these factors will certainly contribute to the combustion instability observed. Persson *et al.* (2004) showed that reducing intake temperature alone in a gasoline engine significantly increased its COV_{IMEP}. Twiney *et al.* (2010) also found in a similar engine that the presence of fuel on the spark plug earth electrode modified the location of the spark and in worst cases, contributed to misfire. The increased presence of un-atomised fuel in these tested cases (which are discussed in *Chapter 5*) contributes to this effect.
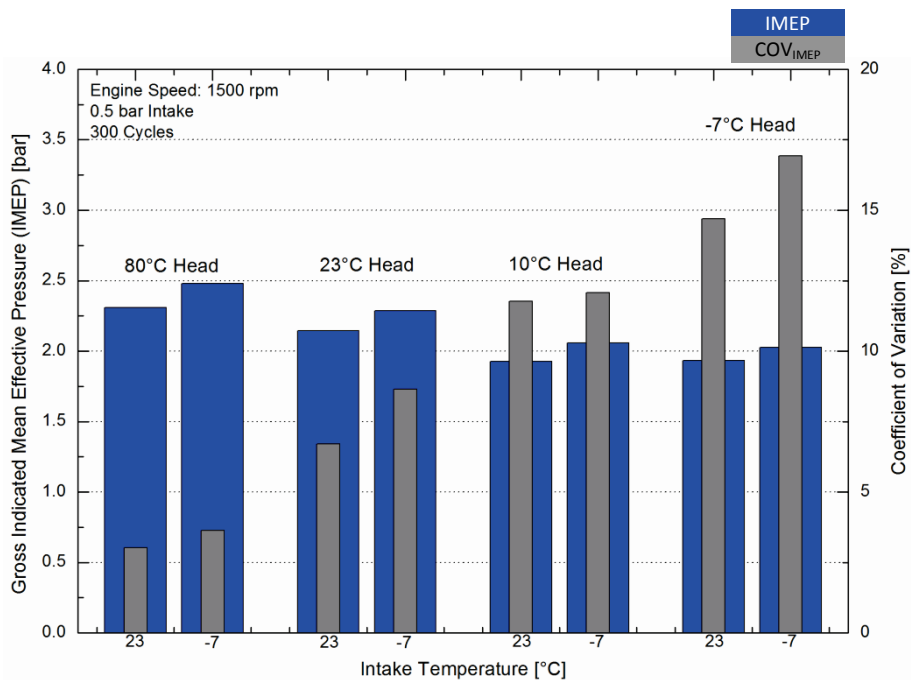
Figure 4.4.6: Mean gross IMEP and corresponding COVs for a range of engine operating temperatures and intake temperatures

4.4.3   In-Cylinder Combustion Imaging

This section of analysis aims to observe the in-cylinder combustion process through the piston crown in order to further explain the engine instabilities and performance effects that have been observed in the processed in-cylinder pressure data.

To understand the progressive growth of the flame after spark ignition, a time sequence of in-cylinder images has been presented at various operating conditions in Figure 4.4.7 to Figure 4.4.11. A crank angle range after ignition timing (AIT) of 15 °CA to 48 °CA in 2 °CA increments was selected as this allowed the early flame kernel growth to be captured along with the combustion of the remaining visible charge. The visible imaging region of the recorded combustion images and the orientation of the intake valves, exhaust valves, spark plug and fuel injector have been presented schematically in *Chapter 3*. The conditions shown in the combustion images are 80°C, 23°C, 10°C and -7°C cylinder head and liner temperatures with a 23°C intake air temperature. The -7°C intake temperature condition is shown for the 80°C cylinder liner and head condition only. The objectives of using these test points was to highlight the key differences in flame growth structure across the cylinder head and liner temperature range and to observe the independent effect that intake air temperature has on the combustion process.

Observation of the start of the combustion imaging time sequence allows flame kernel creation to be detected as early as 5 °CA, 0.55 ms AIT. Over several engine cycles the early flame kernel was seen to be stretched and manipulated in a number of different directions to varying degrees. This represents the differing scales of complex high frequency and small scale turbulent flow components that are present in the pent roof combustion chamber and, notably, in the spark plug region around the time of ignition (Rimmer *et al.* 2009). This initial flame kernel displacement is important in the proceeding propagation of the flame and consumption of unburned charge, since adequate interaction with the in-cylinder turbulent structures are known to be paramount in successful and efficient flame propagation.

High-speed particle image velocimetry (HSPIV) data (Jarvis *et al.* 2006, Rimmer *et al.* 2009) has previously shown that global flow motion in this type of engine around the time of spark ignition is directed from the intake to the exhaust side of the combustion chamber. These conclusions correlate with the presented sets of combustion images and show the global convection of the flame towards the exhaust valves as it propagated through the cylinder. The images following flame kernel establishment show a high magnitude of flame growth speed, which then decreases in magnitude as a higher proportion of the unburned charge is

consumed. During flame growth, local interaction between the flame front and the known small-scale structures of turbulence were apparent in the form of observed flame wrinkling. Striking differences are apparent between the sets of presented combustion images in the form of flame growth speed, high luminosity regions, local flame front structure and global flame luminosity.

The high intensity fuel-rich regions that were abundant in the flame during combustion at -7°C (Figure 4.4.11) represent poorly atomised and un-vaporised liquid fuel. They can be detected in the form of burning regions with diameters up to 2 mm in diameter and ligaments of liquid fuel with regions burning up to 5 mm long, which were seen to form from these droplets. This liquid fuel burned at a much lower rate than the bulk flame and continued to burn later into the expansion stroke due to a combination of lower surface area and local equivalence ratio. These locally fuel-rich regions are known sources of PM generation (Gupta *et al.* 2000) as their high carbon to oxygen ratio results in carbon atoms which can combine to form aromatic ring structures that nucleate to form particulate matter (PM) (Cromas and Ghandhi 2005, Price *et al.* 2006). Mixing after combustion, however, allows some of these particles to oxidize (Cromas and Ghandhi 2005).

In the fully heated engine condition of 80°C with an ambient intake air temperature (Figure 4.4.7), the presence of high luminosity liquid fuel was contrastingly small when compared to the -7°C case. The specific reasons for this are outlined in the next chapter, whereby the fuel spray structure has been analysed at various operating conditions. However, the resulting combustion images indicate that the majority of fuel spray particles were atomising and vaporising adequately to facilitate homogeneous stoichiometric combustion.

The effect that a cooled intake charge has independently on combustion when the head and liner are kept constant at 80°C is shown in Figure 4.4.8. Expectedly, the flame structure, growth speed and luminosity were similar to that of the ambient charge case, which exemplifies the dominant effect the head and liner (and therefore fuel) temperature have on the flame. Interestingly, however, the cooled charge induced the presence of burning liquid fuel droplets with burning regions with sizes up to approximately 1.5 mm, albeit in a lesser quantity than when the head and liner were cooled to -7°C. This highlights the profound effect that intake charge temperature alone has on the atomisation and vaporisation of the interacting fuel spray during intake, along with the potential to create conditions which promote PM formation.

15 °CA AIT   18 °CA AIT   21 °CA AIT

24 °CA AIT   27 °CA AIT   30 °CA AIT

33 °CA AIT   36 °CA AIT   39 °CA AIT

42 °CA AIT   45 °CA AIT   48 °CA AIT

**Figure 4.4.7: Flame imaging sequence through piston crown window
(engine speed = 1500 rpm, intake manifold pressure = 0.5 bar, fuel injection = 80 °CA ATDC,
ignition timing = 325 °CA ATDC, λ = 1.0)**
80°C cylinder head and liner conditions, 23°C intake air temperature

15 °CA AIT · **18 °CA AIT** · **21 °CA AIT**

24 °CA AIT · **27 °CA AIT** · **30 °CA AIT**

33 °CA AIT · **36 °CA AIT** · **39 °CA AIT**

42 °CA AIT · **45 °CA AIT** · **48 °CA AIT**

Figure 4.4.8: Flame imaging sequence through piston crown window
(engine speed = 1500 rpm, intake manifold pressure = 0.5 bar, fuel injection = 80 °CA ATDC,
ignition timing = 325 °CA ATDC, λ = 1.0)
80°C cylinder head and liner conditions, -7°C intake air temperature

The 23°C and 10°C operating condition test points (Figure 4.4.9 and Figure 4.4.10) exhibited similar flame structures with similar levels of un-vaporised fuel contained within the flame. The images highlight a faster flame growth speed in the 23°C condition that was previously confirmed in the mass fraction burned times. The 10°C operating condition consistently displayed a more uneven flame growth than the warmer temperatures, particularly in the earlier phases of the flame kernel. A potential cause of this is poor atomisation and vaporisation producing a less homogeneous charge and reducing the uniformity of the local equivalence ratio, particularly across the interacting flame front. Areas of different equivalence ratios will burn at different rates producing non-spherical flame growth.

Differences in global flame luminosity can be observed across the different operating conditions. The two main forms of light emission that the camera detected were:

i. the incandescence of soot particles within fuel-rich regions of the flame and

ii. natural light emission of combustion known as chemiluminescence, which when using hydrocarbon fuels, originate from combustion radicals OH, CH, C_2 and the broadband emission from CO_2 (Kuwahara *et al.* 1998, Rimmer *et al.* 2012).

The understanding of a flame's dynamic stoichiometry that can be inferred from these light emissions are discussed in *Chapter 6* with the utilisation of colour high-speed combustion imaging. Chemiluminescence can help better understand the differences observed in global flame luminosity, as most of the light emitted in the 80°C case originated from combustion radicals, whilst the majority of high intensity light emission detected in the colder -7°C case was caused by soot incandescence in the rich areas of the flame. Another potential reason for the differences in global luminosity is the uniformity of the local equivalence ratio, particularly across the interacting flame front. Areas of different equivalent ratios would have burned at different speeds, which are observed as inhomogeneous areas of flame luminosity. The wrinkled flame front, as observed in the fully heated condition, is less distinguishable at colder operating conditions. A combination of mixture homogeneity and uneven flame luminosity may have obscured the flame, as it is reasonable to assume that the turbulent flow structures were both still present and similar at the colder operating conditions.

15 °CA AIT   **18 °CA AIT**   **21 °CA AIT**

24 °CA AIT   **27 °CA AIT**   **30 °CA AIT**

33 °CA AIT   **36 °CA AIT**   **39 °CA AIT**

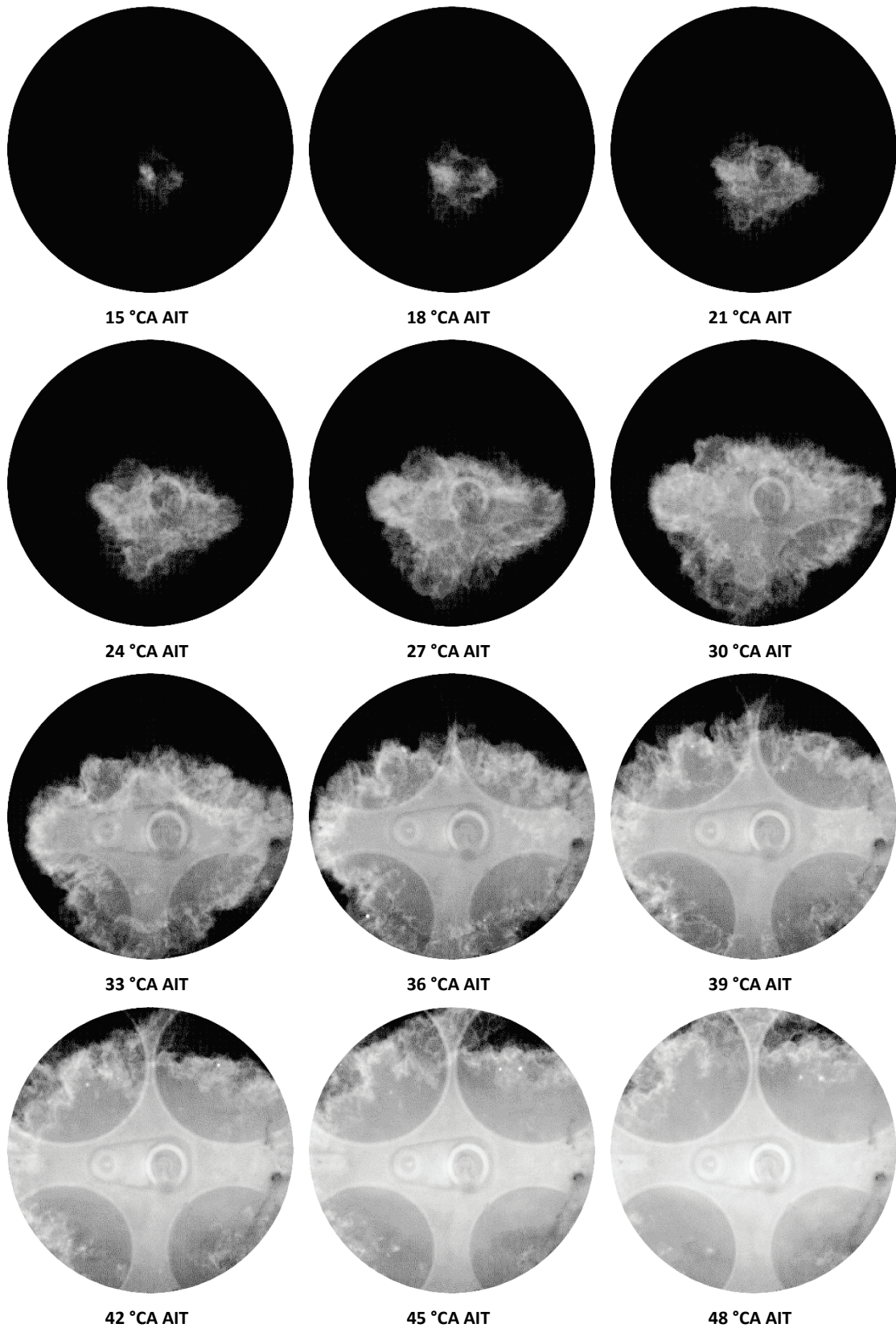**42 °CA AIT**   **45 °CA AIT**   **48 °CA AIT**

Figure 4.4.9: Flame imaging sequence through piston crown window
(engine speed = 1500 rpm, intake manifold pressure = 0.5 bar, fuel injection = 80 °CA ATDC,
ignition timing = 325 °CA ATDC, λ = 1.0)
23°C cylinder head and liner conditions, 23°C intake air temperature

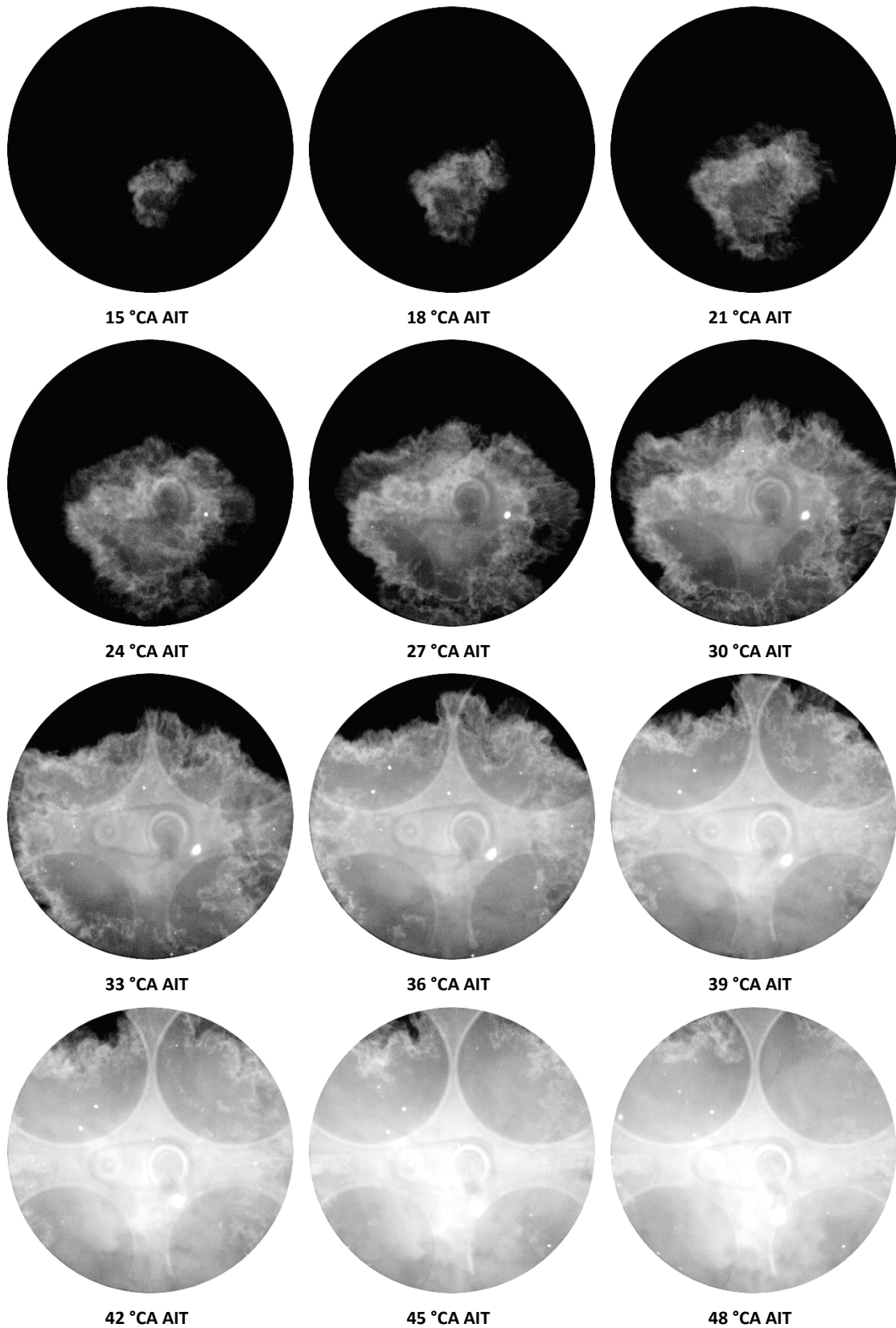| 15 °CA AIT | 18 °CA AIT | 21 °CA AIT |
24 °CA AIT	27 °CA AIT	30 °CA AIT
33 °CA AIT	36 °CA AIT	39 °CA AIT
42 °CA AIT	45 °CA AIT	48 °CA AIT

Figure 4.4.10: Flame imaging sequence through piston crown window
(engine speed = 1500 rpm, intake manifold pressure = 0.5 bar, fuel injection = 80 °CA ATDC,
ignition timing = 325 °CA ATDC, λ = 1.0)
10°C cylinder head and liner conditions, 23°C intake air temperature

15 °CA AIT   **18 °CA AIT**   **21 °CA AIT**

24 °CA AIT   **27 °CA AIT**   **30 °CA AIT**

33 °CA AIT   **36 °CA AIT**   **39 °CA AIT**

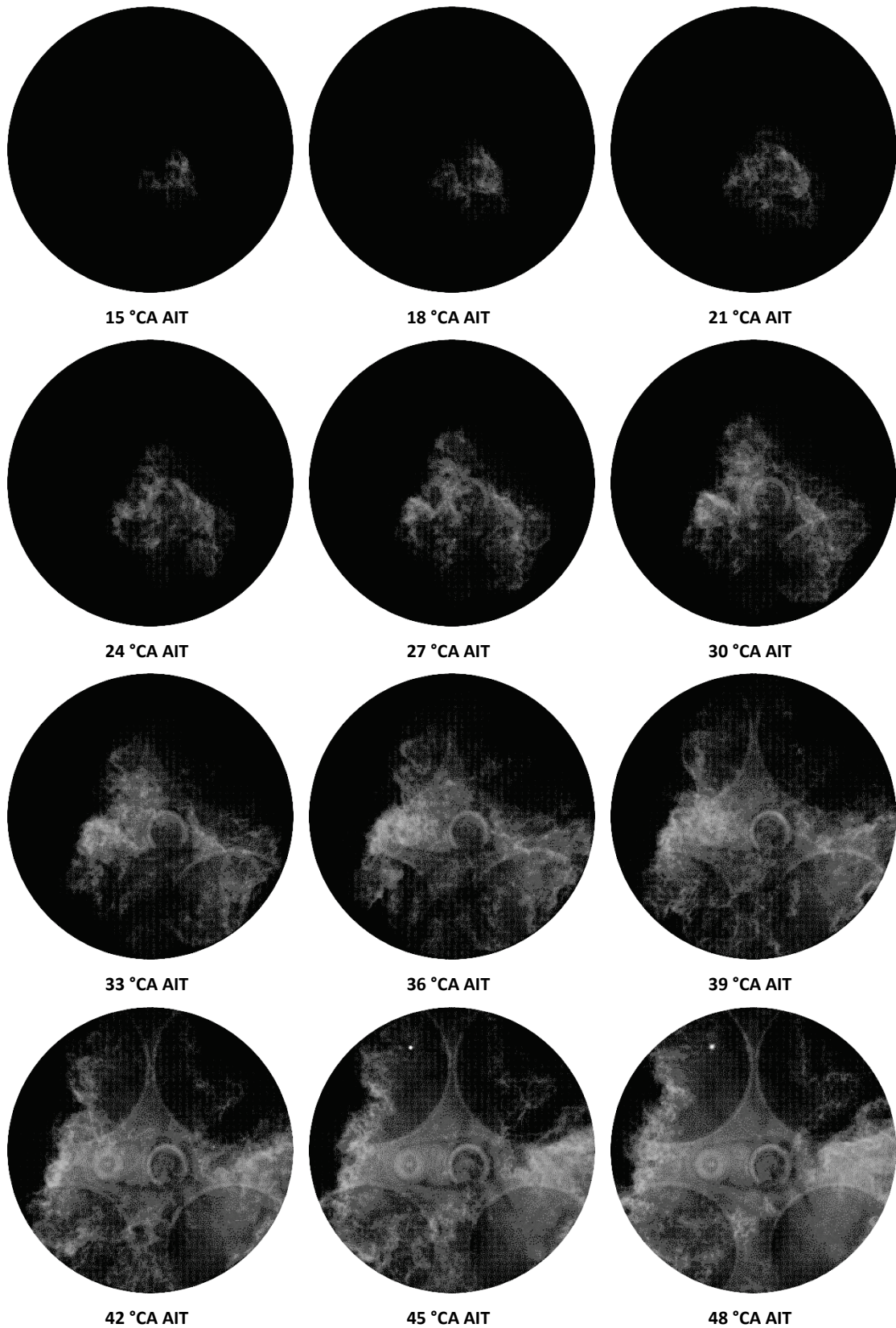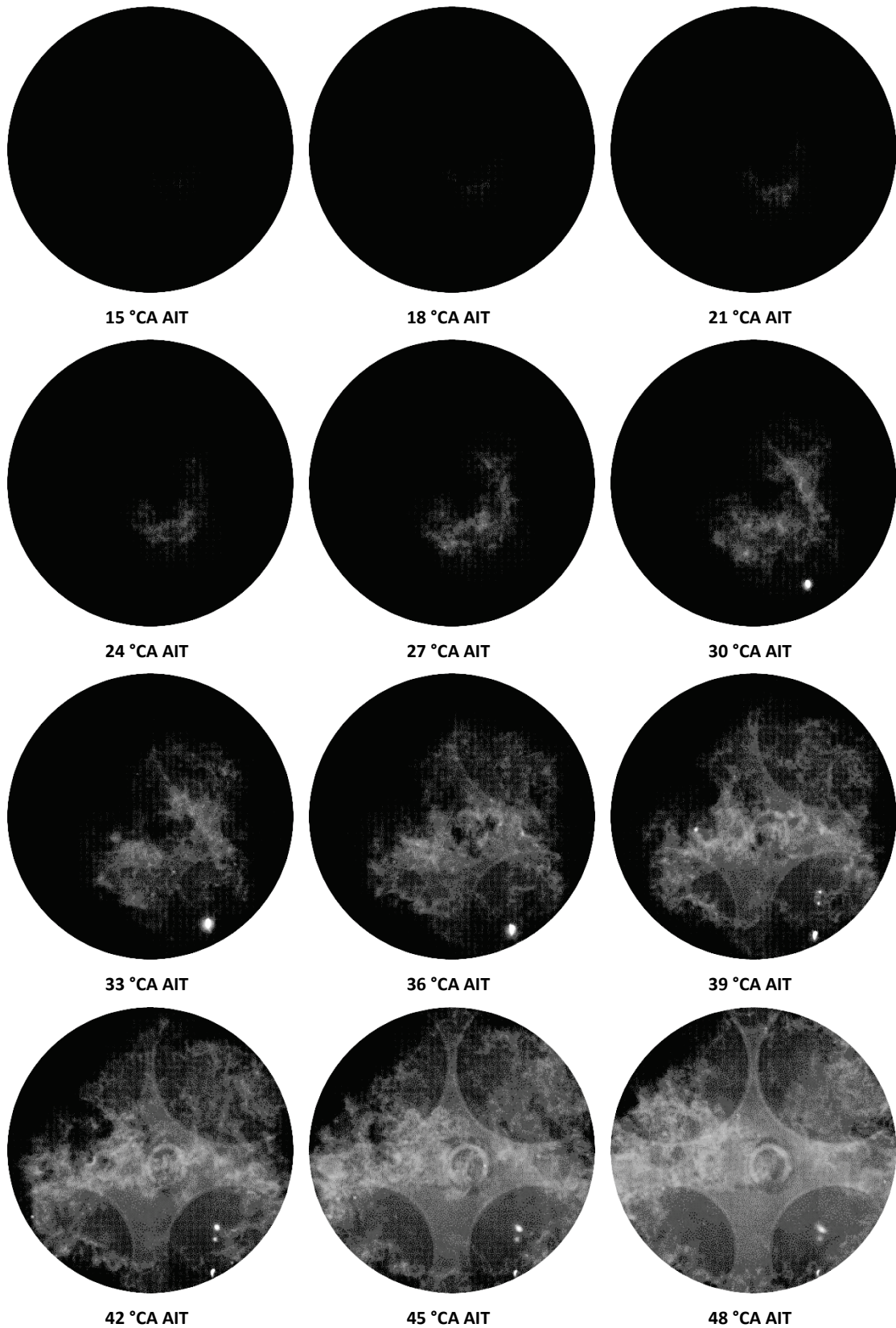**42 °CA AIT**   **45 °CA AIT**   **48 °CA AIT**
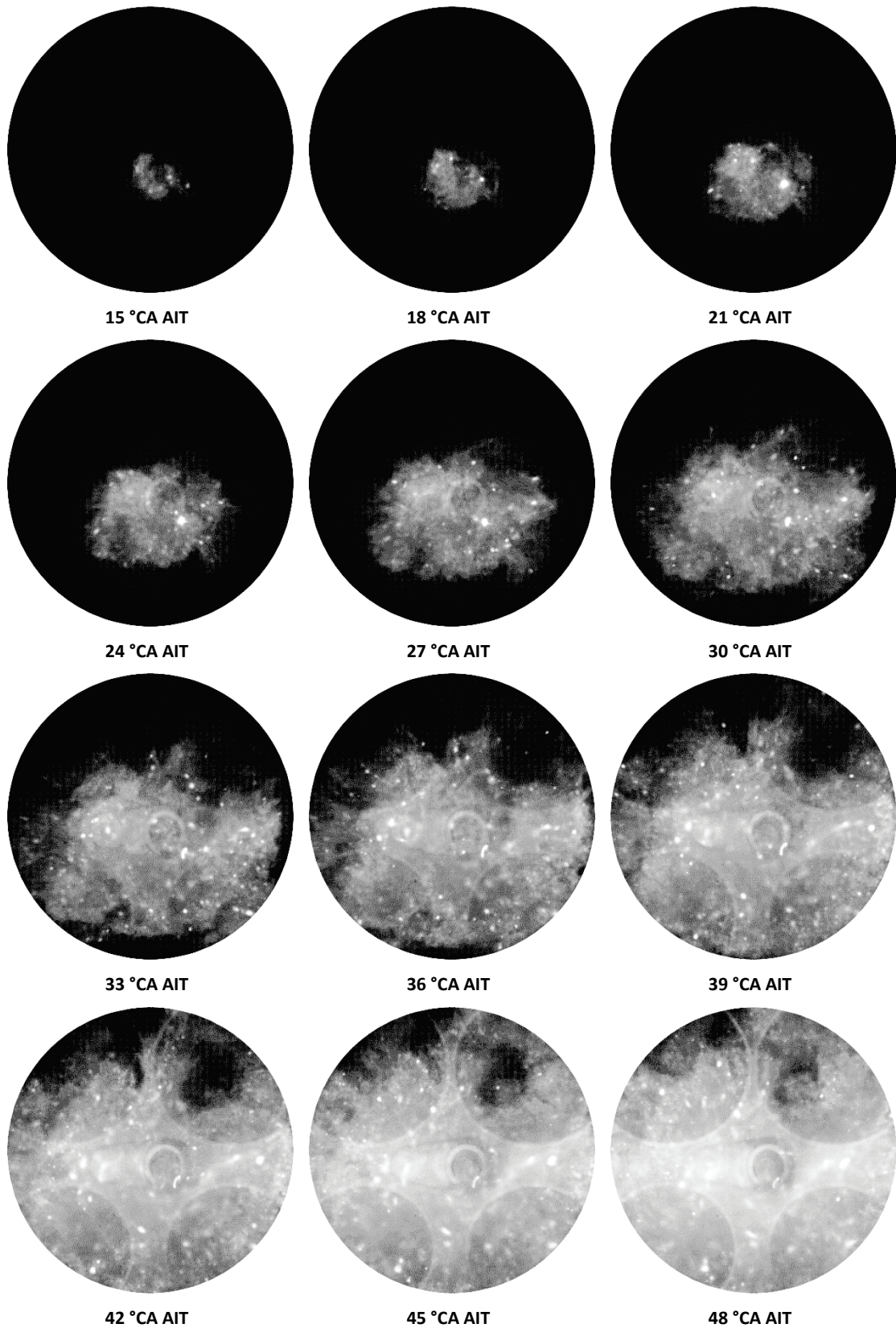
Figure 4.4.11: Flame imaging sequence through piston crown window
(engine speed = 1500 rpm, intake manifold pressure = 0.5 bar, fuel injection = 80 °CA ATDC,
ignition timing = 325 °CA ATDC, λ = 1.0)
-7°C cylinder head and liner conditions, 23°C intake air temperature

The images presented for the -7°C condition (Figure 4.4.11) interestingly appear to show a faster flame growth than both the 10°C and 23°C conditions, which was not consistent with the MFB times calculated from the pressure data. This may be due to a difference in flame luminosity between conditions, which allows an increased fraction of the flame to be visible to the camera. One must also bear in mind that the flame was recorded in a two-dimensional plane so an absolute understanding of the complex three-dimensional flame growth cannot be inferred from this data alone. The next section discusses image processed parameters from the same flame images, so will further the understanding of the flame's growth and structure.

4.4.4   In-Cylinder Combustion Image Analysis

Image processing of the recorded flame images was carried out to better understand the effect that operating temperature had on the flame. As entire data sets can be processed and mean-averaged, statistical analyses also remain accurate. This section has quantified various parameters from the recorded flame images which were presented previously.

Figure 4.4.12 shows the flame growth speeds AIT as for the entire head and liner temperature range at 23°C intake (upper graph) and the two extreme head and liner temperatures tested with both 23°C and -7°C intake temperatures (lower graph). A striking difference can be seen between the 80°C operating condition and the remaining temperatures, with a flame that is detected earlier and reaches a peak of 9.5 m·s^{-1} approximately 5°CA earlier. These findings are analogous with those from the in-cylinder pressure data, which showed the 80°C condition has a notably faster burn rate and peak pressure than the other operating temperatures. The remaining colder temperatures exhibited very similar flame growth speed profiles with peak speeds within a range of 5.0 - 5.5 m·s^{-1}, despite there appearing to be larger differences in the presented images. The colder operating temperatures maintained their peak flame speeds for longer, highlighting the increased time it took for the flame to reach the cylinder wall and therefore consume the unburned charge.

The lower graph (Figure 4.4.12) highlights a profound difference in both the flame growth speed and the time the flame was first detected when a cooled charge was used. This exemplifies the effect a cooled charge has on limiting the speed of the flame, which is detrimental to engine performance. The in-cylinder pressure data analysis did not highlight the effect of the cooled charge as strikingly as the image-processed optical data.

The most extreme case of -7°C head, liner and intake temperature was shown to have a peak flame growth speed not too dissimilar to the average flame growth speed as well as the flame being detected nearly 10°CA later compared to an ambient temperature charge. This delay in the early creation and growth of the flame kernel has a detrimental effect on the flame's growth as the burning charge is not exposed to the highest magnitude in-cylinder frequency components near TDC, which typically aid with rapid flame propagation and consumption rate (Long *et al.* 2008).
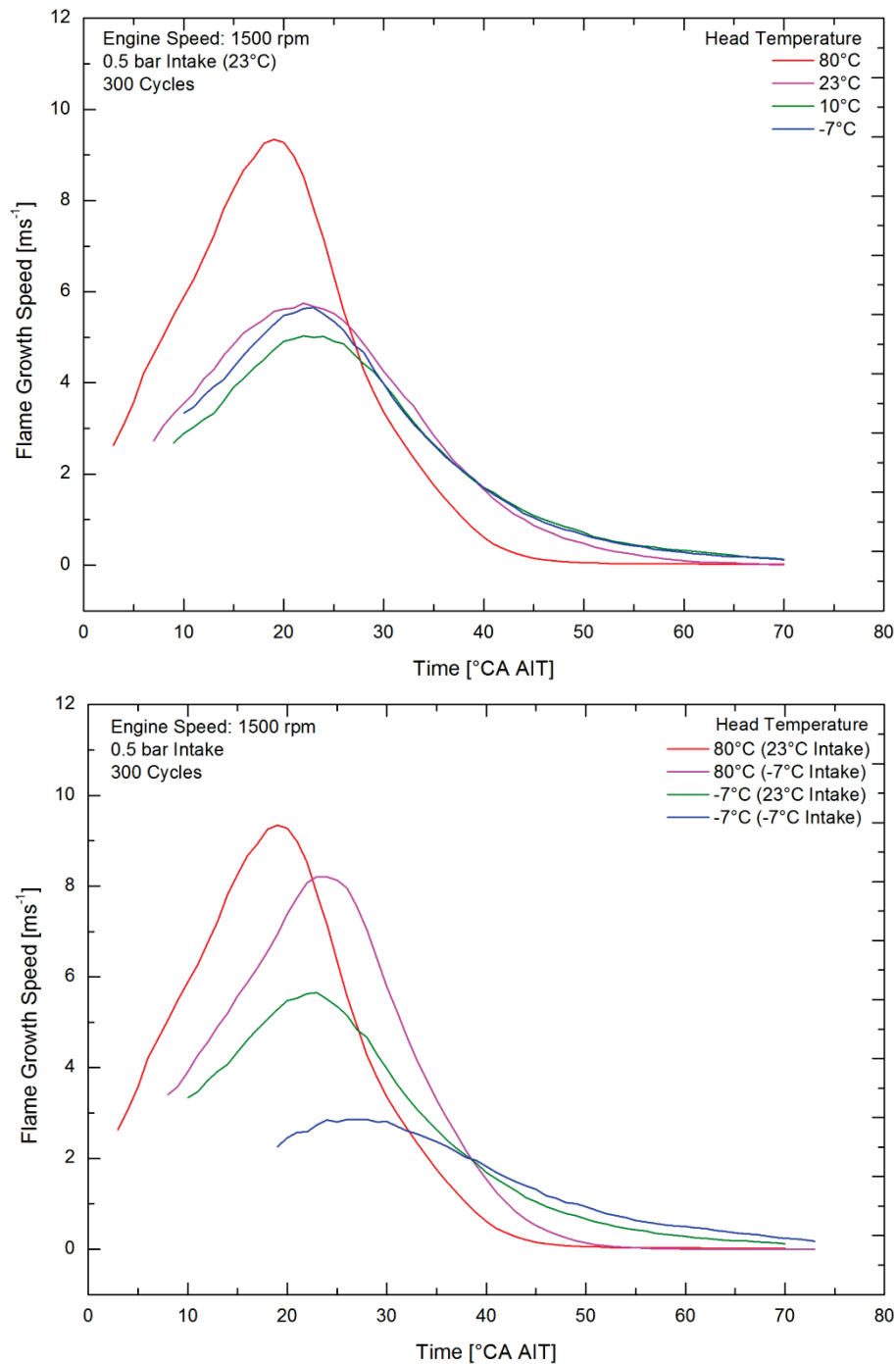
Figure 4.4.12: Flame growth speeds for a range of cylinder head and liner temperatures tested at 23°C and -7°C intake temperatures

4.5   CONCLUDING REMARKS

The effects of cooling an optical DISI engine down to operating temperatures of -7°C have been discussed with a detailed optical analysis of flame combustion and quantitative discussion of in-cylinder pressure data. A number of cylinder head and liner temperatures were tested along with ambient and cooled charge conditions. The results showed significant differences in the flame growth speeds and structures, as well as the calculated engine performance parameters. The main conclusions from this part of the investigation are:

1. In-cylinder peak pressures were seen to drop by up to 5 bar when the engine was cooled from 80°C to -7°C, alongside a rise in COV of 7%. Further processing of the in-cylinder pressure data was completed and showed an overall decrease in IMEP as well as significant increases of COV from 3% to 15%.

2. High-speed imaging of the in-cylinder combustion highlighted contrasting flame growth structures between operating temperatures, and in the coolest cases, the widespread presence of fuel-rich regions and lower flame growth speeds. These rich regions are known areas of particulate formation and highlight the impact that temperature has on the critical early phase of a cold-start.

3. Image processing analysis of the flame images correlated with results seen from the in-cylinder pressure data. The effect of operating temperature was exemplified further with striking differences seen in the time to start of combustion and flame growth speed when comparing the fully heated 80°C condition to the colder temperatures.

The combination of using optical and pressure data analysis allowed a better understanding of the in-cylinder combustion structures and a thorough characterisation of the reasons for the detrimental performance recorded by the in-cylinder pressure transducer.

The next chapter aims to further build on this understanding by analysing the critical phase of fuel injection to observe the effect that operating temperature has on fuel spray atomisation, vaporisation and surface impingement. These factors are fundamental to engine performance and particulate emission formation.

4.6   CHAPTER 4 REFERENCES

BRUNO, B. A., SANTAVICCA, D. A. & ZELLO, J. V. (2003) Fuel Injection Pressure Effects on the Cold Start Performance of a GDI Engine, SAE Paper 2003-01-3163.

CROMAS, J. & GHANDHI, J. B. (2005) Particulate Emissions from a Direct-Injection Spark-Ignition Engine, SAE Paper 2005-01-0103.

DIESELNET (2015) European Union Emission Standards for Cars and Light Trucks, Available from: http://www.dieselnet.com/standards/eu/ld.php, [Accessed 01/06/2015].

EFTHYMIOU, P., DAVY, M., GARNER, C., HARGRAVE, G., RIMMER, J. E. T. & RICHARDSON, D. (2013) Insights into Cold-Start DISI Combustion in an Optical Engine Operating at −7°C. *SAE. Int. J. Engines,* Vol 6(2), pp. 1059-1074.

GUPTA, S., POOLA, R., O.L., K. & SEKAR, R. (2000) Particulate Emissions Characteristics of Port-Fuel Injected SI Engine. *US Dept. of Energy*.

HEYWOOD, J. B. (1988) *Internal Combustion Engine Fundamentals,* 1st Ed., McGraw-Hill, pp. 42-61, 205-278, 400-450, 797-819.

JARVIS, S., JUSTHAM, T., CLARKE, A., GARNER, C. P. & HARGRAVE, G. K. (2006) Motored SI IC Engine In-Cylinder Flow Field Measurement Using Time Resolved Digital PIV For Characterisation of Cyclic Variation, SAE Paper 2006-01-1044.

KUWAHARA, K., YAMAMOTO, S., IWACHIDOU, K. & ANDO, H. (1998) Two-Stage Combustion for Quick Catalyst Warm-up in Gasoline Direct Injection. *The Fourth International Symposium COMODIA 98*, pp. 293-298.

LONG, E. J., RIMMER, J. E. T., JUSTHAM, T., GARNER, C., HARGRAVE, G. K., RICHARDSON, D. & WALLACE, S. (2008) The Influence of In-Cylinder Turbulence upon Engine Performance within a Direct Injection IC Engine. *Seventh International Conference on Modelling and Diagnostics for Advanced Engine Systems.* Sapporo Japan.

OZDOR, N., DULGER, M. & SHER, E. (1994) Cyclic Variability in Spark Ignition Engines A Literature Survey, SAE Paper 940987.

PERSSON, H., AGRELL, M., J., O., JOHANSSON, B. & STRÖM, H. (2004) The Effect of Intake Temperature on HCCI Operation Using Negative Valve Overlap, SAE Paper 2004-01-0944.

PRICE, P., STONE, R., COLLIER, T. & DAVIES, M. (2006) Particulate Matter and Hydrocarbon Emissions Measurements: Comparing First and Second Generation DISI with PFI in Single Cylinder Optical Engines, SAE Paper 2006-01-1263.

RASSWEILER, G. M. & WITHROW, L. (1938) Motion Pictures of Engine Flames Correlated with Pressure Cards, SAE Paper 380139.

RIMMER, J. E. T., DAVY, M. H., GARNER, C. P., HARGRAVE, G. K. & RICHARDSON, D. (2012) Fuel spray structure, flame propagation and charge motion at fuel impingement locations within a DISI engine. *IMechE: Fuel Systems for IC Engines,* Vol 2012, pp. 199-214.

RIMMER, J. E. T., LONG, E. J., GARNER, C. P., HARGRAVE, G. K., RICHARDSON, D. & WALLACE, S. (2009) The Influence of Single and Multiple Injection Strategies on In-Cylinder Flow and Combustion within a DISI Engine, SAE Paper 2009-01-0660.

STANGLMAIER, R. H., LI, J. & MATTHEWS, R. D. (1999) The Effect of In-Cylinder Wall Wetting Location on the HC Emissions from SI Engines, SAE Paper 1999-01-0502.

TWINEY, B., STONE, R., CHEN, X. & EDMUNDS, G. (2010) Investigation of Combustion Robustness in Catalyst Heating Operation on a Spray Guided DISI Engine, Part 1 - Measurements of Spark Parameters and Combustion, SAE Paper 2010-01-0593.

WHITAKER, P., KAPUS, P., OGRIS, M. & HOLLERER, P. (2011) Measures to Reduce Particulate Emissions from Gasoline DI engines, SAE Paper 2011-01-1219.

WILLIAMS, B., EWART, P., STONE, R., MA, H., WALMSLEY, H., CRACKNELL, R., STEVENS, R., RICHARDSON, D., QIAO, J. & WALLACE, S. (2008) Multi-Component Quantitative PLIF: Robust Engineering Measurements of Cyclic Variation in a Firing Spray-Guided Gasoline Direct Injection Engine, SAE Paper 2008-01-1073.

CHAPTER 5

THE EFFECT OF ENGINE OPERATING TEMPERATURE ON DISI FUEL INJECTION

5.1   INTRODUCTION

The significant effects that operating temperature has on in-cylinder combustion were discussed in *Chapter 4*. The most notable was considered the presence of liquid fuel droplets in the flame at colder temperatures. As a known region of PM generation, these areas are of particular interest and are linked directly with the atomisation, vaporisation and surface impingement from the fuel injection event.

This chapter analyses the fuel injection process in detail to better understand the results observed during the combustion process. High-speed optical diagnostics and laser illumination were used in conjunction with a full length optical cylinder liner in order to capture as much information from the fuel injection spray plumes as possible.

The experimental setup was chosen such that it accurately represented the combustion experiments to allow correlation with the findings of the fuel spray studies. The complete engine temperature range from 80°C to -7°C was tested during steady-state motoring of the engine. The test conditions used in the presented results are outlined in this chapter with a more detailed explanation of the overall engine setup previously described in *Chapter 3.*

The detailed optical fuel-spray data were further processed to deliver statistical data relating to the location of the in-cylinder fuel spray during the intake stroke over entire engine runs. A striking difference was observed in both the fuel spray structure and rates of vaporisation when comparing the fully heated operating condition to the colder engine temperatures. These results correlated with the combustion data analysed in *Chapter 4* and help further understand the effects of cold temperatures on the complex in-cylinder processes that lead to the formation of PM.

5.2   OPTICAL ENGINE EXPERIMENTAL CONFIGURATION

Imaging of the in-cylinder fuel injection process was facilitated by utilising both the quartz optical cylinder liner and piston crown as explained in detail in *Chapter 3*. The use of a 28 mm lens with a wide-open aperture of f2.8 allowed the fuel spray droplets to be detected throughout the entire cylinder bore. This was of particular importance since the mechanisms of cold-surface impingement and wall-wetting (that potentially cause PM formation regions) needed to be further understood.

Figure 5.2.1 shows the experimental arrangement of the optical engine during imaging of the fuel spray through the optical cylinder liner. The optical cylinder liner in this image mostly obscured due to the laser safety guarding that minimised the level of scattered laser light from 45° mirror and other reflective engine surfaces.
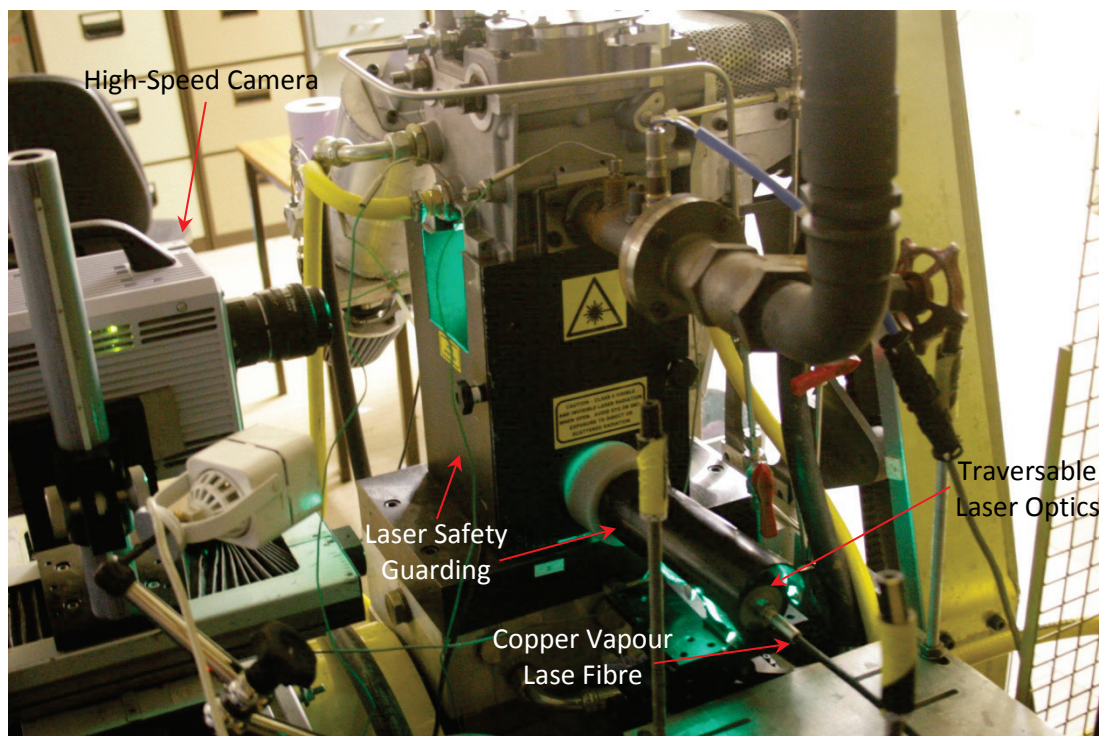
Figure 5.2.1: Experimental setup of optical engine for fuel-spray imaging at various operating temperatures (showing engine cooled to 23°C)

The traversable laser optics (shown in Figure 5.2.2) allowed fine adjustment of a spherical lens relative to the fixed laser fibre. This enabled the precise focussing of the conical beam angle in order to maximise the quantity of light entering the cylinder during the entire intake stroke.
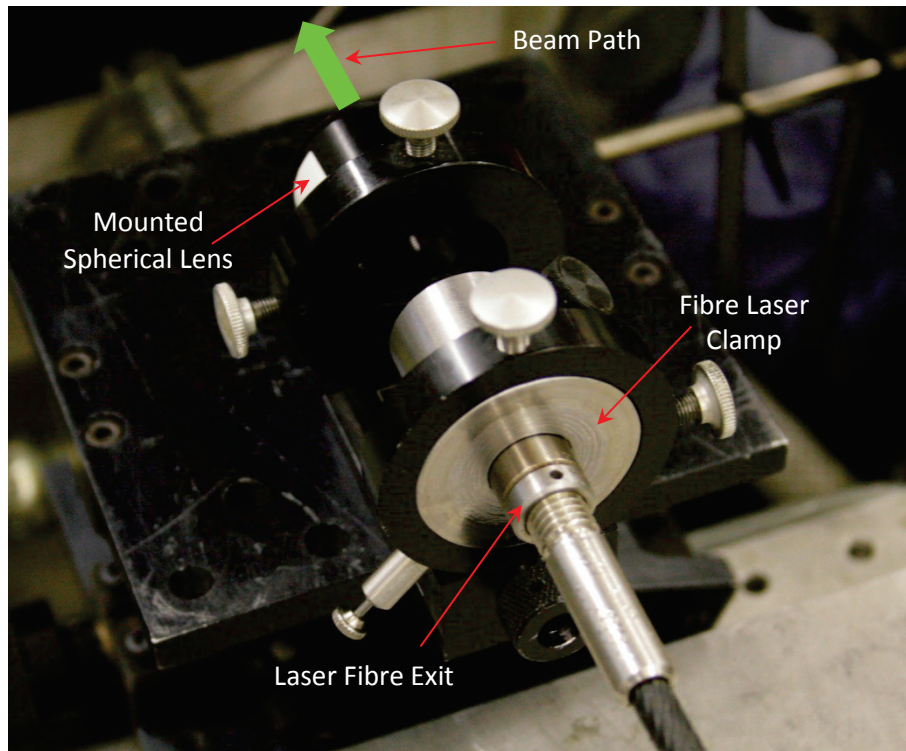
Figure 5.2.2: Traversable lens system used for fine adjustment of conical copper-vapour laser beam

The tested operating conditions of 80°C, 23°C, 10°C and -7°C cylinder head and liner temperatures with 23°C and -7°C intake air temperatures were kept the same as those used in *Chapter 4* so that the fuel-spray imaging best represented previously presented combustion data with a λ ratio of 1.0. Since the quartz liner could not be directly cooled by the vapour chiller, the engine was continuously motored and not fired to prevent temperature build up from combustion. This also kept the injector and fuel sac temperature consistent across engine runs, which allowed repeatable fuel injection events to be captured. To cool the quartz liner and better replicate the cold surface temperatures of the steel liner, the engine was left to 'cold soak' for approximately an hour before each engine run. This period of time allowed the system to sufficiently cool, as confirmed by the thermocouples instrumented across the engine. The differences in thermal properties between the quartz and steel liner were noted when the fuel spray data was analysed.

5.3   FUEL SPRAY DATA ANALYSIS

The captured fuel spray images required no image enhancement and minimal image processing. The well-controlled laser illumination and the smaller diameter of the quartz piston crown window ensured that only the fuel-spray droplets were illuminated and scatter from in-cylinder surfaces was minimised. The presented images were inverted for presentation and to aid the clarity of the fuel droplets, particularly in areas of low droplet density.

As discussed in the literature review in *Chapter 2*, a number of studies have used optical diagnostics techniques to analyse fuel spray parameters such as droplet size, atomisation and vaporisation rate. Wigley *et al.* (1998) commented that a single technique alone can lead to false conclusions regarding the atomisation of fuel and multiple complementary diagnostics techniques such as laser Doppler anemometry (LDA), phase Doppler anemometry (PDA) and imaging analysis helps to facilitate the successful interpretation of a complex spray flow field (Wigley *et al.* 2004). The fuel spray data presented in this chapter was not image processed to calculate parameters such as vaporisation rate and spray angle due to the lack of size distribution data from PDA techniques as well as the fact that all spray plumes had been illuminated, preventing the isolation of a single plume angle. A qualitative and statistical analysis of the fuel spray images proved sufficient due to the wide range of operating conditions being tested and the distinct differences that were observed.

To develop an understanding of the bulk spay structure at each operating condition, the first 25 °CA of each fuel injection event was ensemble mean-averaged at each crank angle across 300 engine cycles. The recording rate of 9 kHz allowed a temporal resolution of 1 °CA/frame equating to 0.11 ms time between frames. This chosen time separation captured the injection process up to the point of impingement on the piston crown, after which the main plume structure collapsed and the visible droplets vaporised. To show an overall representation of the spray structure at each point, these ensemble mean-average images at each crank angle were then averaged. The resulting images highlight the location of visible fuel in the cylinder during this initial spray period. To quantify the level of temporal variability between injections cycles during engine runs, the root mean square (RMS) of the first 25 °CA of each injection was also calculated. The RMS calculation first averaged all spray images before calculating the RMS as shown by

$$RMS = \sqrt{\frac{1}{n-1}\sum_i (x_i - \bar{x})^2}$$

Eqn. (5.3.1)

where *n* is the number of images, x_i is the pixel intensity of image *i* and $\bar{x}$ is the mean across all images, given by

$$\bar{x} = \frac{1}{n}\sum_{i=1}^{n} x_i$$

Eqn. (5.3.2)

5.4 RESULTS AND DISCUSSION

The following section presents both raw, ensemble-averaged and RMS fuel spray images to better understand the fuel injection process and further elaborate on the effect of operating temperature. In-cylinder pressure data and combustion imaging analysis highlighted a detrimental effect on performance as well as stability with lower operating temperatures.

A time sequence of images from a single arbitrary injection event is presented from Figure 5.4.2 to Figure 5.4.7 for the complete range of cylinder head and liner operating conditions. A crank angle range after start of injection (ASOI) of 6 °CA to 20 °CA in 1 °CA increments is shown. This range allowed the entire fuel spray injection event to be captured along with the early spray breakup and fuel mixing.

Observation of the fuel injection sequence at operating conditions of 80°C (Figure 5.4.2) depicts a highly atomised fuel spray with a main body that visibly penetrated a maximum of approximately 30 mm into the cylinder. The early spray plume showed a structure that is representative of the 6-hole injector arrangement discussed in *Chapter 3*. Two groups of 3 holes are seen to form, but due to the level of atomisation, vaporisation and plume divergence, no individual spray plumes were fully distinguishable within the main spray body. As the bulk spray body initially progressed through the cylinder, the interaction of the surrounding air with the spray boundary can be observed. The atomised fuel spray experienced primary breakup, whereby the shear forces at the gas-liquid interface are responsible for the breakup of the liquid jet into droplets (Charalampous *et al.* 2009) and secondary atomisation as described by (Lasheras *et al.* 1998) as it detached itself from the main spray body in the first 10 °CA and was transported to the edges of the cylinder, as is typical in the air distortion process (Heywood 1988). This is an important part of the mixing process since atomised fuel transportation is required to achieve a sufficiently homogeneous mixture before the spark ignition event.

This highly atomised and well distributed fuel spray structure helps elucidate why the 80°C operating condition had the best recorded engine performance, lowest mass fraction burned time and the lowest quantity of liquid fuel present in the flame, as discussed in *Chapter 4*. An in-cylinder peak pressure of up to 40% higher than the colder operating temperatures was recorded, which can be attributed to how well homogenised the charge was prior to spark ignition. This allowed a rapid flame growth that maximised the work delivered at the optimum crank angle during the expansion stroke. The lack of visible high-intensity fuel-rich regions in

the recorded in-cylinder combustion images are a result of the well atomised spray that impinged less on engine surfaces and vaporised more completely before combustion.

In the last 5 °CA of the presented fuel spray images at 80°C (Figure 5.4.2), the dominant effects of the in-cylinder flow structures on the fuel spray are apparent. The right hand plume is observed continuing its path along the cylinder liner wall towards the surface of the piston crown before being swept into a clockwise vortex which re-joins the remaining body of fuel spray. Previous analyses of in-cylinder flow structures in a similarly configured engine during intake (Stansfield *et al.* 2007) showed that at low valve lift, the small effective flow area and large pressure difference across the intake valves resulted in conical jets forming and travelling at velocities of 50 m·s^{-1} during the current engine speed and setup. Rimmer *et al.* (2012) also highlighted the importance of these in-cylinder vortices during the injection process in a similarly configured engine and noted that these flow structures have the potential to assist with the transportation of impinged liquid fuel back into the cylinder to aid vaporisation.

Progression through the latter part of the intake stroke showed a consistent reduction in the luminosity of the light scattered by the fuel spray body indicative of fuel vaporisation taking place. The rate of this observed vaporisation increases as the stroke progresses due to the expanding volume that the spray is exposed to and the time available for the fuel to vaporise. Care must be taken, however, when commenting on vaporisation with the method of visualisation used. The level of detected fuel spray was dependent on the detected scattered light from fuel-spray particles of a particular size range. In this investigation, particles approximately 1 μm and above were detectable.

A cold -7°C temperature charge was introduced into a fully heated engine at 80°C to observe the effects and interaction with the heated fuel spray (shown in Figure 5.4.3). No discernible differences between the -7°C and 23°C intake temperatures were seen in the shape and structure of the spray plume but a slight increase in plume penetration before breakup was apparent. This was especially noticeable at 17 °CA ASOI, where impingement on the piston crown window surface was imminently taking place in the cooled charge case. This small difference in penetration is also highlighted later in this section when the fuel spray images are statistically processed. These results correlate with the data presented in *Chapter 4* that showed a subtle difference of approximately 0.5 bar in peak pressure and 0.25 bar engine performance (IMEP) between 23°C and -7°C intake air temperatures, but did highlight an increase in high intensity fuel-rich regions in the flame at -7°C, which could have been caused by the noted increase in spray plume penetration and therefore impingement.

The cold-start simulated operating condition of -7°C, as well the 23°C and 10°C operating conditions revealed a strikingly different fuel spray structure when compared to the fully heated 80°C case (Figure 5.4.4, Figure 5.4.5 and Figure 5.4.6). As expected at these colder cylinder head and liner conditions, flash boiling of the fuel did not occur, producing a far less vaporised spray with a higher concentration of liquid fuel. The length of the continuous liquid jet core was higher than in the 80°C condition, this important factor determines the extent of the primary atomisation region (Charalampous *et al.* 2009). The initial momentum of these spray particles, due to their mass, caused the spray plumes to penetrate the cylinder at a greater rate than in the full heated engine case. Piston impingement was consistently apparent in all runs and occurred as early as 10 °CA ASOI. The difference in fuel-spray structure at the fully heated engine case was also observed by Serras-Pereira *et al.* (2007) highlighting a reduction in liquid-core spray area of up to 15% at 90°C compared to 50°C in a similarly configured engine.

The consistent piston crown impingement that occurred at the colder operating conditions aligns with the combustion data in *Chapter 4* that highlighted an increased quantity of fuel-rich regions below 80°C and is indicative of impinged fuel unable to vaporise before spark ignition. No detectable differences were observed between the instantaneous imaging data of the three colder operating conditions, with impingement occurring on the piston crown at the same time during the intake stroke and the same level of global luminosity visibly apparent. Image processing described later in this section was utilised to detect the subtle dissimilarities between the three coldest temperatures.

The distillation curve for the Shell Pura gasoline fuel that was used throughout engine testing is shown in Figure 5.4.1. This aids the understanding of why flash boiling occurred at 80°C and not the lower operating temperatures. At 80°C, the graph indicates that approximately 35% of fuel is a vapour, which likely consists of the lighter weight and more volatile compounds of the fuel composition that were seen to flash boil in the fuel spray images. Below 33°C, the graph indicates that the majority of the fuel is composed of liquid, which is why flash boiling was not observed at any of the colder operating conditions and the visible rate of vaporisation appeared lower than that of the 80°C operating condition. As in most SI engine combustion systems, the charge was throttled so the pressure within the cylinder was below atmospheric. In this instance, the vapour pressure of the fuel was higher meaning the saturation temperature was also higher, allowing a larger quantity of fuel to vaporise.
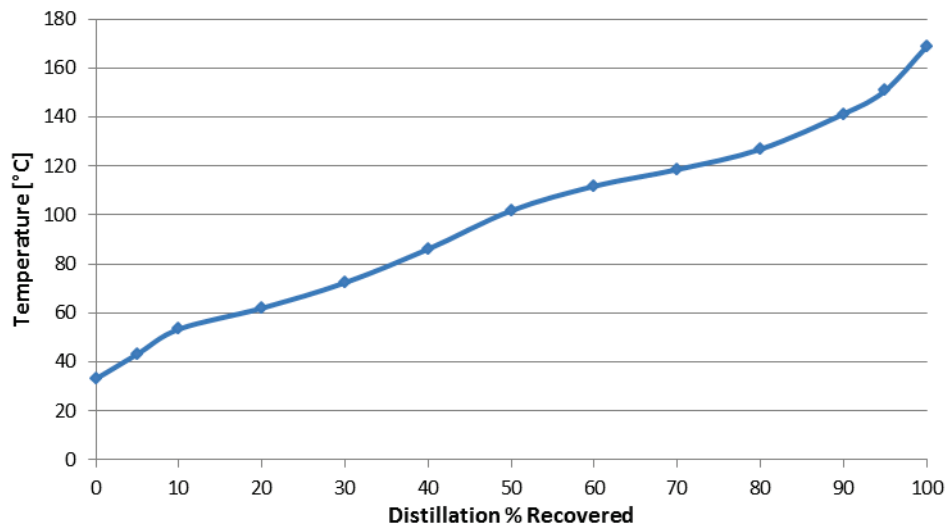
Figure 5.4.1: Distillation curve for Shell Pura gasoline RON: 95.7 (Shell Global Solutions (1998) - See Appendix A)

The fuel spray images were further processed to investigate the consistency of the fuel spay injection events and highlight any dissimilarities that were not detectable in the instantaneous images. Ensemble-averaged and RMS images of the in-cylinder fuel spray were created from 300 engine cycles for each crank angle at all operating conditions. They have been presented as contour plots of spray intensity that range from 0 - 100. The ensemble-averaged images in Figure 5.4.8 illustrate the striking differences in fuel spray structure between the 80°C operating condition and all colder engine temperatures. The flash boiling that is present when the engine is fully heated results in a highly atomised spray with a significantly reduced level of piston crown impingement. This observed and consistent spray structure agree with the previous conclusions made regarding the improved engine performance at 80°C (*Chapter 4)* being a direct result of the fuel spray structure. The highly atomised spray impinged less on the engine surfaces and was more readily transported and vaporised, which produced a more homogeneous charge and burned more efficient during combustion.

Subtle differences were seen in the colder operating conditions in the right hand spray plumes after 20 °CA ASOI. For example, the plumes appear slightly wider and there is a larger impingement region on the piston crown surface as the temperature decreases. Despite these subtleties, the overall structure of the spray remains consistent between the three colder temperatures.

These small differences in surface impingement correlate with the increasing quantity of fuel-rich regions in the flame that were observed in *Chapter 4* when the operating temperature was decreased. It is reasonable to assume that a significant contributor to the fuel rich regions in

the flame was the quantity of impinged fuel that remained from the injection process and was unable to fully vaporise.

The RMS images (Figure 5.4.9) highlight the areas of highest variability across the experimental test run. The 80°C condition exhibited a high variability near the central tip of the spray plume throughout the presented images that increased up to 24 °CA ASOI. This variation in recorded luminosity could be indicative of the dominant interaction between the highly atomised spray and the intake air flow, which has a velocity 10 times that of the mean piston velocity (Heywood 1988) and could have been attributed to the variability of the spray plume. *Chapter 6* highlights the variability in the in-cylinder flow field around the time of injection and analyses the flow field structure to better understand the complex interaction with the fuel spray.

The colder operating conditions highlight very similar areas of high variability to each other, indicating that operating temperature, dominated by fuel temperature, did not affect the variability of the injection process with a spray that had not flash boiled. As with the 80°C condition, high RMS levels were present in the spray plume tip up until the plumes start to break up and impinge on the piston crown surface at 20 °CA ASOI. The reduction in variability after this time was likely due to the strong in-cylinder air flow structures dominating the transportation of the fuel spray once the spray event had relinquished most of the its initial momentum.

The findings from the fuel spray imaging data have helped further explain the main differences observed during combustion between the 80°C operating condition and the three colder temperatures. Conclusive differences in the fuel spray data, however, have not been easily detectable between the 23°C, 10°C and -7°C conditions despite the more profound differences in engine combustion performance noted in *Chapter 4*. This suggests that the differences in engine performance could be attributed to the level of surface impingement and evaporation that is governed by operating condition and surface temperature. This is not conclusive, however, as the Mie scattering technique did not detect the effect of temperature on the smallest of the fuel droplets or vapour distribution, as these were not detectable.

6 °CA ASOI

7 °CA ASOI

8 °CA ASOI

20 mm

9 °CA ASOI

10 °CA ASOI

11 °CA ASOI

12 °CA ASOI

13 °CA ASOI

14 °CA ASOI

15 °CA ASOI

16 °CA ASOI

17 °CA ASOI

18 °CA ASOI

19 °CA ASOI

20 °CA ASOI
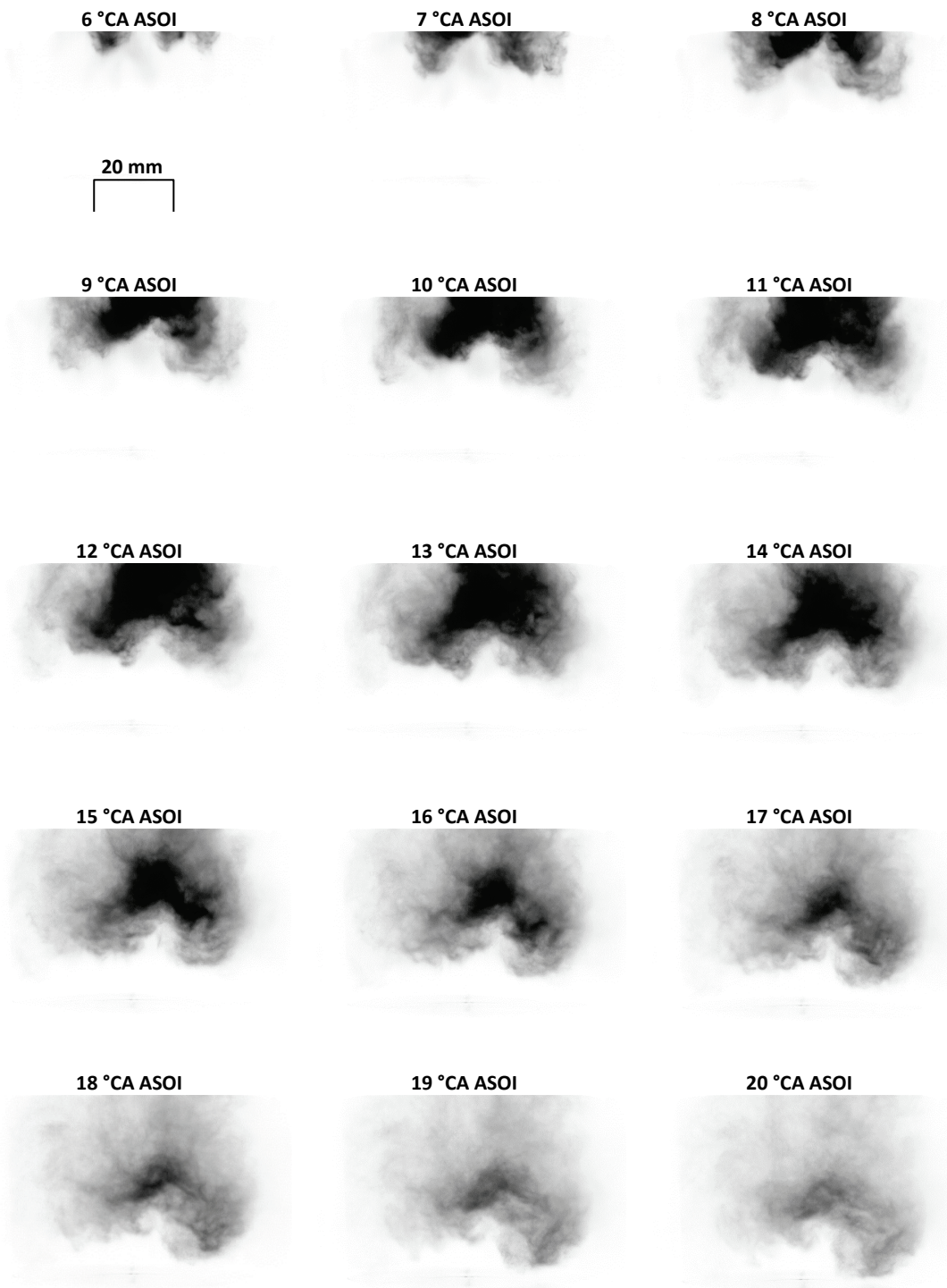
Figure 5.4.2: Fuel injection imaging sequence through piston crown window
(engine speed = 1500 rpm, intake manifold pressure = 0.5 bar, fuel injection = 80 °CA ATDC, λ = 1.0)
80°C cylinder head and liner conditions, 23°C intake air temperature
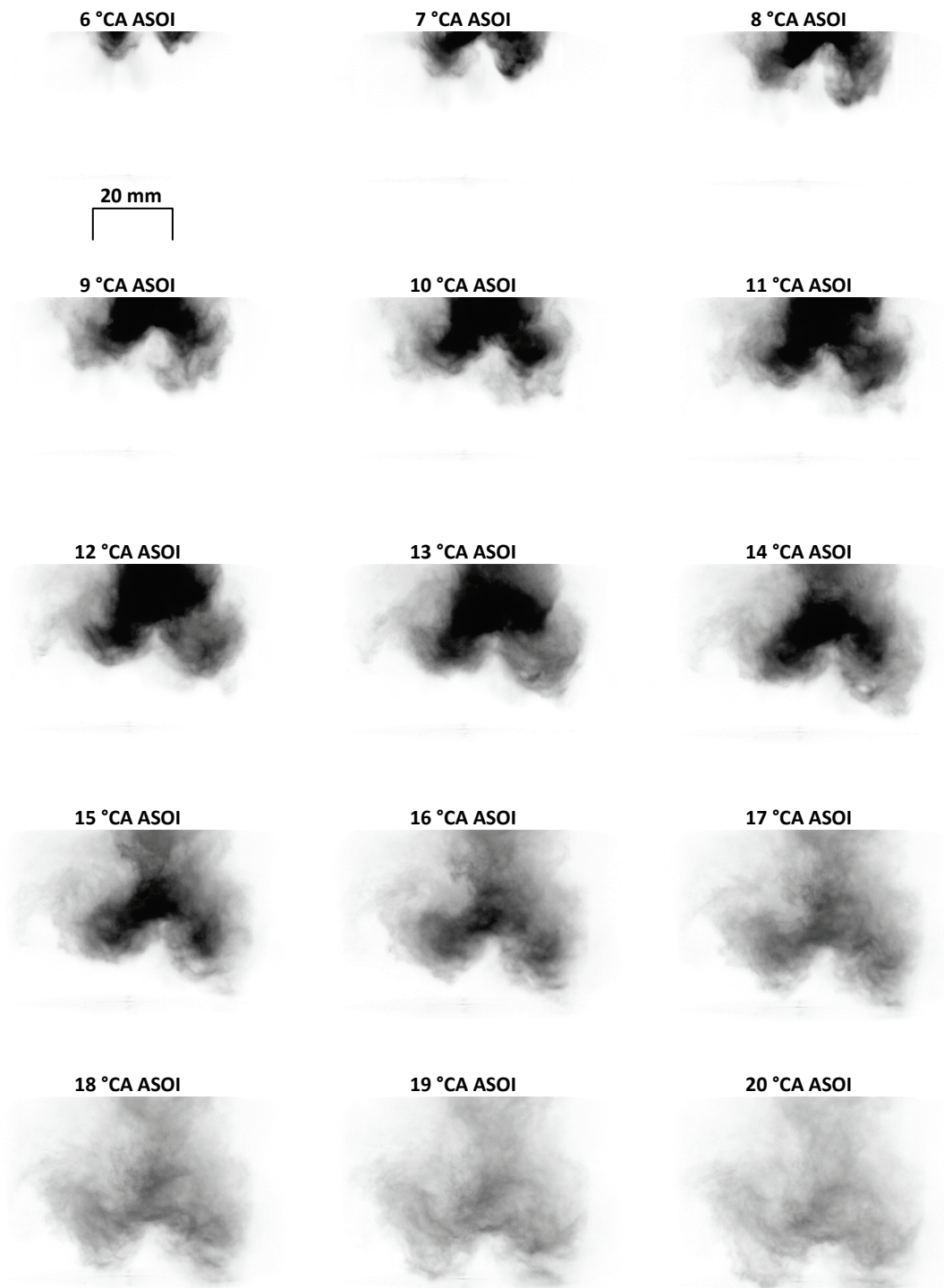
Figure 5.4.3: F Fuel injection imaging sequence through piston crown window
(engine speed = 1500 rpm, intake manifold pressure = 0.5 bar, fuel injection = 80 °CA ATDC, λ = 1.0)
80°C cylinder head and liner conditions, -7°C intake air temperature

6 °CA ASOI　　　　　　　　**7 °CA ASOI**　　　　　　　　**8 °CA ASOI**

20 mm

9 °CA ASOI　　　　　　　　**10 °CA ASOI**　　　　　　　　**11 °CA ASOI**

12 °CA ASOI　　　　　　　　**13 °CA ASOI**　　　　　　　　**14 °CA ASOI**

15 °CA ASOI　　　　　　　　**16 °CA ASOI**　　　　　　　　**17 °CA ASOI**

18 °CA ASOI　　　　　　　　**19 °CA ASOI**　　　　　　　　**20 °CA ASOI**
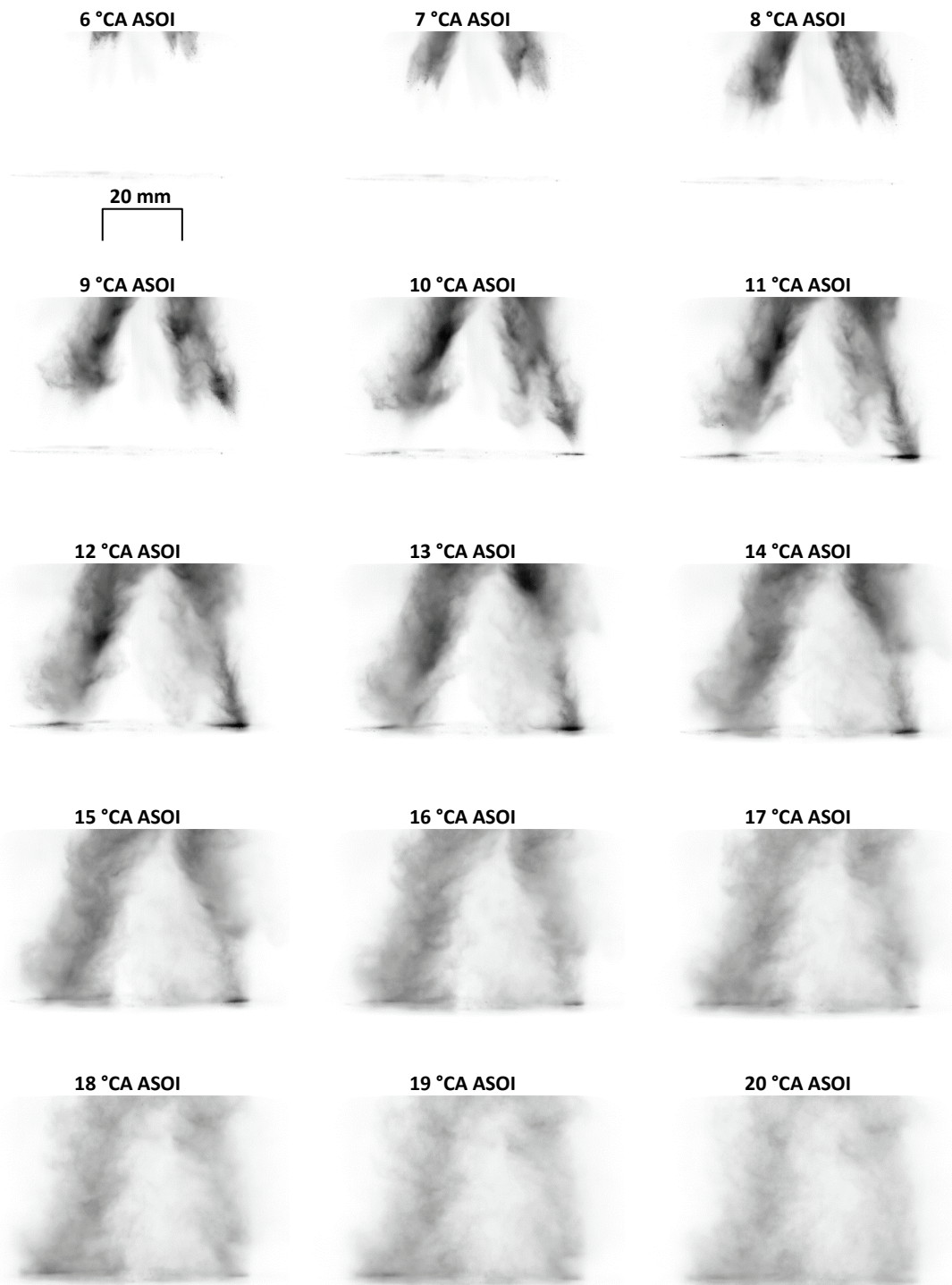
Figure 5.4.4: Fuel injection imaging sequence through piston crown window
(engine speed = 1500 rpm, intake manifold pressure = 0.5 bar, fuel injection = 80 °CA ATDC, λ = 1.0)
23°C cylinder head and liner conditions, 23°C intake air temperature

6 °CA ASOI   **7 °CA ASOI**   **8 °CA ASOI**

20 mm

9 °CA ASOI   **10 °CA ASOI**   **11 °CA ASOI**

12 °CA ASOI   **13 °CA ASOI**   **14 °CA ASOI**

15 °CA ASOI   **16 °CA ASOI**   **17 °CA ASOI**

18 °CA ASOI   **19 °CA ASOI**   **20 °CA ASOI**
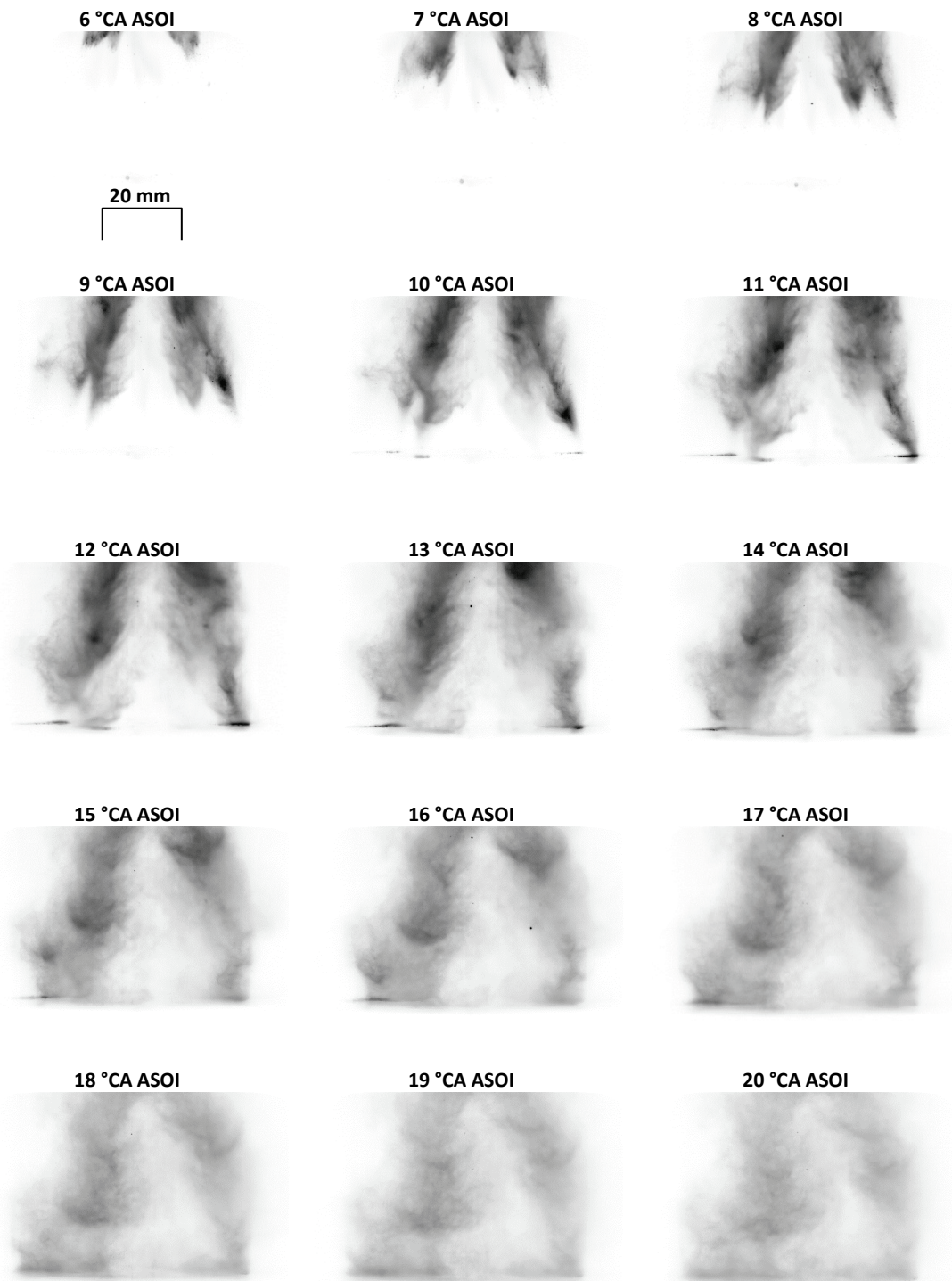
Figure 5.4.5: Fuel injection imaging sequence through piston crown window
(engine speed = 1500 rpm, intake manifold pressure = 0.5 bar, fuel injection = 80 °CA ATDC, λ = 1.0)
10°C cylinder head and liner conditions, 23°C intake air temperature
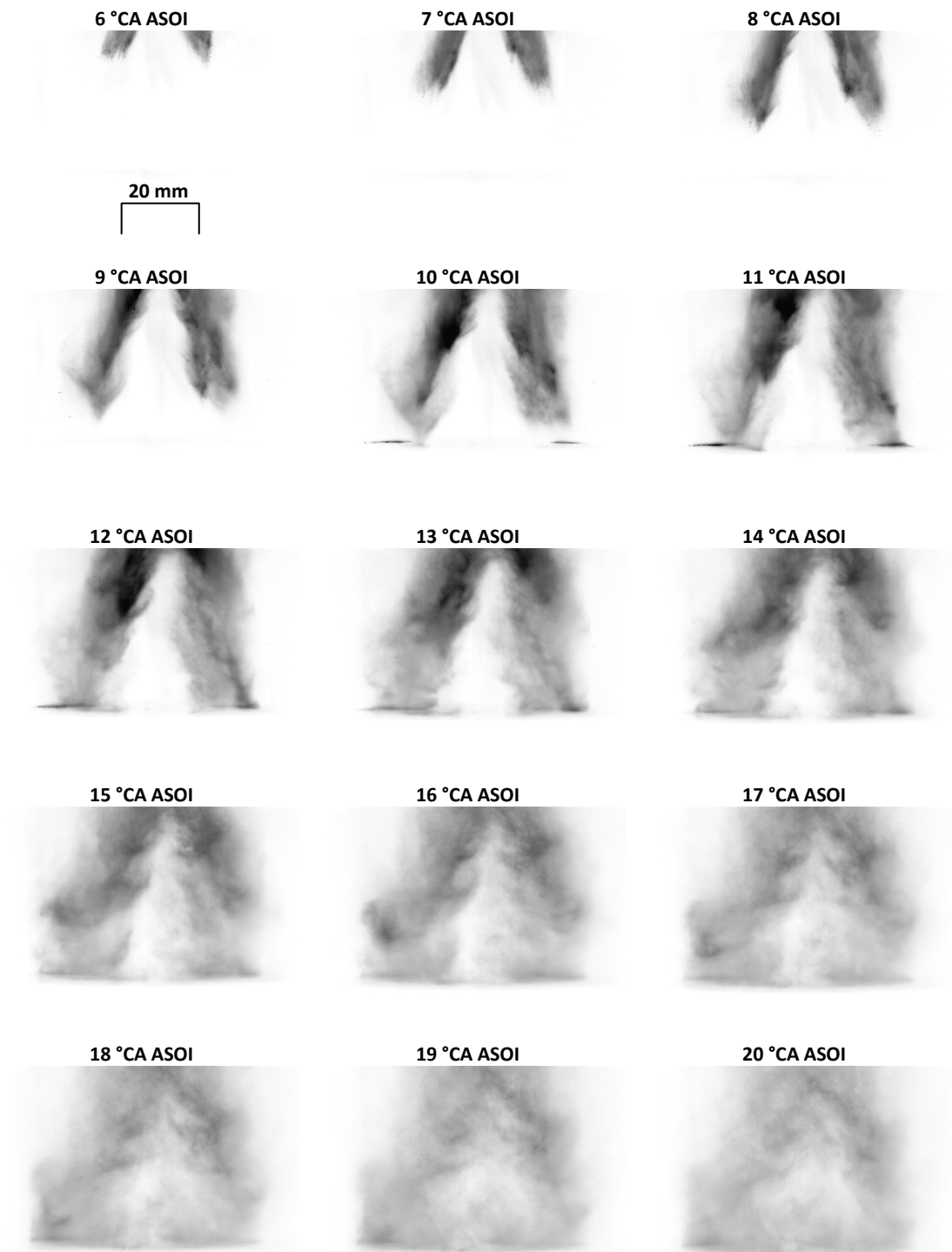
Figure 5.4.6: Fuel injection imaging sequence through piston crown window
(engine speed = 1500 rpm, intake manifold pressure = 0.5 bar, fuel injection = 80 °CA ATDC, λ = 1.0)
-7°C cylinder head and liner conditions, 23°C intake air temperature

6 °CA ASOI　　　　　　**7 °CA ASOI**　　　　　　**8 °CA ASOI**

20 mm

9 °CA ASOI　　　　　　**10 °CA ASOI**　　　　　　**11 °CA ASOI**

12 °CA ASOI　　　　　　**13 °CA ASOI**　　　　　　**14 °CA ASOI**

15 °CA ASOI　　　　　　**16 °CA ASOI**　　　　　　**17 °CA ASOI**

18 °CA ASOI　　　　　　**19 °CA ASOI**　　　　　　**20 °CA ASOI**
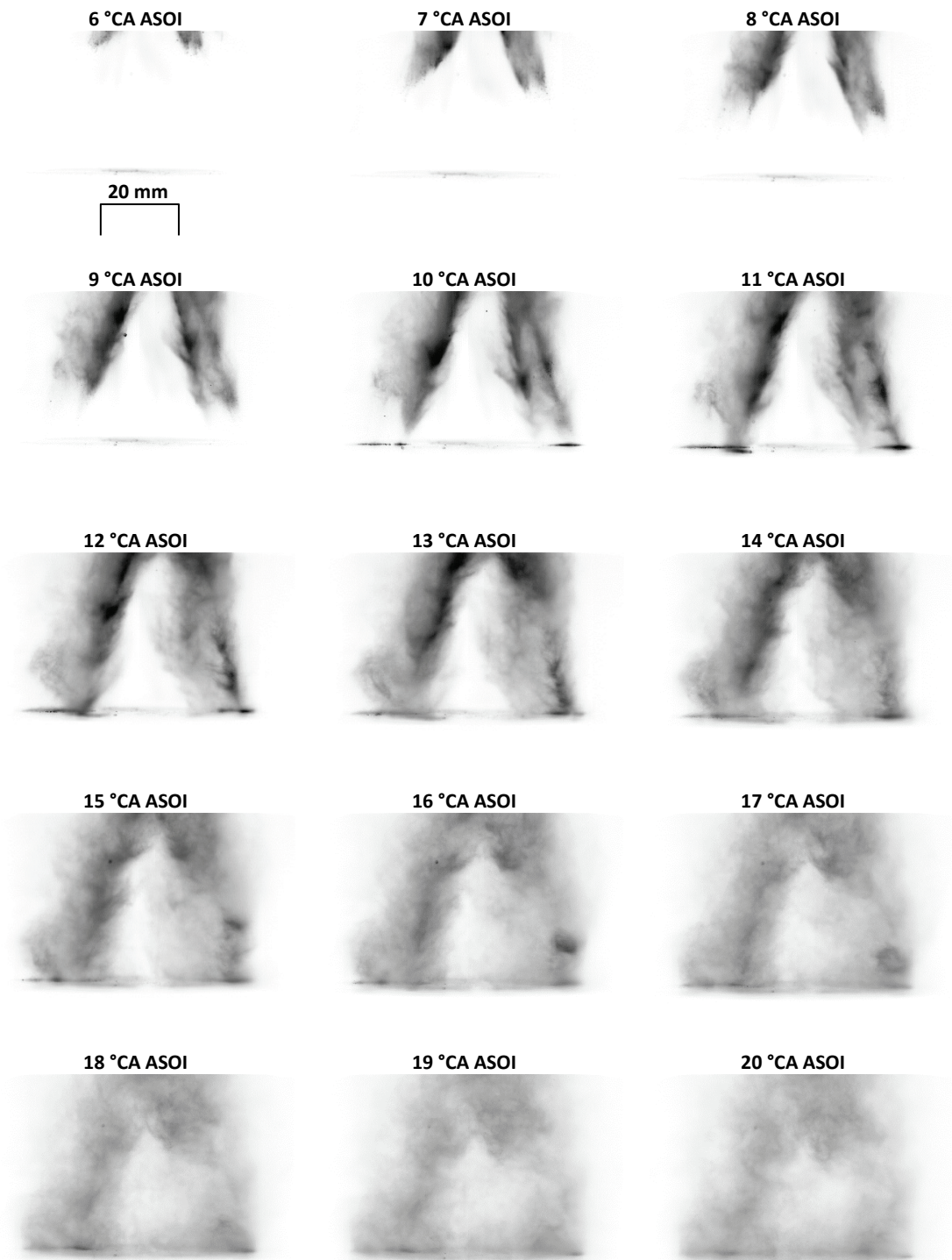
Figure 5.4.7: Fuel injection imaging sequence through piston crown window
(engine speed = 1500 rpm, intake manifold pressure = 0.5 bar, fuel injection = 80 °CA ATDC, λ = 1.0)
-7°C cylinder head and liner conditions, -7°C intake air temperature

Head and Liner Temperature

Figure 5.4.8: Ensemble-averaged imaging sequence of fuel injection through piston crown window at various cranks angles during injection
(engine speed = 1500 rpm, intake manifold pressure = 0.5 bar, fuel injection = 80 °CA ATDC, λ = 1.0)

Head and Liner Temperature

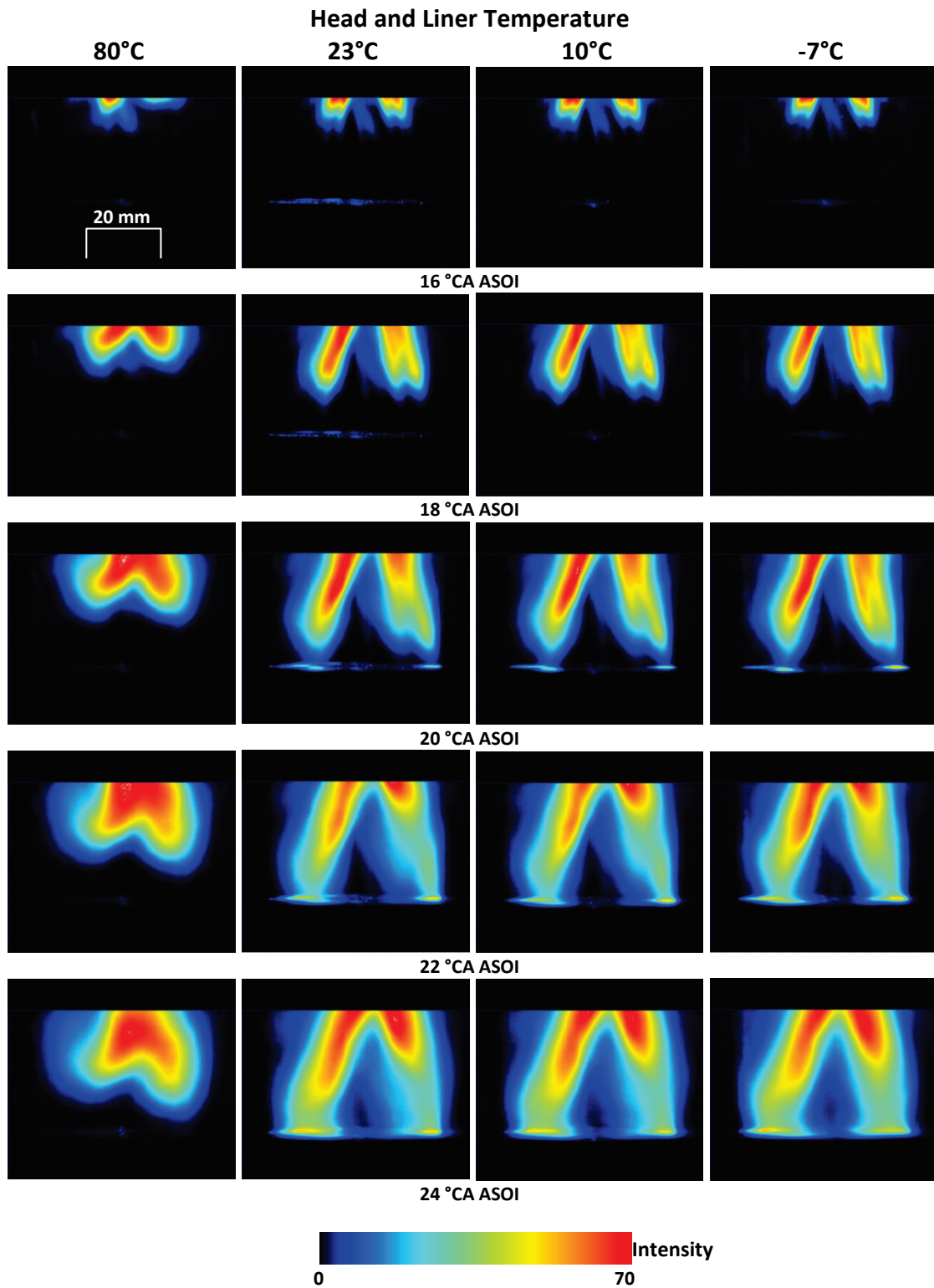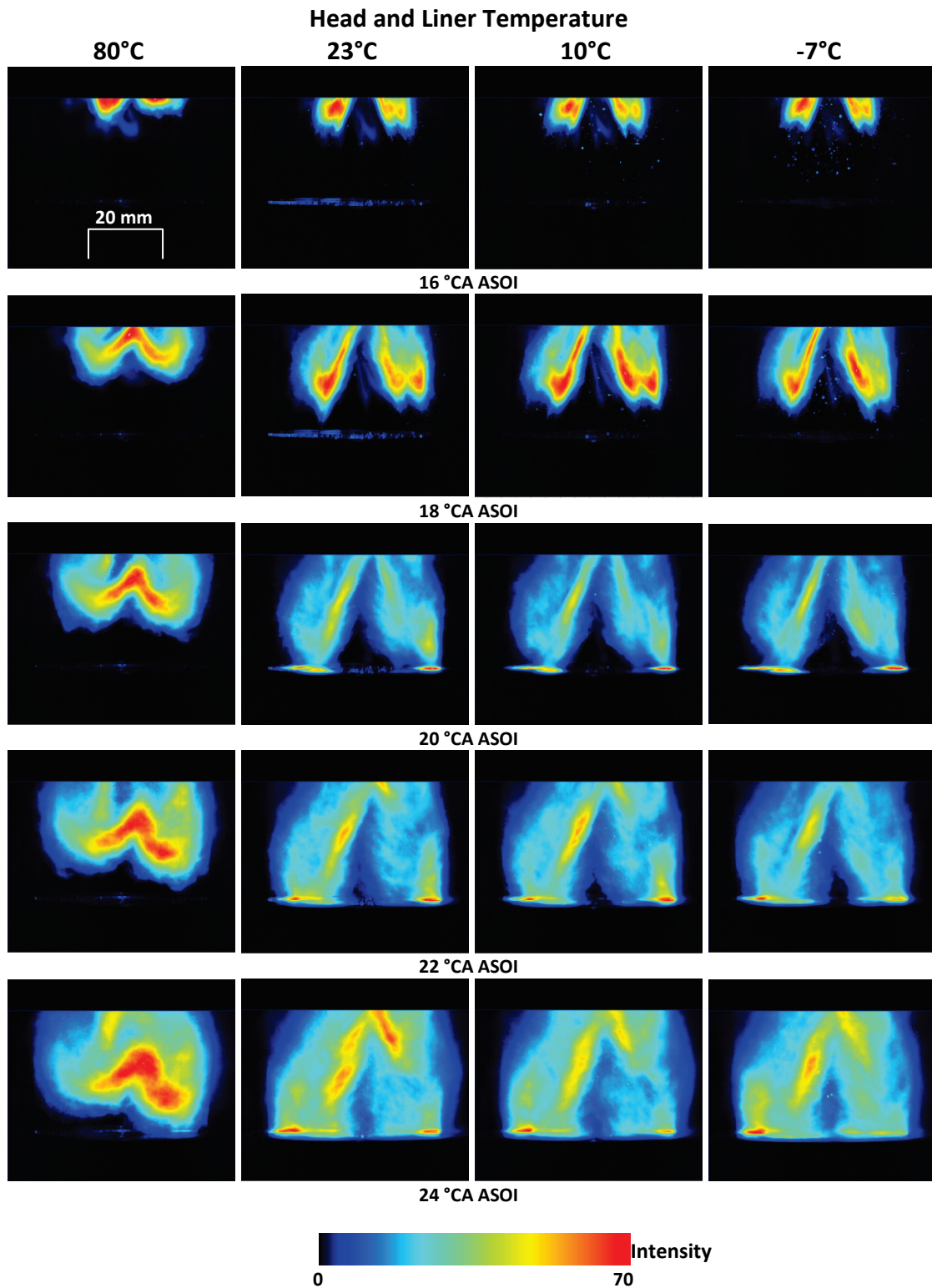Figure 5.4.9: RMS imaging sequence of fuel injection through piston crown window at various cranks angles during injection
(engine speed = 1500 rpm, intake manifold pressure = 0.5 bar, fuel injection = 80 °CA ATDC, λ = 1.0)

5.5   CONCLUDING REMARKS

To better understand the profound effects on the combustion process when an optical DISI was cooled down to an operating temperature of -7°C, the preceding in-cylinder fuel spray process was optically investigated. The same test temperatures were used as the combustion analysis in order to accurately reproduce the conditions and successfully correlate the results. Striking differences were observed in the fuel spray structure between different engine operating conditions and the effects of the in-cylinder flow structures on the fuel spray were also highlighted. The key conclusions from this part of the study are:

1. Flash boiling consistently occurred when the engine was operating at 80°C resulting in a highly atomised fuel spray that penetrated only 30 mm into the cylinder and did not visibly impinge on the piston crown surface. This fuel spray demonstrated a higher level of visible atomisation and was observed to be influenced and transported more by the intake flow structures that were present. This spray structure is a contributing factor in the improved engine performance and flame structure identified in *Chapter 4*.

2. Colder operating temperatures exhibited a very different fuel spray structure that did not flash boil. This structure penetrated much quicker into the cylinder and contained a denser liquid core that consistently impinged on the piston crown surface as early as 10 °CA ASOI. All tested temperatures below 80°C and as low as -7°C show strikingly similar spray structures with only marginal visible differences in structure and penetration depth. This type of spray structure was shown in the previous chapter to result in a lower peak cylinder pressure, poorer combustion performance and the abundance of fuel-rich regions within the flame.

3. Statistical analyses of the fuel spray images illustrated the consistency of the main core of the different plume structures and highlighted the areas of the spray that interacted most with the intake flow structures as having the most variability during the injection process. This demonstrates the important effect that the complex in-cylinder flow structures has on the transportation and vaporisation of the fuel spray as well as the proceeding combustion process.

The complex interaction of in-cylinder flow structures with the fuel spray and combustion processes have been discussed in this chapter and *Chapter 4* and have shown to have a significant effect at all operating temperatures. To further understand and quantify this effect, the next chapter describes the use of optical diagnostics to analyse the in-cylinder flow during the intake and compression strokes of a cold-start strategy used on a production DISI engine as

well as investigating the combustion process to better understand the effects of in-cylinder flow during cold-start.

5.6   CHAPTER 5 REFERENCES

CHARALAMPOUS, G., HARDALUPAS, Y. & TAYLOR, A. M. K. P. (2009) Novel Technique for Measurements of Continuous Liquid Jet Core in an Atomizer. *AIAA,* Vol 47(11), pp. 2605-2615.

HEYWOOD, J. B. (1988) *Internal Combustion Engine Fundamentals,* 1st Ed., McGraw-Hill, pp. 42-61, 205-278, 400-450, 797-819.

LASHERAS, J., VILLERMAUX, E. & HOPFINGER, E. J. (1998) Breakup and Atomization of a Round Water Jet by a High-Speed Annular Air Jet. *Journal of Fluid Mechanics,* Vol 357(1998), pp. 351-379.

RIMMER, J. E. T., DAVY, M. H., GARNER, C. P., HARGRAVE, G. K. & RICHARDSON, D. (2012) Fuel spray structure, flame propagation and charge motion at fuel impingement locations within a DISI engine. *IMechE: Fuel Systems for IC Engines,* Vol 2012, pp. 199-214.

SERRAS-PEREIRA, J., ALEIFERIS, P. G., RICHARDSON, D. & WALLACE, S. (2007) Mixture Preparation and Combustion Variability in a Spray-Guided DISI Engine, SAE Paper 2007-01-4033.

STANSFIELD, P., WIGLEY, G., JUSTHAM, T., CATTO, J. & PITCHER, G. (2007) PIV analysis of in-cylinder flow structures over a range of realistic engine speeds. *Exp Fluids (2007),* Vol 43, pp. 135-146.

WIGLEY, G., GOODWIN, M., PITCHER, G. & BLONDEL, D. (2004) Imaging and PDA analysis of a GDI spray in the near-nozzle region. *Experiments in Fluids 36,* Vol 2004, pp. 565-574.

WIGLEY, G., HARGRAVE, G. K. & HEATH, J. (1998) A High Power, High Resolution LDA/PDA System Applied to Dense Gasoline Direct Injection Sprays. *9th International Symposium on Applications of Laser Techniques to Fluid Mechanics, Lisbon, Portugal*, pp. 9.4.1-9.4.8.

5.7   APPENDIX A

Fuel data sheet for Shell Pura fuel (SPL1995/03) used throughout experimentation.

Owner/Requestor		EN228	GENRL
Description/Ref No		UK	**SPL1995/03**
Description/Ref No			D. Pura
			dye only
Additive info.			
Density @15°C Kg/L		0.720-0.775	0.7243
ISO3675:93/D4052:91			
RVP (Reid Vapour Pressure)	**mbar (hPa)**	S=450-700	574
EN12:94	kPa	W=700-1000	
VLI (10xRVP + 7xE70)			
LEAD	g/L	5mg/L	
TMS401:88/ IP352:90		EN237	
RON		MIN 95.0	95.7
MON		MIN 85.0	87.6
(T) = TRC, (S) = SGS			
DISTILLATION %REC			
ISO3405:88			
IBP	°C		33.1
10%			53.4
20%			62
30%			72.4
40%			86.1
50%			101.8
60%			111.8
70%			118.6
80%			126.9
90%			141.3
95%			150.8
FBP		MAX 210	168.8
Recovery			98.2
Residue		MAX 2	
Loss			
E70		S=20-48, W=22-50	27.9
E100		S=46-71, W=46-71	48.7
E120			72
E150		75 MIN	94.6
E180		S & W = 85 MIN	
E120 - E70			
FIA ANALYSIS (%v)			
Aromatics		42 max	
Olefins		18 max	
Saturates			

Benzene, %v , UK2729-85		1 max.	
GC - CF/STP/36			
C			6.77
H			13.48
O			0
PARAFFINS (%v)	(ALL %v)		7.58
ISO-PARAFFINS			63.53
i +n Paraffins			71.11
OLEFINS			4.41
NAPTHENES			2.47
AROMATICS			21.87
OXYGENATES		2.7 max	0
TOTAL			99.86
Benzene (+ Me CyC5 ene)			0.36
AFR(stoichiometric)			14.74
Enthalpy Comb MJ/Kg (gas)			-43.903
Enthalpy Comb MJ/Kg (liq.)			-43.546
thus, heat of vap. MJ/Kg			0.357
Calculated	H/C		1.99114
	O/C		0.00000
	CWF		0.85682
Sulphur Content, mg/kg			
ASTM D2622-94, (WDXRF, A/43)		150	12
IP 336 (EDXRF, Stanlow)			
MERCAPTAN S, %m/m			
Polar Sulphur mg/kg			
EXISTENT GUM, (IP131)			
Unwashed	mg/100ml		4
Washed	mg/100ml	<5	<1
		ISO 6246	
IR			
ADDITIVE TYPE			
COMMENTS			
INDUCTION PERIOD, mins		360	
(IP40)	100°C		
Copper corrosion		1	
Copper Content, ppb (ug/kg)			
Iron Content, ppb (ug/kg)			
H2S			
WATER UK3367-97 (mg/kg)			
Rusting ASTM D665(mod) (LTP/4)			
Dehazing ASTM D1094(mod) (LTP/3b)		1.5/1/1/1	
APPEARANCE UK 1636			

CHAPTER 6

THE INFLUENCE OF TURBULENT FLOW STRUCTURES ON THE COMBUSTION PROCESS OF DISI ENGINE COLD-START

6.1   INTRODUCTION

The effects of cold-start conditions on the fuel spray and combustion processes were discussed in *Chapters 4 and 5*, which highlighted the detrimental impacts on engine performance and the increase in potential PM generation regions. During the analysis of both the injection and combustion processes, the effects of the in-cylinder flow structures were visibly apparent.

This chapter aims to elaborate on the important influence of the in-cylinder flow structures with the aim of understanding the challenges of cold-start and how to accomplish it efficiently whilst meeting the stringent demands of emissions legislation. It is well understood that the highest concentration of PM emissions in DISI engines occur within the first 100 seconds of the Euro 5 new European drive cycle (NEDC) (Piock *et al.* 2011, Whitaker *et al.* 2011) whilst the engine is still at a cool temperature and during the first transient events.

In the work presented in this chapter, the in-cylinder flow during the intake and compression strokes of a NEDC cold-start process was quantified and analysed. In addition, the proceeding combustion process was analysed utilising high-speed colour optical diagnostics and analysis of the in-cylinder pressure data was performed. This allowed the dynamic stoichiometry of the in-cylinder combustion process to be commented on and correlated with the in-cylinder flow data.

The engine was setup at a temperature of 23°C to simulate an NEDC cold start-up transient cycle. This was achieved by selecting five operating points from the cold start-up and simulating them continuously in steady-state. This enabled a sufficient amount of data to be collected in order to analyse and understand the effects of the transient start-up process. The important test parameters along with a detailed description of the HSPIV setup and error analysis is described in this chapter. A comprehensive description of the complete engine system was given in *Chapter 3*.

Results showed a striking range of flame structures occurring at different times in the start-up cycle with significant differences in flame propagation rates and flame front structures resulting from a wide range of and local AFRs. Analysis of the preceding in-cylinder flow field highlighted clear links between flow structures and the subsequent combustion processes as well as the identification of important turbulence structures that could be enhanced to improve combustion and emissions.

6.2   DISI ENGINE COLD-START STRATEGIES

Several strategies are implemented during DISI cold-start with the ultimate aim of increasing the exhaust gas temperature to achieve catalyst light-off whilst maintaining stable combustion. Retarding the spark timing in SI engines during the warm-up phase of a three-way catalyst (TWC) has been used extensively and has shown to meet the important requirements of increasing exhaust gas temperatures whilst minimising HC emissions before the light-off temperature is reached (Hallgren and Heywood 2003, Eng 2005). This is achieved by minimising the amount of work extracted from the burnt gas, increasing the exhaust temperature. The lower in-cylinder peak pressures reduce the mass of unburnt charge trapped in crevices that are typically oxidised by the flame. A limitation of this method, however, is that cycle-to-cycle variation can increase and the stability of the engine has been shown to decrease (Russ *et al.* 1999, Hallgren and Heywood 2003).

The cold-start process analysed in this chapter contained a two-stage injection strategy. A number of studies (Miyamoto *et al.* 1994, Hattori *et al.* 1995, Ando 1997, Iwamoto *et al.* 1997, Kuwahara *et al.* 1998, Zhao *et al.* 2002) have shown that using a two-stage injection strategy whereby a premixed homogeneous charge is formed during the intake and a rich mixture is created near the spark plug with a subsequent injection, provides a more stable ignition and faster combustion. As a result of the second injection, the exhaust gas temperature is also increased. Kuwahara *et al.* (1998) showed a high luminous diffusion flame from liquid fuel can be observed whilst using this strategy when injecting fuel close to top dead centre (TDC), this can be attributed to the broadband light emission from the incandescence of soot particles in fuel-rich regions.

In addition to these strategies, other important factors contribute to an engine's emissions and stability during start-up. High levels of small-scale turbulence, created from the dissipation of bulk air flow structures (Jarvis *et al.* 2006, Rimmer *et al.* 2009) such as tumble and swirl (discussed in *Chapter 2*) are essential for enhancing the air-fuel mixing process and improving the evaporation of fuel which has impinged onto cold surfaces. Low-speed and transient engine operating conditions, such as those found during engine start-up, typically reduce levels of controlled turbulence and contribute to poorer charge mixture preparation and emissions.

A number of studies have analysed combustion processes, stability and emissions of SI engines during start-up conditions (Kuwahara *et al.* 1998, Yamada *et al.* 2002, Piock *et al.* 2011, Whitaker *et al.* 2011) but there is limited literature that optically analyses cold-start strategies tested on an optical research engine with colour combustion data. This investigation has examined a typical cold-start strategy and optically observed the in-cylinder combustion processes in colour whilst monitoring the in-cylinder pressure. The colour aspect of the optical analysis allows a deeper understanding of the flame's dynamic stoichiometry during the highly variable and complex start-up process of an SI engine. The natural light emission of combustion known as chemiluminescence, allows information regarding flames to be inferred, as these emissions when using hydrocarbon fuels originate from OH*, NH*, CN*, CH*,C_2* and the broadband emission from CO2* (Kuwahara *et al.* 1998, Rimmer *et al.* 2012).

6.3 OPTICAL ENGINE EXPERIMENTAL CONFIGURATION

High-speed colour imaging of the in-cylinder combustion processes was obtained through the quartz optical piston crown as previously shown in the experimental arrangement in *Chapter 4* and detailed in *Chapter 3*. A 105 mm Nikon lens with a wide-open aperture of f2.8 was used to record from the 45° mirror beneath the Bowditch piston, which allowed as much light as possible from the combustion process to be detected without the need for additional illumination and excessive image intensification, in the form of gamma level image correction.

The temperature of the coolant circulating through the cylinder head and liner was controlled with the vapour chiller and set to achieve and maintain an engine operating temperature of 23°C to simulate the typical conditions of a Jaguar Land Rover cold-start test along with an intake air temperature of 23°C. During the recording of high-speed particle image velocimetry (HSPIV) data, the engine was motored without combustion. Fuel injection was also negated as the scattered light from the fuel spray particles obscured the seeding particles. This also allowed the cooled head, liner and in-cylinder charge temperature to remain as consistent as possible.

The pressure data post-processing was completed in the same manner as previous analysis, discussed in *Chapter 4*. Some image intensification was required to clearly reproduce the combustion images for publication due to the lower sensitivity of the colour charge-coupled device (CCD) of the camera. An image gamma correction factor of 0.45 was consistently applied to all combustion images, a method used to improve visual clarity by artificially increasing low light levels in a non-linear representation and enhance images (Svensson *et al.* 2005) .

6.3.1   Experimental Test Point Selection

A typical cold-start strategy was provided by Jaguar Land Rover and a schematic of the first 8 seconds of this strategy are shown in Figure 6.3.1 with detailed parameters given in Table 6.3.2. This type of start-up strategy must draw a careful balance between engine stability, exhaust emissions, exhaust temperature, customer requirements and noise, vibration and harshness (NVH). These factors have been considered when commenting on the quantitative and optical analysis of the engine data.

To simulate the cold-start process, five points were selected that best represented the entire process, the parameters from these points were then run in steady-state operation. The collection of a large amount of data allowed an accurate understanding of the combustion process with the ability to distinguish the combustion effects from engine parameters and due to cycle-to-cycle variation.

Points 1 and 2, which were not designed to be run continuously, were skip-fired due to the amount of excess fuel remaining in the cylinder after each cycle. This was so severe for Point 1 that repeated combustion was not possible due to the overly rich mixture present before spark ignition. This method also enabled repeatable combustion imaging data to be collected across an entire engine run.

The graph in Figure 6.3.1 shows an initial engine cranking period within the first second, after which point the first firing cycle (Point 1) initiates an engine acceleration ramp-up. As this acceleration continues, the crank driven fuel pump starts to increase the common rail fuel pressure (Point 2) until peak pressure is reached and the engine reaches its maximum speed. The peak in engine speed (Point 3) is a customer-driven requirement and does not directly benefit the cold-start combustion process. The next phase of the start-up process focusses on generating high exhaust gas temperatures through a combination of injecting fuel into a pre-existing flame kernel (Point 4) and retarding spark ignition until close to TDC of the compression stroke (Point 5), all of which involve rich combustion. A summary of the selected points and their key attributes is given in Table 6.3.1.

Point 1	Point 2
1. First engine crank motion	1. Engine speed ramp-up
2. Very low fuel pressure	2. Undeveloped fuel pressure
3. Retarded spark	

Point 3	Point 4
1. Engine over-speed (customer-driven)	1. Initial catalyst heating phase
2. Fully developed fuel pressure	2. Double injection
3. Very lean combustion	3. Second injection after ignition

Point 5	
1. Final catalyst heating phase	
2. Double injection	
3. Heavily retarded spark	

Table 6.3.1: Summary of selected points in cold-start strategy
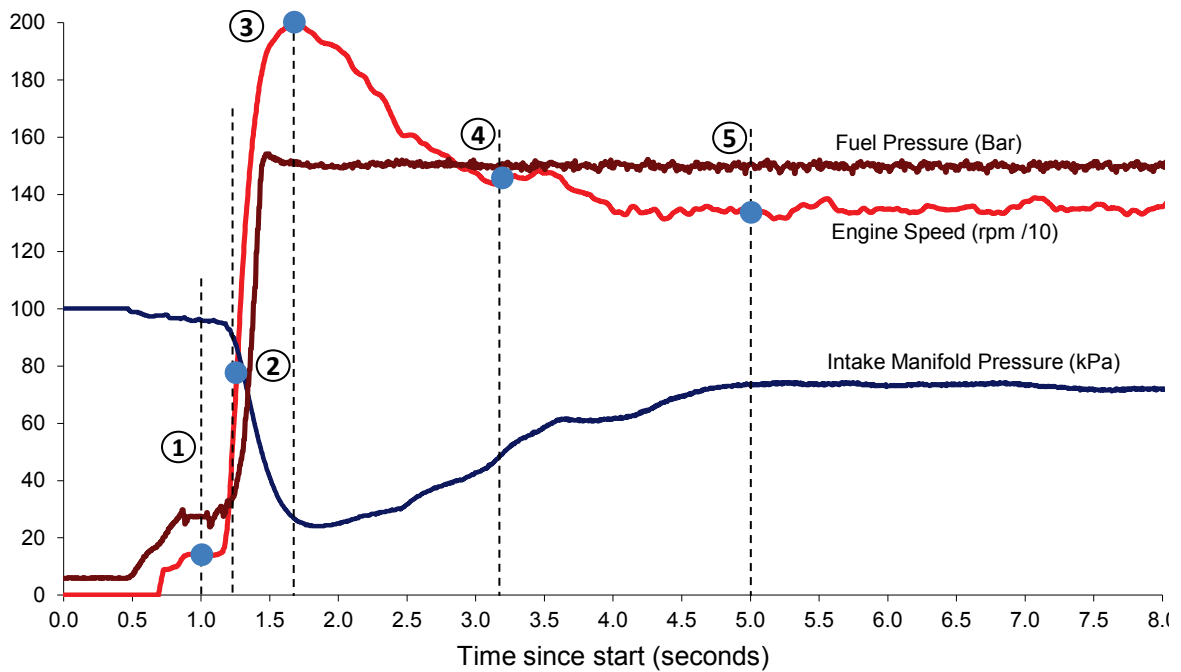
Figure 6.3.1: Schematic graph of cold-start strategy parameters

Engine Test Point	Engine Speed (rpm)	Manifold Pressure (bar)	Injection Pressure (bar)	Injection Timing(s) (°CA)	Spark Timing (°CA)	λ Ratio
1	150	0.96	30	60	335	0.8
2	1500	0.67	80	60	335	1.1
3	2000	0.26	150	60	335	1.5
4	1500	0.5	150	60, 360 (3 : 1)	334	0.7
5	1340	0.74	150	60, 367 (4.5 : 1)	361.5	0.7

Table 6.3.2: Detailed engine test point parameters and timings relative to ATDC of the intake stroke

The next section details the experimental setup of the HSPIV system that simulated the five points from the cold-start process outlined in Figure 6.3.1.

6.4   HIGH-SPEED PARTICLE IMAGE VELOCIMETRY (HSPIV) SETUP

Figure 6.4.1 shows the HSPIV system during engine operation with a detailed experimental arrangement of the individual HSPIV system components on the engine presented in *Chapter 3*. To create a laser sheet with an optimum width of approximately 100 mm and waist thickness of 1 mm within the cylinder, which was measured using a calibration grid within the cylinder, a cylindrical lens with a focal length of -63 mm was used in conjunction with a telescopic spherical lens with an equivalent focal length of 1000 mm. This facilitated the capture of particle images with a size of 60 mm by 90 mm.

Figure 6.4.1: Experimental configuration of PIV system with optical cylinder liner and piston crown

6.4.1   Flow Seeding

Dow Corning 200 silicone oil was used to generate seeding particles due to its high vapour pressure and lubricating properties, which allowed it to be detectable during the compression stroke and lubricate the engine's piston rings at high engine speeds. An important factor for
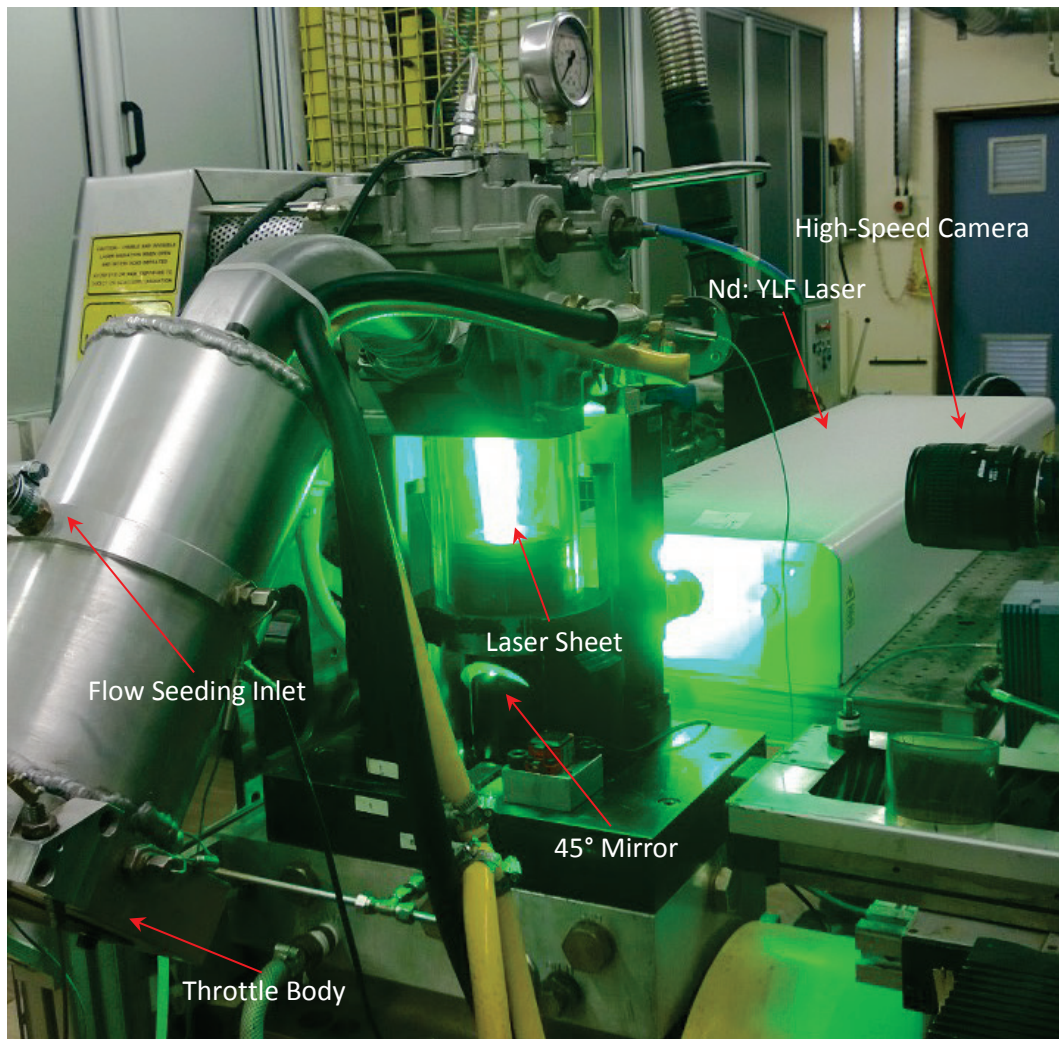
seeding particles is their ability to accurately follow the complex flow that is being measured. Stokes' Drag Law can be used in conjunction with equations of motion for a particle to calculate the viscous drag force being exerted and the associated frequency response of the particle. By neglecting shear effects, the forces due to centripetal acceleration and assuming the seeding particle velocity can differ from the local mean velocity of the fluid by 1%, Drain (1980) showed the radius of the required seeding particle (a_p) is given by

$$a_p^2 < 0.1 \frac{\mu_{fluid}}{f_u \rho_p} \qquad \text{Eqn. (6.4.1)}$$

where μ_{fluid} is the viscosity of the fluid being studied, f_u is the maximum frequency the particles can follow and ρ_p is the density of the seeding particles.

Rearranging the equation and substituting the density of silicon oil, the radius of the seeding particle and the viscosity of air at 300 K yields the result

$$f_u = 0.1 \left(\frac{\mu_{fluid}}{a_p^2 \rho_p} \right) = 0.1 \left(\frac{1.84 \times 10^{-5} [kg \cdot m^{-1} \cdot s^{-1}]}{(0.5 \times 10^{-6})^2 \times 963 [kg \cdot m^{-3}]} \right) \qquad \text{Eqn. (6.4.2)}$$

$$f_u \approx 9.64 \; kHz.$$

Tennekes and Lumley (1972) devised an approximation of the maximum frequency of flow oscillations in an engine to an order of magnitude using the Kolmogorov scale, η_k, defined as

$$\eta_k \cong L Re^{-\frac{3}{4}}$$

where L is approximated as the size of the largest eddies or the width of the flow (Tennekes and Lumley 1972) and given as the engine bore by Heywood (1988). Re is calculated as

$$Re = \frac{uL}{v} = \frac{4.5 \, [m \cdot s^{-1}] \times 89 \times 10^{-3} [m]}{1.539 \times 10^{-5} [m^2 \cdot s^{-1}]} = 26023$$

where u is the mean piston speed (over the typically tested engine speed of 1500 rpm), L is the engine bore and v is the kinematic viscosity of air at 23°C. This yields an approximate maximum frequency of flow oscillations, f_{max}, as

$$f_{max} = \frac{u}{2\pi \eta_k} = \frac{4.5 \, [m \cdot s^{-1}]}{2\pi \; \times 4.344 \times 10^{-5}} = 16.5 \; kHz$$

This shows that maximum of flow oscillations expected in the engine are of the same order that the silicone oil particles are capable of following but are somewhat higher in magnitude. It has been shown that the highest frequency turbulent structures with integral length scales up to 10 mm have been measured in IC engines with frequencies above 600 Hz when cut-off filtering techniques have been applied (Li *et al.* 2004, Rimmer *et al.* 2009). These high-frequency turbulent components are generated during compression and peak around the time of TDC around the spark pent-roof and spark plug area. The presented flow fields focussed on analysing the low-frequency in-cylinder bulk flow structures with a resultant spatial resolution of 0.060 by 0.060 mm/pixel. Furthermore, the intake stroke and early compression stroke were focussed on and flow measurement through the pent-roof window was omitted. This indicates that the maximum frequency flow oscillations have not been measured in the presented HSPIV images due to spatial averaging and any error associated with the seeding particles' ability to follow this flow can be negated within the scope of this study.

6.4.2 Diffraction Limited Particle Imaging

To provide an accurate assessment of particle displacement in digital particle image velocimetry (DPIV) requires control of the particle images recorded on the imaging sensor. Recording an extended two-dimensional flow field results in light waves from the scattered particles diffracting with each other and creating a diffraction pattern (Airy disc) that defines the theoretical maximum resolution for an optical imaging system.

The diffraction limited spot size, d_{diff}, represents the diffraction pattern created by the scattered light of the seeding particle required to accurately detect particles-shift and calculate flow velocity. It is calculated from the equation (Raffel *et al.* 2007)

$$d_{diff} = \sqrt{(Md_p)^2 + (2.44(M + 1)f^\# \lambda)^2}$$ Eqn. (6.4.3)

where d_p is the diameter of the seeding particle, $f^\#$ is the f-number of the camera lens, λ is the wavelength of the laser light and M is the magnification factor, calculated from

$$M = \frac{A_c}{A_i}$$ Eqn. (6.4.4)

where A_c is the camera chip size and A_i is the imaged area size.

Table 6.4.1 lists the parameters used to calculate an estimate of the diffraction limited spot size.

Parameter	Symbol	Units	Result
Magnification Factor	M	-	0.08
Seeding Particle Diameter	d_p	μm	1
F-number	$f^\#$	-	8
Wavelength	λ	nm	527
Diffraction Limited Spot Size	d_{diff}	pixels	2.34

Table 6.4.1: Calculated diffraction limited spot size

The calculated diffraction limited spot size lies meets the optimum size range requirements of at least 2-3 pixels, close to the optimum of 2.5 pixels (Raffel *et al.* 2007) and 2.8 pixels (Anandarajah 2005). This allowed errors in particle displacement (and therefore velocity) to be minimised by avoiding peak-locking, whereby a correlation peak is only 1 pixel wide and locks location to an integer pixel offset (Anandarajah 2005). Particle clipping was also minimised, whereby a particle of too large a size (greater than 3 pixels) is clipped out of the interrogation region, resulting in skewed particle displacement (Anandarajah 2005).

6.4.3 HSPIV Image Recording, Processing and Sources of Errors

The primary aim of the HSPIV investigation was to quantify the flow structures during the intake and compression strokes prior to spark ignition in order to understand the influence they have on the subsequent flame growth. Recording of the flow field during the combustion process, although not required, was not readily available as the silicon seeding particles were vaporised by the propagating flame front. It is well understood that the in-cylinder charge motion prior to spark ignition has a dominant effect on the initial flame growth and the turbulence during this time has been shown to have a strong correlation with MFB times up to 5% (Bianco *et al.* 1991, Johansson 1991, Pajot and Mounaïm-Rousselle 2000, Rimmer *et al.* 2009)

Due to the range of engine speeds tested in the cold-start strategy and the limitations of the camera memory and record-rate, a different number of PIV images were recorded for each engine run in each data point. To ensure an adequate number of recorded cycles to yield an accurate representation of the mean in-cylinder flow field, at least three engine runs, equating to approximately 300 engine cycles, were recorded for each data point. The PIV rate was kept constant at 1.5 kHz and in-cylinder flow data was recorded from 60 °CA ATDC to 320 °CA ATDC (relative to the intake) as this was when the flow field was visible to the camera. Table 6.4.2 lists the PIV parameters for each data point.

Engine Test Point	Engine Speed [rpm]	Seeding Pressure (and jets) [PSI]	Image Pair dT [μs]	Recorded Images Per Cycle	Crank Angle Change Per Frame [°CA/frame]
1	150	10 (2)	200	58	4.5
2	1500	20 (6)	20	43	6
3	2000	20 (6)	10	33	8
4	1500	20 (4)	20	43	6
5	1340	20 (4)	25	49	5.4

Table 6.4.2: Detailed engine test point parameters and timings relative to ATDC of the intake stroke

Each of these parameters represents a source of systematic bias and random errors within the PIV measurement. Considerable past research has been devoted to minimising these errors by identifying and optimising experimental parameters critical to obtaining accurate PIV data (Keane and Adrian 1990, Lawson 1995, Mergerle and Sick 2002, Anandarajah 2005, Raffel *et al.* 2007, Rimmer 2010). The following section discusses the optimisation of these parameters and experimental considerations in order to minimise the impact of these errors.

The HSPIV vector calculation was performed using cross correlation in DaVis with no pre-processing of the raw images or post-processing of the vector fields. A geometric mask was created to shroud the moving piston and avoid any scattered light being detected in the PIV calculation. The cross-correlation routine in DaVis, like most commercial PIV systems, generated the correlation plane in the frequency domain using fast Fourier transforms (FFT). FFTs reduce the computational processing demand with only a small increase in error (Raffel *et al.* 2007), which is beneficial when processing large quantities of temporal PIV data, as with the completed engine HSPIV. A final multi-pass interrogation region size of 16 x 16 pixels was used, equating to approximately 5950 velocity vectors when the cylinder was unobscured by the piston at BDC. An interrogation region that reduced in size was used in DaVis (from 64 x 64 to 16 x 16 pixels) to capture and compensate for particle displacement across different integration regions. This final interrogation region size was chosen to capture any complex flow features, such as vortices, which are typically present within in-cylinder engine flow. The complex nature of engine flow can also produce large velocity gradients that can cause problems in generating a well-defined correlation peak. Peak splintering, whereby the velocity correlation splinters in to a number of peaks can induce errors, as only the highest correlation peak is used to calculate the particle velocity. Maintaining a relatively small interrogation window size of 16 x 16 pixels helped to reduced peak splintering in areas such as cylinder wall boundary layers and intake valve jet flow.

Throughout testing, the strengths of the particle correlation peaks were monitored to ensure that all test parameters remained optimal. Figure 6.4.2 shows an arbitrary three-dimensional vector shift plot from a 32 x 32 pixel interrogation region, highlighting a single strong Gaussian peak from the cross correlation routine. The analysed vector is within a dominant bulk flow structure driven by the intake valve jet flow interaction with the cylinder wall.
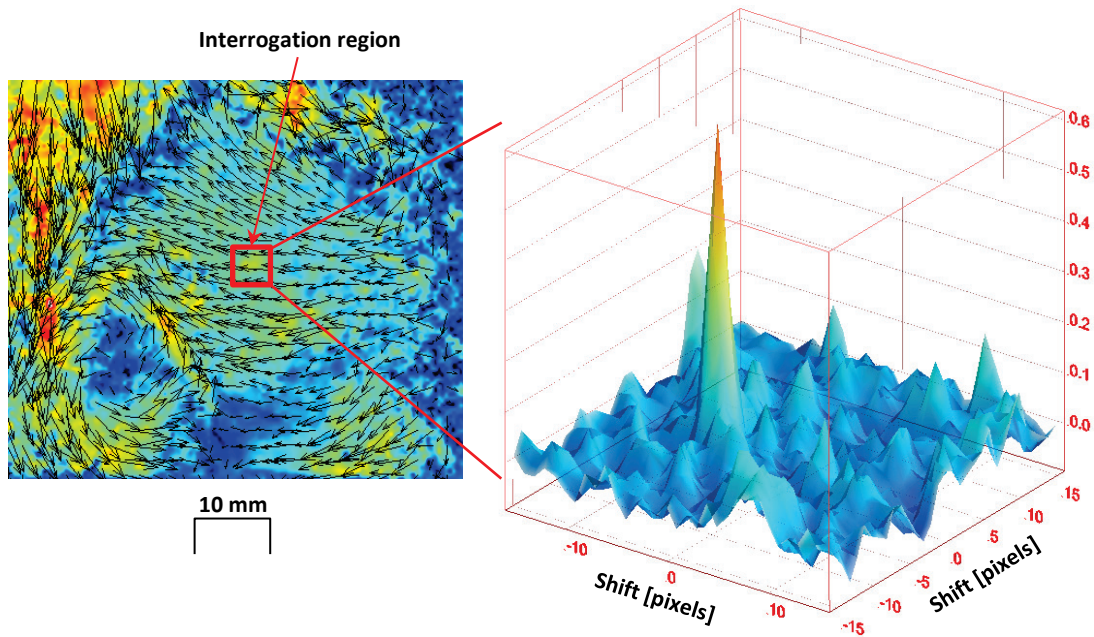

Figure 6.4.2: Pixel shift plot for an arbitrary vector (Point 3) within a 32 x 32 pixel interrogation region

As Table 6.4.2 listed, the seeding pressure and number of jets used in the atomiser was varied in order to maintain an optimum seeding density of approximately 6-8 particles per 16 x 16 pixel interrogation window region. The image pair separation ΔT was also optimised to keep the particle displacement less than a quarter of the 16 pixel interrogation window size, which minimised the amount of out-of-plane displacement across the thickness of the 1 mm laser sheet. The complex three-dimensional nature of the in-cylinder flow consisted of highly-turbulent flow structures with high degrees of curvature, which increased the prevalence of out-of-plane displacement. Optimisation was of paramount importance to avoid bias to lower velocity particles (as higher velocity particles are more likely to leave the interrogation window and plane).

The imaging of PIV image pairs through the curved surface of optical cylinder liner can produce image distortion near the edges of the cylinder where the angle of incidence is at its highest. Reuss *et al.* (2002), however, calculated and demonstrated on a similarly sized optical engine that correlation detection and successful vector production remains above 90% in the central

66 mm region around the cylinder centreline for a similar sized optical engine cylinder. As the recorded velocity vector fields had a width of 60 mm, no distortion correction was applied to the seeding images.

In order to establish a more detailed understanding of the bulk flow motion, the individual flow fields were ensemble-averaged. The ensemble average represents the global motion of flow and was calculated over at least 100 engine cycles at each test point. The DaVis software performed the calculation using the following equation that was applied to each vector field such that

$$\overline{U}_{(\theta,x,y)} = \frac{1}{n}\sum_{i=1}^{n} U_{(\theta,i,x,y)}$$

Eqn. (6.4.5)

where $\overline{U}_{(\theta,x,y)}$ is the ensemble average velocity at crank angle θ, position *x*, *y* and $U_{(\theta,i,x,y)}$ is the instantaneous velocity of cycle for n cycles.

The recording of temporal PIV data facilitated the use of Reynolds decomposition to describe the in-cylinder turbulent velocity fields. This method decomposes the flow into low-frequency bulk motions (ensemble-averaged flow) and high-frequency fluctuations (turbulence intensity). The turbulence intensity, or root mean square (RMS) velocity fluctuation, $u'(\theta)$ was calculated over at least 100 engine cycles at each test point in the DaVis software using the equation

$$u'(\theta) = \sqrt{\overline{(U - \overline{U})^2}} = \sqrt{\frac{1}{N}\sum_{i=1}^{N} (U_{(\theta,i,x,y)} - \overline{U}_{(\theta,x,y)})^2}$$

Eqn. (6.4.6)

The following sections have analysed and correlated the results from the in-cylinder pressure transducer data and combustion imaging before investigating the recorded and processed vector fields, which have been used to help further deduce and understand the flame's complex structure and interaction with the unburned charge and interaction with the fuel injection process.

6.5 IN-CYLINDER PRESSURE MEASUREMENTS

This investigation has examined a typical cold-start strategy and optically observed the in-cylinder combustion processes in colour whilst monitoring the in-cylinder pressure and HC exhaust emissions. The colour aspect of the optical analysis allows a deeper understanding of the flame's dynamic stoichiometry during the highly variable and complex start-up process of an SI engine. The natural light emission of combustion known as chemiluminescence, allows information regarding flames to be inferred, as these emissions when using hydrocarbon fuels originate from OH*, NH*, CN*, CH*, C2* and the broadband emission from CO2* (Kuwahara *et al.* 1998, Rimmer *et al.* 2012).

Mean in-cylinder pressure traces for all test points and a histogram of the mean peak pressures are illustrated in Figure 6.5.1 across 300 engine cycles (relative to after top dead centre (ATDC) of the compression stroke). The upper graph highlights the distinct differences and distribution of peak in-cylinder pressures achieved within the first few seconds of the start-up cycle with a range from 3.20 bar at Point 3 to 15.99 bar at Point 2.

There was also a notable difference in the location of the peak pressure, which is due to parameter scheduling as well as the nature of combustion structures. Point 2 has parameter scheduling which is more typical of the Jaguar Land Rover standard test point optimised for homogeneous stoichiometric combustion and has been used on previous research on the engine (Long *et al.* 2008, Rimmer *et al.* 2009, Rimmer *et al.* 2012, Efthymiou *et al.* 2013). A smooth rise in pressure during the compression stroke is continued after an optimised spark timing, this delivers a maximum in-cylinder peak pressure (located at 30°CA ATDC) and extracts the most amount of work from the cylinder with a near-stoichiometric λ ratio recorded at 1.1. During the initial acceleration ramp-up of an engine, maximising work from the engine is particularly important. Once a faster speed is achieved, mechanically driven pumps such as the fuel pump for example, can deliver the optimum pressure to the fuel rail required for correct fuel atomisation and subsequent idealised combustion. Despite the fuel pressure not being fully developed, resulting in poor atomisation and sub-optimal combustion (discussed in the next section), work extraction has been maximised for this point.
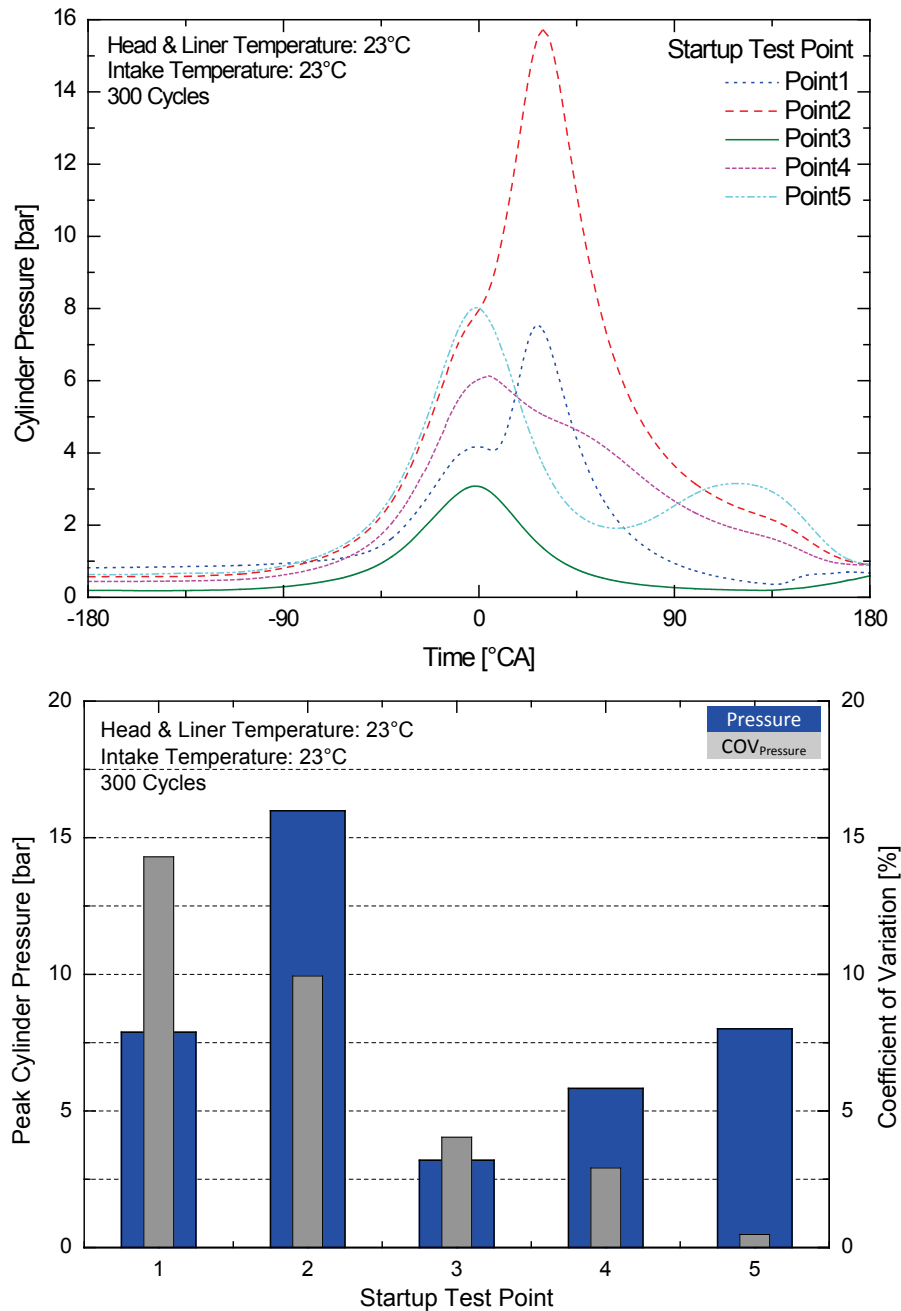
Figure 6.5.1: Mean in-cylinder pressure profiles and peak cylinder pressure bar graphs and corresponding COVs for points tested along the cold-start cycle at 23°C cylinder head, liner and intake conditions

The first firing cycle (Point 1) exhibits an interesting pressure trace in which two peaks are seen occurring at TDC and 30°CA ATDC that is similar to the premixed and main combustion peaks commonly seen in Diesel engines (Heywood 1988, Sahoo *et al.* 2009). It is likely that the very low engine speed and resulting flame speed and structure produced a burn rate lower than that of typical premixed turbulent combustion. The second peak, however, does show that some useful work has been extracted from the cylinder which is required to initiate successful operation of the engine after cranking.

The pressure distribution of the remaining three points of the start-up are similar in the fact that less work is extracted from the cylinder due to the injection and spark scheduling. This produced a peak pressure at TDC of 3.07 bar, similar to mechanically motored piston compression. Point 3 was observed to have unstable lean combustion when run continuously on the optical engine. This point is known to be a customer-driven rapid increase in engine speed and noise so can be assumed to serve no specific benefit to engine emissions or exhaust temperature. A recorded λ ratio of 1.5, however, outlines why combustion instability could have occurred, excess air may have provided an overly lean charge mixture which prevented the flame from successfully propagating. A possible reason for this seemingly lean parameter setup is the presence of excess fuel which was present after combustion in Point 2, requiring skip-firing during testing. This excess fuel will subsequently be present in the cylinder for Point 3. The in-cylinder optical analysis will provide a further insight into this.

Points 4 and 5, from their parameters, can be identified as catalyst warm-up points both with different natures as to how exhaust temperature is generated. Both points use a large amount of fuel injected twice per cycle and in different ratios to combust at a very rich λ ratio of 0.7. The pressure trace for Point 4 demonstrates this late burning with a characteristic low-gradient pressure trace 'tail-off' during the exhaust stroke. Point 5 also exhibits an interesting pressure trace during exhaust which occurs much later. This is due to further retarded spark scheduling that causes combustion to occur after TDC and into the exhaust stroke. Point 5 forms the main period of the catalyst heating phase and entails a higher manifold pressure and a further retarded spark than Point 4 to generate a larger quantity and flow rate of high temperature gas during the exhaust stroke.

The lower graph in Figure 6.5.1 illustrates the mean peak pressures on a histogram and is overlaid with their corresponding coefficients of variation (COV). The COV parameter is a measure of the cycle-to-cycle variability (defined as the ratio of the standard deviation to the mean) of a certain parameter and gives a good indication to engine stability. A distinct correlation was seen between the time from engine start and COV with the last three points having lower COV values. As the final three points generated much lower peak pressures because of the combination of retarded ignitions and partial-burn characteristics, it is reasonable to assume that the COVs in these cases indicated mechanical piston compression variations, which is inherently very low.
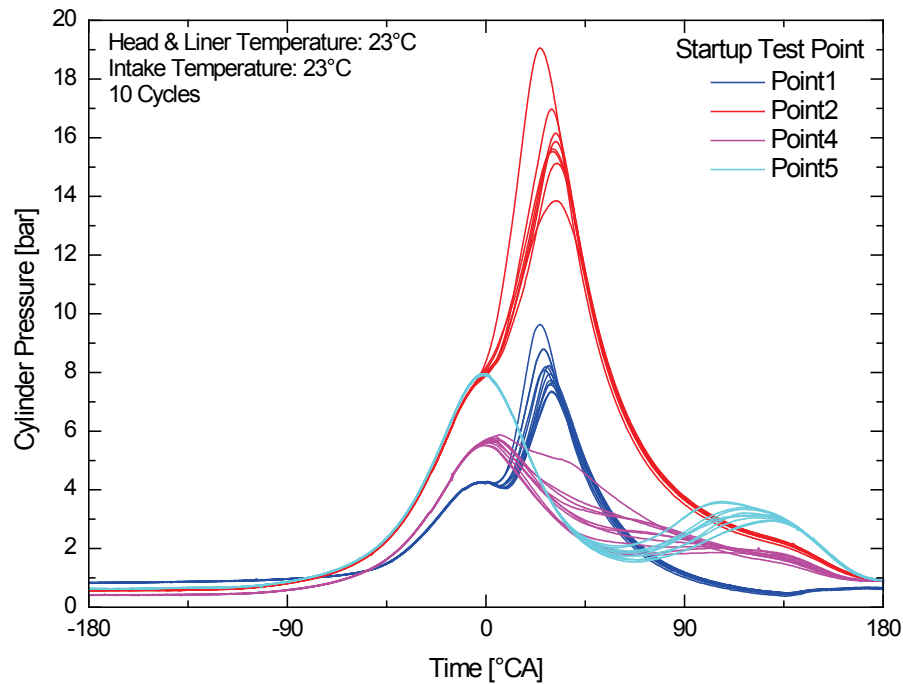
Figure 6.5.2: In-cylinder pressure profiles for 10 arbitrary engine cycles tested along the cold-start cycle at 23°C cylinder head, liner and intake conditions

To help understand the relatively high COV of pressure and IMEP values (discussed later in this section), the graph in Figure 6.5.2 illustrates arbitrary raw pressure traces for 10 arbitrarily selected cycles at Points 1, 2, 4 and 5. The general trend of the pressure trace was fairly consistent for Points 1 and 2, but large differences in peak pressure of up to 3 bar and 5 bar respectively were apparent. Points 4 and 5 on the other hand, exhibited consistent peak pressures to each other with variations in gradient during the expansion stroke, which indicated inconsistencies in combustion, which are discussed in analysis of the combustion imaging.

A better indication of combustion stability is IMEP, which is illustrated in Figure 6.5.3 and is overlaid with their COVs for each point. As expected, the IMEP values themselves mostly correlate with the peak cylinder pressure data, highlighting the work produced by the first two points. The first two points show COVs of 5% and below, indicating good stability, as would be expected from premixed, early-spark conditions that are designed to maximise piston work. The COV of Point 3, can be considered anomalous, due to negligible work being generated above mechanical-piston work, this is further elaborated upon when the in-cylinder combustion is observed in the next section. When the spark is retarded in Points 4 and 5, however, the overly rich and poor combustion performance leads to much lower combustion stability with COV values peaking at 60%. The subsequent in-cylinder combustion imaging elaborates on these identified trends.
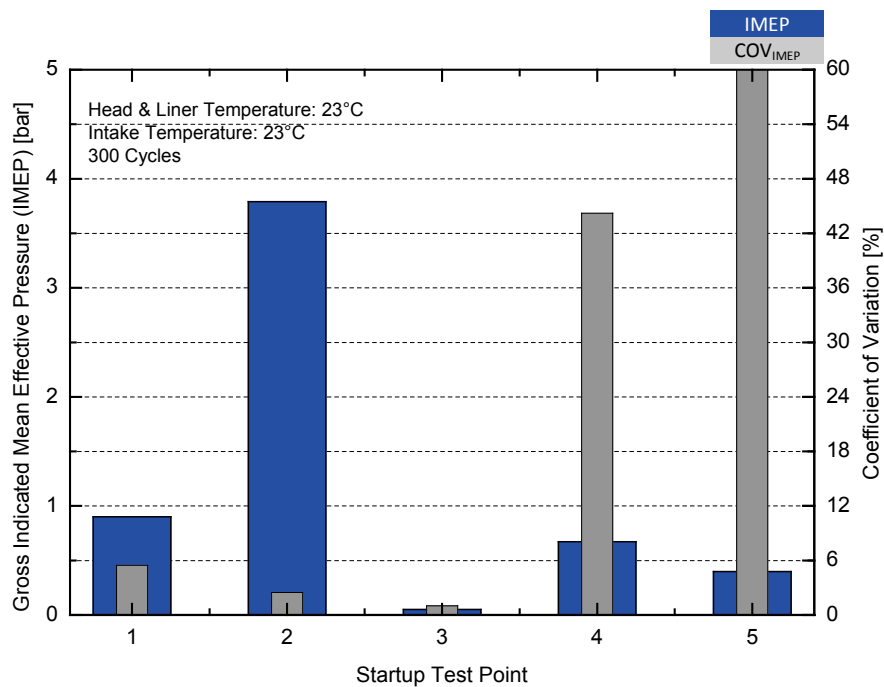
Figure 6.5.3: Mean gross IMEP and corresponding COVs for start-up points 1, 2,4 and 5 at 23°C cylinder head, liner and intake conditions

Figure 6.5.4 presents MFB times for Point 1, 2, 4 and 5 which represent the time taken for each change in pressure with crank angle (dp/dθ) to reach either 10%, 50%, or 90% of the total mass burned. Point 3 has been omitted as the unstable combustion produced times exceeding reasonable tolerances, this indicates that the charge in the cylinder had very little effect over the natural in-cylinder pressure when the engine is motored. The graph shows that Points 1 and 2, despite using a fuel pressure that is not fully developed, produced burn times faster than those of points and 5 (up to 50°CA in the 90% MFB case) and similar to those in a similarly configured engine at 23°C with a fuel pressure of 150 bar (Rimmer *et al.* 2009, Efthymiou *et al.* 2013). This highlights the dominant effect that injection and ignition scheduling had on the latter points in the aim of generating exhaust temperature and the slower burn rate was not detrimental to the primary aim of generating high exhaust temperatures. The COVs of the presented data show the adverse effect of cycle-to-cycle variability on the burn rate of the Point 1. The detrimental effect of scheduling parameters to generate exhaust heat can also be seen in Points 4 and 5, despite having a fully developed fuel rail pressure and well established in-cylinder turbulence at these speeds (Long *et al.* 2008, Rimmer *et al.* 2009). The effect of parameter scheduling on flame kernel creation, growth and speed has been investigated in the next section and aims to build a further understanding upon what has been observed from the in-cylinder pressure data.
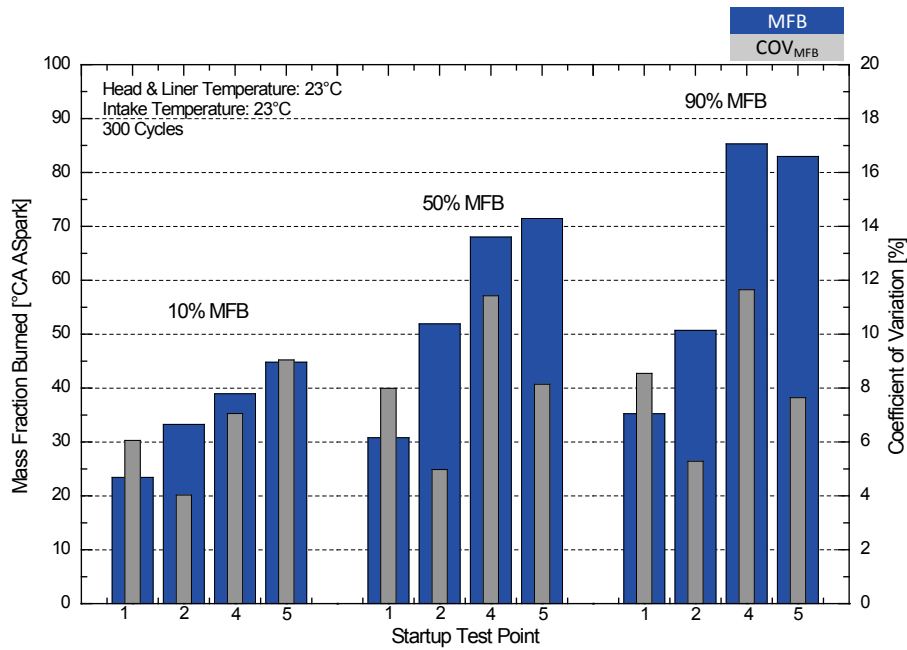
Figure 6.5.4: Mean mass fraction burned to 10%, 50% and 90% times after ignition timing (AIT) and corresponding COVs for start-up points 1, 2,4 and 5 at 23°C cylinder head, liner and intake conditions

6.6 IN-CYLINDER COLOUR COMBUSTION IMAGING

To better understand the nature of combustion and the wide range of parameter configurations encountered during start-up, a sequence of in-cylinder combustion images have been presented from the point after ignition timing (AIT). The crank angle between the images varies from 1 °CA to 6 °CA depending on the flame speed. This range allowed the capture of early flame kernel growth and the combustion of the remaining visible unburned charge up to the cylinder walls. A schematic of the imaging region and the orientation of the valves, injector and spark plug are the same as *Chapter 4* and outlined in *Chapter 3*. Images of all five selected points in the start-up have been presented in order to analyse the unique range of occurring combustion structures Figure 6.6.1 to Figure 6.6.5.

The early flame kernel was visible in all points of the test matrix but varied significantly in shape and the way it initially propagated through the combustion chamber. The initial displacement of the flame is important in the subsequent consumption of the charge and the interaction with in-cylinder turbulence scales. High-speed particle image velocimetry (HSPIV) research has shown that due to the arrangement of the intake ports and pent roof combustion chamber in this type of engine, there is a global flow motion across the spark plug towards the exhaust side of the cylinder near TDC (Rimmer *et al.* 2009). Evidence of this flow motion was visible in all test points apart from Point 1, with the global convection of the flame towards the exhaust side of the cylinder during the expansion stroke. The low engine speed at Point 1 and resulting weaker tumble motion due to less flow energy conserved during the compression stroke significantly reduced this flame convection (Figure 6.6.1).

The flame propagation of Point 1 (Figure 6.6.1) was clearly distinct from typical SI combustion behaviour, in that a laminar flame kernel was seen propagating at a relatively slow rate and took 13 °CA, 14.3 ms after ignition to reach the cylinder walls, compared to a typical turbulent combustion time of around 4 ms (Efthymiou *et al.* 2013). A light blue and smooth unwrinkled flame front was observed throughout the flame's expansion in the cylinder. This was the primary light emission from OH, CH and C_2 (Kuwahara *et al.* 1998, Rimmer *et al.* 2012) and is typical of premixed stoichiometric combustion. In the centre of the flame, orange and white high-luminous regions were observed increasing in intensity as the flame progressed. These features are indicative of the natural infra-red light emission of soot particles formed within fuel-rich regions of the flame. A single ligament of slow-burning fuel was consistently observed near the injector and spark plug region throughout the recorded engine cycles. This feature was potentially an area of fuel impingement on cold surfaces in the pent roof region, likely on the spark plug electrode. Poor atomisation and the spray shape of the fuel at a low injector pressure were the most likely causes of this fuel ligament. An investigation by Berndorfer *et al.* (2013) in a DISI engine, showed similar results in DISI at low injection pressures, which led to the formation of diffusion flames due to poor charge mixing and impingement. These high luminous fuel-rich regions are known sources of soot generation which have the potential to contribute greatly to PN emissions (Gupta *et al.* 2000). The rich areas of the flame continued to burn past the presented images, through the expansion stroke and into the exhaust stroke of the engine.

For Point 2 (Figure 6.6.2), as the engine ramped up in speed along with the fuel rail pressure, a much quicker flame speed was observed that reached the cylinder walls in 42 °CA, 4.6 ms AIT. The highly wrinkled turbulent flame had a blue stoichiometric flame front which interacted with the unburned charge to achieve a more rapid rate of consumption. These small scale high-frequency turbulence structures, generated in the compression stroke are well understood and are of paramount importance to rapid flame propagation in SI engines (Heywood 1988, Rimmer *et al.* 2009). Despite having a recorded overall lean λ ratio at the exhaust of 1.1, a large quantity of rich regions in the form of slow burning liquid droplets and ligaments were seen throughout the presented images in (Figure 6.6.2). This suggests that not all of the in-cylinder charge was completely combusted by the time of exhaust. The visible burning liquid droplets (which had burning regions with an average diameter of approximately 1.5 mm) remained visible throughout the expansion stroke and are known sources of soot generation as their high carbon-to-oxygen ratio results in carbons atoms that can nucleate to form particulate matter (PM) (Price *et al.* 2006). At this test point, the fuel rail pressure was

only at half of its maximum, inhibiting the proper atomisation of the fuel as well as the correct spray penetration and divergence into the cylinder during injection. The presented optical results emphasise the importance of achieving a maximum rail pressure in DISI engines as soon as possible due to the dominant effect the fuel spray can have on the subsequence combustion event.

Point 3 (Figure 6.6.3) used injection and ignition scheduling parameters similar to those of typical stoichiometric operation but with a highly throttled air intake to produce a very lean λ ratio of 1.5. The combustion images for this condition showed an abundance of blue light emission at a very low light intensity with very few fuel-rich regions and soot incandescence present. This indicated premixed stoichiometric combustion at the flame front and in areas of the flame during the entire consumption of the unburned charge. Over several engine cycles, however, a large amount of dissimilarity was apparent in the shape and structure of the flame and the way it propagated, indicating that the flame had reached its lean limit in areas (Heywood 1988). This highlighted the combustion instability that was present during this test point and that was detected previously in the pressure data. A potential reason for this instability was the steady-state method in which this test point was run. It is reasonable to assume that because the initial three test points are scheduled to occur only once during the start-up strategy, they may be affected by residuals left in the cylinder from the previous cycle. During testing of Point 2, excess fuel was certainly present in the cylinder after exhaust due to the poor atomisation of fuel, which remained in crevice regions. This excess fuel may have been enough to increase the AFR of the flame above its lean limit in Point 3 and restore stability when run in transient operation.

The remaining test points of the start-up strategy were focussed on generating high exhaust temperatures by retarding ignition and injecting large quantities of fuel in more than one injection event per cycle. These test points were run continuously without skip-firing as they were intended. Point 4 was unique in the fact that a flame kernel was first established, in a homogeneous charge combustion mode, before another injection took place into the flame itself. The second image at 42 °CA (4.8 ms AIT) in Figure 6.6.4 showed the second fuel spray when it was first detectable. The rich flame kernel was initially disrupted by the un-ignited fuel spray jet, which began to ignite and combust as the jet dispersed into the cylinder. The ignited fuel jets, which were the regions of highest luminosity, were clearly visible from 46 °CA (5.3 ms) AIT until 62 °CA (7.1 ms) AIT. The following images showed an orange and white highly luminous diffusion flame burning slowly towards the centre of the combustion chamber until it was subsequently exhausted. This region was likely to be a dominant soot generation region

contributing to PN. From the presented images and published literature, it is reasonable to assume that the second fuel injection helped maintain a rich region at TDC providing more stable ignition and faster combustion. This would assist in the burning of the charge and maintain stability when injection and spark scheduling are not optimised for engine performance.

Point 5 retarded the flame ignition to near TDC and used a wider throttle to maintain a λ ratio of 0.7 whilst injecting an increased quantity of fuel. The effect of retarding ignition was immediately seen in the flame images with a flame speed that was noticeably slower (Figure 6.6.5). This due to the fact that combustion was not taking place within the peak concentration of high-frequency turbulent flow structures towards the end of the compression stroke. A second injection occurred around the time of spark ignition but was not detectable in the images since the flame kernel had not fully established by this point due to ignition delay.

The slower flame structure in Point 5 had a distinct blue stoichiometric flame front as it propagated towards the cylinder liner wall, which took approximately 11 ms. Slow burning liquid fuel droplets were detected from early in the flame kernel growth that could have been caused by a combination of excess fuel in the cylinder and the second fuel spray near TDC, which was likely to impinge on the piston crown. The peak luminosity of the flame throughout combustion was lower than that of Point 4 indicating that the local AFRs throughout the flame were lower despite the global λ ratio being the same. As with Point 4, the flame had poor homogeneity in its structure.

The next section aims to elaborate on the variety of observed flame structures by analysing the in-cylinder flow field during the intake and compression stroke up to the point of spark ignition. The intake stroke flow field is particularly important in further elucidating the mechanisms of fuel droplet transportation, mixing and vaporisation during conditions that lead to poor fuel atomisation.

Figure 6.6.1: Flame imaging sequence of cold-start Point 1 through piston crown window (engine speed = 150 rpm, intake manifold pressure = 0.96 bar, fuel injection = 60 °CA ATDC, ignition timing = 349.5 °CA ATDC, λ = 0.8)
23°C cylinder head and liner conditions, 23°C intake air temperature

Figure 6.6.2: Flame imaging sequence of cold-start Point 2 through piston crown window (engine speed = 1500 rpm, intake manifold pressure = 0.79 bar, fuel injection = 60 °CA ATDC, ignition timing = 335 °CA ATDC, λ = 1.1)
23°C cylinder head and liner conditions, 23°C intake air temperature

Figure 6.6.3: Flame imaging sequence of cold-start **Point 3** through piston crown window
(engine speed = 2000 rpm, intake manifold pressure = 0.26 bar, fuel injection = 60 °CA ATDC,
ignition timing = 335 °CA ATDC, λ = 1.5)
23°C cylinder head and liner conditions, 23°C intake air temperature

**Figure 6.6.4: Flame imaging sequence of cold-start Point 4 through piston crown window
(engine speed = 1460 rpm, intake manifold pressure = 0.54 bar, fuel injection = 60 °CA & 360 °CA ATDC,
ignition timing = 335 °CA ATDC, λ = 0.7)**
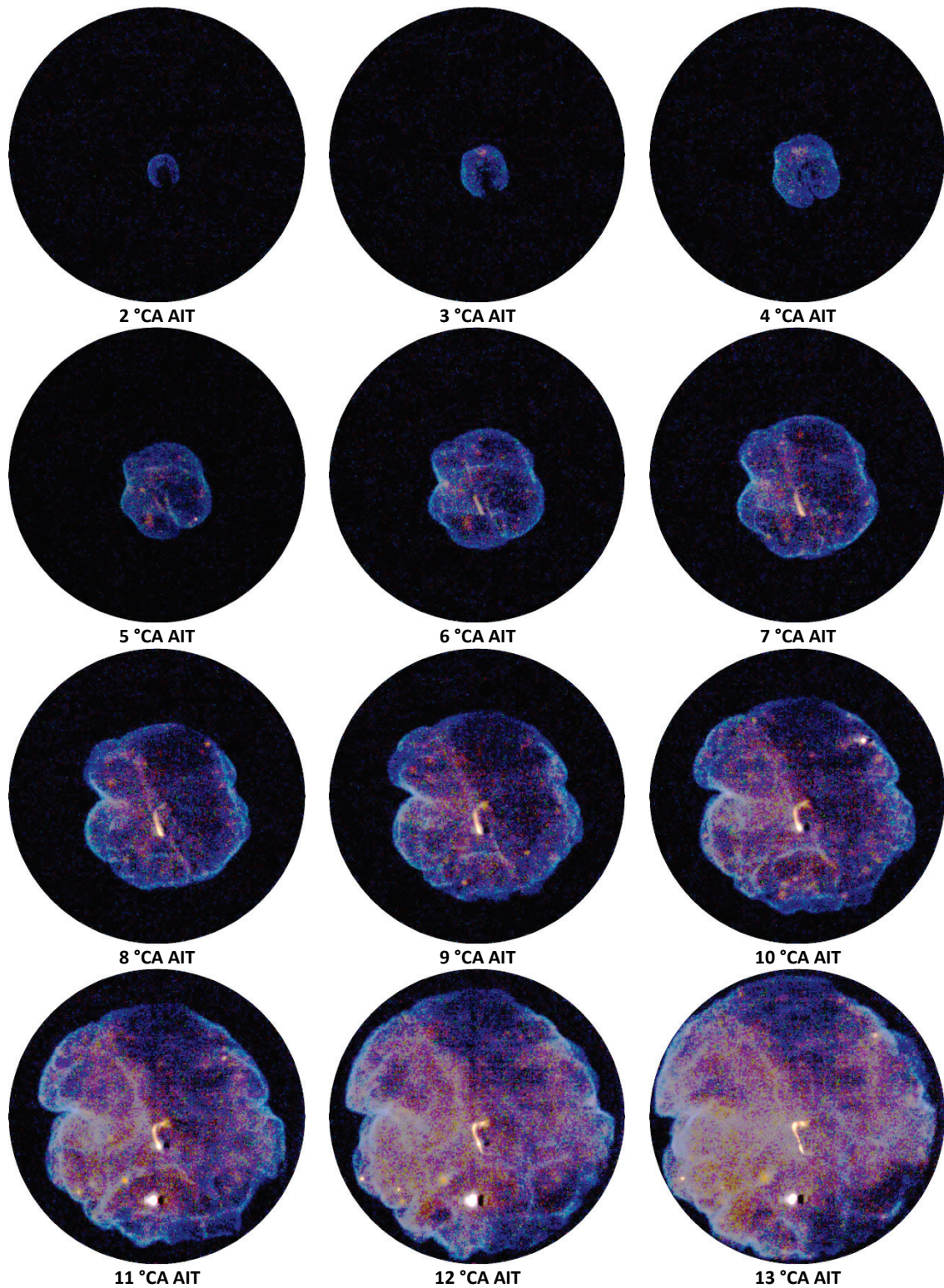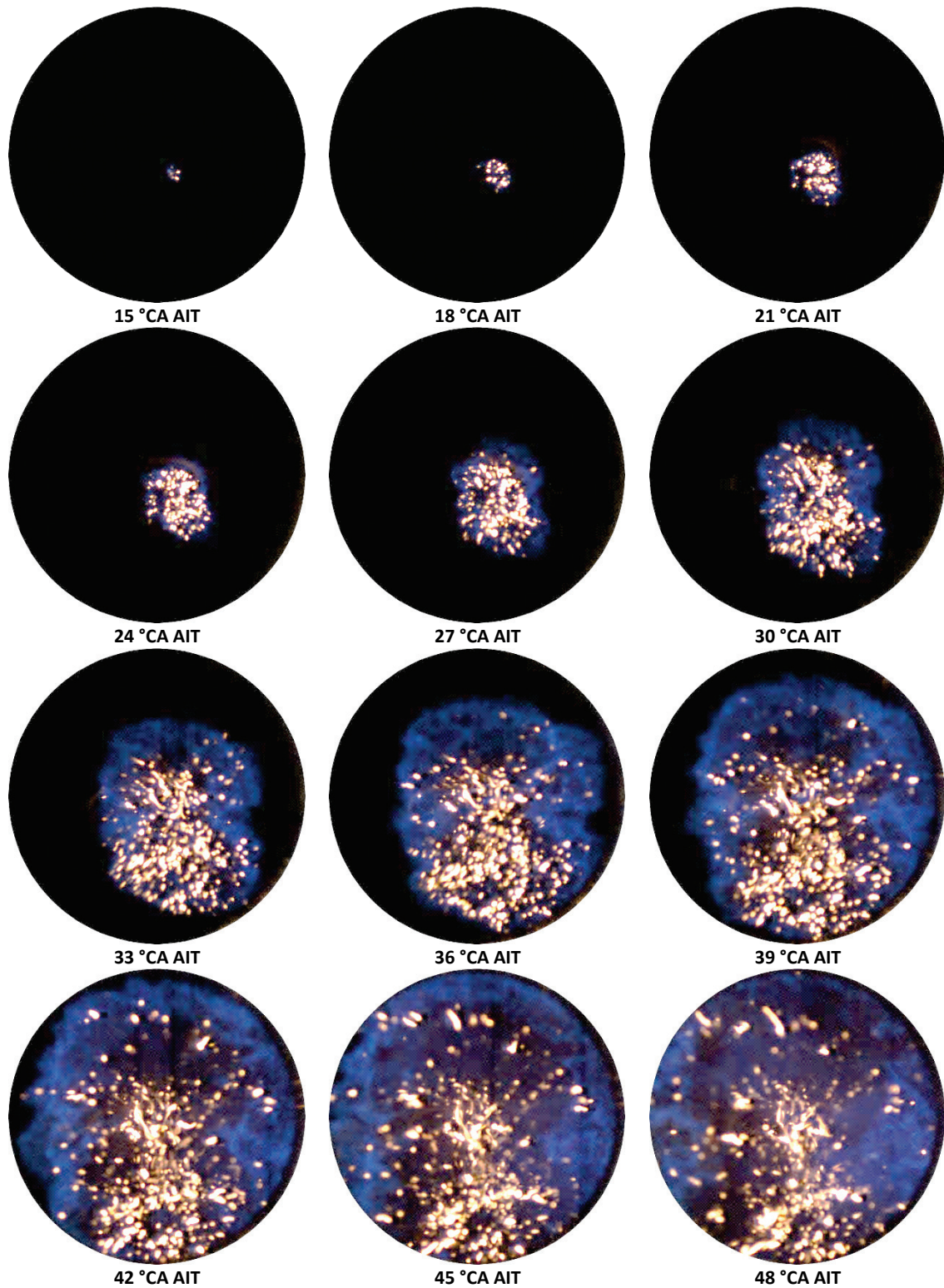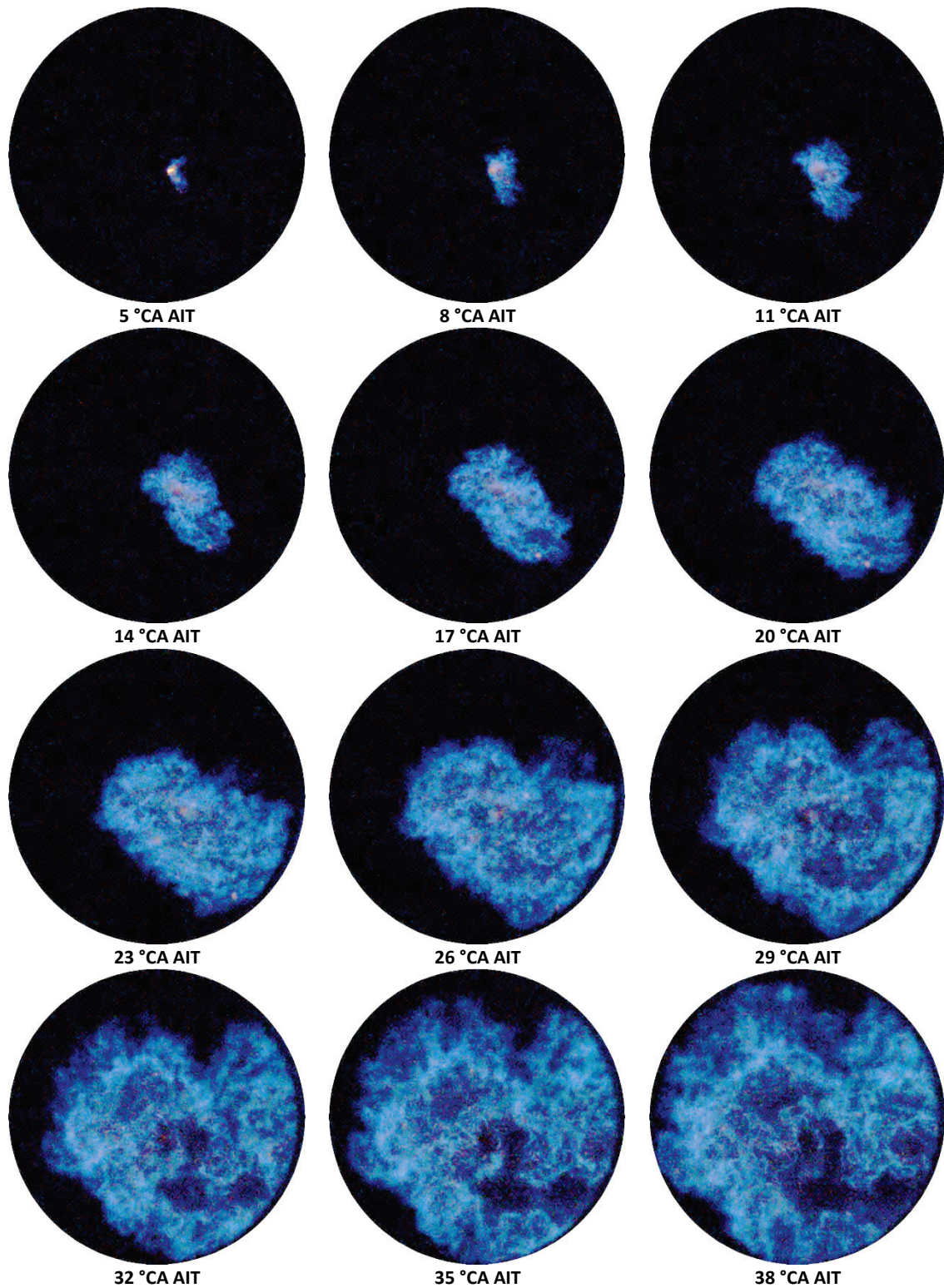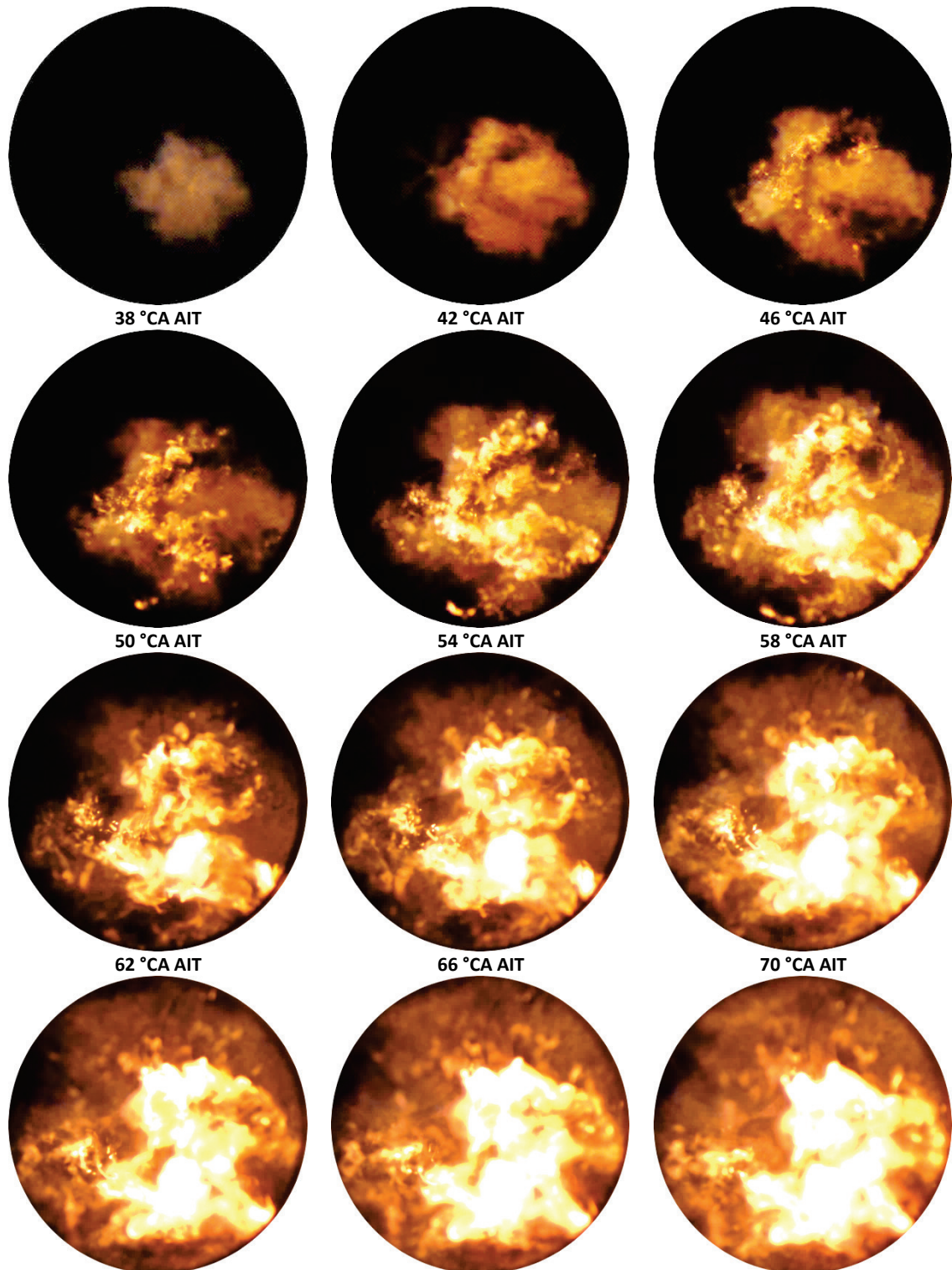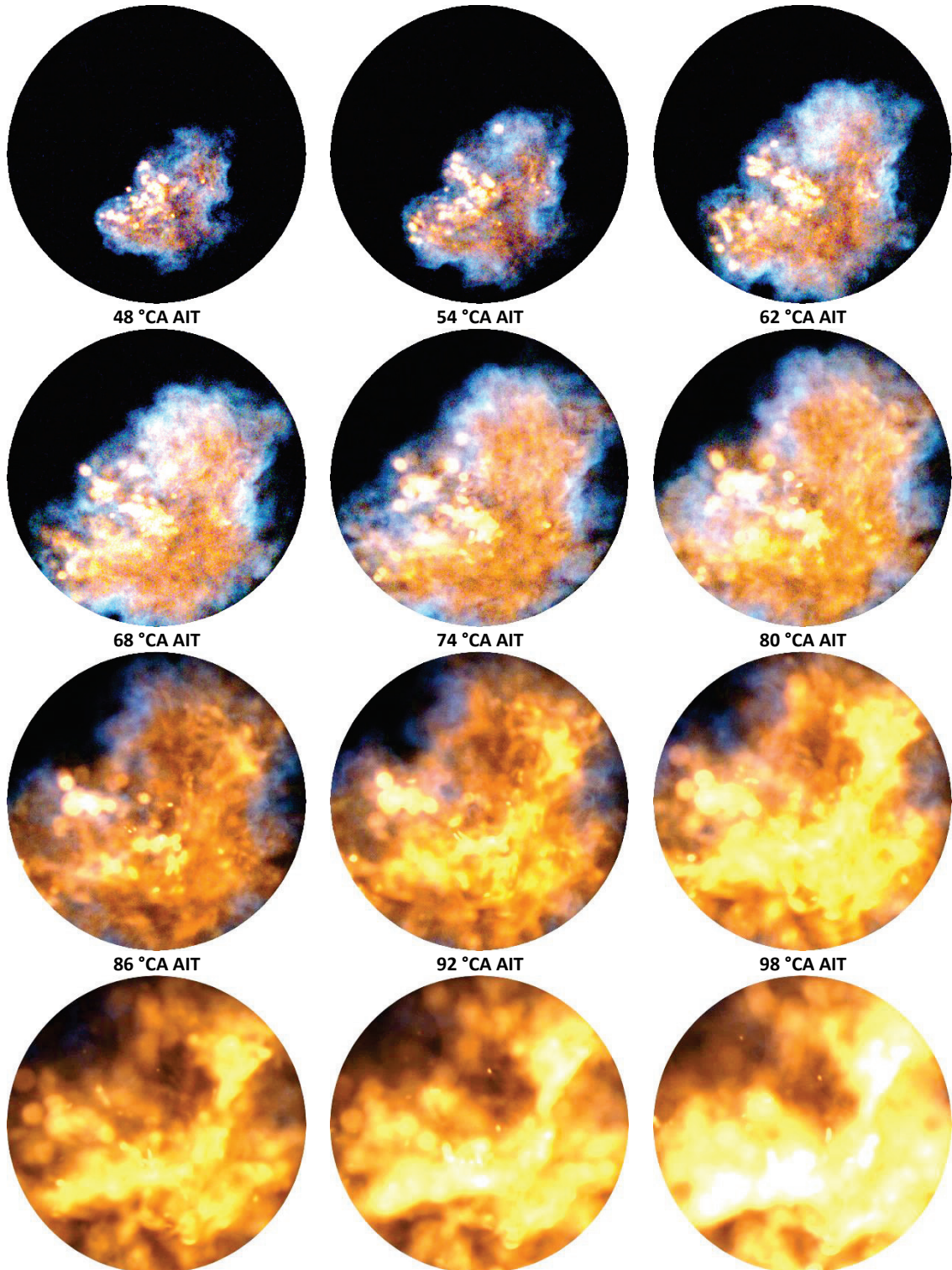**23°C cylinder head and liner conditions, 23°C intake air temperature**

Figure 6.6.5: Flame imaging sequence of cold-start Point 5 through piston crown window
(engine speed = 1340 rpm, intake manifold pressure = 0.74 bar, fuel injection = 60 °CA & 367 °CA ATDC,
ignition timing = 361.5 °CA ATDC, λ = 0.7)
23°C cylinder head and liner conditions, 23°C intake air temperature

6.7   HSPIV RESULTS

To further understand the in-cylinder flow's interaction with the fuel injection and combustion processes, a sequence of flow field vector fields were recorded from 60 °CA TDC to approximately 260 °CA TDC (relative to the intake stroke). The crank angle between images at different test points varies due to differences in engine speed and the subsequent flow velocity. Test Points 2, 4 and 5 have been grouped together and represented by a single series of vectors (Figure 6.7.2 and Figure 6.7.4) due to similar engine speeds and intake pressure producing vector fields and bulk flow structures with no discernible differences. The presented range allows the in-cylinder bulk flow to be observed around the time of fuel injection and the subsequent flow structures, which are of paramount importance in fuel droplet transportation and evaporation. The compression stroke after BDC highlights the formation of characteristic tumble flow structures present in pent-room combustion systems as well as the dissipation of the bulk flow structures in to small-scale turbulence, required for turbulent flame propagation.

At all test points, early in the intake stroke (at approximately 100 °CA for Point 1 and 70 °CA for all other points), the high-velocity jet flow was visible from the upper and lower surfaces of the intake valves, which were located on the upper left hand side of all images. At low valve lift, the small effective flow area and large pressure difference across the valves resulted in conical jets forming within the cylinder. These are visualised more clearly in the instantaneous vector flow field sequence (Figure 6.7.4) as two distinct jets travelling at velocities of over 60 m·s^{-1} within their core, formed as resultant interaction between the two conical intake jets. These velocities were at approximately 10 times the meant piston speed at 1500 rpm, which agree with the expected intake structures during early induction as described by Heywood (1988).

In the early stages of the intake stroke, an anticlockwise rotating vortex was seen on the left surface of the piston in all of the data points presented (Figure 6.7.1 to Figure 6.7.3), which was formed from the intake valve jet recirculating across the piston crown and cylinder wall. As the stroke progressed, this near-vertical jet dissipated and was dominated by the formation of tumble flow. During this early stage of induction, the angle of the valve jet entering the cylinder was primarily influenced by geometric features such as valve seat angle and width. These geometric features of the intake valve have a direct influence on the conical jets and hence the formation and location of the large scale vortices within the cylinder.

At low valve lift these jets propagated horizontally outwards towards both the left side of the cylinder wall and the pent-roof chamber (Figure 6.7.1 to Figure 6.7.3). As the flow propagated from the valve to the cylinder wall, the wall deflected the majority of the flow downwards towards the piston and caused the smaller vortex on the left hand side, which is typical of the flow field in a pent roof chamber (Heywood 1988). As the valve lift increased and the piston travelled towards BDC (at approximately 120 °CA), the direction of flow was less influenced by the geometric features of the valve heads (such as the seat) due to the larger effective flow area. This resulted in the flow being directed more towards the pent roof chamber due to the increased influence from the intake manifold geometry upstream of the valves.

Despite the significant difference in engine speed between Point 1 (Figure 6.7.1) and the other test points (Figure 6.7.2 to Figure 6.7.3), a clearly defined tumble flow was still present during the intake stroke. The reduced piston speed, which created much lower flow magnitudes within the tumble vortex, as well as the reduction of piston squish, meant it was reasonable to assume that the dissipation of large-scale flow couldn't give rise to much high-frequency turbulence and resulted in the laminar flame structure observed during combustion (Figure 6.6.1). This is due to the well understood phenomenon of high frequency turbulence being generated by the squish of large-scale flow structures (Zhao *et al.* 1999, Yasar *et al.* 2006, Stansfield *et al.* 2007), which enables fast flame propagation (Pajot and Mounaïm-Rousselle 2000, Rimmer *et al.* 2009). The remaining test points (Figure 6.7.2 to Figure 6.7.3) operated at similar engine speeds and operating parameters so it is reasonable to assume that similar levels of high-frequency turbulence (not presented) were generated at TDC of the compression stroke. Small variations may have occurred, however, as different quantities of injected fuel have been shown to suppress the mean velocities of bulk flow during intake (Rimmer 2010).

Typical times for the fuel injection event in DISI homogeneous combustion system are around 60 °CA to 80 °CA. At these crank angle positions, striking differences in flow magnitude were seen in Point 1 (Figure 6.7.1), with mean peak valve jet velocities of only 2.0 m·s^{-1} compared to 45 m·s^{-1} – 70 m·s^{-1} at other test points, due to the engine speed. Poorly atomised and vaporised fuel was apparent in the combustion imaging visualised as high luminosity rich regions and the quantified flow structures played an important role in aiding the fuel vaporisation and transportation processes. Although it was noted that the low fuel injection pressure was likely the dominant factor, the lower velocity jet flow will have likely had an effect on the breakup and vaporisation of the injected fuel, as less shear forces were present at the gas-liquid interface, which are responsible for the breakup of the liquid jet into droplets (Charalampous *et al.* 2009). In addition, the lower velocity flow will have decreased the effect

of the tumble flow on impinged fuel, which has been shown to aid the transportation of liquid fuel deposits on the piston crown back into the centre of the cylinder (Rimmer *et al.* 2012).

Observation of the ensemble-averaged intake flow between Points 2, 4, and 5 (Figure 6.7.2) compared to Point 3 (Figure 6.7.3), which was operating at a 500 rpm faster engine speed, revealed near-identical large-scale flow structures. The mean velocities of the flow structures in Point 5 were higher, however, and the structures were better defined, indicating that the strong induced flow structures (such as valve flow and tumble) drove the generation of these flow structures and reduced cycle-by-cycle variability. The reduction in variability, however, did not have a prominent effect on the flame propagation at Point 3, which was observed to be inconsistent and unstable. This was due to the operating parameters being close to the lean-limit and having a dominant effect on the combustion process.

The compression stroke in all test points (Figure 6.7.1 to Figure 6.7.3) exhibited similar trends of bulk convection from the exhaust to the intake side along the surface of the piston once the intake valves had closed and the valve jet flow was no longer distinctly detectable (from approximately 170 °CA). This demonstrated the continuation of the tumble flow during the compression stroke until its eventual dissipation. The resultant high-frequency turbulence components, generated from piston squish, were not observable in the presented vector fields due to the spatial resolution of the vectors fields, but are well understood and have been measured in a similar engine configuration by (Jarvis *et al.* 2006, Long *et al.* 2008, Rimmer *et al.* 2009, Justham 2010, Rimmer 2010). The next part of this section aims to understand the variability in the flow using the processed temporal data available.

The instantaneous flow fields from Points 2, 4 and 5 (Figure 6.7.4) highlighted the presence of smaller scale flow features due to the variability of the flow, contained within the bulk flow structures observed from the ensemble-averaged vector fields. The areas of high contrasting velocity demonstrated the complexity of three-dimensional flow with the engine when viewed from the selected tumble plane. To quantify this variability further, Reynolds decomposition was performed on the temporal PIV data. Figure 6.7.5 illustrated the turbulence fluctuation velocity, or root mean square (RMS) velocity fluctuation from the mean for Points 2, 4 and 5. Peak areas of turbulence intensity corresponded to the strong valve jet flow from 60 °CA, which exemplified the effect that these flow structures had on fuel spray penetration and vaporisation throughout the stroke, as their presence remained in the cylinder until 120 °CA. The high levels of turbulence were seen to dissipate towards the latter part of the intake stroke, where the global turbulence steadily decreased through to the compression stroke.

The region near the intake valves, corresponding to the main valve jets, maintained a higher level of turbulence intensity throughout the presented images, which demonstrated the important effect that valve jet flow and the formation of tumble had on fuel transportation, as well as the generation of high-frequency turbulence scales during compression.

60 °CA ATDC   **73.5 °CA ATDC**   **87 °CA ATDC**

100.5 °CA ATDC   **114 °CA ATDC**   **127.5 °CA ATDC**

172.5 °CA ATDC   **217.5 °CA ATDC**   **262.5 °CA ATDC**
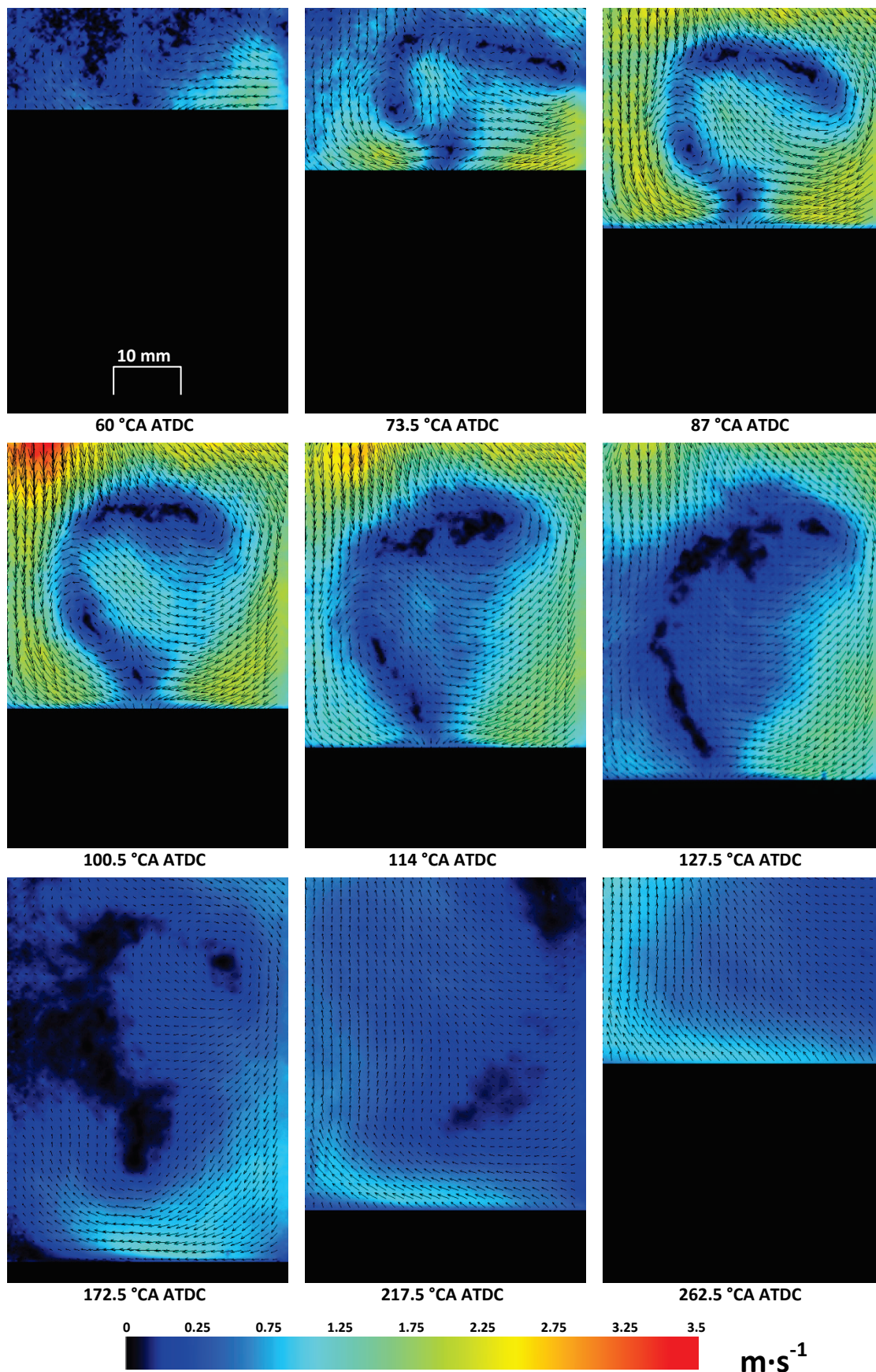
Figure 6.7.1: Ensemble average vector field sequence at Point 1 through cylinder liner (engine speed = 150 rpm, intake manifold pressure = 0.96 bar)
23°C cylinder head and liner conditions, 23°C intake air temperature

Figure 6.7.2: Ensemble average vector field sequence at Points 2, 4 and 5 through cylinder liner (engine speed = 1500 rpm, intake manifold pressure = 0.67 bar) 23°C cylinder head and liner conditions, 23°C intake air temperature

60 °CA ATDC   **76 °CA ATDC**   **92 °CA ATDC**

108 °CA ATDC   **124 °CA ATDC**   **140 °CA ATDC**

172 °CA ATDC   **212 °CA ATDC**   **252 °CA ATDC**

Figure 6.7.3: Ensemble average vector field sequence at Point 3 through cylinder liner (engine speed = 2000 rpm, intake manifold pressure = 0.26 bar)
23°C cylinder head and liner conditions, 23°C intake air temperature

Figure 6.7.4: Instantaneous vector field sequence at Points 2, 4 and 5 through cylinder liner
(engine speed = 1500 rpm, intake manifold pressure = 0.67 bar)
23°C cylinder head and liner conditions, 23°C intake air temperature

Figure 6.7.5: Turbulence fluctuation velocity contour plots at **Points 2, 4 and 5** through cylinder liner
(engine speed = 1500 rpm, intake manifold pressure = 0.67 bar)
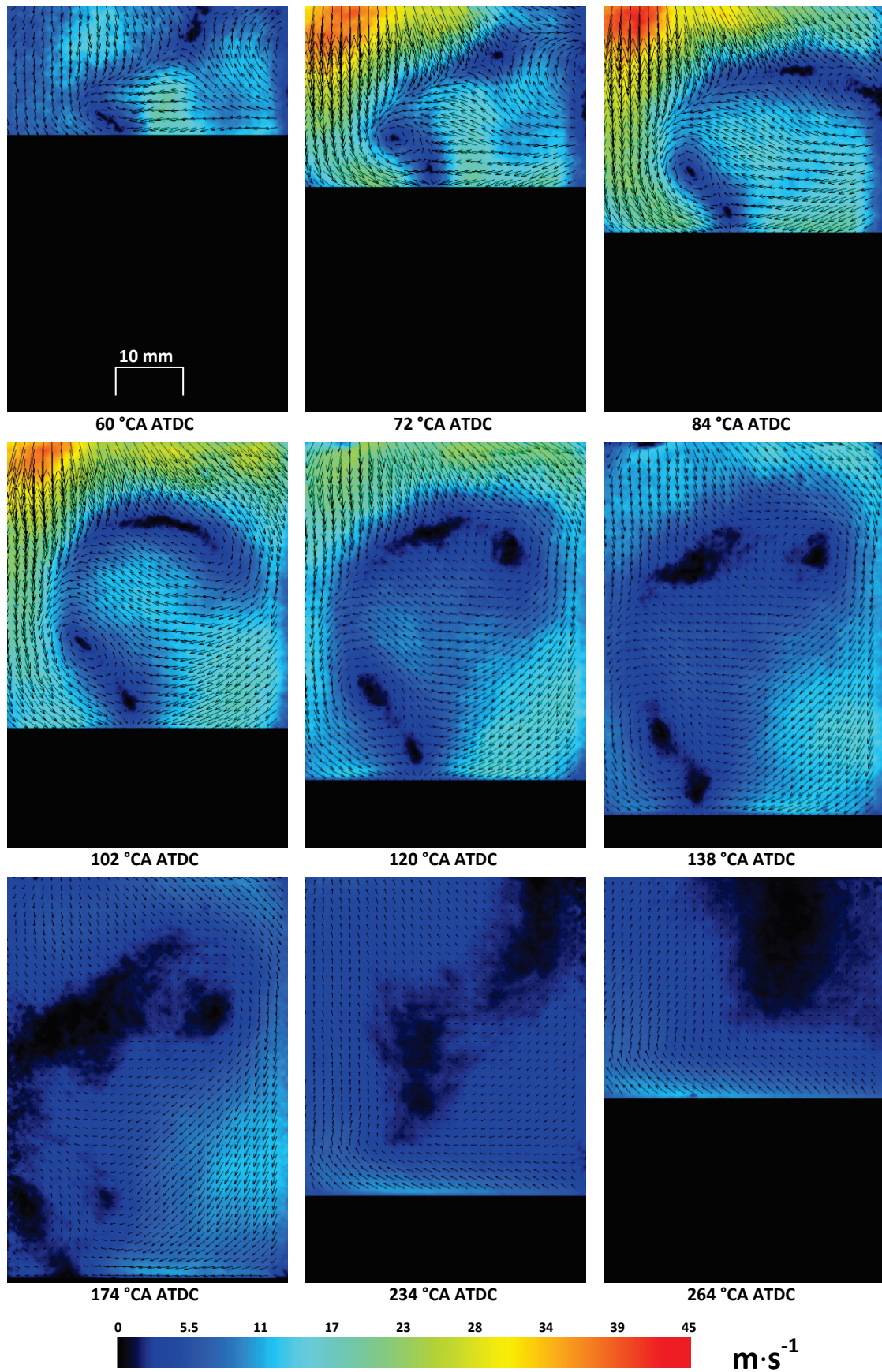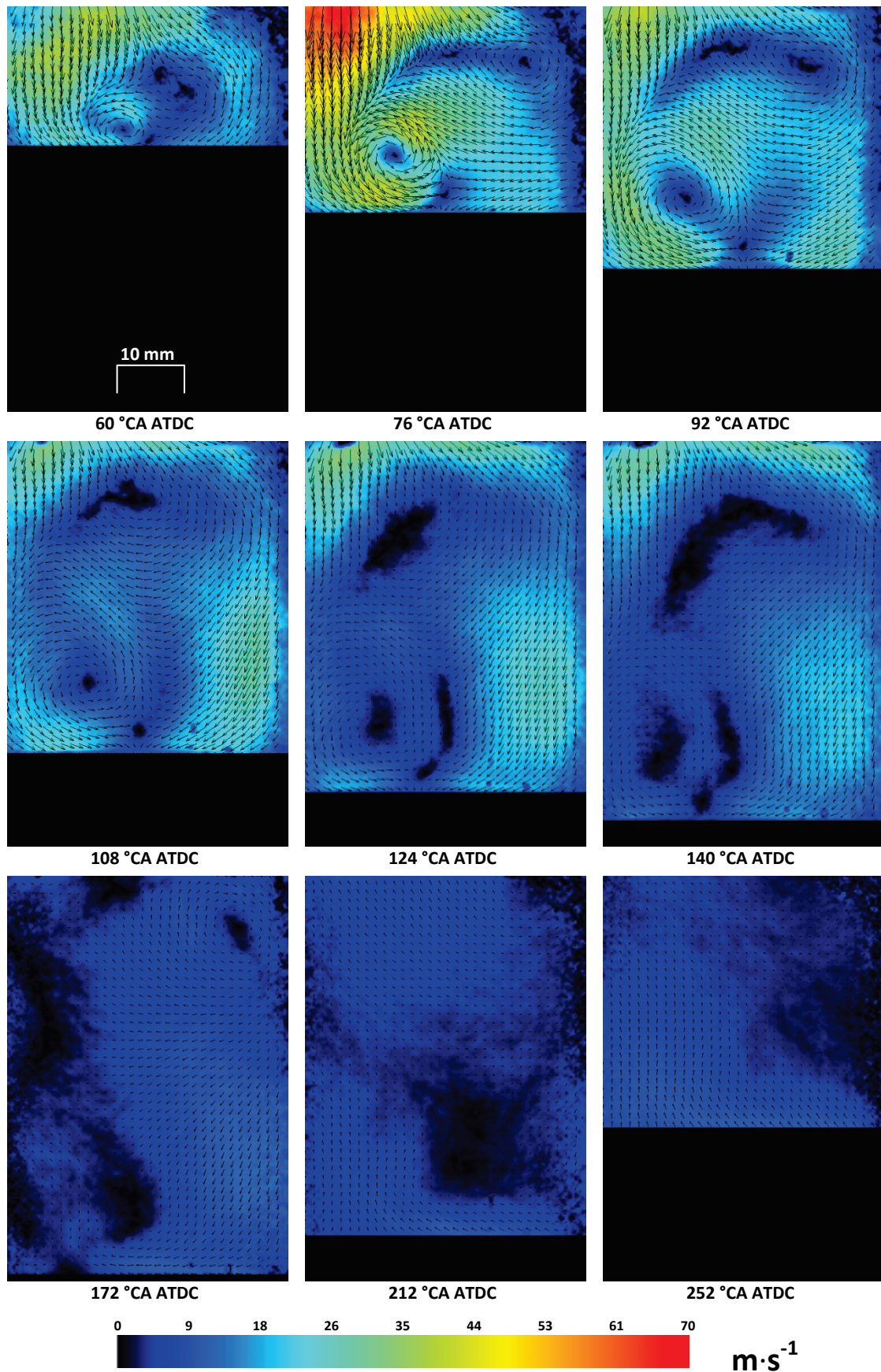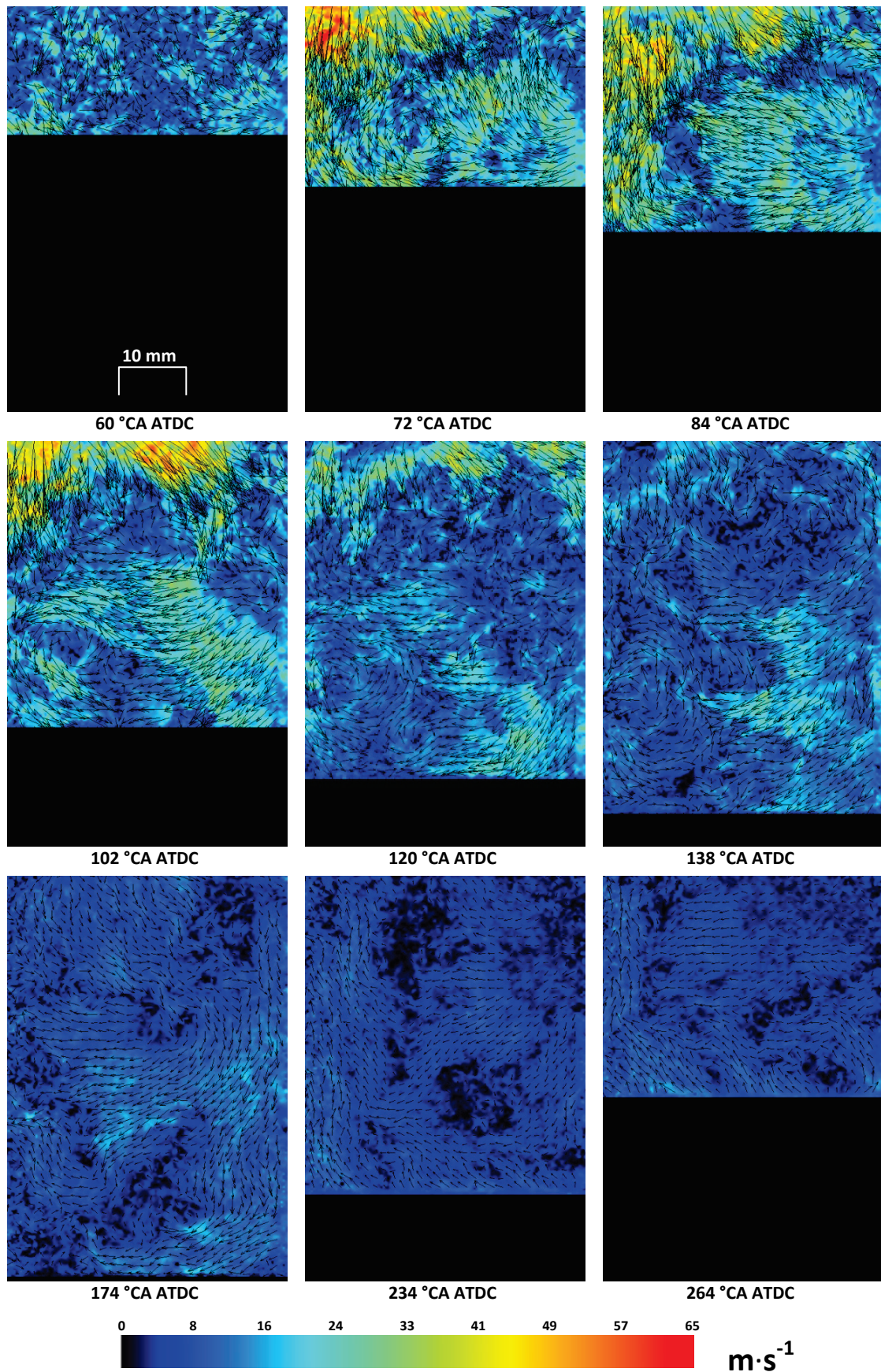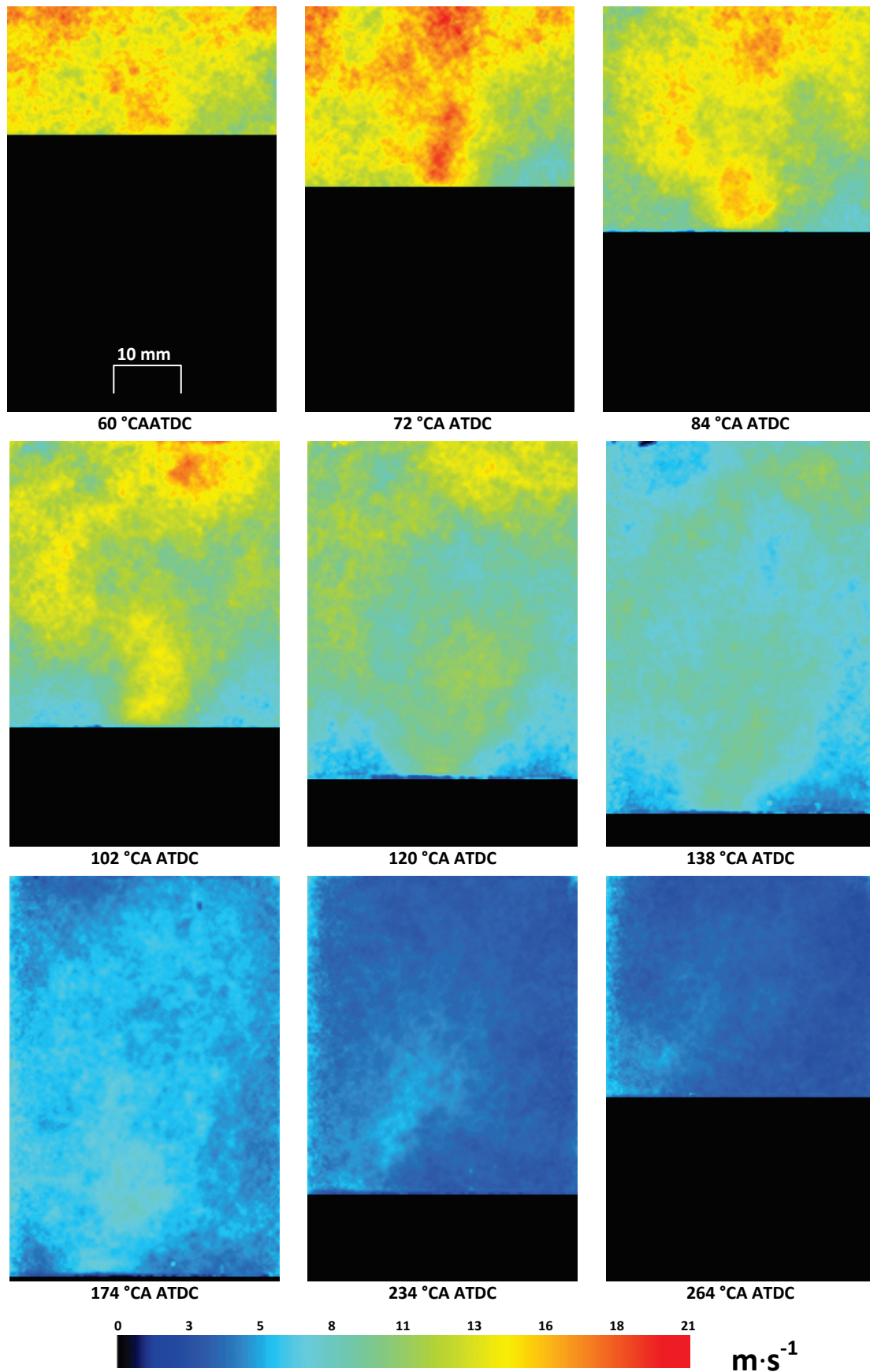**23°C cylinder head and liner conditions, 23°C intake air temperature**

6.8 CONCLUDING REMARKS

To further understand the effect of cold-start on a production engine start-up, this chapter simulated an engine cold-start and utilised colour optical and pressure data analysis, along with HSPIV to examine the preceding in-cylinder flow field. The colour combustion analysis enabled the complex flame stoichiometry to be observed, extending the understanding of the flame propagation processes observed during cold-start in earlier chapters. To elucidate the creation of these flame propagation structures, HSPIV facilitated the quantification of the in-cylinder flow field during intake and compression and allowed various scales of intake flow and turbulence to be linked to the subsequent combustion events. The key conclusions are:

1. In-cylinder peak pressures were shown to have varied significantly in the first few seconds of the cold-start cycle with a variation of 12.8 bar across the 5 chosen test positions and a range in COV of 13.8%, highlighting the key differences in operating modes, each with a different objective to the engine's operation. MFB times also showed a wide variation with up to a 50 °CA difference in burn time and 8.5% difference in COV for the 90% MFB case.

2. The effect of fuel pressure was shown to have a prominent effect on both the in-cylinder pressure and combustion imaging data as well as a likely effect on engine emissions with a vast array of in-cylinder stoichiometry observed. This emphasizes the importance of pressurising the fuel rail in a short as time as possible during DISI engine cold-start.

3. Combustion imaging was correlated with the recorded in-cylinder pressure, identifying an array of contrasting combustion flame structures that behaved in very different ways depending on their parameter scheduling, fuel pressure and intake and flow conditions.

4. High-speed imaging of the in-cylinder combustion identified a number of soot formation regions in nearly all of the experimental test points, which will have a detrimental effect on the PN count emissions.

5. In-cylinder HSPIV flow field analysis identified the critical flow structures and turbulence that had an effect on fuel injection, transportation and mixing, as well as the subsequent combustion process, all of which were driven by engine speed. The identification of how these flow processes can affect combustion allowed potential flow enhancement techniques to be deduced during cold-start.

The next chapter will correlate the in-cylinder pressure, injection, combustion and flow field analyses with exhaust emissions by measuring the PN and HC exhaust emissions during cold-start. This will allow the levels of PN generation to be linked to temperature and operating parameters as well as precisely identifying the main sources of HC emission within the cylinder, utilising a fast FID HC analyser. The understanding of the sources of these emissions is of paramount importance to reducing their levels and meeting the stringent targets set within current emissions legislation.

6.9   CHAPTER 6 REFERENCES

ANANDARAJAH, K. (2005) Digital particle image velocimetry (DPIV): Limitations to measurement accuracy, PhD Thesis, Loughborough University.

ANDO, H. (1997) Mitsubishi GDI engine strategies to meet the European requirement. *Proceedings of AVL Conference on Engine and Environment,* Vol 2, pp. 55-77.

BERNDORFER, A., BREUER, S., PIOCK, W. & BACHO, P. V. (2013) Diffusion Combustion Phenomena in GDi Engines caused by Injection Process, SAE Paper 2013-01-0261.

BIANCO, Y., CHENG, W. K. & HEYWOOD, J. B. (1991) The effects of initial flame kernel conditions on flame development in SI engines, SAE Paper 912402.

CHARALAMPOUS, G., HARDALUPAS, Y. & TAYLOR, A. M. K. P. (2009) Novel Technique for Measurements of Continuous Liquid Jet Core in an Atomizer. *AIAA,* Vol 47(11), pp. 2605-2615.

DRAIN, L. E. (1980) *The Laser Doppler Technique,* New York, John Wiley & Sons.

EFTHYMIOU, P., DAVY, M., GARNER, C., HARGRAVE, G., RIMMER, J. E. T. & RICHARDSON, D. (2013) Insights into Cold-Start DISI Combustion in an Optical Engine Operating at −7°C. *SAE. Int. J. Engines,* Vol 6(2), pp. 1059-1074.

ENG, J. A. (2005) The Effect of Spark Retard on Engine-out Hydrocarbon Emissions, SAE Paper 2005-01-3867.

GUPTA, S., POOLA, R., O.L., K. & SEKAR, R. (2000) Particulate Emissions Characteristics of Port-Fuel Injected SI Engine. *US Dept. of Energy*.

HALLGREN, B. E. & HEYWOOD, J. B. (2003) Effects of Substantial Spark Retard on SI Engine Combustion and Hydrocarbon Emissions, SAE Paper 2003-01-3237.

HATTORI, H., OTA, M., SATO, E. & KADOTA, T. (1995) Fundamental study on DISC engine with two-stage fuel injection. *JSME Int J 1995,* Vol B38(1), pp. 129-35.

HEYWOOD, J. B. (1988) *Internal Combustion Engine Fundamentals,* 1st Ed., McGraw-Hill, pp. 42-61, 205-278, 400-450, 797-819.

IWAMOTO, T., NOMA, K., YAMAUCHI, T. & ANDO, H. (1997) Development of gasoline direct injection, SAE Paper 970541.

JARVIS, S., JUSTHAM, T., CLARKE, A., GARNER, C. P. & HARGRAVE, G. K. (2006) Motored SI IC Engine In-Cylinder Flow Field Measurement Using Time Resolved Digital PIV For Characterisation of Cyclic Variation, SAE Paper 2006-01-1044.

JOHANSSON, B. (1991) Influence of the velocity near the spark plug on early flame development, SAE Paper 930481.

JUSTHAM, T. (2010) Cyclic Variation in the Flow Field Behaviour within a Direct Injection Spark Ignition Engine: A High Speed Digital Particle Image Velocimetry Study, Loughborough, PhD Thesis, Loughborough University.

KEANE, R. D. & ADRIAN, R. J. (1990) Optimisation of Particle Image Velocimeters. Part I: Double Pulsed Systems. *Meas. Sci. and Technol.,* Vol 1, pp. 1202-1215.

KUWAHARA, K., YAMAMOTO, S., IWACHIDOU, K. & ANDO, H. (1998) Two-Stage Combustion for Quick Catalyst Warm-up in Gasoline Direct Injection. *The Fourth International Symposium COMODIA 98*, pp. 293-298.

LAWSON, N. J. (1995) The Application of Particle Image Velocimetry to High-Speed Flow, PhD Thesis, Loughborough University.

LI, Y., ZHAO, H., LEACH, B., MA, T. & LADOMMATOS, N. (2004) Characterization of an in-cylinder flow structure in a high-tumble spark ignition engine. *Int. J. Engine Res.,* Vol 5(5), pp. 375-400.

LONG, E. J., RIMMER, J. E. T., JUSTHAM, T., GARNER, C., HARGRAVE, G. K., RICHARDSON, D. & WALLACE, S. (2008) The Influence of In-Cylinder Turbulence upon Engine Performance within a Direct Injection IC Engine. *Seventh International Conference on Modelling and Diagnostics for Advanced Engine Systems.* Sapporo Japan.

MERGERLE, M. & SICK, V. R., D.L. (2002) Measurement of digital particle image velocimetry precision using electro-optically created particle image displacements. *Meas. Sci. and Technol.,* Vol 13, pp. 997-1005.

MIYAMOTO, N., OGAWA, H., SHUDO, T. & TAKEYAMA, F. (1994) Combustion and emissions in a new concept DI stratified charge engine with two-stage fuel injection, SAE Paper 940675.

PAJOT, O. & MOUNAÏM-ROUSSELLE, M. (2000) Instantaneous Flow Field Effects on the Flame Instantaneous Flow Field Effects on the Flame Optical Diagnostics, SAE Paper 2000-01-1796.

PIOCK, W., HOFFMANN, G., BERNDORFER, A., SALEMI, P. & FUSSHOELLER, B. (2011) Strategies Towards Meeting Future Particulate Matter Emission Requirements in Homogeneous Gasoline Direct Injection Engines, SAE Paper 2011-01-1212.

PRICE, P., STONE, R., COLLIER, T. & DAVIES, M. (2006) Particulate Matter and Hydrocarbon Emissions Measurements: Comparing First and Second Generation DISI with PFI in Single Cylinder Optical Engines, SAE Paper 2006-01-1263.

RAFFEL, M., WILLERT, C. E., WERELEY, S. T. & KOMPENHANS, J. (2007) *Particle Image Velocimetry: A Practical Guide,* 2nd Ed., Springer-Verlag.

REUSS, D. L., MEGERKE, M. & SICK, V. (2002) Particle-image velocimetry measurement errors when imaging through a transparent engine cylinder. *Meas. Sci. Technol.,* Vol 13(2002), pp. 1029-1035.

RIMMER, J. E. T. (2010) An Optical Investigation into the Effect of Fuel Spray, Turbulent Flow and Flame Propagation on DISI Engine Performance, Loughborough, PhD Thesis, Loughborough University.

RIMMER, J. E. T., DAVY, M. H., GARNER, C. P., HARGRAVE, G. K. & RICHARDSON, D. (2012) Fuel spray structure, flame propagation and charge motion at fuel impingement locations within a DISI engine. *IMechE: Fuel Systems for IC Engines,* Vol 2012, pp. 199-214.

RIMMER, J. E. T., LONG, E. J., GARNER, C. P., HARGRAVE, G. K., RICHARDSON, D. & WALLACE, S. (2009) The Influence of Single and Multiple Injection Strategies on In-Cylinder Flow and Combustion within a DISI Engine, SAE Paper 2009-01-0660.

RUSS, S., LAVOIE, G. & DAI, W. (1999) SI Engine Operation with Retarded Ignition: Part 1 - Cyclic Variations, SAE Paper 1999-01-3506.

SAHOO, B. B., SAHOO, N. & SAHA, U. K. (2009) Effect of engine parameters and type of gaseous fuel on the performance of dual-fuel gas diesel engines—A critical review. *Renewable and Sustainable Energy Reviews,* Vol 13(2009), pp. 1151-1184.

STANSFIELD, P., WIGLEY, G., JUSTHAM, T., CATTO, J. & PITCHER, G. (2007) PIV analysis of in-cylinder flow structures over a range of realistic engine speeds. *Exp Fluids (2007),* Vol 43, pp. 135-146.

SVENSSON, K. I., MACKRORY, A. J., RICHARDS, M. J. & TREE, D. R. (2005) Calibration of an RGB, CCD Camera and Interpretation of its Two-Color Images for KL and Temperature, SAE Paper 2005-01-0648.

TENNEKES, H. & LUMLEY, J. L. (1972) *A First Course in Turbulence*, The MIT Press, Vol. 1.

WHITAKER, P., KAPUS, P., OGRIS, M. & HOLLERER, P. (2011) Measures to Reduce Particulate Emissions from Gasoline DI engines, SAE Paper 2011-01-1219.

YAMADA, T., GARDNER, D. V., BRUNO, B. A., ZELLO, J. V. & SANTAVICCA, D. A. (2002) The Effects of Engine Speed and Injection Pressure Transients on Gasoline Direct Injection Engine Cold Start, SAE Paper 2002-01-2745.

YASAR, A., SAHIN, B., AKILLI, H. & AYDIN, K. (2006) Effect of inlet port on the flow in the cylinder of an internal combustion engine. *Proc. IMechE Part C: J. Mechanical Engineering Science,* Vol 220, pp. 73-82.

ZHAO, F., HARRINGTON, D. L. & LAI, M. C. (1999) Automotive spark-ignited direct-injection gasoline engines. *Progress in Energy and Combustion Science 25,* Vol 1999, pp. 437-562.

ZHAO, F., HARRINGTON, D. L. & LAI, M. C. (2002) *Automotive Gasoline Direct-Injection Engines*, SAE International, pp. 1-50, 166-188, 223-260.

CHAPTER 7

THE EFFECT OF DISI ENGINE

COLD-START ON EMISSIONS

7.1   INTRODUCTION

The optical diagnostics and pressure data analyses presented in *Chapters 4, 5 and 6* have quantified the effects of operating temperature and cold-start operation on in-cylinder flow, fuel injection and combustion processes. The analysis highlighted the prevalence of regions for particulate and hydrocarbon (HC) formation.

In this chapter, data is presented that links the in-cylinder optical diagnostics data with exhaust emissions analysis. Data was collected that measured the hydrocarbon (HC) and particulate number (PN) emissions during cold conditions similar conditions to those previously tested, in order to correlate the in-cylinder data with emissions. Steady-state operation of the engine from 80°C to -7°C with a 23°C and -7°C intake air temperature was completed as tested in *Chapters 4 and 5.*

A new exhaust manifold was manufactured to facilitate the measurement and monitoring of up to seven sample points simultaneously, this has been detailed in *Chapter 3*, along with setup of the exhaust measurement equipment. In order to collect as much data as possible and observe the emissions for an extended period of time it was necessary to overcome the temperature-limited maximum operating time of 3 minutes for the optical engine. This was completed using thermodynamic versions of the optical piston crown and pent roof window to allow combustion operating times of 10 minutes and above.

A clear link between PN emissions and operating temperature was found, along with differences in particle size distribution at different temperatures. The fast flame ionisation detector (FID) analyser revealed the quantity and precise location of UHCs during the exhaust stroke to help elucidate the formation regions of these exhaust emissions.

7.2   EXPERIMENTAL SETUP

To keep emissions results consistent with the steady-state in-cylinder optical data obtained in *Chapters 4 and 5,* the temperature of the coolant was set to achieve the engine operating temperatures outlined in Table 4.2.1 in conjunction with intake temperatures of 23°C and -7°C.

Cylinder Head and Liner Temperature	Description
80°C	Fully heated engine
23°C	Ambient lab conditions
10°C	Intermediate condition
-7°C	Euro 6 cold-start temperature

Table 7.2.1: Description of selected engine head and liner temperatures

Two types of sampling equipment were used to characterise the exhaust gas particulate matter (PM) and unburned hydrocarbon (UHC) emissions during the outlined cold-start conditions. The Cambustion DMS500 MkII fast particle spectrometer measured particulate number (PN) count emissions of particles sized from 5 nm to 1 μm and the Cambustion HFR500 fast flame ionisation detector (FID) was used to measure the UHC levels up to 10,000 ppm. The operating principles and detailed experimental setup of both these pieces of equipment are described in *Chapter 2*.

The experimental test methodology comprised cold-soaking the engine until the desired operating temperature was achieved and then sampling from the exhaust manifold momentarily before firing the engine. This ensured the early emissions from misfire or poor combustion were captured and accurately recorded. During fired operation, the continuously cooled coolant was circulated through the engine whilst emissions measurements were recorded. This continuous cooling created a lengthened warm-up period as the operating temperature naturally increased due to combustion and is a method that has been used for other cold-start experimentation by (Price *et al.* 2007). This lengthened period allowed the engine to run for longer and enabled a larger amount of PM emissions data to be collected.

Due to the nature of both types of emissions (low quantity PM and high variability HC), procedures were taken to ensure that data was kept accurate and repeatable. At least six separate engine test runs were completed for every operating condition. Each data set was examined to ensure that the emissions data followed the general trend and modal average of the other test runs and determine if further repeat testing was needed.

7.2.1 DMS 500 Particle Analyser

The sample pipe for the DMS500 entered the exhaust manifold at approximately 35 mm away from the exhaust head surface, centred axially with a 90° bend towards the direction of flow to prevent the stagnation of particles near the tube orifice (as shown in Figure 7.2.1).
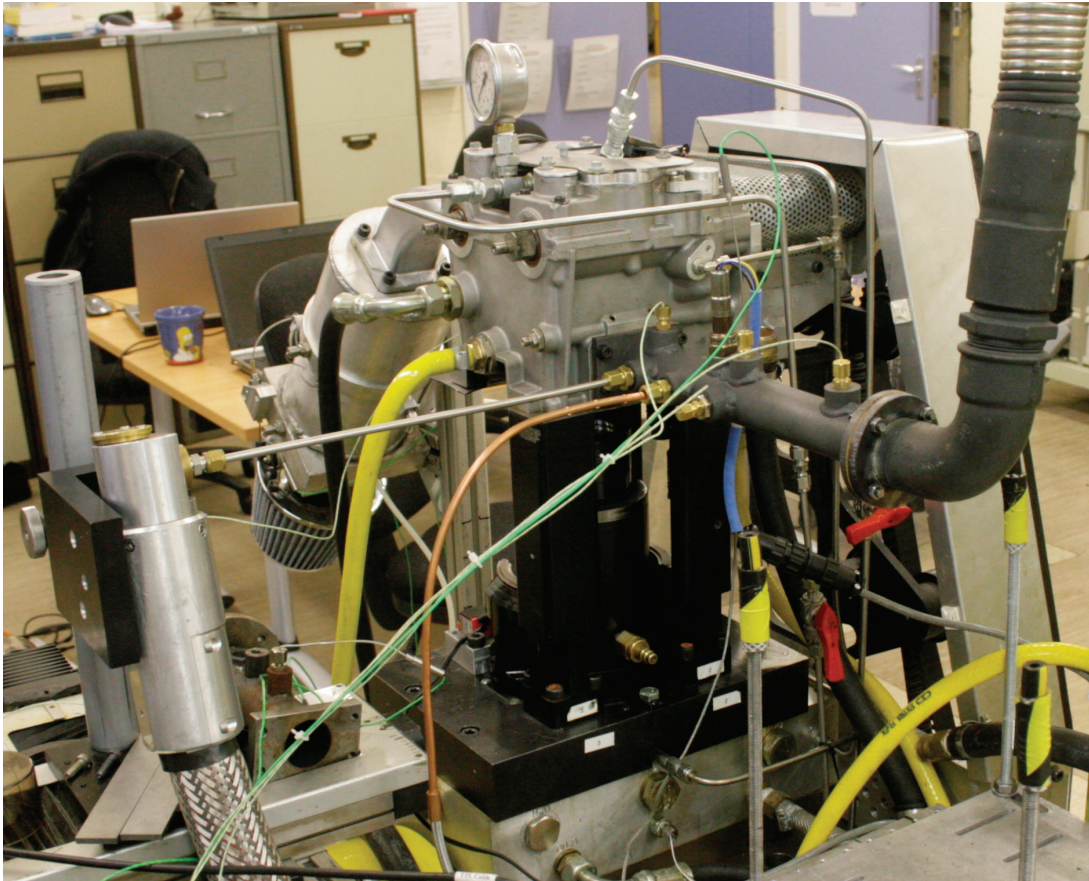
Figure 7.2.1: Modified optical engine exhaust manifold highlighting DMS500 sample point

A sample pipe of approximately 700 mm was used to allow the sampled exhaust gas to cool sufficiently before entering the heat sample line, which had an inner plastic tube that could withstand up to 120°C. In order to optimise the concentration of particulates entering the DMS500 for measurement accuracy and to prevent saturation, primary and secondary dilution were applied (listed in Table 7.2.2). As the temperature of the engine increased in each experimental run period of 10 minutes, the particulate concentration was inherently affected and the dilution was adjusted accordingly to maintain the dynamic measurement range of the DMS500. These dynamic changes to dilution ratio expectedly produced momentary anomalies in the sampled particulate measurements, which have been considered in the analysis of the presented data.

Operating Temperature	Primary Dilution Factor		Secondary Dilution Factor	
	(Initial)	(Final)	(Initial)	(Final)
80°C	5		20	
23°C	5	5	30	20
10°C	5	5	30	1
-7°C	5	5	50	1

Table 7.2.2: Primary and secondary dilution factors at each engine operating temperature

7.2.2 HFR Fast FID UHC Analyser

As detailed in *Chapter 3*, the fast FID exhaust probe was installed in the exhaust manifold via an adaptor that located it approximately 5 mm from one of the exhaust valve heads to minimise the measurement response time. The fast response time (0.7 ms) of the fast FID analyser coupled with the fact that the signal was recorded using the in-cylinder pressure DAQ enabled a high resolution signal of 0.1 °CA to be recorded. As with the DMS500, the Fast FID required calibration at each operating temperature test point to maximise the dynamic recording range of the equipment (which had a maximum output voltage of 10 V), this has been outlined in Table 7.2.3. A course 'voltage gain' option was first selected at each operating condition and then a fine potentiometer was adjusted to give a voltage to parts per million (ppm) relation. A span gas consisting of propane with 5000 ppm was used to perform the output voltage calibration and a zero gas consisting of bottled compressed air was used to zero the fast FID between each test point to accommodate for any voltage drift.

Operating Temperature	Gain	Resultant Calibration
80°C	500	1.0 V = 500 ppm
23°C	500	1.0 V = 500 ppm
10°C	500	1.0 V = 500 ppm
-7°C	200	1.0 V = 1000 ppm

Table 7.2.3: Fast FID gain values at each engine operating temperature

A similar skip-firing technique to the one detailed in *Chapter 6* was used for sampling UHCs at the coldest operating temperatures. This allowed all traces of UHCs to be exhausted from the cylinder and repeatable data to be collect during an engine run.

7.3   RESULTS AND DISCUSSION

This section presents particulate number (PN) emissions data and unburned hydrocarbon (HC) emissions data over the engine operating temperature range described in the previous section and aligned with the testing throughout this thesis. The results have been correlated to the previously discussed in-cylinder fuel spray, combustion and pressure data presented in *Chapters 4, 5 and 6* where possible in order to attain a more complete understanding of the in-cylinder combustion processes occurring during cold-start.

7.3.1   PN Emissions Measurements

Particulate number (PN) emissions data has been presented in two forms to help further interpret the effect that operating temperature had on particulate generation. A contour-time plot has been created for each operating temperature, this displays particle number concentration ($dN/dlogD_P/cm^3$) and particle diameter (nm) over the entire engine run time of 600 seconds. This plot helps understand when different particle sizes were emitted and how the size distribution evolved over time as the engine warmed up. Furthermore, a particle size number distribution graph has been presented, encompassing all operating temperatures and highlighting the contrasting particle sizes emitted.

Figure 7.3.1 to Figure 7.3.4 shows contour time plots for the four operating temperatures with a 23°C intake air temperature. In addition, Figure 7.3.1 illustrates the 80°C head and liner condition with a -7°C intake temperature for comparison. The effect of a -7°C intake charge on the colder head and liner temperatures was much less discernible, so was omitted.

Major and minor striations within the contour plots can be observed in all the figures. As previously discussed, the major striations were caused due to the dilution factor being changed during the test run, in order to optimise the measurement range of the equipment. These can be observed as momentary changes in colour (striations) across the majority of the particle size range that lasted for a few seconds, until the equipment equalised the flow rate. The major striations could have been removed from the data but act as useful indicators of when dilution factor changes had taken place and prevent the misinterpretation of the data. The first dilution factor change typically occurred between 80 and 150 seconds after the start of the engine run, when an initial 'drop-off' of PN was seen due to the natural increasing of the engine operating temperature during combustion.

The minor striations (more prevalent at the 80°C operating condition) have been attributed to a number of factors. Fundamentally, the single cylinder research engine that operated at a throttled condition produced a relatively low quantity of PM along with an exhaust flow of a more defined pulsatile nature. As a result, the signal-to-noise ratio was low (compared to a multi-cylinder production engine), which is exemplified in the 80°C condition (Figure 7.3.1) in which a lower quantity of PM required a lower dilution factor and produced the noisiest signal. Additionally, the cycle to cycle variability that is inherent in IC engines will have had some contributory effect the PN signal instability.

The 80°C operating condition with a 23°C intake temperature (shown in the top graph in Figure 7.3.1) highlighted a clear but short peak in the PN emissions (1×10^8 dN/dlogD$_P$/cm^3) of particles up to 100 nm in the first 10 seconds when the engine was at its coolest. A sudden decrease in the emission of particles 20 nm – 100 nm to the order 1×10^7 dN/dlogD$_P$/cm^3 is then observed whilst a peak in large particles is then observed up to 200 nm. Particles of 20 nm and below continue to be emitted for a further 140 seconds. At approximately 150 seconds after the start of the test run, another decrease in PN emissions occurred to the point where small quantities of particles of 10 nm and lower were emitted and the signal was dominated by noise for the remainder of the test run (due to the low dilution factor required to detect any PN emissions). A more detailed discussion of the particle sizes emitted and their modes is given later in this section when referring to the particle size number distribution graphs in Figure 7.3.5 and Figure 7.3.6.

The -7°C intake condition (shown in the lower graph in Figure 7.3.1) showed a similar trend but the larger particles up to 200 nm were emitted from the start of the test run and for a longer period. This increase in particle size emission can be attributed to the cold intake air's interaction with fuel spray, which was shown to have a notable effect on the presence of liquid fuel in the fuel spray and subsequent combustion in *Chapters 4 and 5.* The colder intake air was previously shown to increase the presence of larger fuel droplet in the fuel spray and rich regions in the flame, which are known areas of PM generation. The -7°C intake air condition with operating temperatures lower than 80°C had no notable effect on the PN emission contour plots. A similar result was observed with the in-cylinder fuel spray and combustion data and it is reasonable to assume that the smaller temperature differences between the intake air and engine (when compared to the 80°C operating condition) minimised its effect.

The significant drop-off in the quantity of PN emissions and their size observed in the 80°C test condition (Figure 7.3.1) around 130 seconds after engine start was most probably due to a

number of factors. Over time, the combustion process gradually heated up the internal surfaces such as the cylinder liner, piston crown and pent roof combustion chamber, which aided vaporisation of impinged fuel to a point that adequately minimised its presence by the time of spark ignition. The heating of the fuel injector tip, which was important at all operating conditions, will have also increased the effect of localised flash boiling of the fuel during injection (as observed in the 80°C condition in *Chapter 5*) promoting good atomisation and minimising impingement.
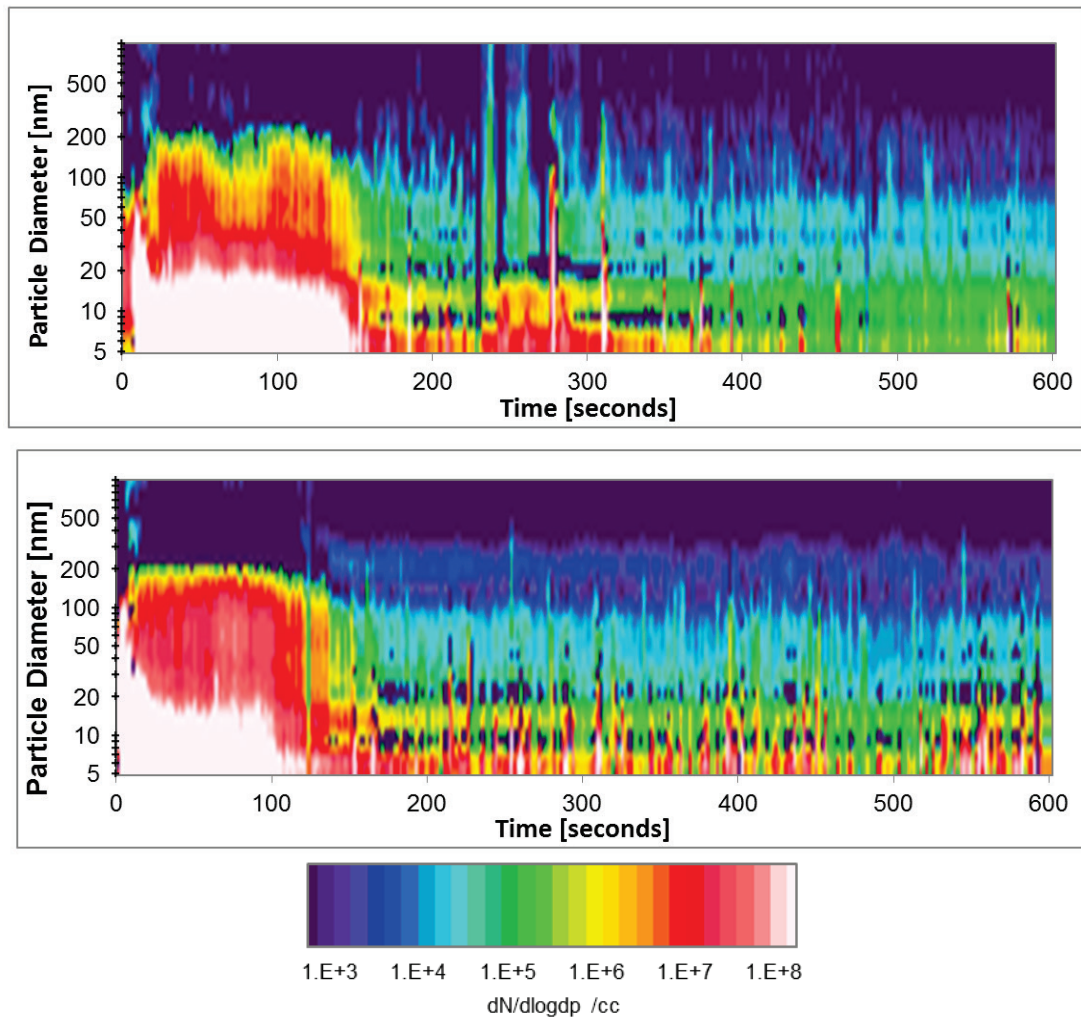
Figure 7.3.1: DMS500 contour plot at 80°C operating temperature and 23°C intake (top) and -7°C (bottom)

The colder operating conditions exhibit contrasting contour time plots to the 80°C condition in that significant drop-offs in PN emissions were not apparent (Figure 7.3.2, Figure 7.3.3 and Figure 7.3.4). Unlike the hottest operating temperature, particles of 5 nm – 200 nm at orders of 1×10^6 dN/dlogD$_P$/cm^3 and higher were consistently emitted. This was likely due to the colder recirculating coolant preventing the engine operating temperature rising, however, over longer operating times (approximately 300 seconds), it would be reasonable to assume that

the engine would heat up and affect the PN emissions in the same way that occurred in the 80°C condition.

The 23°C (Figure 7.3.2) and 10°C (Figure 7.3.3) operating conditions exhibited very similar emissions contour plots over time, as may be expected due to the similarity between their operating temperatures. Both contour plots highlighted the initial emission of particles up to 200 nm at a high magnitude of 1×10^8 dN/dlogD$_P$/cm^3 before a reduction in particle emissions sized from 20 nm – 200 nm and the continued high magnitude emission of particles 20 nm and smaller. A second reduction in the emission in larger sized particles is then observed leaving the continued emission of particles sized 7 nm and lower at a magnitude of at least 1×10^7 dN/dlogD$_P$/cm^3 until the end of the test run. The most apparent difference between the 23°C and 10°C test condition was that the 10°C condition emitted larger size particles for approximately 20 seconds longer before each of the described reductions, which could be attributed to the difference in the initial operating temperature and the time required for the combustion process to heat the engine.
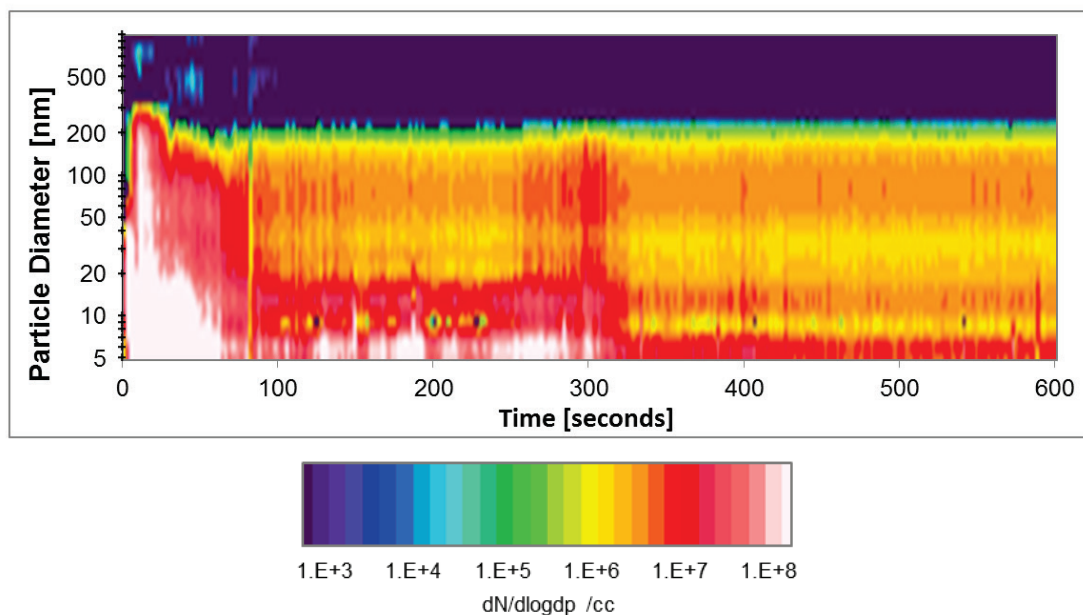

Figure 7.3.2: DMS500 contour plot at 23°C operating temperature and 23°C intake
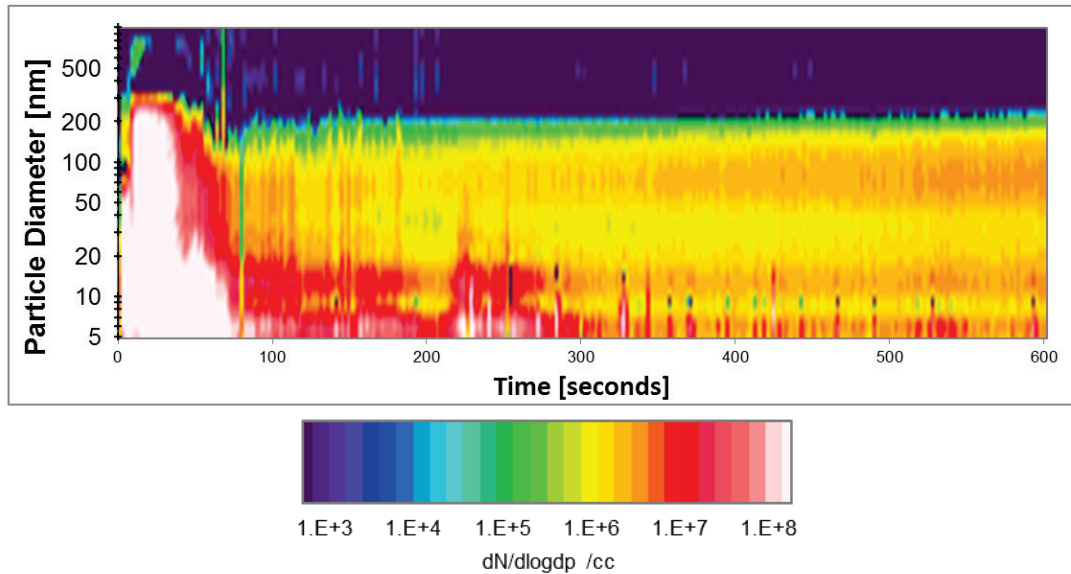
Figure 7.3.3: DMS500 contour plot at 10°C operating temperature and 23°C intake

The -7°C operating condition (Figure 7.3.4), like the in-cylinder combustion flame imaging data, exhibited strikingly different results to all the other operating conditions, with a PN concentration comparable to that of diesel engines under steady-state operating conditions (Andersson *et al.* 1999, Kittelson *et al.* 2003, Price *et al.* 2007) . The flame imaging data presented in *Chapter 4* highlighted a dramatically increased number of fuel rich regions with a high luminosity throughout the flame that consisted of large fuel droplets and ligaments. It was commented that these carbon-rich regions are known sources of PM generation as carbons atoms can combine to form aromatic ring structures that in turn nucleate to form PM (Gupta *et al.* 2000, Cromas and Ghandhi 2005, Price *et al.* 2006). These processes were confirmed in the PM emission data for the -7°C operating condition. A consistent emission of particles up to 200 nm at a magnitude of 1×10^8 dN/dlogD$_P$/cm^3 was recorded for the first 80 seconds of the test, which was the highest by some margin. A more gradual reduction in the size of particles being emitted at this peak magnitude (as opposed to the highly stepped reductions seen previously) was then recorded until approximately 280 seconds when the highest magnitude of any particle size emitted reduced to 1×10^7 dN/dlogD$_P$/cm^3. This more gradual reduction was most probably due to the colder coolant (approximately -10°C) circulating though the engine throughout the test, which would have reduced the time for combustion to raise the engine operating temperature. By approximately 400 seconds into the test run, the PM emissions were comparable to the 10°C and 23°C conditions, which indicated that the engine had heated up to a similar temperature to these conditions (this was confirmed from the thermocouple measurements). A reduction in PN concentration (similarly by an order of magnitude) when coolant temperature was increased in a similarly configured

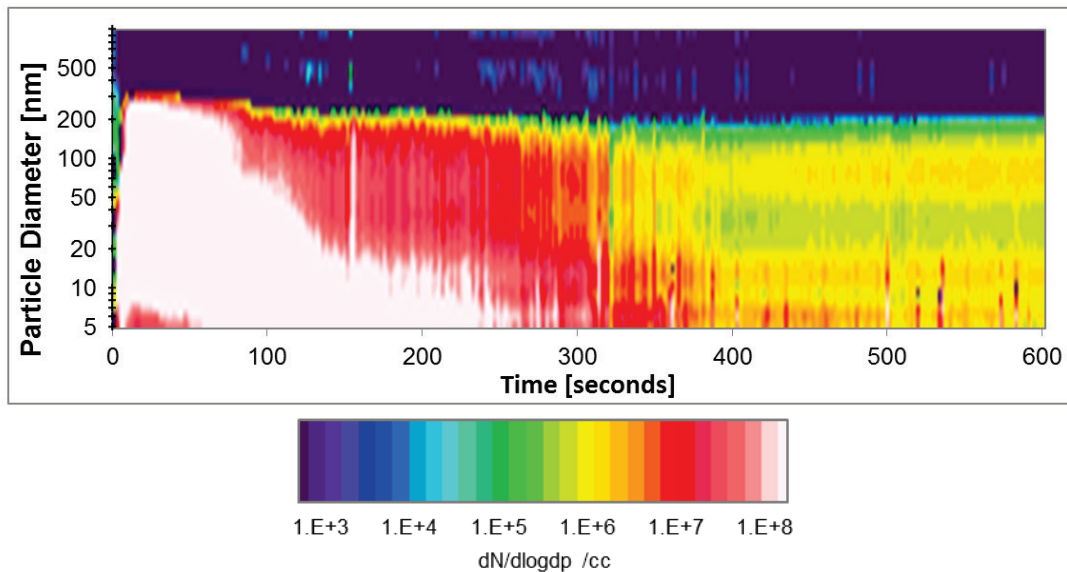engine has been shown by Price *et al.* (2007) and during a cold-start test by Samuel *et al.* (2010).

Figure 7.3.4: DMS500 contour plot at -7°C operating temperature and 23°C intake

The next analysis interprets the PM emissions data on particle size number distribution graphs, which represent particles emitted in the nucleation and accumulation modes. There are a number of nucleation mode and accumulation mode size ranges that have been published, with slight differences between them. The work presented in this section has used the size ranges defined by (Kulkarni *et al.* 2011) with nucleation mode size range of d_p = 5-100 nm and accumulation mode size range of d_p = 100-1000 nm. It is well understood that primary soot particles, sized within the nucleation mode, are typically generated within the rich regions of combustion flames due to the heterogeneous charge mixtures (Heywood 1988, Virtanen *et al.* 2004). This is dependent on engine load, however, as Andrews and Ahamed (1999) suggested that the soot fraction of PM generally only constitutes a small fraction of the total PM mass and Price *et al.* (2007) showed this to be only 29% in a DISI engine, whilst Andersson *et al.* (1999) conversely discovered that PM emissions in a DISI engine were more similar to that of a diesel engine, with a 72% soot concentration. Accumulation mode particles can be considered to be agglomerates of these soot particles along with volatile matter, which have been shown to form from such compounds as HCs (Samuel *et al.* 2010). PM generation from lubrication oil can be neglected, as the optical research engine utilised torlon piston rings that required no form of lubrication when used with the steel liner.

Figure 7.3.5 shows a size number distribution graph comparing all engine operating temperatures with a 23°C intake temperature. The 80°C condition showed a lognormal distribution of particles with a peak centred at round 8 nm within the nucleation mode. As the operating temperature was decreased to 23°C and then 10°C, the number concentration of particles around 8 – 10 nm decreased but the lognormal distribution of particles started to transition to bimodal with some particles being emitted in the accumulation mode. This was also represented in the previously presented contour plots as brief peaks in particle emissions up to 200 nm at the start of each run.

The -7°C operating condition shows a striking rise in the number concentration of particles and a bimodal lognormal distribution with a large peak at 12 nm and a smaller peak 140 nm. This rise correlates with the PM contour plot distribution over time and the in-cylinder flame analysis detailed in *Chapter 4*. At all test conditions, the emitted particles had a tendency towards the larger accumulation mode size range at the start of the test run before trending towards the nucleation mode as the engine heated up due to combustion, which was also shown by Price *et al.* (2007) in a similarly configured engine with a starting coolant temperature of -10°C.
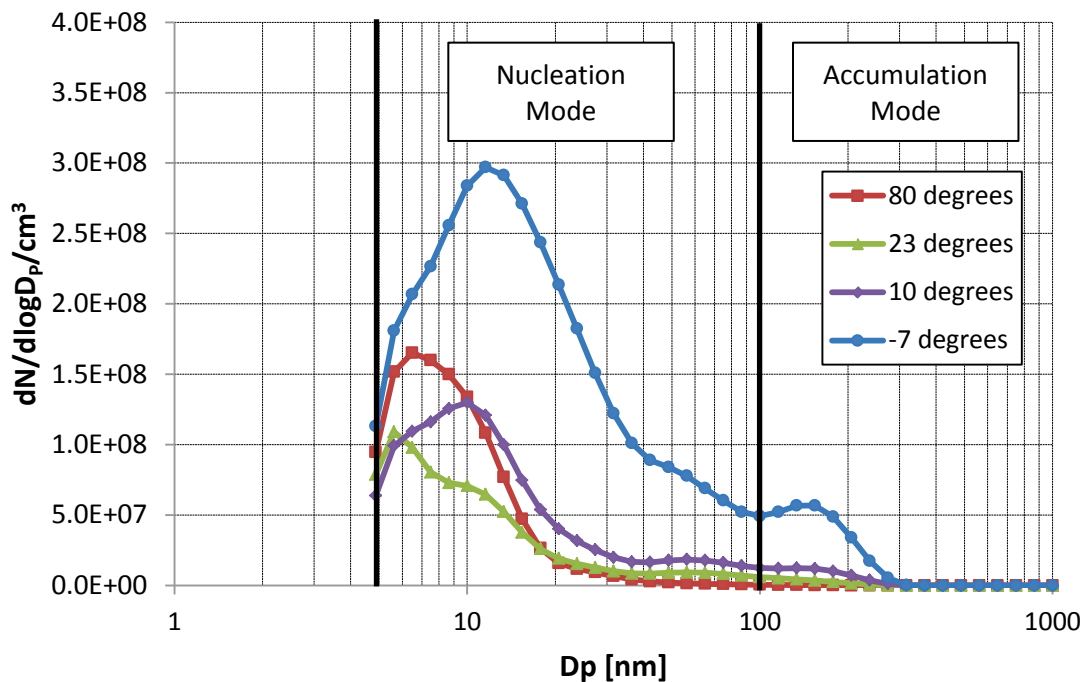

Figure 7.3.5: DMS500 size number distribution at all operating temperatures and 23°C intake

To independently observe the effects of a -7°C charge temperature on the emissions process, Figure 7.3.6 shows a PM size number distribution graph of the 80°C and -7°C operating conditions with both intake air temperatures. With the 80°C condition, a smaller number concentration of particles with a lognormal distribution centred around 6 – 8 nm was measured but a higher concentration of particle emissions up to a size of 100 nm was recorded. This increase in larger particle emissions correlated with the in-cylinder flame data discussed in *Chapter 4,* whereby the -7°C temperature charge was observed to interact with the fuel spray and cause locally rich areas of poorly vaporised fuel in the flame. In the -7°C operating condition, the effect of charge temperature was much less profound with no clear difference in lognormal size distribution.
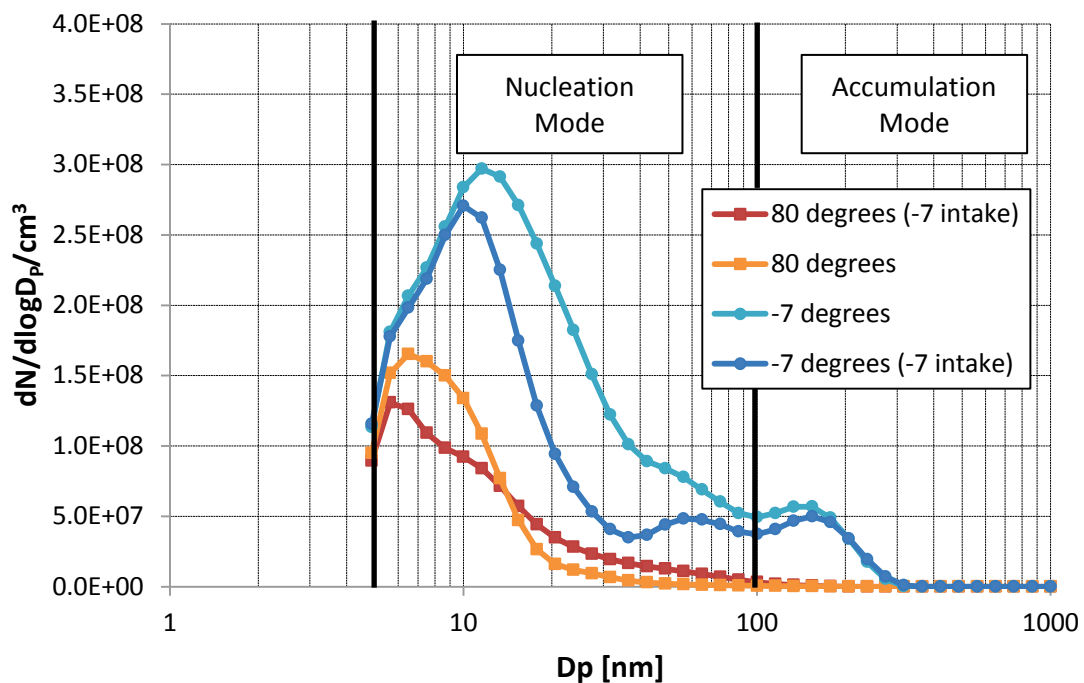
Figure 7.3.6: DMS500 size number distribution at 80°C and -7°C operating temperatures and 23°C and -7°C intake

The PM emissions from the engine that were emitted during the range of tested operating temperatures are dominated by particles of less than 100 nm. This correlates with emissions data from a similarly configured engine by Price *et al.* (2007) who also characterised these emissions as consisting of condensed material such as anamorphous and graphitised elemental carbon using transmission electron microscopy.

One must also bear in mind the effect that a three-way catalyst (TWC), although not installed on this research engine, will have on PM emissions once it has achieved light-off temperatures. Once heated, the TWC has been shown to reduce PN number concentrations of all size ranges, but in particular, those within the accumulation modes (Samuel *et al.* 2010) and has been shown to remove up to 30% of carbon from cold-start conditions (Andrews and Ahamed 1999).

It has been shown that HC emissions can participate in the formation of volatile nanoparticles in the dilution system of PM measurement equipment such as the DMS500 (Samuel *et al.* 2010). As it has been deduced that a significant quantity of HC species exist in exhaust under cold-start conditions (Samuel *et al.* 2010) the fast FID HC analysis will aid the interpretation of the sources of PM emissions in addition to the in-cylinder sources of HC emissions.

7.3.2   HC Emissions Measurement

Mean unburned HC emissions data has been presented for the complete range of engine operating conditions over the entire 300 engine cycle data set between a crank angle range of 116 °CA to 366 °CA ATDC$_C$ in order to capture the exhaust valves opening and closing events. Outside of this crank angle range when the exhaust valves were closed, the HC emissions of the stagnant flow around the fast FID detector were measured, so were not included in the presented graph. Mean in-cylinder pressure data was overlaid on the same graph between a crank angle range of -90 °CA to 450 °CA ATDC$_C$ to help interpret the timing of the exhaust event after combustion. HC data was recorded using the DAQ system that captured in-cylinder pressure data in order to align the emissions data with valve events. Between exhaust valve opening (EVO) and exhaust valve closing (EVC) event, 1500 samples of HC emissions data was collected over a time period of 15 ms. The results from a cooled intake charge have been omitted as no considerable effect was observed in the HC emissions data.

Figure 7.3.7 shows mean ensemble-averaged HC emissions plot for each operating condition as well as the mean in-cylinder pressure trace overlaid and EVO and EVC events indicated. In all plots, the HC emissions trace began with a background level before the exhaust valve opened. This is due to the quiescent gas left around the exhaust port area and in the vicinity of the fast FID probe from the previous firing cycle whilst the exhaust valves were still closed. Each of the HC plots exhibited a similar trend between the exhaust valve events that can be used to describe the location and nature of the HC emission. The initial level of HC emissions in all plots after the EVO event (around 110 °CA) represented the HC emissions from crevice regions in the valve area, this may include those around the valve seat or in the pent-roof

combustion chamber area in general. The plots then decreased gradually in HC levels until approximately 240 °CA, which represented the majority of the burned gas being exhausted from the cylinder. Exhaust HC measurements on a PFI engine typically reduce at a much greater rate after the exhaust valve is opened (Hoard and Moilanen 1997). The more gradual decrease shown in Figure 7.3.7 at all operating temperatures highlighted the increased presence of less vaporised fuel in the cylinder before and consequently after combustion, due to the nature of DISI in-cylinder fuel injection.

From 240°CA in the exhaust stroke, up to TDC of the exhaust stroke (360 °CA) represented the 'scroll-up' HC emissions. These 'scroll-up' emissions originated from the cylinder walls and crevice regions in the piston ring pack as the piston moved toward TDC (Hoard and Moilanen 1997). The HC emissions then rose as the exhaust valves started to close and reached a peak at TDC that remained until the exhaust valves opened in the next cycle. This peak in emissions represented the stagnation of crevice HCs around exhaust port and the fast FID probe, which dipped slightly due to flow momentum before remaining stagnant.

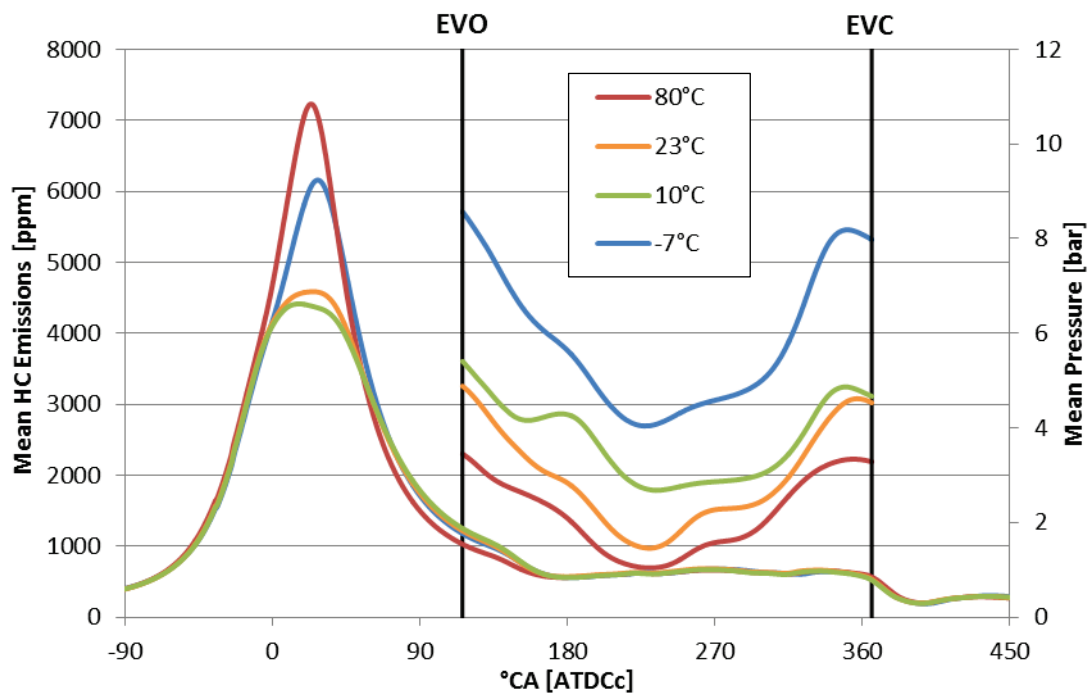**Figure 7.3.7: Fast FID mean HC emissions graph at all operating temperatures with in-cylinder pressure overlaid for 300 engine cycles (23°C intake)**

As with the PN emissions, the levels of HC emissions clearly correlate with engine operating temperature in that cooling the engine down produced an increased quantity of HC emissions (shown in Figure 7.3.7). The -7°C condition exhibited considerably higher mean HC emissions

concentration throughout the exhaust stroke when compared to the other conditions, with the emissions peaking at around 5500 ppm when the exhaust valves opened and remaining above 2700 ppm throughout the stroke.

The shape of the mean emissions plot for -7°C condition (Figure 7.3.7) masked some of the subtle trends shown in the other temperature cases due to the variability of each individual HC emissions plot. This variability has been expounded later in this section. The 10°C condition displayed a short and distinct peak in HC emissions at approximately 180 °CA, which showed the consistent presence of HCs in the bulk of the burned gas during the exhaust stroke. The -7°C operating condition also exhibited this trend when instantaneous emissions cycles were observed (Figure 7.3.8). This is consistent with the increased presence of rich-burning regions observed in the flame at colder operating temperatures, which was analysed in *Chapter 4* and indicated the presence of HC emissions. The imaged fuel spray in *Chapter 5* consistently highlighted the presence of surface impingement, particularly with the colder operating temperatures. It is reasonable to assume that the observed fuel impingement considerably contributed to the generation of HCs that were measured in the exhaust.
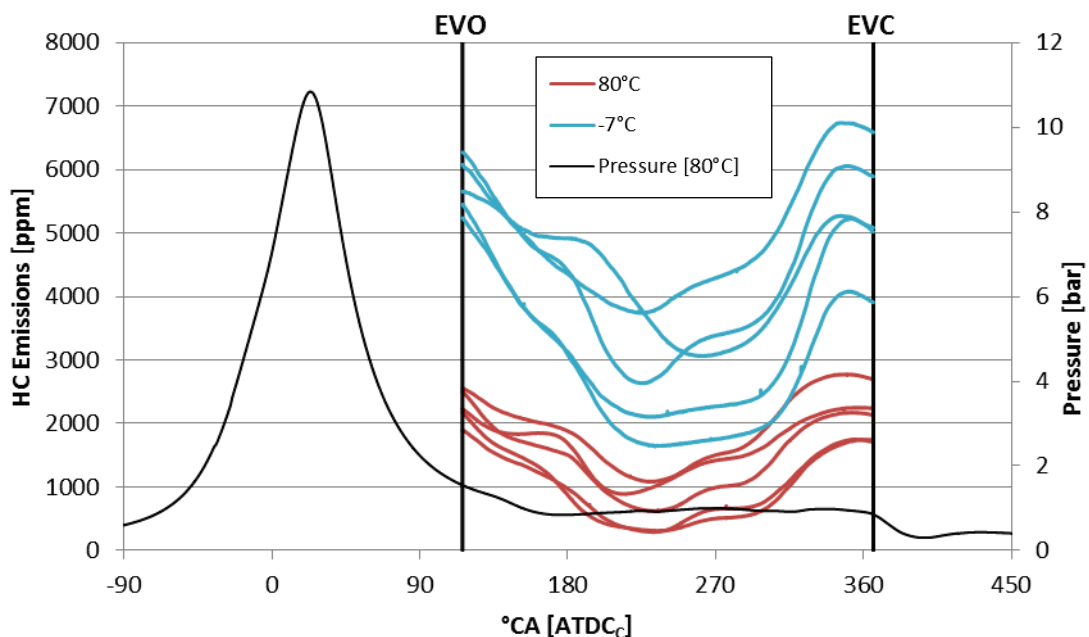
Figure 7.3.8: Fast FID instantaneous HC emissions graph of 5 arbitrary at 80°C and -7°C operating temperatures with in-cylinder pressure overlaid (23°C intake)

To analyse the consistency of HC emissions between individual engine cycles Figure 7.3.8 presents five arbitrary HC emissions plots for the 80°C and -7°C operating temperatures. A striking inconsistency between cycles was observed at both operating temperatures and highlighted the inherent cycle-to-cycle variability that contributed to the HC emissions. This

considerable variability also elucidates why no clear effect was shown on by cooling the intake air.

The 80°C HC emissions plots followed the same general trends as each other but were different in absolute magnitude. Conversely, the -7°C condition exhibited strikingly differences in the levels of HC emissions as well as the trends of these emissions. This correlates with the increasing COV of IMEP that was calculated in *Chapter 4* and revealed a decrease in engine combustion stability at lower operating temperatures.

7.4   CONLCUDING REMARKS

In order to further elucidate and correlate operating temperature with in-cylinder fuel spray, combustion and pressure, this chapter presented data for measured PM and HC emissions of the optical engine at a range of operating temperatures. The PN emissions data allowed the lognormal distribution of particles along with their concentration to be recorded and correlated with both operating temperature and the warm-up process of the engine. The fast FID analysis provided cycle-resolved HC emissions data, which enabled the precise in-cylinder sources of HCs to be commented on. A distinct correlation was shown between these emissions and operating temperature along with a clear link to the previous in-cylinder analyses. The main conclusions from this part of the investigation are:

1. A clear correlation between the size distribution and number concentration of particulates and operating temperature was shown. The coolest -7°C condition exhibited a number concentration of 3×10^8 dN/dlogD$_P$/cm^3 over a wider lognormal distribution of particle sizes, compared to approximately 1.5×10^8 dN/dlogD$_P$/cm^3 for the remaining temperature conditions. The presence of larger PM particles sized within the accumulation mode was also recorded for the coolest condition. This correlation agreed with both the HC emissions data and the in-cylinder flame analysis, which identified fuel-rich regions in the flame and highlighted the dominant effect of cooling the engine down to -7°C.

2. At an engine operating temperature of 80°C, the independent effect of cooling the intake air to -7°C was shown to generated particulates that were 100 nm larger than using an intake air temperature of 23°C. This effect was previously observed in the flame and fuel spray imaging analyses as droplets of fuel that subsequently formed rich regions in the flame.

3. The fast FID analysis identified the dominant sources of HC emissions within the cylinder during the exhaust stroke across the range of operating conditions and drew particular focus to the striking inconsistencies between individual exhaust cycle emissions, particularly at colder temperatures. The analysis also helped determine the in-cylinder location of HC emissions, which are linked to fuel spray impingement observed in *Chapter 5.*

This chapter has brought together the knowledge gained from optical diagnostics, in-cylinder pressure data and emissions data to help build an understanding of the effect that operating temperature has on the complex in-cylinder processes of the engine that subsequently form exhaust emissions. The next chapter will bring together the catalogue of achievements and conclusions from this thesis and recommend the potential areas for further investigation.

7.5   CHAPTER 7 REFERENCES

ANDERSSON, J., COLLIER, A., GARRETT, M. & WEDEKIND, B. (1999) Particle and Sulphur Species as Key Issues in Gasoline Direct Injection Exhaust, SAE Paper 9935842 (JSAE).

ANDREWS, G. E. & AHAMED, F. M. (1999) The Composition of Spark Ignition Engine Steady State Particulate Emissions, SAE Paper 1999-01-1143.

CROMAS, J. & GHANDHI, J. B. (2005) Particulate Emissions from a Direct-Injection Spark-Ignition Engine, SAE Paper 2005-01-0103.

GUPTA, S., POOLA, R., O.L., K. & SEKAR, R. (2000) Particulate Emissions Characteristics of Port-Fuel Injected SI Engine. *US Dept. of Energy*.

HEYWOOD, J. B. (1988) *Internal Combustion Engine Fundamentals,* 1st Ed., McGraw-Hill, pp. 42-61, 205-278, 400-450, 797-819.

HOARD, J. & MOILANEN, P. (1997) Exhaust Valve Seat Leakage, SAE Paper 971638.

KITTELSON, D. B., WATTS, W. F., JOHNSON, J. B., ZARLING, D., SCHAUER, J., KASPER, A., BALTENSPERGER, U. & BURTSCHER, H. (2003) Gasoline Vehicle Exhaust Particle Sampling Study. *Proceeding of the 9th Diesel Engine Emission Reduction Conference (DEER 2003),.* Newport, RI.

KULKARNI, P., BARON, P. A. & WILLEKE, K. (2011) *Aerosol Measurement Principles, Techniques and Application*, Wiley, Vol. 3.

PRICE, P., STONE, R., COLLIER, T. & DAVIES, M. (2006) Particulate Matter and Hydrocarbon Emissions Measurements: Comparing First and Second Generation DISI with PFI in Single Cylinder Optical Engines, SAE Paper 2006-01-1263.

PRICE, P., STONE, R., OUDENIJEWEME, D. & CHEN, X. (2007) Cold Start Particulate Emissions From a Second-Generation DI Gasoline Engine, SAE Paper 2007-01-1931.

SAMUEL, S., HASSANEEN, A. & MORREY, D. (2010) Particulate Matter Emissions and the Role of Catalytic Converter During Cold Start of GDI Engine, SAE Paper 2010-01-2122.

VIRTANEN, A. K. K., RISTIMAKI, J. M., VAARASLAHTI, K. M. & KESKINEN, J. (2004) Effect of Engine Load on Diesel Soot Particles. *Environ. Sci. Technol. 2004,* Vol 38(9), pp. 2551-2556.

CHAPTER 8

CONCLUSIONS AND RECOMMENDATIONS FOR FURTHER WORK

8.1   RESEARCH SUMMARY

A single cylinder DISI optical research engine has been used to investigate the effects of cold-start temperatures on combustion, fuel spray and emissions. The modifications to the research engine to simulate cold-start conditions and the range of experimental and analytical techniques used for analysis have been presented in this thesis.

In-cylinder visualisation of both the combustion and fuel injection processes at a range of operating conditions has provided novel, new and valuable information to better understand the complex effects of cold-start. The dominant effects that engine operating and intake temperatures as low as -7°C have on flame propagation, fuel spray structure, fuel spray impingement and particulate formation have been identified. In-cylinder pressure and engine performance data has been collected and shown to correlate with optical analyses to help further classify these effects.

A novel approach has been made that simulated a production engine cold-start strategy on an optical research engine over repeated engine cycles. Colour optical and in-cylinder pressure analysis of the combustion process have revealed a broad range of striking flame regimes and helped identify the dynamic stoichiometry of the flame propagation process and a number of sources of particulate generation. HSPIV was used to collect detailed temporal flow and turbulence data of complex in-cylinder flow field and identify its effect on the fuel injection and combustion processes, which ultimately lead to particulate formation.

A thorough exhaust sampling study on particulates and unburned HCs has been used to validate much of the in-cylinder optical analyses and accurately quantify the effect of operating temperature on emissions. The different size regimes of emitted particulates and the in-cylinder location of emitted unburned HC have been accurately quantified.

8.2   CONCLUSIONS

The work conducted has led to an improved understanding of cold-start and the effects that cold-start temperatures have on the complex combustion, fuel spray and emissions processes during DISI engine operation. The major conclusions that can be drawn from this experimental investigation are:

Chapter 3 – Experimental Setup and Equipment

1. The modification to an optical engine coolant system and air intake has enabled a -7°C cold-start condition and production cold-start strategy to be accurately simulated and the effects of this condition to be accurately analysed using a combination of high-speed optical diagnostics, in-cylinder pressure measurements and exhaust gas measurements.

Chapter 4 – The Effect of Operating Temperature on DISI Engine Combustion

2. Cooling the engine operating temperature to -7°C was shown to dramatically affect the in-cylinder peak pressure, performance and engine stability during the combustion process. Peak pressures were shown to drop by up to 5 bar when the engine was cooled from 80°C to -7°C and the COV of peak pressure rose by 7%. Gross IMEP decreased by 0.5 bar and the COV of gross IMEP increased by up to 15%.

3. High-speed imaging of the in-cylinder combustion process highlighted contrasting flame growth structures at different operating temperatures and at lower operating temperatures, identified the widespread presence of fuel-rich regions, areas of flame heterogeneity and lower flame growth speeds. These fuel-rich regions are known areas of particulate formation and highlight the impact that temperature as on the early phase during cold-start.

4. Flame image processing highlighted a striking difference in peak flame growth speed of up to $4\,\mathrm{m\cdot s^{-1}}$ between the fully heated 80°C operating condition and the colder conditions. The processed flame data correlated well with the in-cylinder pressure data, highlighting high-speed flame imaging as a useful diagnostics tool in the analysis of engine combustion.

Chapter 5 – The Effect of Operating Temperature on DISI Fuel Injection

5. High-speed fuel spray imaging at range of operating temperature revealed that flash boiling of the fuel spray consistently occurred when the engine was operating at 80°C. This resulted in a highly atomised fuel spray that penetrated only 30 mm into the cylinder and did not visibly impinge on the piston crown surface. The flash-boiled spray demonstrated a higher level of visible atomisation and was observed to be influenced and transported more by intake flow structures in the cylinder, resulting in better charge mixing. These factors help understand the improved engine combustion performance and flame structure previously identified at an operating condition of 80°C.

6. The fuel spray imaging at colder temperatures exhibited highly contrasting fuel spray structures that did no flash boil at lower operating temperatures. These fuel spray structures penetrated in to the cylinder at a quicker ate and contained a denser liquid core that was observed to consistently impinge on the piston crown surface as early as 10 °CA ASOI. This type of fuel spray structure was shown to contribute to a lower peak cylinder, pressure, poorer combustion performance and the abundance of fuel-rich regions in the flame, as highlighted in the previous combustion analyses.

7. Statistical analyses of the fuel spray images over 300 cycles showed that the fuel sprays for the 23°C, 10°C and -7°C operating conditions exhibited very similar structures with only marginal differences in penetration depth. RMS analysis of the fuel spray images highlighted the tip of the spray plumes (that interact with the intake flow structures) as having the most variability during the injection process. This reiterated the important effect that the complex in-cylinder flow structures have on the transportation and vaporisation of the fuel spray.

Chapter 6 – The Influence of Turbulent Flow Structures on DISI Engine Cold-Start

8. When simulating a production engine cold start-up process, in cylinder peak pressures were shown to vary significantly across the five test points representing the first few seconds of the cold start-up. A variation of 12.8 bar in peak pressure and range of COV of peak pressure of 13.8% was observed, highlighting the key differences in chosen operating modes, each with a different objective to the engine's operation. MFB times also showed a wide variation with up to a 50 °CA difference in burn time and 8.5% difference COV for the 90% MFB case.

9. The effect of fuel pressure, which varied considerably during the cold start-up, was shown to have a prominent effect on both the in-cylinder pressure and flame data. A vast array of in-cylinder stoichiometry was observed, which likely had an effect on the subsequent engine emissions and emphasised the importance of pressurising the fuel rail in a short as time as possible during DISI engine cold-start.

10. Combustion imaging data during the cold start-up correlated with the recorded in-cylinder pressure, identifying an array of contrasting flame structures that behaved in very different ways depending on their parameter scheduling, fuel pressure and intake and flow conditions. The very first firing cycle at 140 rpm, for example, exhibited an in-cylinder pressure trace that was analogous to diesel combustion and the flame imaging data revealed a laminar flame front that took nearly four times as long to reach the cylinder walls.

11. High-speed imaging of the combustion process during the cold start-up identified a number of soot formation regions in nearly all of the experimental test points and highlight the detrimental effect that cold start-up has on PN count emissions.

12. In-cylinder HSPIV flow field analysis of the cold start-up process identified the critical flow structures and turbulence present that had an effect on fuel injection, transportation and mixing, as well as the subsequent combustion and emissions formation processes. Over the five test points, the mean peak valve jet velocities were shown to range from 2.0 m·s^{-1} to 70 m·s^{-1} due to the range in engine speed.

Chapter 7 – The Effect of DISI Engine Cold-Start on Emissions

13. The particulate emissions analysis highlighted a clear correlation between the size distribution and number concentration of particulates with operating temperature. The coldest -7°C condition exhibited a number concentration of 3×10^{8} $\text{dN/dlogD}_P/\text{cm}^3$ over a wider lognormal distribution of particle sizes, compared to approximately 1.5×10^{8} $\text{dN/dlogD}_P/\text{cm}^3$ for the remaining temperature conditions. The presence of larger PM particles that were sized within the accumulation mode was also recorded for the -7°C condition. This correlation agreed with both the HC emissions data and the in-cylinder flame analysis, which identified fuel-rich regions in the flame and highlighted the dominant effect of cooling the engine down to -7°C.

14. At an engine operating temperature of 80°C, the independent effect of cooling the intake air to -7°C was shown to generated particulates that were 100 nm larger than using an intake air temperature of 23°C. This effect was previously observed in the flame and fuel spray imaging analyses as droplets of fuel that subsequently formed rich regions in the flame.

15. The fast FID analysis identified the dominant sources of HC emissions within the cylinder during the exhaust stroke across the range of operating conditions. These were shown to be the crevice regions around the exhaust valves at the time of opening and the cylinder walls and piston ring pack as the piston moved towards TDC. HC emissions levels showed a strong correlation with engine operating temperature and also drew particular focus to the striking inconsistencies between individual exhaust cycle emissions, particularly at colder temperatures.

8.3   RECOMMENDATIONS FOR FURTHER WORK

The work presented in this thesis has led to a number of significant conclusions regarding an improved understanding of the cold-start combustion, injection and emissions processes of DISI engines. During the course of this investigation, several areas of further study were identified that would further improve knowledge within this area and further aid the reduction of PN emissions to meet the needs of stringent upcoming PN legislation:

1. *Chapter 6* investigated a production cold start-up process by simulated five test points across the process in steady-state. Although this held the benefit of allowing the collection of a large amount of continuous cycle data, it was not how the start-up process was intended to operate. Operating the engine in a fully transient manner, with an engine driven fuel pump and fully variable intake throttle would facilitate the ability to run an engine cold start-up from a stationary engine speed. This would enable the effect of residual fuel from cycle-to-cycle to be observed and allow a novel methodology of cold start-up strategy testing to be devised. Considerable infrastructure upgrades would be required to facilitate this capability, which would include an upgraded motor control system, a new fuel pump and common rail system and an electronic intake valve and ECU system.

2. The presented in-cylinder velocity flow field data captured high temporal resolution data over a large area of the cylinder plane using HSPIV at a rate of 1.5 kHz. This single-camera technique only allowed two components of velocity to be quantified in the desired plane, which limited the understanding of the highly complex three-dimensional in-cylinder flow. Using high-speed stereoscopic PIV will facilitate the ability to quantify three components of velocity within the desired measurement area. This will enable a much more accurate understanding of the complex in-cylinder flow and critically, the interaction with the fuel spray and combustion processes. This can help improve the understanding of the charge mixing process as well as how to aid charge mixing and minimise heterogeneity, particularly at low engine velocities during cold-start, which have a limited presence of turbulence flow structures. To enable the extra optical access required by two cameras imaging the same plane, modifications would be required to the cylinder head supports of the engine.

3. Utilising laser-induced fluorescence (LIF) on the engine during cold-start conditions would vastly improve the understanding of charge homogeneity during the charge mixing process and help identify critical areas of improvement, especially during cold-start. A multi-component fuel and tracer would need to be selected that provides the best excitation signal for the test conditions used. QPLIF could be used, as was performed by Williams *et al.* (2008), but the extensive time in selecting a suitable tracer, doping levels and calibration will limit its effectiveness when compared to standard LIF measurements.

REFERENCES

REFERENCES

ABRAHAM, J., WILLIAMS, F. A. & BRACCO, F. V. (1985) A Discussion of Turbulent Flame Structure in Premixed Charges, SAE Paper 850345.

AHMED, F., KAWAHARA, N., TOMITA, E. & MAMORU, S. (2010) Characterization of the Spray of the DISI Multi-hole Injector by Means of Phase Doppler Anemometer. Journal of Thermal Science and Technology, Vol 5(1), pp. 36-47.

ALEIFERIS, P. G., TAYLOR, A. M. K. P., ISHII, J. & URATA, Y. (2000) The Relative Effects of Fuel Concentration, Residual Gas Fraction, Gas Motion, Spark Energy and Heat Losses to the Electrodes in a Lean-Burn Spark-Ignition Engine. Journal of Automobile Engineering (Proceedings of IMechE, Part D), Vol 218, pp. 411-425.

ALEIFERIS, P. G., TAYLOR, A. M. K. P. & WHITELAW, J. H. (2000) Cyclic Variations of Initial Flame Kernel Growth in a Honda VTEC-E Lean-Burn Spark-Ignition Engine, SAE Paper 2000-01-1207.

ALGER, T., HALL, M. & MATTHEWS, R. D. (2000) Effects of Swirl and Tumble on In-Cylinder Fuel Distribution in a Central Injected DISI Engine, SAE Paper 2000-01-0533.

ALKIDAS, A. C. & TAHRY, S. H. (2003) Contributors to the Fuel Economy Advantage of DISI Engines Over PFI Engines, SAE Paper 2003-01-3101.

ANANDARAJAH, K. (2005) Digital particle image velocimetry (DPIV): Limitations to measurement accuracy, PhD Thesis, Loughborough University.

ANDERSSON, J., COLLIER, A., GARRETT, M. & WEDEKIND, B. (1999) Particle and Sulphur Species as Key Issues in Gasoline Direct Injection Exhaust, SAE Paper 9935842 (JSAE).

ANDERSSON, M., WÄRNBERG, J., HEMDAL, S., DAHLANDER, P. & DENBRATT, I. (2011) Evaporation of Gasoline-Like and Ethanol-Based Fuels in Hollow-Cone Sprays Investigated by Planar Laser-Induced Fluorescence and Mie Scattering SAE Paper 2011-01-1889.

ANDO, H. (1997) Mitsubishi GDI engine strategies to meet the European requirement. Proceedings of AVL Conference on Engine and Environment, Vol 2, pp. 55-77.

ANDREWS, G. E. & AHAMED, F. M. (1999) The Composition of Spark Ignition Engine Steady State Particulate Emissions, SAE Paper 1999-01-1143.

ANNAND, W. J. D. & ROE, G. E. (1974) Gas Flow in the Internal Combustion Engine. Yeovil Annual Book of ASTM Standards - Test Methods for Rating Motor, Diesel and Aviation Fuels, Vol 05(04).

ARCOUMANIS, C., HU, Z. & WHITELAW, J. H. (1993) Steady flow characterization of tumble-generating four-valve cylinder heads. Proc Instn Mech Engrs, Vol 207, pp. 203-210.

ASMUS, T. W. (1982) Valve Events and Engine Operation, SAE Paper 820749.

BERNDORFER, A., BREUER, S., PIOCK, W. & BACHO, P. V. (2013) Diffusion Combustion Phenomena in GDi Engines caused by Injection Process, SAE Paper 2013-01-0261.

BEVAN, K. E. & GHANDI, J. B. (2008) Particle Image Velocimetry Measurements of In-Cylinder Flow in a Four-Stroke Utility Engine and Correlation With Combustion Measurements. ASME Journal of Engineering for Gas Turbines and Power, Vol 130.

BIANCHI, G. M., CANTORE, G. & FONTANESI, S. (2002) Turbulence Modelling in CFD Simulation

of ICE Intake Flows: The Discharge Coefficient Prediction, SAE Paper 2002-01-1118.

BIANCO, Y., CHENG, W. K. & HEYWOOD, J. B. (1991) The effects of initial flame kernel conditions on flame development in SI engines, SAE Paper 912402.

BLOCK, B., OPPERMANN, W. & BUDACK, R. (2000) Luminosity and Laser-Induced Incandescence Investigations on a DI Gasoline Engine, SAE Paper 2000-01-2903.

BOHREN, C. F. & HUFFMAN, D. R. (1998) Absorption and Scattering of Light by Small Particles, Wiley-Interscience, Vol. 2.

BONANDRINI, G., GIOIA, R. D., PAPALEO, D. & VENTUROLI, L. (2012) Numerical Study on Multiple Injection Strategies in DISI Engines for Particulate Emission Control, SAE Paper 2012-01-0400.

BRADLEY, D., HAQ, M. Z., HICKS, R. A., KITAGAWA, T., LAWES, M., SHEPPARD, C. G. W. & WOOLLEY, R. (2003) Turbulent burning velocity, burned gas distribution, and associated flame surface definition. Combustion and Flame 133, Vol 133(2003).

BRADLEY, D., LAWES, M. & SHEPPARD, C. G. W. (2000) Combustion and the thermodynamic performance of spark ignition engines. Proc Instn Mech Engrs, Vol 214(C), pp. 257-268.

BRUNO, B. A., SANTAVICCA, D. A. & ZELLO, J. V. (2003) Fuel Injection Pressure Effects on the Cold Start Performance of a GDI Engine, SAE Paper 2003-01-3163.

CALENDINI, P. O. & DURVEGER, T. (2000) In-Cylinder Velocity Measurements with Stereoscopic Particle Image Velocimetry in a SI Engine, SAE Paper 2000-01-1798.

CAMBUSTION (2013) Cambustion DMS50 MkII, Available from: http://www.cambustion.com/sites/default/files/instruments/DMS500/DMS500aeroso l.pdf, [Accessed 06/11/2013].

CHAPMAN, J., GARRETT, M. W. & WARBURTON, A. (1991) A new standard for barrel swirl movement. IMechE Birmingham, 12-15 November 1991, Vol C427/18/156, pp. 157.

CHARALAMPOUS, G., HARDALUPAS, Y. & TAYLOR, A. M. K. P. (2009) Novel Technique for Measurements of Continuous Liquid Jet Core in an Atomizer. AIAA, Vol 47(11), pp. 2605-2615.

CHEN, X., FU, H., SMITH, S. & SANDFORD, M. (2009) Investigation of Combustion Robustness in Catalyst Heating Operation on a Spray Guided DISI Engine, SAE Paper 2009-01-1489.

CHOI, J., LEE, S., SHIN, H. & BAE, C. (2000) Fuel-Spray Characteristics of High Pressure Gasoline Injection in Flowing Fields. JSME Int J Fluids Thermal Eng B Vol 43, pp. 576-581.

CHRYSSAKIS, C. A., ASSANIS, D. N., LEE, J. K. & NISHIDA, K. (2003) Fuel Spray Simulation of High-Pressure Swirl-Injector for DISI Engines and Comparison with Laser Diagnostic Measurements, SAE Paper 2003-01-0007.

COLLINS, D. & STOKES, J. (1983) Gasoline combustion chambers - compact or open?, SAE Paper 830866.

CROMAS, J. & GHANDHI, J. B. (2005) Particulate Emissions from a Direct-Injection Spark-Ignition Engine, SAE Paper 2005-01-0103.

DAVY, M. H., WILLIAMS, P. A. & ANDERSON, R. W. (1998) Effects of Injection Timing on Liquid-Phase Fuel Distributions in a Centrally-Injected Four-Valve Direct-Injection Spark-Ignition Engine, SAE Paper 982699.

DE BOER, C. D., JOHNS, R. J. R., GRIGG, D. W., TRAIN, B. M., DENBRATT, I. & LINNA, J. R. (1990) Refinement with performance and economy for four-valve automotive engines. Proc. I.Mech.E. Conf. on Automotive Power Systems, Vol Paper C394(53), pp. 147-155.

DIESELNET (2015) European Union Emission Standards for Cars and Light Trucks, Available from: http://www.dieselnet.com/standards/eu/ld.php, [Accessed 01/06/2015].

DISCH, C., KUBACK, H., SPICHER, U., PFEIL, J., ALTENSCHMIDT, F. & SCHAUPP, U. (2013) Investigations of Spray-Induced Vortex Structures during Multiple Injections of a DISI Engine in Stratified Operation Using High-Speed-PIV, SAE Paper 2013-01-0563.

DRAIN, L. E. (1980) The Laser Doppler Technique, New York, John Wiley & Sons.

EFTHYMIOU, P., DAVY, M., GARNER, C., HARGRAVE, G., RIMMER, J. E. T. & RICHARDSON, D. (2013) Insights into Cold-Start DISI Combustion in an Optical Engine Operating at −7°C. SAE. Int. J. Engines, Vol 6(2), pp. 1059-1074.

EFTHYMIOU, P., DAVY, M. H., GARNER, C. P., HARGRAVE, G. K. & RIMMER, J. E. T. (2013) An optical investigation of a cold-start DISI engine startup strategy. IMechE: Fuel Systems for IC Engines, Vol 2013, pp. 33-52.

ENG, J. A. (2005) The Effect of Spark Retard on Engine-out Hydrocarbon Emissions, SAE Paper 2005-01-3867.

ERDIL, A. & KODAL, A. (2007) A comparative study of turbulent velocity fields in an internal combustion engine with shrouded valve and flat/bowl piston configurations. Proc. IMechE Part C: J. Mechanical Engineering Science, Vol 221, pp. 1597-1607.

EUROPEAN ENVIRONMENT AGENCY (EEA) (2014) Monitoring CO2 emissions from passenger cars and vans in 2013. EEA Technical Report, Vol 19(2014), pp. 14 - 30.

EUROPEAN PARLIAMENT, COUNCIL (2007) REGULATION (EC) No 715/2007 OF THE EUROPEAN PARLIAMENT AND OF THE COUNCIL of 20 June 2007 on type approval of motor vehicles with respect to emissions from light passenger and commercial vehicles (Euro 5 and Euro 6) and on access to vehicle repair and maintenance information. Official Journal of the European Union, Vol COD 2005/0282.

FISCHER, J., KETTNER, M., NAUWERCK, A., PFEIL, J. & SPICHER, U. (2002) Influence of an Adjustable Tumble-System on In-Cylinder Air Motion and Stratification in a Gasoline Direct Injection Engine, SAE Paper 2002-01-1645.

FRAIDL, G. K., MIKULIC, L. A. & QUISSSEK, F. (1990) Development strategies for low emission high performance four-valve engines. Proc. Instn Mech. Engrs, Part D, Vol 204(D1), pp. 59-65.

FRANCQUEVILLE, L. D., BRUNEAUX, G. & THIROUARD, B. (2010) Soot Volume Fraction Measurements in a Gasoline Direct Injection Engine by Combined Laser Induced Incandescence and Laser Extinction Method, SAE Paper 2010-01-0346.

GANDHI, H. S., GRAHAM, G. W. & MCCABE, R. W. (2003) Automotive exhaust catalysis. Journal of Catalysis, Vol 216(2003), pp. 433-442.

GHANDHI, J. B., HEROLD, R. E., SHAKAI, J. S. & STRAND, T. E. (2005) Time-resolved particle image velocimetry measurements in an internal combustion engine, SAE Paper 2005-01-3868.

GILLESPIE, L., LAWES, M., SHEPPARD, C. G. W. & WOOLLEY, R. (2000) Aspects of Laminar and Turbulent Burning Velocity Relevant to SI Engines, SAE Paper 2000-01-0192.

GREENBERG, J. B., MCINTOSH, A. C. & BRINDLEY, J. (1999) Instability of a flame front propagating through a fuel-rich droplet–vapour–air cloud. Combust. Theory Modelling, Vol 3(1999), pp. 567-584.

GUPTA, S., POOLA, R., O.L., K. & SEKAR, R. (2000) Particulate Emissions Characteristics of Port-Fuel Injected SI Engine. US Dept. of Energy.

HALLGREN, B. E. & HEYWOOD, J. B. (2003) Effects of Substantial Spark Retard on SI Engine Combustion and Hydrocarbon Emissions, SAE Paper 2003-01-3237.

HAN, Z., FAN, L. & REITZ, R. D. (1997) Multidimensional Modelling of Spray Atomization and Air-Fuel Mixing in a Direct-Injection Spark-Ignition Engine, SAE Paper 970884.

HAN, Z., REITZ, R. D., YANG, J. & ANDERSON, R. W. (1997) Effects of Injection Timing on Air-Fuel Mixing in a Direct-Injection Spark-Ignition Engine, SAE Paper 970625.

HARGRAVE, G. K., WIGLEY, G., ALLEN, J. & BACON, A. (2000) Optical Diagnostics and Direct Injection of Liquid Fuel Sprays. Journal of Visualization, Vol 2(3/4 2000), pp. 293-300.

HATTORI, H., OTA, M., SATO, E. & KADOTA, T. (1995) Fundamental study on DISC engine with two-stage fuel injection. JSME Int J 1995, Vol B38(1), pp. 129-35.

HEYWOOD, J. B. (1988) Internal Combustion Engine Fundamentals, 1st Ed., McGraw-Hill, pp. 42-61, 205-278, 400-450, 797-819.

HOARD, J. & MOILANEN, P. (1997) Exhaust Valve Seat Leakage, SAE Paper 971638.

HONG, H., PARVATE-PATIL, G. B. & GORDON, B. (2004) Review and analysis of variable valve timing strategies - eight ways to approach. Proc. Instn Mech. Engrs, Part D: J. Automobile Engineering, Vol 218, pp. 1179-1200.

IC ENGINE GROUP (2004) Combustion Burn Rate Analysis and Data Processing (COBRA), Department of Engineering Science, University of Oxford.

IWAMOTO, T., NOMA, K., YAMAUCHI, T. & ANDO, H. (1997) Development of gasoline direct injection, SAE Paper 970541.

JARVIS, S., JUSTHAM, T., CLARKE, A., GARNER, C. P. & HARGRAVE, G. K. (2006) Motored SI IC Engine In-Cylinder Flow Field Measurement Using Time Resolved Digital PIV For Characterisation of Cyclic Variation, SAE Paper 2006-01-1044.

JOHANSSON, B. (1991) Influence of the velocity near the spark plug on early flame

development, SAE Paper 930481.

JUSTHAM, T. (2010) Cyclic Variation in the Flow Field Behaviour within a Direct Injection Spark Ignition Engine: A High Speed Digital Particle Image Velocimetry Study, Loughborough, PhD Thesis, Loughborough University.

JUSTHAM, T., JARVIS, S., CLARKE, A., GARNER, C. P., HARGRAVE, G. K. & HALLIWELL, N. A. (2006) Simultaneous Study of Intake and In-Cylinder IC Engine Flow Fields to Provide an Insight into Intake Induced Cyclic Variations. Journal of Physics: Conference Series, Vol 45, pp. 146-153.

JUSTHAM, T., JARVIS, S., GARNER, C. P., HARGRAVE, G. K. & CLARKE, A. (2006) Single Cylinder Motored SI IC Engine Intake Runner Flow Measurement Using Time Resolved Digital Particle Image, SAE Paper 2006-01-1043.

KALGHATGI, G. T. (1987) Spark Ignition, Early Flame Development and Cyclic Variation in IC Engines, SAE Paper 870163.

KAPITZA, L., IMBERDIS, O., BENSLER, H. P., WILLAND, J. & THÉVENIN, D. (2010) An experimental analysis of the turbulent structures generated by the intake port of a DISI-engine. Exp Fluids (2010), Vol 48, pp. 265-280.

KEANE, R. D. & ADRIAN, R. J. (1990) Optimisation of Particle Image Velocimeters. Part I: Double Pulsed Systems. Meas. Sci. and Technol., Vol 1, pp. 1202-1215.

KIRCHWEGER, W., HASLACHER, R., HALLMANNSEGGER, M. & GERKE, U. (2007) Applications of the LIF method for the diagnostics of the combustion process of gas-IC-engines. Exp. Fluids, Vol 43, pp. 329-340.

KITTELSON, D. B., WATTS, W. F., JOHNSON, J. B., ZARLING, D., SCHAUER, J., KASPER, A., BALTENSPERGER, U. & BURTSCHER, H. (2003) Gasoline Vehicle Exhaust Particle Sampling Study. Proceeding of the 9th Diesel Engine Emission Reduction Conference (DEER 2003),. Newport, RI.

KULKARNI, P., BARON, P. A. & WILLEKE, K. (2011) Aerosol Measurement Principles, Techniques and Application, Wiley, Vol. 3.

KUME, T., IWAMOTO, Y., LIDA, K., MURAKAMI, M., AKISHINO, K. & ANDO, H. (1996) Combustion Control Technologies for Direct Injection SI Engine, SAE Paper 960600.

KUWAHARA, K., YAMAMOTO, S., IWACHIDOU, K. & ANDO, H. (1998) Two-Stage Combustion for Quick Catalyst Warm-up in Gasoline Direct Injection. The Fourth International Symposium COMODIA 98, pp. 293-298.

LAGET, O., ZACCARDI, J. M., GAUTROT, X., MANSION, T. & COTTE, E. (2010) Establishing New Correlations Between In-Cylinder Charge Motion and Combustion Process in Gasoline Engines Through a Numerical DOE. SAE Int. J. Engines, SAE Paper 2010-01-0349, Vol 3(1).

LASHERAS, J., VILLERMAUX, E. & HOPFINGER, E. J. (1998) Breakup and Atomization of a Round Water Jet by a High-Speed Annular Air Jet. Journal of Fluid Mechanics, Vol 357(1998), pp. 351-379.

LAWSON, N. J. (1995) The Application of Particle Image Velocimetry to High-Speed Flow, PhD Thesis, Loughborough University.

LEE, J. & FARRELL, P. V. (1993) Intake Valve Flow Measurements of an IC Engine Using Particle Image Velocimetry, SAE Paper 930480.

LEE, K., BAE, C. & KANG, K. (2007) The effects of tumble and swirl flows on flame propagation in a four-valve S.I. engine. Elsevier, Applied Thermal Engineering, Vol 27, pp. 2122-2130.

LEE, K. & LEE, C. S. (2003) Effects of tumble and swirl flows on turbulence scale near top dead centre in a four-valve spark ignition engine. Proc. Instn Mech. Engrs, Part D: J Automobile Engineering, Vol 217, pp. 607-615.

LEE, S., BAE, C., LEE, Y. & TAESIK, H. (2002) Engine, Effects of Engine Operating Conditions on Catalytic Converter Temperature in an SI, SAE Paper 2002-01-1677.

LEE, S., OH, Y. & PARK, S. (2013) Characterization of the spray atomization process of a multi-hole gasoline direct injector based on measurements using a phase Doppler particle analyser. Proc IMechE Part D: J Automobile Engineering, Vol 227(7), pp. 951-965.

LI, Y., LEACH, B., MA, T. & LADOMMATOS, N. (2004) Characterization of an in-cylinder flow structure in a high-tumble spark ignition engine. Int. J. Engine Res., Vol 5(5), pp. 375-400.

LI, Y., ZHAO, H. & LADOMMATOS, N. (2002) Analysis of large-scale flow characteristics in a four-valve spark ignition engine. Proc Instn Mech Engrs, Vol 216 Part C: J Mechanical Engineering Science, pp. 923-928.

LI, Y., ZHAO, H., LEACH, B., MA, T. & LADOMMATOS, N. (2003) Optimisation of In-Cylinder Flow for Fuel Stratification in a Three-Valve Twin-Spark-Plug SI Engine, SAE Paper 2003-01-0635.

LI, Y., ZHAO, H., LEACH, B., MA, T. & LADOMMATOS, N. (2004) Characterization of an in-cylinder flow structure in a high-tumble spark ignition engine. Int. J. Engine Res., Vol 5(5), pp. 375-400.

LONG, E. J. (2010) The Influence of Reactant Flow Structure on Flame Front Propagation, Loughborough, PhD Thesis, Loughborough University.

LONG, E. J., RIMMER, J. E. T., JUSTHAM, T., GARNER, C., HARGRAVE, G. K., RICHARDSON, D. & WALLACE, S. (2008) The Influence of In-Cylinder Turbulence upon Engine Performance within a Direct Injection IC Engine. Seventh International Conference on Modelling and Diagnostics for Advanced Engine Systems. Sapporo Japan.

LUMLEY, J. L. (1999) Engines: An Introduction, Cambridge University Press.

MAHMOOD, Z., CHEN, A. & YIANNESKIS, M. (1996) On the structure of steady flow through dual-intake engine ports. International Journal for Numerical Methods in Fluids, Vol 23, pp. 1085-1109.

MALY, R. & VOGEL, M. (1978) Initiation and Propagation of Flame Fronts in Lean CH4-Air Mixtures by the Three Modes of Ignition Spark. 17th Symposium (International) on Combustion, Vol 821-831.

MANSION, T., CROTEAU, D., FLOCH, A., TELLIER, A. & MOUNAÏM-ROUSSELLE, C. (2008) Experimental analysis of the effect of tumble motion on ignition and instabilities. The Seventh International Conference on Modelling and Diagnostics for Advanced Engine Systems (COMODIA 2008), Sapporo, Japan.

MEDERER, T., WENSING, M. & LEIPERTZ, A. (2012) Laser-Induced Fluorescence to Visualize Gas Mixture Formation in an Optically Accessible Hydrogen Engine. COMODIA. Fukuoka, Japan.

MERGERLE, M. & SICK, V. R., D.L. (2002) Measurement of digital particle image velocimetry precision using electro-optically created particle image displacements. Meas. Sci. and Technol., Vol 13, pp. 997-1005.

MIYAMOTO, N., OGAWA, H., SHUDO, T. & TAKEYAMA, F. (1994) Combustion and emissions in a new concept DI stratified charge engine with two-stage fuel injection, SAE Paper 940675.

MORITA, K., SONODA, Y., KAWASE, T. & SUZUKI, H. (2005) Emission Reduction of a Stoichiometric Gasoline Direct Injection Engine, SAE Paper 2005-01-3687.

MORIYOSHI, Y., NOMURA, H. & SAISYU (1997) Evaluation of a Concept for DI Gasoline Combustion Using Enhanced Gas Motion, SAE Paper 980152.

MULLER, S. H. R., BOHM, B., GLEISNER, M., GRZESZIK, R., ARNDT, S. & DREIZLER, A. (2010) Flow field measurements in an optically accessible, direct injection spray guided internal combustion engine using high-speed PIV. Exp. Fluids, Vol 48, pp. 281-290.

OMORI, S., IWACHIDO, K., MOTOMOCHI, M. & HIRAKO, O. (1991) Effect of Intake Port Flow Pattern on the In-Cylinder Tumbling Air Flow in Multi-Valve SI Engine, SAE Paper 910477.

OZDOR, N., DULGER, M. & SHER, E. (1994) Cyclic Variability in Spark Ignition Engines A Literature Survey, SAE Paper 940987.

PAJOT, O. & MOUNAÏM-ROUSSELLE, M. (2000) Instantaneous Flow Field Effects on the Flame Instantaneous Flow Field Effects on the Flame Optical Diagnostics, SAE Paper 2000-01-1796.

PATEL, R., LADOMMATOS, N., STANSFIELD, P., WIGLEY, G., GARNER, C. P., PITCHER, G., TURNER, J. W. G. & NUGLISCH, H. (2008) Comparison between Unthrottled, Single and Two-valve Induction Strategies Utilising Direct Gasoline Injection: Emissions, Heat-release and Fuel Consumption Analysis, SAE Paper 2008-01-1626.

PERSSON, H., AGRELL, M., J., O., JOHANSSON, B. & STRÖM, H. (2004) The Effect of Intake Temperature on HCCI Operation Using Negative Valve Overlap, SAE Paper 2004-01-0944.

PIOCK, W., HOFFMANN, G., BERNDORFER, A., SALEMI, P. & FUSSHOELLER, B. (2011) Strategies Towards Meeting Future Particulate Matter Emission Requirements in Homogeneous Gasoline Direct Injection Engines, SAE Paper 2011-01-1212.

PISCHINGER, S. & HEYWOOD, J. B. (1990) How heat losses to the spark plug electrodes affect flame kernel development in an SI Engine, SAE Paper 900021.

PITCHER, G. & WIGLEY, G. (2001) LDA Analysis of the Tumble Flow Generated in a Motored 4 Valve Engine. 9th Internal Conference, Laser Anemometry Advances and Applications. Limerick.

PRICE, P., STONE, R., COLLIER, T. & DAVIES, M. (2006) Particulate Matter and Hydrocarbon Emissions Measurements: Comparing First and Second Generation DISI with PFI in Single Cylinder Optical Engines, SAE Paper 2006-01-1263.

PRICE, P., STONE, R., OUDENIJEWEME, D. & CHEN, X. (2007) Cold Start Particulate Emissions From a Second-Generation DI Gasoline Engine, SAE Paper 2007-01-1931.

PULKRABEK, W. W. (2004) Engineering Fundamentals of the Internal Combustion Engine, Pearson Prentice-Hall, Vol. 2, pp. 198-230.

QUEIROZ, C. & TOMANIK, E. (1997) Gasoline Direct Injection Engines - A Bibliographical Review, SAE Paper 973113.

RAFFEL, M., WILLERT, C. E., WERELEY, S. T. & KOMPENHANS, J. (2007) Particle Image Velocimetry: A Practical Guide, 2nd Ed., Springer-Verlag.

RASSWEILER, G. M. & WITHROW, L. (1938) Motion Pictures of Engine Flames Correlated with Pressure Cards, SAE Paper 380139.

REEVES, M., HASTE, M., GARNER, C. P. & HALLIWELL, N. A. (1999) Barrel swirl breakdown in spark-ignition engines: insights from particle image velocimetry measurements. Proc Instn Mech Engrs, Vol 213(Part D), pp. 595-609.

REEVES, M., TOWERS, D. P., TAVENDER, B. & BUCKBERRY, C. H. (2000) A technique for routine, cycle-resolved 2-D flow measurements and visualisation within SI engine cylinders in an engine development environment. Proceedings of the 10th International Symposium on Applications of Laser Techniques to Fluid Mechanics. Lisbon, Portugal.

REUSS, D. L. (2000) Cyclic Variability of Large-Scale Turbulent Structures in Directed and Undirected IC Engine Flows, SAE Paper 2000-01-0246.

REUSS, D. L., MEGERKE, M. & SICK, V. (2002) Particle-image velocimetry measurement errors when imaging through a transparent engine cylinder. Meas. Sci. Technol., Vol 13(2002), pp. 1029-1035.

RIMMER, J. E. T. (2010) An Optical Investigation into the Effect of Fuel Spray, Turbulent Flow and Flame Propagation on DISI Engine Performance, Loughborough, PhD Thesis, Loughborough University.

RIMMER, J. E. T., DAVY, M. H., GARNER, C. P., HARGRAVE, G. K. & RICHARDSON, D. (2012) Fuel spray structure, flame propagation and charge motion at fuel impingement locations within a DISI engine. IMechE: Fuel Systems for IC Engines, Vol 2012, pp. 199-214.

RIMMER, J. E. T., LONG, E. J., GARNER, C. P., HARGRAVE, G. K., RICHARDSON, D. & WALLACE, S. (2009) The Influence of Single and Multiple Injection Strategies on In-Cylinder Flow and Combustion within a DISI Engine, SAE Paper 2009-01-0660.

RUSS, S., LAVOIE, G. & DAI, W. (1999) SI Engine Operation with Retarded Ignition: Part 1 - Cyclic Variations, SAE Paper 1999-01-3506.

SAHOO, B. B., SAHOO, N. & SAHA, U. K. (2009) Effect of engine parameters and type of gaseous

fuel on the performance of dual-fuel gas diesel engines—A critical review. Renewable and Sustainable Energy Reviews, Vol 13(2009), pp. 1151-1184.

SAMUEL, S., HASSANEEN, A. & MORREY, D. (2010) Particulate Matter Emissions and the Role of Catalytic Converter During Cold Start of GDI Engine, SAE Paper 2010-01-2122.

SANFORD, M., PAGE, G. & CRAWFORD, P. (2009) The All New AJV8, SAE Paper 2009-01-1060.

SCHMIDT, L., SEABROOK, J., STOKES, J., FAIZAN, M., ZUHDI, A., BEGG, S., HEIKAL, M. & KING, J. (2011) Multiple Injection Strategies for Improved Combustion Stability under Stratified Part Load Conditions in a Spray Guided Gasoline Direct Injection (SGDI) Engine, SAE Paper 2011-01-1228.

SCHREIBER, D., FORSS, A. M., MOHR, M. & DIMOPOULOS, P. (2007) Particle Characterization of Modern CNG, Gasoline and Diesel Passenger Cars, SAE Paper 2007-24-0123.

SCHWEITZER, P. H. (1938) Penetration of Oil Sprays. J. Appl. Phys., Vol 9(735), pp. 735-741.

SERRAS-PEREIRA, J., ALEIFERIS, P., RICHARDSON, D. & WALLACE, S. (2007) Spray Development in a Direct-Injection Spark-Ignition Engine, SAE Paper 2007-07-2712.

SERRAS-PEREIRA, J., ALEIFERIS, P. G., RICHARDSON, D. & WALLACE, S. (2007) Mixture Preparation and Combustion Variability in a Spray-Guided DISI Engine, SAE Paper 2007-01-4033.

SHELEF, M. & MCCABE, R. W. (2000) Twenty-five years after introduction of automotive catalysts: what next? Catalysts Today, Vol 62(2000), pp. 35-50.

SINGH, A. P., GUPTA, A. & AGARWAL, K. (2015) Tomographic Particle Image Velocimetry for Flow Analysis in a Single Cylinder Optical Engine. SAE Int. J. Mater. Manf., Vol 8(2).

SPEGAR, T. D. (2011) Minimizing Gasoline Direct Injection (GDi) Fuel System Pressure Pulsations by Robust Fuel Rail Design, SAE Paper 2011-01-1225.

STACH, T., SCHLERFER, J. & VORBACK, M. (2007) New Generation Multi-hole Fuel Injector for Direct-Injection SI Engines - Optimization of Spray Characteristics by Means of Adapted Injector Layout and Multiple Injection, SAE Paper 2007-01-1404.

STANGLMAIER, R. H., LI, J. & MATTHEWS, R. D. (1999) The Effect of In-Cylinder Wall Wetting Location on the HC Emissions from SI Engines, SAE Paper 1999-01-0502.

STANSFIELD, P., WIGLEY, G., GARNER, C. P., PATEL, R., LADOMMATOS, N., PITCHER, G., TURNER, J. W. G., NUGLISCH, H. & HELIE, J. (2007) Unthrottled Engine Operation using Variable Valve Actuation: The Impact on the Flow Field, Mixing and Combustion, SAE Paper 2007-01-1414.

STANSFIELD, P., WIGLEY, G., JUSTHAM, T., CATTO, J. & PITCHER, G. (2007) PIV analysis of in-cylinder flow structures over a range of realistic engine speeds. Exp Fluids (2007), Vol 43, pp. 135-146.

STEVENS, R. E., MA, H., STONE, C. R., WALMSLEY, H. L. & CRACKNELL, R. (2006) On planar laser-induced fluorescence with multi-component fuel and tracer design for quantitative determination of fuel concentration in internal combustion engines. Proc IMechE Part D, Vol 221, pp. 713-721.

STONE, C. R., CARDEN, T. R. & PODMORE, I. (1993) Analysis of the effect of inlet valve disablement on swirl, combustion and emissions in a spark ignition engine. Proc Instn Mech Engrs, Vol 207, pp. 295-305.

STONE, R. (1999) Introduction to Internal Combustion Engines, 3rd Ed., MacMillan Press Ltd., pp. 25-35, 285-293.

SVENSSON, K. I., MACKRORY, A. J., RICHARDS, M. J. & TREE, D. R. (2005) Calibration of an RGB, CCD Camera and Interpretation of its Two-Color Images for KL and Temperature, SAE Paper 2005-01-0648.

TENNEKES, H. & LUMLEY, J. L. (1972) A First Course in Turbulence, The MIT Press, Vol. 1.

TOMODA, T., SASAKI, S., SAWADA, D., SAITO, A. & SAMI, H. (1997) Development of direct injection gasoline engines - study of stratified mixture formation, SAE Paper 970539.

TOWERS, D. P. & TOWERS, C. E. (2004) Cyclic variability measurements of in-cylinder engine flows using high-speed particle image velocimetry. Meas. Sci. and Technol., Vol 15, pp. 1917-1925.

TUTTLE, J. H. (1982) Controlling Engine Load by Means of Early Intake-Valve Closing, SAE Paper 820408.

TWINEY, B., STONE, R., CHEN, X. & EDMUNDS, G. (2010) Investigation of Combustion Robustness in Catalyst Heating Operation on a Spray Guided DISI Engine, Part 1 - Measurements of Spark Parameters and Combustion, SAE Paper 2010-01-0593.

TWINEY, B., STONE, R., CHEN, X. & EDMUNDS, G. (2010) Investigation of Combustion Robustness in Catalyst Heating Operation on a Spray Guided DISI Engine, Part II - Measurements of Spray Development, Combustion Imaging and Emissions, SAE Paper 2010-01-0603.

UCHIDA, R., TANAKA, D. & NODA, T. (2015) Impingement Behaviour of Fuel Droplets on Oil Film, SAE Paper 2015-01-0913.

VIRTANEN, A. K. K., RISTIMAKI, J. M., VAARASLAHTI, K. M. & KESKINEN, J. (2004) Effect of Engine Load on Diesel Soot Particles. Environ. Sci. Technol. 2004, Vol 38(9), pp. 2551-2556.

VISNIC, B. (2011) Mazda DISI Proves Timing is Everything, Ward's AutoWorld. Available from: http://wardsautoworld.com/ar/auto_story_behind_wards_2/, [Accessed 17th May].

WHELAN, I., TIMONEY, D., SMITH, W. & SAMUEL, S. (2013) The Effect of a Three-Way Catalytic Converter on Particulate Matter from a Gasoline Direct-Injection Engine During Cold-Start. SAE Int. J. Engines, Vol 6(2).

WHITAKER, P., KAPUS, P., OGRIS, M. & HOLLERER, P. (2011) Measures to Reduce Particulate Emissions from Gasoline DI engines, SAE Paper 2011-01-1219.

WIGLEY, G., GOODWIN, M., PITCHER, G. & BLONDEL, D. (2004) Imaging and PDA analysis of a

GDI spray in the near-nozzle region. Experiments in Fluids 36, Vol 2004, pp. 565-574.

WIGLEY, G., HARGRAVE, G. K. & HEATH, J. (1998) A High Power, High Resolution LDA/PDA System Applied to Dense Gasoline Direct Injection Sprays. 9th International Symposium on Applications of Laser Techniques to Fluid Mechanics, Lisbon, Portugal, pp. 9.4.1-9.4.8.

WILLIAMS, B., EWART, P., STONE, R., MA, H., WALMSLEY, H., CRACKNELL, R., STEVENS, R., RICHARDSON, D., QIAO, J. & WALLACE, S. (2008) Multi-Component Quantitative PLIF: Robust Engineering Measurements of Cyclic Variation in a Firing Spray-Guided Gasoline Direct Injection Engine, SAE Paper 2008-01-1073.

WILLIAMS, F. A. (1985) Combustion Theory: The fundamental theory of chemically reacting flow systems, The Benjamin/Cummings Publishing Company.

WILSON, T., HASTE, M., XU, H., RICHARDSON, S., YAP, D. & MEGARITIS, T. (2005) In-cylinder Flow with Negative Valve Overlapping - Characterised by PIV Measurement, SAE Paper 2005-01-2131.

XU, M., NISHIDA, K. & HIROYASU, H. (1992) A Practical Calculation Method for Injection Pressure and Spray Penetration in Diesel Engines, SAE Paper 920624.

XU, M., ZHANG, Y., ZENG, W., ZHANG, G. & ZHANG, M. (2013) Flash Boiling: Easy and Better Way to Generate Ideal Sprays than the High Injection Pressure. SAE Int. J. Fuels Lubr., Vol 6(1), pp. 137-148.

YAMADA, T., GARDNER, D. V., BRUNO, B. A., ZELLO, J. V. & SANTAVICCA, D. A. (2002) The Effects of Engine Speed and Injection Pressure Transients on Gasoline Direct Injection Engine Cold Start, SAE Paper 2002-01-2745.

YASAR, A., SAHIN, B., AKILLI, H. & AYDIN, K. (2006) Effect of inlet port on the flow in the cylinder of an internal combustion engine. Proc. IMechE Part C: J. Mechanical Engineering Science, Vol 220, pp. 73-82.

ZENG, W., XU, M., ZHANG, M., ZHANG, Y. & CLEARY, D. (2010) Characterization of Methanol and Ethanol Sprays from Different DI Injectors by Using Mie-scattering and Laser Induced Fluorescence at Potential Engine Cold-start Conditions, SAE Paper 2010-01-0602.

ZHAN, R., EAKLE, S. T. & WEBER, P. (2010) Simultaneous Reduction of PM, HC, CO and NOx Emissions from a GDI Engine, SAE Paper 2010-01-0365.

ZHAO, F., HARRINGTON, D. L. & LAI, M. C. (1999) Automotive spark-ignited direct-injection gasoline engines. Progress in Energy and Combustion Science 25, Vol 1999, pp. 437-562.

ZHAO, F., HARRINGTON, D. L. & LAI, M. C. (2002) Automotive Gasoline Direct-Injection Engines, SAE International, pp. 1-50, 166-188, 223-260.

ZHAO, F. & LADOMMATOS, N. (1998) Optical diagnostics for soot and temperature measurement in diesel engines. Progress in Energy and Combustion Science, Vol 24(3), pp. 221-255.

ZHAO, F. & LAI, M. C. (1995) Optical diagnostics for soot and temperature measurement in diesel engines, SAE Paper 950506.